

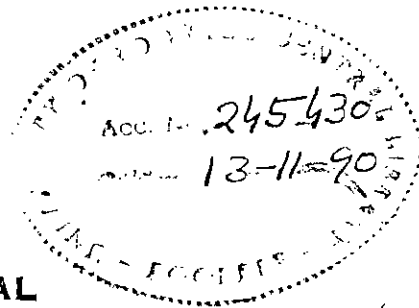
BEHAVIOUR OF FERROCEMENT BOX GIRDER ELEMENTS

A THESIS

Submitted in fulfilment of the requirements
for the award of the degree
of
DOCTOR OF PHILOSOPHY
in
CIVIL ENGINEERING

By

VIJAY KUMAR SEHGAL



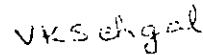
DEPARTMENT OF CIVIL ENGINEERING
UNIVERSITY OF ROORKEE
ROORKEE-247 667 (INDIA)
NOVEMBER, 1989

CANDIDATE'S DECLARATION

I hereby certify that the work which is being presented in the thesis entitled **BEHAVIOUR OF FERROCEMENT BOX GIRDER ELEMENTS** in fulfilment of the requirement for the award of the Degree of Doctor of Philosophy submitted in the Department of Civil Engineering of the University of Roorkee, is an authentic record of my own work carried out during a period from August 1985 to September 1989 under the supervision of **Dr. S.K. Kaushik**, Professor of Civil Engineering and **Dr. N.M. Bhandari**, Reader in Civil Engineering, University of Roorkee, Roorkee (U.P.).

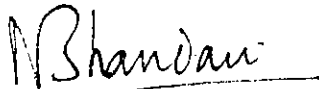
The matter embodied in this thesis has not been submitted by me for the award of any other degree.

Candidate's Signature




(VIJAY KUMAR SEHGAL)

This is to certify that the above statement made by the candidate is correct to the best of our knowledge.



(N.M. BHANDARI)
Reader
Department of Civil Engg.,
University of Roorkee
ROORKEE 247 667



(S.K. KAUSHIK)
Professor
Department of Civil Engg.,
University of Roorkee
ROORKEE 247 667

(Signature of Supervisors)

Date : 4.11.89.

The candidate has passed the viva-voce examination held on
at The thesis is recommended for award of
the Ph.D. degree.

Signature of Guide(s)

Signature of External Examiner

ABSTRACT

Ferrocement has been used in a variety of applications such as boats, tanks, silos and roofs. For roofing purposes, its behaviour has been investigated by many researchers in the form of channel sections, ribbed slabs, folded plates and shells of various shapes. Only channel sections and ribbed slabs provide a flat top surface. Due to their small flexural rigidities, these elements undergo large deflections and cracking at service loads. To reduce deflection and cracking and also to have a flat top surface, a new type of roofing/flooring element in the form of box girder shape has been investigated experimentally and analytically in the present study.

The experimental investigation has been carried out by testing near prototype size ferrocement box girders. Two box girders were tested under uniformly distributed load (udl) over the entire top flange and two other under udl over half flange width and full span. Two box girders were joined at the level of top flange. The combined box girder was loaded and unloaded under various load combinations in the uncracked stage. The girder was later subjected to monotonically increasing sustained loads of short durations. One composite box girder made of bottom flange and side webs of ferrocement and top flange of reinforced concrete was cast and tested under udl over the entire top flange. After unloading it was again subjected to sustained loads of short durations upto the penultimate load and for ten and half months at maximum applied load.

For the elastic analysis of threedimensional ferrocement structures such as folded plates and shells of various shapes, beam theory, membrane theory, membrane-bending theory and finite element method have been used by various researchers. The analysis in the cracked range has been reported only in the case of folded plates using beam theory to predict deflections, first crack

(ii)

load and ultimate load. Even the elastic analysis of folded plates using beam theory is an approximate one because it does not take into account the distortion and warping of the cross-section. The analysis in the cracked range is even more approximate as it does not take into account the changing rigidity of the material at different sections, material anisotropy and yielding of the reinforcement leading to local redistribution of stresses.

To overcome above deficiencies, finite element method has been used to predict the behaviour of ferrocement box girders through the elastic, cracked and ultimate stages. Further to economize the finite element solution, the conventional layered approach has been suitably modified for thin ferrocement plated structures. Instead of considering the element to be consisting of suitable number of layers of mortar and reinforcement, the element is assumed to be consisting of single mortar layer in the uncracked stage, uncracked and cracked mortar layers in the cracked stage and smeared layers of wire mesh and skeletal steel. In the cracked stage, the depth of cracked/yielded/crushed mortar is determined. The stiffness of the element in the cracked stage is obtained by adding the contributions due to uncracked mortar layer, cracked/yielded mortar layer and unyielded layers of wire mesh and skeletal steel.

The finite element analysis has been carried out under dead loads and monotonically increasing live loads. A rectangular flat shell element capable of representing membrane action, bending action and the interaction between membrane and bending action is adopted. Only material nonlinearity due to cracking of mortar, tension stiffening effect of mortar between the cracks and the nonlinear stress-strain relationships for the mortar, wire mesh and skeletal steel is considered. Since the box section provides large flexural and torsional rigidity, the deflections in the cracked range are found to be small and hence, geometrical nonlinearity is not considered. Also not considered

in the analysis are bond slip between the reinforcement and mortar, time dependent and thermal effects.

An incremental iterative procedure capable of taking advantage of both the tangent and constant stiffness approach has been used for the nonlinear analysis. A general computer program has been developed to facilitate computer aided analysis.

The validation of the proposed analytical formulation has been checked by comparing the predicted results with the reported experimental/analytical results of typical test problems taken from the literature as well as with the experimental results of the present investigation.

The predicted values from the proposed analytical method are generally in good agreement with the experimental values except near the ultimate failure load where predicted values are on the flexible side.

The experimental investigation shows that the limit state of serviceability for ferrocement box girders is governed by the maximum crack width. At the recommended crack width of 0.1 mm, the span/deflection ratio is much above the value of 250 as permitted by I.S. Code. At a span/deflection ratio of 250, the load taken by the girders is close to the yielding of the reinforcement.

The double cell box girder under various combinations of symmetric and unsymmetric loads in the uncracked stage has behaved as one single unit by undergoing downward deflections along the entire length and width. This demonstrates the large load distribution capability of the box section.

Replacing the top ferrocement flange by a reinforced concrete one results into the lowering of the first crack load and ultimate load.

The failure of the girders is characterized by well distributed flexural cracks over the bottom flange and the side webs. Shear cracks which developed near ultimate load were not significant. The girders have shown high ductility by undergoing deflection at ultimate load equal to 5.0 to 6.0 times the deflection at the appearance of first cracks. The ultimate load was found to be 2.0 to 3.0 times the first crack load.

The predicted crack-patterns of the bottom flange and the side webs (at ultimate or maximum applied loads) of various girders show good agreement with the experimental crack-patterns. The added advantage of the analytical method is the prediction of cracks on the bottom surface of the top flange (being inside the box) at ultimate or near ultimate loads.

The increase in deflections or strains due to monotonically increasing sustained loads of short duration is maximum in the initial portion of the cracked range. The instantaneous deflection of the girder is reduced due to the sustained loading at lower load levels as compared to the instantaneous deflection that would have occurred under monotonically increasing loads. The sustained loading also leads to an increase in the width of cracks and the region of cracks formation. However, the ultimate load of the girder is not affected by monotonically increasing sustained loads of short duration.

ACKNOWLEDGEMENTS

The author is deeply indebted to Dr. S.K. Kaushik, Professor of Civil Engineering, University of Roorkee, Roorkee, for unfolding new vista of ferrocement technology to him and for his able guidance coupled with patience and benediction. The valuable assistance rendered by Dr. Kaushik by way of numerous discussions, arranging facilities and constant encouragement despite his hectic schedule is gratefully acknowledged.

The able guidance rendered by Dr. N.M. Bhandari, Reader in Civil Engineering, University of Roorkee, Roorkee in the analytical work and computer techniques is thankfully acknowledged. His keen interest and meticulous corrections, made this work reach the present stage.

The author is grateful to Dr. D.N. Trikha, Professor of Civil Engineering, for suggesting the nonlinear analysis using finite element method. The valuable suggestions given by Dr. G.C. Nayak, Professor & Head of Civil Engineering Department are gratefully acknowledged.

The author thanks the Department of Science and Technology, Government of India, New Delhi for providing financial assistance in carrying out the experimental investigations of the present study.

The author is also thankful to the Principal, Regional Engineering College, Kurukshetra for sanctioning him three years of study leave to pursue the Ph.D. programme.

Heartful thanks are due to all the staff of the concrete laboratory, test hall and workshop of Civil Engineering Department who fully cooperated with the author during the experimental work. The author also thanks the staff of the Regional Computer Centre, University of Roorkee, Roorkee for the facilities and help during computational work.

The author also thanks Ashok K. Sharma for elegantly typing the manuscript and S.S. Gupta and K.D. Saini for preparing the tracings.

The author is deeply moved by the allround support given throughout the period of this work by his friends namely A.K. Sharma, Manoj Arora, R.C. Bhattacharjee and U.B. Chitranshi and his family. Their affection and help is thankfully acknowledged.

Last but not the least, the author expresses his indebtedness to his wife Sujata, daughter Mahima and son Vineet as the present work is much because of their continued understanding, help and personal sacrifices.

CONTENTS

Chapter	Page No.
CERTIFICATE	
ABSTRACT	(i)
ACKNOWLEDGEMENT	(v)
LIST OF SYMBOLS	(xii)
I. INTRODUCTION	
1.1 Ferrocement	1
1.2 Historical Development	3
1.3 Object and Scope	9
1.4 Thesis Organisation	11
II. LITERATURE REVIEW	
2.1 General	12
2.2 Mechanical Properties	12
2.2.1 Ferrocement in Tension	12
2.2.2 Ferrocement in Compression	19
2.2.3 Ferrocement in Flexure	22
2.2.4 Shear Strength	33
2.2.5 Fatigue Resistance	33
2.2.6 Impact Resistance	36
2.2.7 Shrinkage and Creep	37
2.2.8 Durability	40
2.3 Behaviour of Joints	43
2.4 Brief Detail of Investigations Carried out on Various Types of Roofing Elements	
2.4.1 Channel Sections	44
2.4.2 Ribbed Slabs/Shells	46
2.4.3 Folded Plates	47

2.4.4	Cylindrical Shells	51
2.4.5	Hyperbolic Paraboloid Shell	52
2.4.6	Funicular Shells	52
2.4.7	Tension Ribbon	53
2.5	Concluding Remarks	54
III.	METHOD OF ANALYSIS	
3.1	General	58
3.2	Brief Review of Various Methods of Analysing Thin Walled Box Girder Elements	59
3.3	Choice of the Method of Analysis	60
3.4	Finite Element Formulation of the Problem	
3.4.1	Choice of the Element	62
3.4.2	Basic Formulation for Elastic Analysis	64
3.4.3	Material Modelling and failure Criteria	
3.4.3.1	Mortar	75
3.4.3.2	Wire meshes and skeletal steel	82
3.4.4	Rigidities of the Composite Material	82
3.4.5	Nonlinear Analysis	
3.4.5.1	Method of nonlinear analysis	91
3.4.5.2	Convergence criteria	94
3.5	Computer Program	96
3.6	Test Problems	
3.6.1	Test Problem for Elastic Analysis	100
3.6.2	Test Problems for Nonlinear Analysis	101
3.7	Concluding Remarks	109
IV.	EXPERIMENTAL PROGRAMME	
4.1	Introduction	129

4.2	Materials	130
4.2.1	Cement	130
4.2.2	Sand	130
4.2.3	Aggregate	132
4.2.4	Wire mesh	132
4.2.5	Skeletal Steel Bars	133
4.2.6	Water	133
4.2.7	Superplasticizer	133
4.2.8	Chromium trioxide	133
4.2.9	Cement-Sand Mortar and Concrete Mix	134
4.3	Casting of Box Girders	134
4.4	Testing Arrangement	140
4.5	Testing of Girders	142
4.6	Presentation of Test Results	144
4.6.1	Single Cell Box Girders	145
4.6.1.1	Girders subjected to udi over the entire top flange	145
4.6.1.2	Girders subjected to udl over half flange width and full span	150
4.6.2	Double Cell Box Girder	155
4.6.2.1	Double cell box girder subjected to various combinations of symmetric and unsymmetric loads in uncracked stage	155
4.6.2.2	Double cell box girder subjected to monotonically increasing sustained loads of short durations	161
4.6.3	Composite Box Girder	166
4.6.3.1	Composite box girder subjected to udl over the entire top flange	166
4.6.3.2	Reloading of the composite box girder and subjected it to sustained loading	168

V. TEST RESULTS AND COMPARISON WITH ANALYTICAL PREDICTIONS

5.1	Introduction	179
5.2	Single Cell Ferrocement Box Girders Subjected to udl Over the Entire Top Flange	179
5.2.1	General Test Behaviour	179
5.2.2	Finite Element Idealization	180
5.2.3	Comparison of Results	181
5.3	Single Cell Ferrocement Box Girders Subjected to udl Over the Half Flange Width and Full Span	187
5.3.1	General Test Behaviour	187
5.3.2	Finite Element Idealization	188
5.3.3	Comparison of Results	189
5.4	Composite Single Cell Box Girder with Top Flange of Reinforced Concrete	194
5.4.1	General Test Behaviour	194
5.4.2	Finite Element Idealization	195
5.4.3	Comparison of Results	195
5.5	Double Cell Box Girder	199
5.5.1	Unsymmetric Loading Cases	200
5.5.2	Symmetric Loading cases	204
5.6	Crack Width and Crack Spacing	207
5.7	Concluding Remarks	212

VI. BEHAVIOUR UNDER SUSTAINED LOADS OF SHORT DURATION

6.1	General	247
6.2	Experimental Investigations	248
6.3	Finite Element Idealization and Comparison of Results	249
6.4	Crack Widths and Crack Spacing	252

6.5	Reloading the Composite Box Girder and Subjected it to Sustained Loading at Various Load Levels	255
-----	---	-----

6.6	Concluding Remarks	256
-----	--------------------	-----

VII. CONCLUSIONS AND SCOPE FOR FURTHER WORK

7.1	Summary	267
-----	---------	-----

7.2	Conclusions	269
-----	-------------	-----

7.3	Scope for Further Work	272
-----	------------------------	-----

	REFERENCES	274
--	------------	-----

a
b
c
d
e
f
g
h
i
j
k
l
m
n
o
p
q
r
s
t
u
v
w
x
y
z

LIST OF SYMBOLS

The following list contains the main symbols and notations used in the text. Sometimes a symbol may have an alternative meaning but the context is sufficient to avoid confusion.

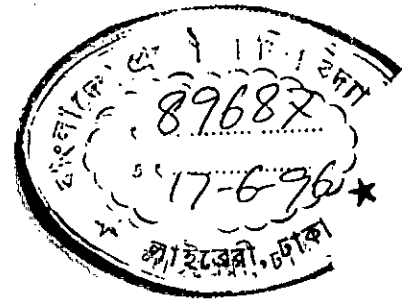
A, A_j	constant, constant of the series, element area
A_e	effective area of mortar below the neutral axis
A_f	area of mesh reinforcement in the cross-section
A_{ff}	area of cross-section of the wire
A_{ftx}, A_{fty}	area of mesh per unit width above the reference plane along x direction, along y direction
A_{fbx}, A_{fby}	area of mesh per unit width below the reference plane along x direction, along y direction
A_g	gross area of the cross-section
A_m	area of mortar in the cross-section
A_{mm}	matrix area of the assumed model
A_s, A_{sc}, A_{st}	area of skeletal steel in the cross-section, in the compression zone and in the tension zone
A_{stx}, A_{sty}	area of skeletal steel per unit width above the reference plane along x direction, along y direction
A_{sbx}, A_{sby}	area of skeletal steel per unit width below the reference plane along x direction, along y direction
a	distance from extreme compressive face to the level under consideration or side of the rectangular element along x axis.
B	constant
$[B], [B_m], [B_b]$	strain derivative matrices
b	side of the rectangular element along y axis
C, C_b	constant, bond correction factor
C_i, C_j	weighting coefficients
c	cosine of the angle between x and x' axis
D	constant, depth of the section
D_e	effective depth of the section
$[D], [D_T], [D'_T], [D'_t], [D'_b], [D'_f]$	material property matrices
$[D_{mm}], [D_{mb}], [D_{bb}], [D'_{mm}]$	
$[D'_{mb}], [D'_{bb}]$	membrane, membrane-bending and bending rigidities

$D_{tx}, D_{ty},$ D_{stx}, D_{sty}	distances of smeared wire mesh/skeletal steel layers along x/y directions above the reference plane
$D_{bx}, D_{by},$ D_{sbx}, D_{sby}	distances of smeared wire mesh/skeletal steel layers along x/y directions below the reference plane
d	diameter of the wire
E	constant
E_c, E_m E_f, E_s	modulus of elasticity of the composite, mortar, wire mesh and skeletal steel
E_{cr}	modulus of elasticity of the cracked composite
$\ E_R\ , \ E_f\ $	energy norm due to residual forces, applied loads
$F(t)$	constant
$\{F\}, \{\bar{F}\}$	nodal force vector general, transformed
$\{F_m\}$	membrane forces at gauss points
$\ F\ $	norm of applied loads
G	shear modulus of the mortar
I_e, I_{cr}	moment of inertia of gross transformed equivalent section, cracked transformed equivalent section
$K, K_1, K_2,$ K_t, K_b	constants
$[K]^e, [K]$	stiffness matrix of the element, structure
$[K_{mm}], [K_{mb}],$ $[K_{bb}]$	membrane, membrane-bending and bending stiffness of the element
L	effective span of the member
M	moment due to applied load
M_{cr}, M_u	moment at first crack, at ultimate failure
M_{fu}, M_{su}	moment contribution from mesh-mortar combination, from skeletal steels of compression and tension zones
$\{M\}$	bending moments at gauss points
m	modular ratio equal to E_f/E_m
N	number of cycles to failure or number of terms of the series
N_f	fatigue life in kilocycles,
$[N], [N_m],$ $[N_b]$	shape function, general, membrane, bending
l, m, n	direction cosines

P_m, P_s	ratio of mesh, skeletal steel reinforcement to the area of cross-section
P_u	ultimate load
$\{p\}$	body force vector
R	ratio of volume fraction of mortar to the volume fraction of mesh or also equal to A_{mm}/A_{ff}
R'	ratio of the distances to the neutral axis from the extreme tension fiber and from the centre of extreme layer of wiremesh
$\{R_o\}$	unbalanced nodal force vector
r	ratio of number of cycles to the number of cycles to failure
S	maximum repeated load expressed as percentage of the ultimate static load
S_f	spacing of transverse wires
S_L, S_{LT}	specific surface of the mesh reinforcement in loading direction in direct tension, in flexure
S_r	stress range in the extreme layer of wire mesh
S_{ms}	sum of mesh-mortar and mesh-skeletal steel parameters
s	sine of the angle between x and x' axis
$[T], [\bar{T}]$	transformation matrices
t	thickness of the element
t_{top}, t_{bot}	depths of the mortar cracked or yielded/crushed
t_{cu1}, t_{cu2}	depths of the mortar crushed
u_o, \bar{u}_o	displacement along local x axis, along global X axis
V	volume of the element
V_m, V_f	volume fractions of mortar and mesh in the loading direction
v_o, \bar{v}_o	displacement along local y axis, along global Y axis
w_o, \bar{w}_o	displacement along local z axis, along global Z axis
w_{avg}, w_{max}	average, maximum, design average crack widths
w_d	average, maximum, design average crack widths
x	distance of neutral axis from extreme compressive face
\bar{x}	distance between the centre of compression and tension zone skeletal steels
y_c	distance of the extreme tension fiber to the neutral axis
y_t	distance from reference plane
z	distance from reference plane
α	constant
β	constant depending upon the loading, the angle between x and x' axis
γ_{xy}	shear strain
δ	vertical deflection

$\{\delta\}, \{\bar{\delta}\}$	
$\{\delta_m\}, \{\delta_b\}$	nodal deformation vector, general, transformed, membrane, bending
ξ, η	dimensionless coordinates
n	effectiveness factor of the mesh
n'	ratio of bond strength between mesh and mortar to the tensile strength of mortar
Ψ, Ψ_y	curvature at a given load, at yielding of mesh
$\lambda_{avg}, \lambda_{max}$	spacing of cracks, average, maximum
$\theta_x, \theta_y, \theta_z,$ $\bar{\theta}_x, \bar{\theta}_y, \bar{\theta}_z$	rotations about local x, y, z axis; rotations about global X, Y, Z, axis.
ν	Poisson's ratio
$\sigma_{cr}, \sigma_{crb}$	first crack stress in tension, in bending
σ_{cu}	crushing strength of mortar
σ_f, σ_f'	
σ_{fy}, σ_{fu}	stress in any mesh layer, in extreme layer of wire mesh, yield strength and ultimate strength of wire mesh
σ_{fp}, σ_{fr}	strength of ferrocement plate, modulus of rupture of mesh mortar combination
σ_{mu}, σ_{mr}	tensile strength, modulus of rupture of mortar
σ_{sy}	yield strength of skeletal steel
σ_{ty}	yield stress of the composite
σ_{ub}	bending tensile stress in extreme fibre of the composite at ultimate
τ_u	ultimate bond strength of mortar
$\{\sigma\}, \{\sigma_0^i\}$	stress vector, generalized, initial
ϵ_a	strain in mortar fibre at distance 'a' below the extreme compression face
ϵ_{cr}	cracking strain of the mortar
ϵ_f'	tensile strain in extreme layer of wire mesh
ϵ_{ty}	strain at which composite yields
$\{\epsilon_0\}, \{\chi_0\}$	membrane strains and curvatures of the reference plane
$\{\epsilon_0^i\}$	initial strain vector

CHAPTER I
INTRODUCTION



1.1 FERROCEMENT

ACI Committee 549⁽¹⁾ defined ferrocement in a broader sense as a type of thin wall reinforced concrete commonly constructed of hydraulic cement mortar reinforced with closely spaced layers of continuous and relatively small diameter mesh. The mesh may be made of metallic or other suitable materials. The development of ferrocement evolved from the fundamental concept behind reinforced concrete that concrete can withstand large strains in the neighbourhood of the reinforcement, and the magnitude of the strains depends on the distribution and subdivision of the reinforcement throughout the mass of the concrete⁽²⁾. Ferrocement behaves as a composite because the properties of its brittle mortar matrix are improved due to the presence of ductile wiremesh reinforcement. The closer spacing of the wiremeshes (distribution) in the rich cement sand mortar and the smaller spacing of wires in the mesh (subdivision) impart ductility and better crack arrest mechanism to the material. The surface area to volume ratio (specific surface) of its reinforcement is an order of magnitude higher than that of ordinary reinforced concrete⁽³⁾. This results in a much higher first crack strength of the composite. The first crack strength of the composite can be further increased by including short steel fibres^(4,5) or by short steel fibers and polymer dispersion⁽⁶⁾. Its ultimate strength depends almost entirely upon the volume fraction of the wiremesh⁽⁴⁾. At working loads, its behaviour is characterized by well distributed fine cracks as compared to a few random cracks of relatively larger crack width in ordinary reinforced concrete. The optimum use of ferrocement lies in areas where its high tensile strength and small thickness is judiciously utilized.

Due to its small thickness, the self weight of ferrocement elements per unit area is quite small as compared to reinforced concrete elements. The thickness of ferrocement elements normally ranges from 10 mm to 40 mm, where as in reinforced concrete elements, the minimum thickness used for shell or plate elements is around 75 mm. Low self weight and high tensile strength make ferrocement a favourable material for prefabrication. Its construction does not require heavy plant and machinery. However, it is labour intensive. It becomes economical in situations where the cost of the raw materials is high and the labour is cheap. Such situation prevails in developing countries like India and other third world countries. Ferrocement construction may be made competitive in developed countries by mechanising the construction methods.

The basic raw materials required for ferrocement are cement, sand, water, wire meshes and small diameter mild steel rods. The cement should normally be of ordinary portland type. It should conform to the specifications of I.S. 269-1976⁽⁷⁾ or ASTM Standard C-150⁽⁸⁾. The sand should conform to the specifications of I.S. 383 -1970⁽⁹⁾ or ASTM Standard C-33⁽¹⁰⁾ and C-40⁽¹¹⁾. The water should be free from impurities. The water which is good for drinking should be used in the mortar. The cement sand ratio in the mortar varies from 1:1.5 to 1:2.5 and water cement ratio from 0.35 to 0.50 by weight. Wire meshes of different types such as hexagonal (chicken wiremesh), square woven, welded, expanded metal and Watson mesh⁽¹²⁾ are available. Most common of these are hexagonal, square woven and welded wire-meshes. The main requirement is that it should be easily handled and, if necessary, flexible enough to be bent around sharp corners. The ACI Committee 549-Ferrocement Guide⁽¹³⁾ has specified the minimum yield strength and effective modulus of elasticity for wiremeshes. The wiremeshes may be galva-

nized or ungalvanized. If the wiremesh is galvanized and used alongwith ungalvanized mild steel bars, then chromiumtrioxide^(14,15) at the rate of 100 to 300 parts per million by weight of water should be added in preparing the mortar. This effectively reduces the reaction between the galvanized mesh and the ungalvanized spacing steel between the layers of mesh. The wire meshes are generally made of 0.5 mm to 1.0 mm diameter wire and spaced at 5 mm to 25 mm apart. The volume fraction of the mesh ranges from 1 to 8 percent of the total volume of the element. The mild steel rods of 4 mm to 10 mm diameter are used in some situations to act as skeletal steel. If their spacing is around 300 mm centre to centre, then these are treated as spacer bars between the meshes. If the spacing is around 75 mm centre to centre, then these also act as reinforcing bars alongwith the mesh reinforcement. The minimum cover to the outermost mesh layer is around 2 mm to 5 mm.

1.2 HISTORICAL DEVELOPMENT

The credit of using ferrocement in the present day form goes to Joseph Louis Lambot who in 1848 constructed several rowing boats, plant pots, seats and other items from a material he called 'Ferciment'⁽¹⁶⁾. Lambot's construction consisted of a mesh or grid reinforcement made up of two layers of small diameter iron bars at right angle and plastered with a cement mortar with a thin cover to the reinforcement. Lambot's rowboats were 3.66 m long, 1.22 m wide and 25 mm to 38 mm thick. These were reinforced with grid and wire netting. One of the boat built by him, still in remarkably good condition, is on display in the museum at Brignoles, France.

Using Lambot's technique, many boats were built in the latter half of the nineteenth century. The famous among them is a scow called Zeemeeuw.

(the Seagull) built in 1887^(17). A few small motor boats and river crafts were built in the early part of the twentieth century. It was during the First and Second World Wars that serious attention was paid to the use of ferrocement for shipbuilding. This was due to a severe shortage of good quality timber and steel plates.

In the early 1940's, Pier Luigi Nervi conducted the first tests on ferrocement slabs. It was observed that mortar reinforced with layers of wiremesh produced a material which possessed the mechanical properties of a homogeneous material, and showed great resistance to impact, and increase in elasticity in proportion to the distribution and subdivision of the reinforcement throughout the mass⁽¹⁸⁾.

In 1945, Nervi built the 165 ton motor yacht 'Irene' on a supporting frame of 6.35 mm dia rods spaced 101.6 mm apart with four layers of wire-mesh on each side of rods. It was plastered by hand with a rich cement mortar resulting in a total thickness of about 35 mm. It weighed five percent less than a comparable wooden hull and cost forty percent less at that time.

In 1947, Nervi built the first terrestrial ferrocement structure, a storage ware house of about 10.7 m x 21.3 m size. The strength of the structure was due to the corrugations of the wall and roof, which were 44.45 mm thick.

In 1948, Nervi used ferrocement in the first public structure, the Turin Exhibition Building. The Central hall of the building, which spans 91.4 m, was built of prefabricated ferrocement elements connected by reinforced concrete arches at the top and bottom of the undulations. Prefabricated ferrocement beams were used in the erection of the peripheral undulated roof of Hall C of the exhibition building. Prefabricated ferrocement elements made possible the short construction schedule and the need for very light main structures covering large spans.

Nervi used ferrocement elements in a number of structures. Notable among them are the roofs of the swimming pool of the Italian Naval Academy, Leghorn, 1949 and the Palazetto Dello Sport, Rome, 1960^(2). He also used ferrocement to act as formwork for casting reinforced concrete elements in Bologna Tobacco Factory, 1949; Gatty Wood Factory, Rome, 1951 and Fiat Factory, Turin, 1954.

In 1953, Oberti^(19) carried out model tests to support the design of the hemicycle shaped central pavillion of the Milan Exhibition Building. Ferrocement models built on a scale of one fifth of the prototype were tested under uniformly distributed loads. Results of the model tests were found to be of decisive importance for assessing the safety of the structure and also for comparison with insitu measurements on the real structure subsequently built.

It has been recently reported that the Chinese have been building ferrocement boats even before the Second World War. It is estimated that they have built about 2000 boats. Most of these boats are 12 m to 15 m long and are mainly used in carrying goods.

Despite the successful use of ferrocement by Nervi, it gained wide acceptance only in the early part of 1960's in the United Kingdom, New Zealand and Australia. However, its application remained confined only to the area of boat building.

12. In Soviet Union, the first ferrocement structure - a vaulted roof over a shopping centre was built in Leningrad in 1958⁽²⁰⁾. By shifting to mechanized method of production, ferrocement elements have been used in different types of structures. About 10 million square meters of roofs have been built in different parts of the U.S.S.R. Prefabricated roofing elements^(20) in the

form of pyramidal slabs, ribbed slabs and cylindrical shells have been used to cover spans ranging from 12 m to 30 m. These roofing structures were used for auditoriums, exhibition halls, shopping centres, restaurants, sports and agricultural buildings. These were 20 to 40 percent economical as compared to reinforced concrete and steel structures and have shown good structural performance.

In 1963, a 16 m long yacht 'Awahnee' was built in New Zealand for an American Veterinarian to his own specifications. In 1967, Awahnee circumnavigated the world without serious damage although it encountered 70 Knot gales, collided with an iceberg and was rammed by a steel-hulled yacht⁽²¹⁾.

In 1970, a prototype factory-built ferrocement home⁽²²⁾ was constructed in U.S.A. The house was found to be much lighter in weight and higher in resistance to dynamic load than the conventionally built brick or block house. The modular home was road tested on a trailer at speed upto 80 km/hr under normal road conditions. The prototype units, under extensive road testing, showed no evidence of any structural change.

In 1971, Barberio⁽²³⁾ designed and built a series of cupolas for a fish farm in Italy. The paraboloid cupolas had a span of 16.67 m, height varying from 3.80 m to 4.80 m and an average thickness of 30 mm. The cupolas were built without the formwork. The reinforcement consisted of 12 mm and 20 mm diameter steel rods with three layers of galvanized wiremesh of 12.5 mm x 12.5 mm size with wire diameter of 0.9 mm. The construction was economical and competitive, eventhough the foundations gave considerable problems.

In 1971, a ferrocement trawler named 'Rosylin I' was built in Hong Kong. It had an overall length of 26 m and a displacement of 250 tons and is claimed to be the World's largest ferrocement fishing boat⁽²⁴⁾.

In 1973, 'the Helsal' a 22 m long prestressed vessel, won the Sydney-Hobart ocean sailing classic in Australia⁽²⁵⁾. During 1973-78, it was the only ferrocement ocean racing yacht. During 1979-81, it was a chartered boat in the Philippines. In May 1981, Helsal was driven into a coral some 120 miles south of Manila. She was subjected to 6 days of massive tidal movements before being salvaged. The expert who inspected the hull for damage concluded that it could be repaired to full insurance standards.

In 1974, an amateur boatbuilder launched the 'New Freedom' a 25.6 m long ferrocement yacht which is believed to be the largest ocean racing yacht built in Britain since the war.

In 1975, two ferrocement aqueducts⁽²⁶⁾ were designed and built for rural irrigation in China. The aqueducts are simply supported on arch type and frame type base structures. The aqueducts are still in good service condition. The aqueducts were examined in 1984. A few visible cracks of crackwidth 0.05 mm to 0.20 mm were found in the bottom part of the shell in the mid span region of frame type base structures. The cracks are generally located near the skeletal steel. The cracks are primarily due to poor quality control during construction. During operation, water infiltrated through a number of cracks but the phenomena of leakage never happened. To avoid leakage, rubber cement was plastered on the internal surface of the shell. The aqueducts have proved to be more economical than reinforced concrete for flow capacity less than $1 \text{ m}^3/\text{sec}$.

In 1978, an elevated metro station 43.5 m x 1.60 m in size with continuous ferrocement roofing was erected in Leningrad⁽²⁰⁾. The Leningrad Research Institute for Standardized and Experimental Design of Residential and Public Building is aiming to develop an egg-shaped ferrocement 'systems' house for inhospitable regions like Siberia. The 'systems' house is light in weight,

strong and equipped with all modern amenities. Its walls are 100 mm to 120 mm thick. The floor area is 30 m^2 to 35 m^2 . The floor area can be increased by combining two units together. The weight of the fully furnished and equipped house is 49 kN. It can be easily transported by land, air or sea. It only requires a hole and a bed of sand for its erection⁽²⁷⁾.

In 1984, ferrocement was used in the construction of a shaking table⁽²⁸⁾ for the large scale earthquake simulation facility at the State University of New York at Buffalo. The table is a prestressed composite sandwich structure consisting of a steel frame, a superimposed prestressed-reinforced concrete grid and ferrocement faces. The ferrocement was found to be particularly useful as the table surface layer. Its unique characteristics led to a very thin and yet stiff facing, which greatly improved the overall dynamic behaviour of the table.

In the last two decades, ferrocement has been extensively used in different types of structures. These include barges, docks, submarine structures, caissons, hydraulic gates, swimming pools, storage bins, cooling towers, wind tunnels, chimneys, pipes, small deck bridges, culverts, and formwork for conventional concrete construction^(12, 29-31).

In developing countries, the ferrocement construction is mostly manual. Ferrocement boats, small size water tanks, food grain storage bins, biogas digesters, small size roofs and irrigation channels are found to be economical as compared to reinforced concrete. Semi-mechanized methods are being developed to further reduce the cost.

In developed countries, the ferrocement construction may be made economical by using mechanized methods. It has been economically used in large span roofs of complex shapes where low self weight of the structure was a key factor.

Even though Nervi built his successful ferrocement structures during 1947-1960, systematic research into its material behaviour started in the late sixties. Since then a large number of researchers have investigated its behaviour in tension, compression and flexure. Many researchers have investigated shrinkage, creep, fatigue, impact and durability of ferrocement. Due to the small cover to the reinforcing mesh, corrosion studies on ferrocement structures built during the last 10 to 20 years have been carried out. Researchers have also investigated the use of short steel fibres and polymer dispersion with a view to attain increased first crack strength and better durability.

For the analysis of ferrocement elements, conventional reinforced concrete or composite material theory has been used. Some researchers have neglected the contribution of mortar in tension while others have incorporated it in the analysis. A few researchers have used finite element method in analysing complex shell shapes in the uncracked range and ferrocement plates in uncracked and cracked range.

1.3 OBJECT AND SCOPE

Ferrocement has been used in a variety of applications such as boats, tanks, silos and roofs. For roofing purposes, its behaviour has been investigated by many researchers in the form of channel sections, ribbed slabs, folded plates and shells of various shapes. Only channel sections and ribbed slabs provide a flat top surface. Due to their small flexural rigidities, these elements undergo large deflections and cracking at service loads. To reduce deflection and cracking and also to have a flat top surface, a new type of roofing/flooring element in the form of box girder shape has been investigated. Apart from providing flat top surface, the space in the box section can be used for utility services. In the present study, the behaviour of ferrocement box girder elements has been investigated experimentally and analytically through elastic, cracked and ultimate stages.

Ferrocement box girders of near prototype size were cast and tested

under simply supported end conditions. The span, width and depth of the girders was kept constant. Two ferrocement box girders were tested under udl over the entire top flange. Two ferrocement box girders were tested under udl over half flange width and full span. Two ferrocement box girders were joined at the level of the top flange. The combined box girder was loaded and unloaded under various load combinations in the uncracked stage. Finally the girder was tested under monotonically increasing sustained loads of short durations applied over the entire top flange. One box girder with bottom flange and side webs of ferrocement and top flange of reinforced concrete was cast and tested under udl over the entire top flange. After unloading, it was again subjected to sustained loads of short durations upto the penultimate load and for ten and half months at maximum applied load.

In the present study, the ferrocement box girder elements have been analysed by the finite element method under dead loads and monotonically increasing live loads. The analysis includes tracing the load deformation response, crack propagation and internal stresses in mortar, wire mesh and skeletal steel upto the collapse load.

A rectangular flat shell element capable of representing membrane action, bending action and the interaction between membrane and bending action has been adopted. The element has been assumed to be consisting of single mortar layer in the uncracked stage, uncracked and cracked mortar layers in the cracked stage and smeared layers of wire mesh and skeletal steel. Only material nonlinearity due to cracking of mortar, tension stiffening effect of mortar between the cracks and the nonlinear stress-strain relationships for the mortar, wire mesh and skeletal steel is considered. Geometrical nonlinearity, bond slip between the reinforcement and mortar, time dependent effects and thermal effects have not been considered.

A general computer program has been developed to implement the analysis. Validity of the method is checked by comparing the analytical results with

experimental data available in the literature. Finally, the test results of the the present investigation are compared with the analytical results obtained by the proposed method.

1.4 THESIS ORGANISATION

The concept, importance, applications, complexities and historical background of the problem are highlighted in Chapter I.

Chapter II deals with the basic mechanical properties of ferrocement. A brief review of investigations carried out on different types of roofing elements by various researchers is also presented.

Chapter III deals with the finite element method using displacement approach in brief and its application to nonlinear analysis. A rectangular flat shell element with general composite material properties is developed. Modelling of the constituent materials, tension stiffening and failure criteria are described. Explicit expressions for membrane, bending and membrane-bending interaction rigidities are developed. Salient features of the computer program developed are described. Validity of the method is checked by comparing the analytical results with the experimental data available in the literature.

Chapter IV describes the casting and testing of the box girders. The information about materials, specimens, method of casting, curing, instrumentation and test set up is also given. The experimental results for various girders are presented in tabular forms.

In Chapters V & VI, test results of the box girders are compared with the analytical results obtained by the proposed method. Experimentally obtained average spacing of cracks and maximum crackwidths are compared with the analytical/empirical expressions given by various researchers.

The conclusions, suggestions and scope for further work are described in Chapter VII.

CHAPTER II

LITERATURE REVIEW

2.1 GENERAL

Box girder elements carry the applied load due to membrane action, bending action and interaction between membrane and bending actions. Interaction between membrane and bending actions is due to unsymmetrical material properties of the element with respect to the reference plane or the middle plane. In ferrocement elements, membrane-bending interaction will occur when the wiremesh and skeletal steel reinforcement is not symmetrically placed with respect to the middle plane. It becomes more pronounced when the element is cracked. In order to have a better understanding of the structural behaviour of ferrocement box girders, a brief review of its mechanical properties is presented in this chapter. Also presented in this chapter is a critical review of different types of roofing elements investigated by various researchers.

2.2 MECHANICAL PROPERTIES

2.2.1 Ferrocement in Tension

The tensile behaviour of ferrocement elements depends upon the distribution and subdivision of reinforcement in the mortar matrix. The distribution of reinforcement is expressed by the volume fraction which is defined as the total volume of reinforcement divided by the volume of the composite. Subdivision of reinforcement is expressed by the specific surface which is defined as the total surface area of reinforcement divided by the volume of the composite.

A ferrocement element, under the action of direct tensile load, behaves as a homogeneous elastic material upto the appearance of first cracks. With

further increase in load, more cracks develop. The number of cracks keep on increasing with the increase in load till the mesh reinforcement yields. Upto this stage, the increase in crackwidth of cracks formed earlier is small. The number of cracks also stabilize at this stage. A further increase in the load leads to the widening of the cracks, and finally the element fails due to snapping of the wiremeshes.

Several researchers have investigated the behaviour of ferrocement in tension. The ultimate tensile strength of the composite is found to be the same as the load carrying capacity of the reinforcement in the loading direction⁽³²⁻³⁶⁾. The tensile strength is found to depend upon the orientation of mesh layers to a large extent. Johnston and Mattar⁽³⁵⁾ found that the effect of orientation of the reinforcing layers is most marked for expanded metal and is partially associated with differences in the effective area of steel. They found that the absolute strength of ferrocement panels reinforced with expanded metal in the weaker direction is 8.6% and 17.9% of that in the other direction, while the effective area of steel in the weaker direction is 18.7% and 34.9% of that in the other direction. The effect of orientation is also important for the welded mesh where the areas of steel are equal in both directions. Strength for the $45^{\circ}/45^{\circ}$ orientation is 56% of that for the $0^{\circ}/90^{\circ}$ orientation. The significant dependence of strength on orientation is particularly important in application involving biaxial tension. In the case of expanded metal the orientation of the layers must be alternated to achieve equal composite strength in both directions. In the case of welded mesh, the weakness in the $45^{\circ}/45^{\circ}$ orientation may be significant under biaxial tensile stresses and the design should be based on failure at 45° to the applied stresses. In terms of effective longitudinal area of steel, expanded metal and welded mesh in their normal orientations offer approximately equal strength. Their performance is found to be better than the woven mesh.

The effect of skeletal steel on the ultimate tensile strength of ferrocement has been studied by Pama, Sutharatanachaiyaporn and Lee⁽³⁴⁾ and Lee, Raisinghani and Pama⁽³⁷⁾. They found that the skeletal steel has no contribution on the ultimate tensile strength because of premature bond failure due to its poor dispersity in the matrix as characterized by its low specific surface.

The modulus of elasticity of ferrocement in uncracked range (E_c) can be approximately predicted by the law of mixtures of composite materials⁽³²⁾. Huq and Pama⁽³⁸⁾ theoretically derived the following expression by considering the geometry and orientation of the mesh :

$$E_c = E_m \cdot V_m + E_f \cdot V_f \cdot \eta \quad (2.1)$$

where E_c , E_m and E_f are the modulus of elasticity of the composite, mortar and mesh respectively. V_m and V_f are the volume fractions of mortar and mesh in the loading direction and η is the effectiveness factor of the mesh. Effectiveness factor η , when multiplied by the volume fraction or specific surface of reinforcement gives the equivalent volume fraction or specific surface in the loading direction. They have also given the theoretical values of η for different types of meshes. Naaman and McCarthy⁽³⁹⁾ have called η as global efficiency factor and have experimentally determined its value for hexagonal meshes.

The stress at the appearance of first crack is found to be a function of the specific surface of reinforcement^(32, 40). Using Naaman's⁽⁴¹⁾ empirical formula, the first crack stress, σ_{cr} , may be obtained from

$$\sigma_{cr} = 24.52 S_L + \sigma_{mu} \quad (\text{in MPa}) \quad (2.2)$$

where S_L is the specific surface of the reinforcement in the loading direction in mm^{-1} and σ_{mu} is the ultimate strength of the mortar in direct tension in MPa.

The modulus of elasticity of the composite in the cracked range (E_{cr}) depends upon the relevant mechanical properties of wiremesh and mortar. Huq and Pama⁽³⁸⁾ theoretically derived the expression of E_{cr} as

$$E_{cr} = \frac{\sigma_{ty} - \sigma_{cr}}{\epsilon_{ty} - \epsilon_{cr}} \quad (2.3)$$

where σ_{ty} and ϵ_{ty} are the stress and strain at which the composite yields and σ_{cr} and ϵ_{cr} are the stress and strain at the appearance of first crack.

Naaman and Shah⁽³²⁾ gave the following lower bound expression of E_{cr} which compared well with their experimental results :

$$E_{cr} = E_f \cdot V_f \quad (2.4)$$

The spacing and width of cracks depends upon the stress (or strain) in the reinforcement, the tensile and bond strengths of mortar, the modulus of elasticity of mortar and reinforcement, mortar cover and volume fraction and specific surface of reinforcement.

Naaman and Shah⁽³²⁾ predicted the average spacing of cracks (λ_{avg}) by the following expression :

$$\lambda_{avg} = \frac{1.5}{1.6} \frac{1}{S_L} \quad (2.5)$$

This expression is essentially the same as that derived for reinforced concrete by Robinson^(42,43). In the above expression, it is assumed that the average crack spacing is 1.5 times the minimum crack spacing and the ratio of bond strength between the mesh and mortar to the tensile strength of the mortar is 1.6. The above expression seems to give an upper bound value to the experimental results on ferrocement and the deviation has been attributed to the presence of transverse reinforcement.

Naaman⁽⁴⁴⁾ proposed the following two expressions to predict maximum crackwidth (w_{\max}) in ferroceement elements reinforced with square meshes :

$$(i) \text{ for } \sigma_f \leq 3450 S_L$$

$$w_{\max} = 3500 / E_f \quad (2.6a)$$

where σ_f is the stress in the reinforcement in MPa, S_L in mm^{-1} , w_{\max} in mm and E_f in MPa.

$$(ii) \text{ for } \sigma_f > 3450 S_L$$

$$w_{\max} = \frac{20}{E_f} [175 + 3.69 (\sigma_f - 34.5 S_L)] \quad (2.6b)$$

Here σ_f is assumed to be less than the yield strength and in any case less than 414 MPa.

Huq and Parma⁽³⁸⁾ derived the following expressions to predict the maximum spacing of cracks (λ_{\max}) and maximum crackwidth by using the model of Bianchini, Kesler and Lott⁽⁴⁵⁾ for conventional reinforced concrete :

$$(i) \lambda_{\max} = \frac{\sigma_{mu} \cdot A_{mm}}{d \cdot \tau_u} \quad (\text{in mm}) \quad (2.7)$$

where A_{mm} is the matrix area of the assumed model in mm^2 , d is the diameter of wire in mm and τ_u is the ultimate bond strength of the mortar in MPa. The maximum crack spacing is twice the minimum crack spacing.

$$(ii) w_{\max} = \frac{\pi}{S_L} \cdot \frac{\sigma_{mu}}{E_f \cdot C_b \cdot \tau_u} \left[\sigma_f - \frac{\sigma_{mu}}{2} (R + m) \right] \quad (\text{in mm}) \quad (2.8)$$

where C_b is the bond correction factor, $R = V_m/V_f = A_{mm}/A_{ff}$, $m = E_f/E_m$ and A_{ff} is the area of cross section of the wire in mm^2 .

Pama et.al⁽⁴⁶⁾ investigated the cracking behaviour of ferrocement in tension by assuming a one-dimensional model in which the steel wire is assumed to be aligned in the direction of the applied stress. Based on the bond-slip characteristic of the fiber, the expressions for crackwidth and elongation of the composite for various combinations of steel stress and bond stress were derived. The determination of the crackwidth becomes difficult because the value of bond stress at crack location is not known. However, the expression becomes useful if the value of bond stress is taken equal to the ultimate bond strength. The relation between steel stress and crackwidth upto the yield strength was found to be linear and thereafter a rapid increase in crackwidth. The crack spacing and crackwidth decreases with an increase in volume fraction of reinforcement and slip modulus. An increase in the tensile strength of mortar causes an increase in the crack spacing and crackwidth. Variation of ultimate bond stress has significant effect on the width and spacing of cracks only in highly stressed ferrocement elements.

Sornayaji and Naaman⁽⁴⁷⁾ studied the influence of transverse reinforcement, spacing of the transverse reinforcement, the type of mesh, the apparent modulus of the mesh system, the mortar cover, the volume fraction and the specific surface of the reinforcement on the stress-strain response and cracking behaviour of ferrocement in tension. In spite of testing a large number of specimens, they could not isolate and study the influence of any one parameter on the cracking behaviour of the composite. Spacing of cracks and crackwidth data showed a wide scatter. They concluded that a statistical evaluation or multiple correlation study of the crackwidth data could only give a meaningful quantitative result.

Somayaji and Shah⁽⁴⁸⁾ developed a theoretical model to predict the stress-strain response and cracking behaviour of the composite from the

experimental results of specimens reinforced only with the longitudinal wires. They assumed the following function for bond stress distribution :

$$\frac{d^2 w_x}{dx^2} = A e^x + B e^{-x} + C \quad (2.9)$$

where w_x is the local bond slip and x is the distance from the primary crack.

$$\text{or } w_x = A e^x + B e^{-x} + C \frac{x^2}{2} + D x + E \quad (2.10)$$

The five constants A to E were determined by the cross sectional properties of the specimen, the constitutive relations of steel and mortar and the relation between the applied load and the transfer length. The latter relation was assumed linear and was determined from pull-out tests. By using the above equation, the strain in steel and mortar, bond stress, crack width and tension stiffening contribution were computed. A good agreement between the theoretical results and the experimental data of their investigation as well as the experimental data from investigations on conventionally reinforced concrete was found.

Recently Akhtaruzzaman and Pama⁽⁴⁹⁾ from their study on cracking behaviour of ferrocement in tension found that the value of slip modulus, ultimate bond strength and modulus of elasticity of mortar has negligible influence on crack spacing. The parameters which significantly influence the crack spacing are the ultimate tensile strength of mortar and volume fraction of mesh reinforcement. The crack width is greatly influenced by volume fraction, modulus of elasticity of steel and ultimate bond strength but very small effects are observed for slip modulus, modulus of elasticity of mortar and tensile strength of mortar.

2.2.2 Ferrocement in Compression

Unlike in tension, the mortar matrix contributes directly to the compressive strength of the composite in proportion to its cross sectional area. Its ultimate strength is due to the contribution of mortar, longitudinal reinforcement (adequately restrained along the length) and confinement provided by the transverse reinforcement to develop triaxial compressive state of stress in the matrix core.

Bezukladov⁽⁴⁰⁾ and Rao and Gowder⁽⁵⁰⁾ tested solid prisms reinforced with wiremeshes and found a very small increase in ultimate strength due to the reinforcement. Desayi and Jacob⁽⁵¹⁾ tested solid and hollow prisms reinforced with wiremeshes. An increase in the compressive strength was found linearly related to the mesh-mortar parameter, a nondimensionalized quantity given by $p_m \cdot \sigma_{fu} / \sigma_{cu}$ where p_m , σ_{fu} and σ_{cu} are percentage mesh reinforcement, ultimate tensile strength of wire and ultimate crushing strength of mortar cube respectively. Pama et.al⁽³⁴⁾ from their experimental results found that the ultimate compressive strength of the composite is lower than that of an equivalent pure mortar.

Johnston and Mattar⁽³⁵⁾ carried out tests on solid prisms with a polystyrene core. Only welded mesh and expanded metal were considered as reinforcement due to their superior performance as compared to woven meshes in providing stiffness and strength to ferrocement. The welded mesh was found to be much superior to expanded metal as compression reinforcement. Specimens reinforced with expanded metal gave an ultimate load even less than the sum of calculated load due to mortar and effective longitudinal steel. This was attributed to the scissoring action and consequent inability of expanded metal to provide effective lateral confinement to the mortar. The effect

of polystyrene core is negligible in columns reinforced with expanded metal and significant in columns with welded mesh for small reinforcement ratios only. In columns reinforced with welded mesh, the contribution of lateral reinforcement to the ultimate strength is more than that of longitudinal reinforcement.

The modulus of elasticity in direct compression in the uncracked range can be satisfactorily computed from the law of mixtures. The computed values compare well with the experimental results of various investigators^(37, 50, 52).

Rao and Rao⁽⁵³⁾ carried out tests on hollow cylindrical specimens in direct compression. The stress-strain curve of ferrocement is linear upto 50% - 60% of ultimate strength and thereafter nonlinear and similar to a reinforced concrete specimen in compression. The Poisson's ratio was nearly constant in the linear portion of the stress-strain curve and thereafter it increases gradually and reaches maximum value at the ultimate load. A similar variation in Poisson's ratio was also observed by Johnston and Mattar⁽³⁵⁾.

Desayi and Joshi⁽⁵⁴⁾ conducted compression tests on undulated ferrocement wall elements to determine the influence of slenderness ratio and the amount of reinforcement. All the elements were 20 mm thick and about 1.50 m long. 75 mm thick diaphragms were provided at the ends for load transfer. The wall elements behaved like short columns upto a slenderness ratio of 38. The elements in general failed with a cracking noise and with the spalling off of the mortar cover over the meshes. At some locations, the meshes buckled. Local buckling of the plates of the wall element or overall instability of the elements was not noticed. There was no appreciable difference in the strengths of ferrocement plates and plain mortar plates (150 mm x 20 mm x 300 mm size) in the range of mesh quantity used and

the strength of the plates was about 83% of the strength of 100 mm mortar cubes. Methods used for the prediction of ultimate load of reinforced concrete wall elements gave conservative values for ferrocement units. The expressions which gave good theoretical predictions compared to the experimental results are the following :

$$(i) \quad P_u = K \cdot \sigma_{cu} \cdot A_m + \sigma_{fy} \cdot A_f \quad (2.11)$$

where P_u , K , σ_{fy} , A_m and A_f are the ultimate load, reduction factor assumed equal to 0.67, yield strength of wiremesh, area of mortar and area of wiremesh in compression respectively.

$$(ii) \quad P_u = \sigma_{fp} \cdot A_g \quad (2.12)$$

where σ_{fp} and A_g are the strength of ferrocement plate and gross area of ferrocement wall unit respectively.

In the above expressions, the contribution of skeletal steel is neglected.

$$(iii) \quad P_u = K_1 \cdot \sigma_{cu} \cdot A_g \left[1 - \left(\frac{L}{40 D} \right)^2 \right] + K_2 (\Lambda_f \cdot \sigma_{fy} + A_s \cdot \sigma_{sy}) \quad (2.13)$$

where $K_1 = K_2 = 0.67$, L is the effective length of the column, D is the depth of the section and σ_{sy} and A_s are the yield strength and area of the skeletal steel respectively. In this expression, the effect of slenderness ratio of the wall element and skeletal steel is included.

Sandowicz and Grabowski⁽⁵⁵⁾ conducted tests on hollow ferrocement pipes and ferrocement pipes filled with concrete. The pipes had an internal diameter 167 mm, outer diameter 206 mm and overall length 1000 mm. Number of mesh layers were varied. The tests on ferrocement pipes showed that the effect of the reinforcement upon the load carrying capacity of the pipes is negligible. The failure of the pipes was rapid. It was preceded by a

hollow sounding crack after which the spalling of the mortar took place. In the fractured region, the wires of the mesh showed buckling into longitudinal waves. Tests on ferrocement pipes filled with concrete showed that its load carrying capacity was higher than that of reinforced concrete columns having similar diameters and volumetric percentage of reinforcement due to confining effect.

Winokur and Rosenthal⁽⁵⁶⁾ conducted compression tests on three ferrocement plane elements 800 mm x 35 mm in cross section and 2800 mm long and three L-shaped columns made of two such plane elements at right angle. The elements were reinforced with 8 wiremesh layers (4.2 mm square, 0.56 mm wire diameter) equally distributed on both sides of four 12 mm diameter longitudinal mild steel bars. All the plane elements were stiffened by supports on both sides while L-shaped elements were stiffened by horizontal triangular ferrocement diaphragms. The slenderness ratio for plane and L-shaped elements were 70 and 93 respectively.

The failure of the elements was preceded by horizontal bending accompanied by extensive microcracking on the tensile face. At this stage, the plane elements acquired an s-shaped form. Typical failure of all the elements was by buckling halfway between the supports or stiffeners followed by crushing of the mortar. In the L-shaped elements, buckling was followed by lateral distortion of the whole section. From the test results, it was concluded that ferrocement can be satisfactorily used in compression elements, with the buckling effect controlled by lateral diaphragms provided in sufficient number.

2.2.3 Ferrocement in Flexure

The behaviour of ferrocement in flexure is governed by the combined influence of factors that affect its behaviour in tension and compression.

Collen and Kirwan⁽⁵⁷⁾ and Rao and Gowder⁽⁵⁸⁾ investigated the behaviour of ferrocement in flexure by varying the amount of mesh reinforcement. It was observed that the elasticity and bending strength of ferrocement increase with an increase in the mesh reinforcement. Desayi and Jacob⁽³³⁾ observed that the ultimate flexural strength of ferrocement increases with an increase in mesh-mortar parameter.

Logan and Shah⁽⁵⁹⁾ carried out tests on ferrocement beams 76.2 mm wide, 50.8 mm deep, 762 mm long and reinforced with varying sizes and layers of welded mesh. The first crack stress in bending (σ_{crb}) in the extreme mortar fiber was found to be linearly related to the specific surface of the reinforcement in the tension zone (S_{LT}). From regression analysis, the following relationship was obtained :

$$\sigma_{crb} = 28.02 S_{LT} + \sigma_{mr} \quad \text{in MPa} \quad (2.14)$$

where σ_{crb} is the bending tensile stress in extreme mortar fiber calculated on the basis of transformed elastic section ; S_{LT} is the ratio of the surface area of reinforcement in the longitudinal direction and the initial mortar volume in the tension zone in mm^{-1} ; and σ_{mr} is the modulus of rupture of the mortar in MPa.

The ultimate strength of ferrocement beams was satisfactorily predicted by the ultimate strength method of conventional reinforced concrete. The average spacing of cracks was predicted by the theoretical equation (2.5) given by Naaman and Shah⁽³²⁾ for ferrocement elements in direct tension. The maximum width of cracks was predicted by the following empirical equation which compared well with their experimental results :

$$w_{max} = \frac{2.3045 \times 10^{-5} \times \sigma_f^{4/3}}{S_{LT}^{1/3}} \quad (\text{in mm}) \quad (2.15)$$

where σ_f' = stress in the outermost layer of the mesh in MPa ; and
 S_{LT} = specific surface as defined above in mm^{-1} .

The width of cracks in ferrocement beams for the same percentage of reinforcement and steel stress was found to be an order of magnitude smaller than the reinforced concrete beams.

Johnston and Mowat⁽⁶⁰⁾ carried out tests on ferrocement beams 150 mm wide, 25 mm thick, 914 mm long and reinforced with meshes of different types and orientations. The geometry and orientation of the reinforcement was found to have a marked effect on the strength of systems reinforced with expanded metal and welded mesh. For a given effective cross-sectional area of steel, expanded metal and welded mesh in their normal orientations perform significantly better than woven mesh. For any given steel content, and by implication cost, the order of performance for uniaxial bending is expanded metal, standard bars, welded mesh and woven mesh. However, for biaxial bending, the orientation effect in expanded metal precludes its use in other than long narrow units unless the orientation of the layers is alternated. Welded mesh, on the other hand, offers equal strength in both directions and is more effective than woven meshes.

Surya Kumar and Sharma⁽⁶¹⁾ from their tests on ferrocement beams found that the ultimate and first crack strengths of the composite increase linearly with an increase in the percentage area of mesh reinforcement. Based on the test results, the following empirical equations were obtained for extreme fiber tensile stress of the composite at first crack and ultimate failure.

$$\sigma_{crb} = 1.96 p_m + 3.33 \quad \text{in MPa} \quad (2.16)$$

$$\sigma_{ub} = 7.26 p_m + 3.33 \quad \text{in MPa} \quad (2.17)$$

where σ_{crb} and σ_{ub} are the stresses in extreme tensile fiber of the composite at first crack and ultimate failure, based on homogeneous section and neglecting the transformation of steel area.

The ultimate moment capacity of the beams using conventional reinforced concrete theory was computed and a good correlation with the experimental values was obtained.

Balaguru, Naaman and Shah⁽⁶²⁾ conducted tests on ferrocement beams to predict deflection and crackwidth. The beams were 127 mm wide, 13 mm thick, 457 mm long and reinforced with various layers of 12.7 mm x 12.7 mm woven and welded meshes of 1.07 mm wire diameter and 6.35 mm x 6.35 mm woven mesh of 0.635 mm wire diameter. The experimental load deflection curves consisted of three distinct stages (i) steep linear portion before cracking of mortar ; (ii) after the first cracking of mortar but before yielding of mesh ; and (iii) after yielding of meshes when the slope becomes almost parallel to the deflection axis (Fig. 2.1). The end of the first stage of the curve corresponds to the first cracking of mortar. The load at first cracking of the mortar was about the same for the different types and amount of meshes. This is in contradiction of the result obtained by Logan and Shah⁽⁵⁹⁾. Soon after the first cracking of mortar, a large number of cracks appeared on the tension face. The cracks ran through the entire width of the beam. The total number of cracks usually equalled the number of transverse wires in specimens reinforced with woven and welded meshes of 12.7 mm x 12.7 mm size. The location of cracks coincided with the location of transverse wires. This trend was not observed in specimens reinforced with woven mesh of 6.35 mm x 6.35 mm size except for the group with six layers at near ultimate load.

An analytical model was developed to predict the flexural behaviour. The experimentally observed stress-strain values of mortar and mesh were represented by the following trigonometrical expression :

$$\sigma = \sum_{j=1}^N A_j \cdot \sin \left(\frac{(2j-1)\pi \cdot \epsilon}{l} \right) \quad (2.18)$$

where σ = stress ; ϵ = strain ; A_j are the constants of the series ; N is the number of terms in the series ; and l is a constant whose value was taken 1.5 times the observed maximum strain.

By assuming a linear distribution of strain across the depth and neglecting the contribution of mortar in tension beyond a tensile strain of 0.000167, the depth of neutral axis, moment of resistance and curvature were calculated. The ultimate moment of resistance was taken as the minimum value obtained when either the extreme compressive strain of the mortar reached a value of 0.006 or the extreme layer of wiremesh reached failure strain.

Moments and curvatures were calculated at various points along the span. The curvatures were numerically integrated twice to calculate the deflections at load points. The predicted deflections compared well with the experimental values upto the second stage and were less than the experimental near ultimate load.

A regression analysis of the observed crackwidths showed that the average crackwidth primarily depends on steel strain in the extreme layer of mesh. To predict an upper bound value of average crackwidths, the following design equation was proposed :

$$w_{\max} = \epsilon'_f \cdot S_f \cdot R' \quad (2.19)$$

where ϵ_f' = tensile strain in the extreme layer of wiremesh ; S_f = spacing of the transverse wires ; and R' = ratio of the distances to the neutral axis from the extreme tension fiber and from the centre of extreme layer of wiremesh. For the above design equation, it was assumed that the mortar between the cracks is completely free from tension and that the number of cracks equal the number of transverse wires.

Huq and Pama⁽⁶³⁾ analysed the ferrocement elements in flexure by assuming an idealized elastic - perfectly plastic stress-strain diagram of ferrocement in compression and a tri-linear stress-strain diagram in tension (Fig. 2.2). Assuming linear distribution of strain across the depth, moments and curvatures were determined for various strain states. Moment curvature relations were approximated by tri-linear curve and the deflections at various stages of loading were determined using area-moment method. The analytically predicted ultimate moments were compared with the experimental results of Balaguru et. al⁽⁶²⁾ and were found to be on the conservative side. Analytically predicted deflections compared well with the averaged experimental values of Balaguru et. al⁽⁶²⁾ in the cracked range but differed in the yield range (Fig. 2.3). The average spacing of cracks and maximum width of cracks in flexure were predicted by equations (2.7) and (2.8) derived for direct tension case.

By comparing the test results of Balaguru et. al⁽⁶²⁾ and Logan and Shah⁽⁵⁹⁾, Balaguru⁽⁶⁴⁾ observed that the crack spacing is a function of the specific surface of reinforcement and curvature of the beam. Based on principles of mechanics, the following equations for average crack spacing and average crackwidth (w_{avg}) were derived :

$$\lambda_{avg} = \sqrt{\frac{\Psi_y}{\Psi}} \cdot \frac{\theta}{\eta'} \cdot \frac{1}{S_{LT}} \quad (2.20)$$

$$w_{avg} = \sqrt{\Psi \cdot \Psi_y} \frac{\theta (D - x)}{\eta' \cdot S_{LT}} \quad (2.21)$$

where Ψ_y = curvature of the beam at the onset of yielding, Ψ = curvature of the beam at a given load level, θ = ratio of average crack spacing to minimum crack spacing, η' = ratio of bond strength between the mesh and the mortar to the tensile strength of the mortar, D = depth of the beam and x = distance of neutral axis from extreme compression face of the beam.

Based on the test results of Balaguru et. al⁽⁶⁵⁾, he gave the following expression of maximum crackwidth with 98 percent probability :

$$\begin{aligned} w_{max} &= 1.5 w_{avg} \\ &= 1.5 \sqrt{\Psi \cdot \Psi_y} \cdot \frac{(D - x)}{\eta' \cdot S_{LT}} \end{aligned} \quad (2.22)$$

Taking $\theta = 1.5$ and $\eta' = 1.6$, the analytically predicted crackwidths compared well with the test results of Balaguru et. al⁽⁶⁵⁾ and Logan and Shah⁽⁵⁹⁾.

Swamy and Al-wash⁽⁶⁶⁾ studied the deflection and cracking behaviour of ferrocement plates of size 300 mm x 25 mm x 1000 mm in flexure. The type and amount of mesh reinforcement, mortar cover and thickness of the section were the main variables. The mortar matrix incorporated flyash as a replacement of both cement and fine aggregate. Mild steel mesh and high tensile steel mesh were the two types of reinforcements. The specimens with mild steel mesh reinforcement showed the three stages of load-deflection curve, namely, the elastic, cracked and yield stages, whereas in high tensile steel mesh reinforced specimens, these three stages appeared in some form in only those specimens which were reinforced upto four layers (Fig. 2.4). The specimens reinforced with high tensile steel gave reduced

crack spacing and crack width at failure. The average crack spacing stabilized in mild steel and high tensile steel reinforced specimens at specific surface values of about 0.2 mm^{-1} and 0.15 mm^{-1} respectively. The crack spacing was influenced to some extent by the mesh opening, mortar cover and section thickness.

Swamy and Spanos⁽⁶⁷⁾ studied the deflection and cracking behaviour of ferrocement with grouped reinforcement and fiber reinforced matrix. Grouped reinforcement was in the form of welded wiremesh layers provided at top and bottom of 8 mm diameter high yield strength deformed bars. Welded wiremeshes of size 25 mm x 25 mm with wire diameter of 1.6 mm and 50 mm x 50 mm size with wire diameter of 2.0 mm were used. The mortar matrix consisted of 0.5 : 0.5 : 1.8 of cement : fly ash : sand with a water to cement plus fly ash ratio of 0.42. A superplasticizer equal to 2 percent of the weight of cement and fly ash was used for preparing the mortar. Various types of steel, glass, and polypropylene fibers were used.

Ferrocement plates 300 mm x 25 mm x 1000 mm were tested over an effective span of 900 mm under third point flexural loading. The load deflection curves of ferrocement plates with steel fibers did not show any marked deviation from linearity after the appearance of first crack. Even after extensive cracking, the change in the slope of the curve was gradual. In ferrocement plates with no fiber reinforcement, majority of the cracks appeared at about 25 percent of the ultimate moment. In plates with high specific surface fibers, most of the cracks occurred at about 60 percent of the ultimate moment. In general all the initial cracks were formed at the location of transverse wires. The presence of fibers caused additional cracks to form between the main cracks. The final deflections of all the specimens were high. From serviceability point of view, span/deflection ratio of 250 was reached

at relatively low loads of about 20-30 percent of the ultimate load for all the specimens.

In majority of specimens, an average crack spacing of about 12.5 mm was reached soon after first cracking. They proposed the following design average crack width (w_d) equation :

$$w_d = 12.5 \cdot \epsilon_f \quad (\text{in mm}) \quad (2.23)$$

The design equation gave upper bound values of average crack widths at all stages of loading.

Desayi and Ganesan⁽⁶⁸⁻⁷⁰⁾ predicted the spacing and maximum width of cracks in ferrocement flexural elements of channel, trapezoidal and built-up I sections by modifying the method proposed by Desayi⁽⁷¹⁾ for reinforced concrete members (Figs. 2.5, 2.6). The following modified expressions were proposed to predict average crack spacing, maximum crack spacing, average crack width and maximum crack width at any level along the depth of the element for a given load :

$$\lambda_{avg} = \frac{K_t \cdot \sigma_{mu} \cdot A_e}{K_b \cdot \left(\frac{M}{M_u}\right)^n \Sigma \tau_u \cdot \left(\frac{a-x}{D_e-x}\right) \pi \cdot d} \quad (2.24)$$

$$\lambda_{max} = \frac{K_t \cdot \sigma_{mu} \cdot A_e}{K_b \cdot \left(\frac{M_{cr}}{M_u}\right)^n \Sigma \tau_u \cdot \left(\frac{a-x}{D_e-x}\right) \cdot \pi \cdot d} \quad (2.25)$$

$$w_{avg} = \lambda_{avg} \cdot \epsilon_a \cdot F(t) \quad (2.26)$$

and

$$w_{max} = \lambda_{max} \cdot \epsilon_a \cdot F(t) \quad (2.27)$$

where K_t , K_b , n and $F(t)$ are constants, M = moment at the cross-section due to applied load, M_{cr} = moment at first crack, M_u = ultimate moment capacity of the element, A_e = effective area of mortar below the neutral axis, a = distance from extreme compressive face to the level under consideration, D_e = effective depth of the section and ϵ_a = strain in mortar fiber at distance 'a' below the extreme compressive face calculated on the basis of cracked elastic analysis.

The above equations reduce to the case of reinforced concrete by taking $n = F(t) = 1$

The constant $F(t)$ was determined by the statistical best fit of observed strains with the corresponding theoretical strains. The constants K_t , K_b and n were determined by statistical analysis. The set of values of K_t , K_b and n which gave best values of the average and lowest coefficient of variation of theoretical crack width/experimental crack width were taken to represent the values of K_t , K_b and n . For built-up I sections, these values were 2/3, 2/3 and 0.4 and were determined by taking the maximum values of theoretical and experimental crack widths. By substituting the values of these coefficients in equations (2.24) to (2.27), the theoretical values of average and maximum crack spacing and crack width were determined. These values compared satisfactorily with the experimental values.

Yen and Su⁽⁷²⁾ studied the influence of skeletal steel on the flexural behaviour of ferrocement. The effect of skeletal steel on the first crack moment (or first crack load) was found to be negligible. However, the presence of skeletal steel increased the ultimate moment capacity and ductility of the composite.

Mansur and Paramasivam⁽⁷³⁾ investigated the behaviour of ferrocement beams by varying the volume fraction of reinforcement and water-cement ratio of mortar. They found that both the first crack and ultimate moments increase with an increase in either the matrix grade (by decreasing the water-cement ratio) or the volume fraction of reinforcement. For a given volume fraction of reinforcement, a lower grade matrix gives larger number of cracks with smaller crack width. However, as the load approaches the ultimate value, the cracks open up more rapidly. For a given grade of matrix, higher volume fraction of reinforcement provides more effective control of crackwidth.

Based on the concept of plastic analysis, a simple method to predict the ultimate moment capacity was proposed. The method gave satisfactory prediction of ultimate moments of their own investigation as well as the test results of Logan and Shah⁽⁵⁹⁾.

Kaushik et. al⁽⁷⁴⁾ compared the behaviour of simply supported and horizontally restrained ferrocement beams. The restrained beams showed an increase in the first crack moment and ultimate moment capacity and decrease in ultimate deflection, crack spacing and crackwidths as compared to simply supported beams.

Prawel and Reinhorn⁽⁷⁵⁾ investigated the behaviour of under-reinforced ferrocement slabs in two way bending. They observed that the plates having meshes (with square opening) oriented at $30^{\circ}/60^{\circ}$ to the principal direction gave the lowest ultimate load carrying capacity while those with mesh orientation of $45^{\circ}/45^{\circ}$ gave the maximum value.

Trikha et. al⁽⁷⁶⁾ and Meek⁽⁷⁷⁾ studied the behaviour of two way slabs. They found that the ultimate load carrying capacity of the slabs depended not only on the flexural action but also on the membrane action mobilized by large deformation.

2.2.4 Shear Strength

Very little research work has been done to evaluate the shear strength of ferrocement. Most of the applications of ferrocement have been in structures where high tensile strength or small crackwidth is the governing criteria. Ferrocement panels used for roofing purposes, normally have a large span/depth ratio in flexure which precludes the shear as a failure criteria. Collen and Kirwan⁽⁵⁷⁾ tested ferrocement specimens reinforced with woven mesh and skeletal bars in bending at a shear span/depth ratio of 0.4. The shear strength of ferrocement elements was equal to about 35 percent of their flexural strength over a fairly wide range of steel contents (288 - 480 kg/m³).

Mansur and Ong⁽⁷⁸⁾ and Venkata Krishna and Basa Gouda⁽⁷⁹⁾ found that the shear strength of ferrocement depends upon the strength of mortar, volume fraction and strength of wiremesh. Shear strength of ferrocement beams with welded wiremesh was found to be more than the shear strength of beam reinforced with woven or hexagonal wiremesh.

2.2.5 Fatigue Resistance

The fatigue behaviour of ferrocement has been found to depend on the fatigue properties of the reinforcement. So far only the flexural fatigue behaviour has been investigated by a few researchers.

Picard and Lachance⁽⁸⁰⁾ found that the maximum load causing failure at 10^6 cycles was about 46% of the ultimate static load. McKinnon and Simpson⁽⁸¹⁾ found that ungalvanized wiremesh imparted greater fatigue strength than galvanized wiremesh. Karasudhi, Mathew and Nimityongskul⁽⁸²⁾ studied the effect of different types of wiremeshes. In all the specimens it was found that the wires in the tensile zone of the ferrocement section were cut off due to fatigue effect, though the stresses in the wires and skeletal steel bars

were below their yield stresses. In specimens with welded wiremesh and expanded metal, the failure was mostly at the nodes. The chicken wiremesh showed greater fatigue resistance as compared to welded mesh and expanded metal. The following load-cycle (S-N) relationships for ferrocement specimens reinforced with three different types of meshes were suggested :

$$\log_{10} N = 12.227 - 0.128 S \quad (\text{welded square mesh}) \quad (2.28)$$

$$\log_{10} N = 7.417 - 0.031 S \quad (\text{expanded metal mesh}) \quad (2.29)$$

$$\log_{10} N = 9.750 - 0.073 S \quad (\text{chicken wire mesh}) \quad (2.30)$$

where N and S are the number of cycles to failure and the maximum repeated load expressed as percentage of the ultimate static load.

Balaguru, Naaman and Shah⁽⁸³⁾ studied the fatigue life, deflection and crack widths of ferrocement beams reinforced with square welded and woven meshes. The beams were subjected to load levels of $\pm 40\%$, $\pm 50\%$ and $\pm 60\%$ of the yield load capacity of the specimens. The failure of specimens was due to the fracture of the extreme layer of wiremesh. Based on the test results, the fatigue life (N_f) was predicted by the following equation:

$$S_r = 0.6433 - 0.1345 \log_{10} N_f \quad \text{in MPa} \quad (2.31)$$

where N_f is the fatigue life in Kilocycles and S_r is the stress range in the extreme layer of wiremesh in MPa, calculated on the basis of cracked elastic section.

The deflection and crack widths in ferrocement beams for a given load level and after a given number of cycles, were predicted by an equation of the form :

$$y = A \cdot e^{Br} \quad (2.32)$$

where y = the value of deflection, average crack width or maximum crack width, A = the value of deflection or crack width under static maximum load, B = the constant related to the fatigue contribution to deflection or crack width and r = the ratio of number of cycles at which y is predicted to the number of cycles to failure.

The values B for deflection and crack widths were predicted by the following equations :

$$B = 0.3291 + 0.1925 \times 10^{-2} N_f - 0.275 \times 10^{-5} N_f^2 \quad 0.667 \quad (\text{for deflection}) \quad (2.33)$$

$$B = 0.816 + 0.445 \times 10^{-2} N_f - 0.495 \times 10^{-5} N_f^2 \quad 1.670 \quad (\text{for crack width}) \quad (2.34)$$

Paramasivam, Das Gupta and Lee⁽⁸⁴⁾ investigated the fatigue strength for three different volume fractions of galvanized square woven meshes. They found that the failure load for all the specimens at 10^6 cycles was about 45% of their ultimate static load. It was also observed that the cracks in specimens failing by fatigue were much fewer and wider than those specimens which failed under static loads.

Bennet, Fakhri and Singh⁽⁸⁵⁾ studied the fatigue behaviour of ferrocement beams reinforced with galvanized and ungalvanized welded wire meshes. They found that the fatigue strength of ferrocement (expressed in terms of stress in steel) increased with an increase in number of mesh layers. The specimens with galvanized welded mesh had higher fatigue strength compared to the specimens with ungalvanized welded mesh. This is in contradiction with the test results of McKinnon and Simpson⁽⁸¹⁾. The spacing and number of cracks did not appear to be influenced by the type of welded mesh

or the diameter of the wire. The crackwidths increased with an increase in the load level and the number of load cycles.

Raisinghani and Sai⁽⁸⁶⁾ studied the fatigue behaviour of ferrocement slabs under pulsating loads. All the slabs were reinforced with various layers of chicken wire mesh. The lower load limit of the pulsating machine was about 130% to 180% of the first crack load of the specimens. For specimens subjected to upper load level quite less than the static ultimate load, the residual deformations first increased with the increase in load cycles, then reached a stable condition and again increased with load cycles till the fracture occurred. Such specimens withstood 1 to 3 million cycles. Those specimens which failed within 10^6 cycles, exhibited a continuous increase in the residual deformation.

Few specimens were subjected to peak loads of short durations (60 to 120 seconds) after every six hours. The peak loads were about 115% of the upper load level. Those specimens which were subjected to high value of upper load level and failed in less than 10^6 cycles, the peak loads of short duration accelerated the failure. No appreciable effect of peak loads was observed in specimens which were subjected to low value of the upper load level.

2.2.6 Impact Resistance

The impact resistance of ferrocement is found to depend on the specific surface, strength and type of reinforcement and the thickness of the element. Bezukladov et. al⁽⁴⁰⁾ compared the impact strength of reinforced concrete and ferrocement plates by using a falling weight. They found that the dispersion of reinforcement promotes increase in the impact strength. While reinforced concrete plates had large cleavings, the crushed mortar in ferrocement

was held back by the meshes from disintegrating. Shah and Key⁽⁸⁷⁾ observed that the damage to ferrocement plates decreased with an increase in specific surface or the strength of the mesh reinforcement. Greenius and Smith⁽⁸⁸⁾ found that the provision of skeletal steel bars along with mesh reinforcement improved the strength and deformability characteristics under impact. Burgess and Allen⁽⁸⁹⁾ found that the increase in thickness of ferrocement increases the impact resistance. Nimityongskul et. al⁽⁹⁰⁾ found that the impact resistance increases with the increase in steel content or in the specific surface of mesh reinforcement. It was observed that under an almost practical maximum steel content condition, the impact resistance does not always increase with the increase in the specific surface of mesh reinforcement. Srinivasa Rao et. al⁽⁹¹⁾ found that the specimens reinforced with welded meshes offer the highest impact resistance followed by woven and chicken wiremeshes for a given steel percentage. Recently Grabowski⁽⁹²⁾ observed that an increase in the slab thickness and specific surface of reinforcement led to the increase in the number of cracks and decrease in their width and length.

2.2.7 Shrinkage and Creep

Shrinkage and creep characteristics of ferrocement are function of shrinkage and creep potential of the mortar and the restraint offered by the mesh reinforcement.

Bezukladov et. al⁽⁴⁰⁾ investigated the effect of sustained load on the deflection characteristics of ferrocement beams under pure bending. Their test results indicate that the specimens reinforced with mesh and skeletal steel show higher deflection than the specimens reinforced with mesh alone. Brauer⁽⁹³⁾ found that ferrocement reinforced with ungalvanized wiremesh exhibits higher creep than the one with galvanized wiremesh.

Ravindrarajah and Tom⁽⁹⁴⁾ studied the shrinkage and creep behaviour of ferrocement slabs reinforced with square woven wiremeshes. The shrinkage of the mortar matrix was found to decrease with an increase in the volume fraction of reinforcement. The shrinkage of ferrocement specimens with two and four layers of reinforcement, (equal to volume fractions of 0.9% and 1.8%) was 70% and 65% of that for plain mortar specimens after 95 days of drying.

The ratio of time-dependent deflection to instantaneous deflection (termed as creep deflection coefficient) was found to vary from 1.45 to 2.65 for all the specimens for sustained load varying from 15% to 100% of the first crack load. At sustained load level equal to 30% of the first crack load, the span to total deflection ratio was well above the commonly used minimum of 250. The total instantaneous deflection under a load was observed to reduce when the load was applied in steps with the first increment sustained for a period of time before adding the next increment. The total recovery in deflection after the removal of sustained load was about 50%. The average ratio of time-dependent recovery to instantaneous recovery was about 0.4. Under sustained flexural loading, tensile creep strain was much more than the compressive creep strain and the ratio between them decreased with an increase in the volume fraction of reinforcement and also when the sustained load was applied in steps.

Raisinghani and Sai⁽⁸⁶⁾ studied the flexural creep characteristics of ferrocement slabs subjected to sustained central line load for a period upto ninety days. It was observed that the specimens subjected to stresses less than the cracking stress of ferrocement, creep increases at a decreasing rate and attains steady state. Whereas, for specimens subjected to stresses higher than the cracking stress, steady state was not reached in 45 to 50 days.

At stresses upto cracking stress, the creep is linearly proportional and there is no effect of reinforcement percentage. But for stresses higher than the cracking stress, the creep increases at a faster rate and depends on the percentage of reinforcement. It decreases with increase in percentage of reinforcement. It was also observed that creep rates were less for specimens which were subjected initially to sustained loads for 30 to 45 days. The creep specimens after loading were tested to collapse. These specimens withstood 10-15 percent higher collapse loads compared to their virgin parallels.

Swamy and Spanos⁽⁹⁵⁾ conducted tests on ferrocement plates subjected to flexural loading. The type of matrix, type and amount of wiremesh and the stress level of applied load were the main variables. The wiremeshes were ungalvanized. The creep deflection coefficient varied from 0.20 to 0.92 with an average of 0.55 for the sustained load varying from 15% to 50% of the ultimate load. The specimens with high steel strength mesh gave the lowest values of creep deflection coefficient. The specimens subjected to higher stress/strength ratio took longer time for the creep deflections to stabilize. The average values of creep strain coefficients of the composite were 1.12 and 0.66 in compression and tension respectively compared to 1.20 and 1.11 for plain mortar specimens. The creep Poisson's ratio was on an average 0.10 for ferrocement specimens as compared to 0.14 for plain mortar specimens. Flyash mortar mixes showed early stabilization of creep strains partly due to their increased strength development and partly due to their reduced shrinkage. The average and maximum crack widths at the end of the loading periods (80 to 365 days) were on an average 1.55 and 1.69 times the instantaneous values. The value of the ultimate crack width creep coefficient was between 0.55 and 0.69, which is smaller than that reported for reinforced concrete⁽⁹⁶⁾. The specimens loaded at 30% of their ultimate flexural strength showed crack widths much less than 0.10 mm.

The high steel strength and welded mesh showed better crack control under creep. The fly ash mixes produced a more uniform distribution of cracks. The time-dependent recovery of strains and deflections after sustained loading varied from 10% - 20% of the instantaneous recovery for both mortar and ferrocement specimens. The ratio of total deformation recovery to total deformation was about 80% for plain mortar and about 65% for ferrocement specimens. The sustained loading had no adverse effect on ultimate flexural strength of ferrocement.

2.2.8 Durability

The successful performance of ferrocement in an aggressive environment depends to a great extent on its durability against the environment than on its strength properties. For ferrocement to be durable, its component materials, namely, mortar and wiremesh reinforcement should retain their bond and strength and do not disintegrate over a period of time. The disintegration of mortar is due to volume change caused by various weathering agents such as cyclic thermal changes and alternate wetting and drying. The action of aggressive chemicals on hardened cement paste, particularly sulfates, causes volume change and cracking in the mortar. The mesh reinforcement is normally protected by the alkalinity of the mortar and the cover. The cover in ferrocement elements is about 2 mm to 4 mm. This increases the corrosion risk to mesh reinforcement. To prevent corrosion, galvanized wiremesh is commonly used. The use of galvanized wiremesh along with ungalvanized skeletal steel bars creates the galvanic cell problem. Christensen and Williamson⁽¹⁴⁾ were the first to identify this problem and also gave the solution. They suggested the use of Chromium trioxide at the rate of 100-300 ppm by weight of water in preparing the mortar. If the cracks are not wider than 0.1 mm, Greenius⁽⁹⁷⁾ found that corrosion was not severe even when the depth of cover was 0.5 mm.

From his extensive tests, limiting water-cement ratio seemed to be adequate under sea water exposure for satisfactory performance. Naaman and Sabnis⁽⁹⁸⁾ suggested a net cover of 2 mm. They even suggested a smaller depth of cover for those ferrocement elements in which reinforcement was galvanized, surface painting was used and low limiting crack width was adopted. Bigg⁽⁹⁹⁾ also suggested the use of galvanized wiremesh.

During last 4-5 years, the corrosion and durability aspect of ferrocement has been extensively investigated by several researchers. Mathews, Achyutha and Rao⁽¹⁰⁰⁾ subjected cracked ferrocement specimens to accelerated corrosion tests by alternate wetting and drying using sea water for 30 days. They found that the ultimate tensile strength of the specimens with initial crack-widths of about 0.05 mm and 0.10 mm was reduced by 4% and 12% respectively.

Trikha et. al⁽¹⁰¹⁾ investigated the extent of corrosion in 12 ferrocement structures of various types with ages ranging from 6 to 12 years. They concluded that in mechanically cast ferrocement structures using galvanized steel mesh and well graded sand for mortar, corrosion is only mild with or without protective coating. However, inadequate cover, bad compaction and poor workmanship all lead to an increase in the incidence and rate of corrosion.

Selvi Rajkumari et. al⁽¹⁰²⁾ studied the corrosion resistance of polymer impregnated ferrocement and unimpregnated ferrocement specimens. Accelerated corrosion tests were performed by subjecting the specimens to alternate drying and wetting in salt water (3.5% NaCl). The corrosion damage of unimpregnated ferrocement specimens was found to be nearly 10 times more than in the polymer impregnated ferrocement specimens.

Chowdhury and Nimityongkul⁽¹⁰³⁾ studied the corrosion in cracked and uncracked ferrocement specimens by subjecting them to alternate wetting

and drying in sea water and urine. The depth of mortar cover was the main variable. A considerable improvement in corrosion protection was obtained by increasing the depth of cover from 1 mm to 3 mm and very small improvement was obtained beyond 4 mm. The presence of cracks are contributory factor for small covers and their effect becomes negligible when cover thickness is 4 mm or higher. The intensity of corrosion is higher in the case of urine than the sea water. With 4 mm depth of cover, the degree of corrosion comes down to the same level as that for sea water.

Ravindrarajah and Paramasivam⁽¹⁰⁴⁾ studied the effects of alternate drying and wetting in sea water and of curing in 6% NaCl solution on the strength and stiffness of ferrocement in direct tension and flexure. The test results indicated that the ultimate strength and stiffness of ferrocement were not affected by 1000 cycles of drying and wetting in sea water or by exposing in 6% NaCl solution for 9 weeks. However, the first crack strength showed improvement due to maturity gain for the mortar component. The ferrocement specimens which were initially subjected to first crack load, did not suffer any loss in the ultimate strength due to the above exposure conditions.

Recently Yozuqullu⁽¹⁰⁵⁾ studied the durability of sulphur impregnated ferrocement specimens. These specimens were found to be practically impermeable with a noticeable increase in strength together with an improved resistance against acid attack.

The durability of ferrocement can also be improved by mixing an acrylic latex solution⁽¹⁰⁶⁾ in the mortar used for final plastering. Coating of ferrocement surfaces by appropriate paints⁽¹⁰⁷⁾ also improves its durability.

2.3 BEHAVIOUR OF JOINTS

In the construction of ferrocement structures, two kinds of joints occur. The first kind of joint occurs when the size of wire mesh is not sufficient and hence overlapping of meshes is provided. This may be in one single element or in some cases, two precast elements are to be joined by overlapping of their meshes. The second kind of joint occurs, when the casting operation is completed in more than one stage.

Paramasivam and Mansur⁽¹⁰⁸⁾ investigated the effect of joints on tensile and flexural behaviour of ferrocement. The type of joints investigated were : (i) the joint between two precast elements by providing overlap of meshes, (ii) the joint provided due to overlapping of meshes in the same element, and (iii) the joint provided by casting the same element at two different times. They provided an overlap of 60 mm which was about 70 times the wire diameter. The failure of the joints was avoided due to slippage of wiremeshes (i.e. due to insufficient development length).

The tension tests of the specimens showed that the specimens with continuous reinforcement exhibited higher first crack strength than the specimens with discontinuity of reinforcement or the mortar. However, the ultimate strength of the specimens was not affected by the provision of joints. The specimens containing a joint showed considerably less ductility than the specimens with no joint. The specimens without a joint failed by the formation of a number of well distributed cracks. In contrast, only a single crack appeared in the specimens with a discontinuity in the mortar and two major cracks in the specimens with spliced reinforcement.

The flexural tests showed that the specimens with continuous reinforcement cracked at a load smaller than the specimens with overlapping of reinforcement. However, the ultimate moment of the specimens with a joint

was lower than the specimens with no joint. The specimens with continuous reinforcement, but containing a joint in the mortar exhibited a number of well distributed cracks, while the specimens with spliced reinforcement failed by only two major cracks at the free ends of the spliced wires. However, the maximum crack width in specimens with spliced reinforcement was smaller than the specimens with no joint (due to increase in volume fraction by overlapping of meshes).

Kaushik et. al.⁽¹⁰⁹⁾ carried out flexural tests on ferrocement plates by varying the length of mesh overlap. They found that the first crack and ultimate loads approach the value corresponding to a continuous mesh when the mesh overlap is sufficient to develop the requisite strength through bond for the same amount of steel. When the mesh overlap is insufficient, bond failure occurs due to slippage at the overlap and the first crack load is much lower than that of a continuous mesh reinforcement. They suggested a minimum overlap of 100 mm for wiremeshes.

2.4. BRIEF DETAIL OF INVESTIGATIONS CARRIED OUT ON VARIOUS TYPES OF ROOFING ELEMENTS

2.4.1 Channel Sections

Channel sections are the simplest form of roofing elements. Their use for roofing purposes has been demonstrated by several researchers⁽¹¹⁰⁻¹¹²⁾. Desayi and Ramesh⁽¹¹⁰⁾ investigated the behaviour of 9 channel shaped ferrocement elements under symmetrical third point loading. The span/depth ratio and the percentage of steel reinforcement were the main variables. The channel section was idealized as an equivalent T-section. The first crack moment was determined by the following expression :

$$M_{cr} = \sigma_{cb} I_c / y_t$$

where I_e = moment of inertia of gross transformed equivalent section, y_t distance of the extreme tension fiber to the neutral axis, $\sigma_{cb} = 0.1755 \sqrt{\sigma_c}$ in MPa and $\sigma_c = 0.8614 \sigma_{cu} (1 + 1.095 \frac{p_m \cdot \sigma_{fy}}{\sigma_{cu}})$.

The ultimate moment of resistance was determined by the following expression :

$$M_u = M_{fu} + M_{su} \quad (2.36)$$

where M_{fu} is the moment contribution from mesh-mortar combination and given by,

$$M_{fu} = \sigma_{fr} \cdot I_e / y_t \quad (2.37)$$

where σ_{fr} is modulus of rupture of mesh-mortar combination and depends on the ratio $p_m \sigma_{fy} / \sigma_{cu}$ and is determined from Fig. 2.7, which is a result obtained from their flexural studies of ferrocement specimens⁽³³⁾. M_{su} is the moment contribution of skeletal steel and determined by steel beam theory in the following manner :

$$M_{su} = \text{Minimum of } A_{sc} \cdot \sigma_{sy} \cdot \bar{y} \text{ and } A_{st} \cdot \sigma_{sy} \cdot \bar{y} \quad (2.38)$$

where A_{sc} and A_{st} are the areas of steel bars in the compression and tension zones and \bar{y} is the distance between the areas of these two groups of steels.

The vertical deflection at mid span was calculated by the following expression :

$$\delta = \frac{L^2 M}{E_c \cdot I_e} \quad \text{for } M \leq M_{cr} \quad (2.39)$$

$$\text{and } \delta = \frac{\beta L^2 M_{cr}}{E_c \cdot I_e} + \frac{\beta L^2 (M - M_{cr})}{\alpha E_c \cdot I_{cr}} \quad \text{for } M > M_{cr} \quad (2.40)$$

in which $E_c = 1765.8 \sqrt{\sigma_c}$ in MPa, I_{cr} = moment of inertia of cracked transformed equivalent section, β = constant depending on the loading, M = the

moment at mid span and α is given by,

$$\alpha = 0.003 [S_{ms}^{0.1958} \left(\frac{L}{D}\right)^2] + 0.133 \quad (2.41)$$

$$\text{where } S_{ms} = \frac{p_s \cdot \sigma_{sy}}{\sigma_{cu}} + \frac{p_m \cdot \sigma_{ly}}{\sigma_{cu}} \quad (2.42)$$

in which p_s is the ratio of area of longitudinal steel bars to the mortar area.

The theoretically predicted first crack moment, ultimate moment and deflections compared satisfactorily with the experimental results.

2.4.2 Ribbed Slabs/Shells

Sardid, Tatsa and Bljoger⁽¹¹³⁾ investigated the behaviour of ribbed ferrocement slabs and observed that the stiffness and ultimate strength of the slab could be increased by reducing the rib spacing or by increasing the depth of the ribs. Bljoger⁽¹¹⁴⁾ later showed the use of ribbed elements in the construction of modular prismatic shell roofs of 12 m and 22 m spans.

In U.S.S.R., ribbed shell elements have been used in constructing vaulted roofs of 18 m, 21 m and 24 m spans. Lukashenko et. al⁽¹¹⁵⁾ carried out tests on three hinged ferrocement vault of 18 m span and 9 m rise. The three hinged vault consisted of two ribbed ferrocement shell elements of 3 m x 12.7 m size with flange thickness of 15 mm. Under design snow and wind loads and line loads at the crown, the maximum deflection and tensile stress were within the permissible range and no distress was observed at any section in the span.

Kaushik et. al⁽¹¹⁶⁾ tested 24 ferrocement ribbed slabs under uniformly distributed load and studied the effect of rib spacing, volume fraction, mesh mortar parameter and specific surface ratio on the deflection, crack width and the magnitudes of first crack and ultimate loads.

The ribbed slab was analysed by treating it as an equivalent orthotropic plate. The orthotropic plate theory was assumed to be valid even upto the yield stage. At collapse, the failure pattern was assumed to follow Johansen's yield line theory and the ultimate load was calculated from the cracked transformed sections.

The theoretically predicted first crack loads and the loads at the first yield of steel compared satisfactorily with the experimental results. The predicted ultimate loads were found to be 10 to 15 percent more than the experimental results in the specimens reinforced with hexagonal mesh. The average ratio of ultimate load to the first crack load was about 2.2 for all the slabs. The first crack load, the load at first yield of steel and the ultimate loads increased with an increase in the number of ribs, specific surface, volume fraction and the mesh-mortar parameter. The average crack spacing decreased with an increase in the specific surface or the stress in the extreme layer of wiremesh. The square meshes showed a better cracking behaviour as compared to hexagonal wiremeshes.

2.4.3 Folded Plates

Vishwanath, Mhatre and Seetharamulu⁽¹¹⁷⁾ carried out the first test on a ferrocement folded plate of 1.83 m plan width, 0.65 m depth, 5.33 m effective span and 25.4 mm thickness. For constructing the folded plate, each panel was separately cast. The panels were then joined in position by welding the overlapped steel bars of the adjacent panels. In the longitudinal direction, the fold line steel bar was welded with the overlapped steel bars of the panels. All the panels were reinforced with two layers of galvanized steel mesh (19.0 mm x 19.0 mm size with wire diameter of 1.65 mm) separated by longitudinal and transverse skeletal steel bars designed for flexure and shear. Two tests, each consisting of three cycles of loading and unloading,

were conducted on the folded plate. The first test was conducted by keeping the fold joints unplastered. The maximum applied load seemed to be near the first crack load. The second test was conducted after plastering the fold joints. The stiffness of the folded plate with plastered fold joints was found to be higher than the unplastered joints. The ultimate failure was in shear along the fold line joints at the diaphragms. The major contribution to deflection was caused by flexure. The deflections caused by transverse slip and shear were small. The theoretical prediction of first crack load, ultimate load, load deflection response, crack spacing and crack widths were not reported.

Fernandes et. al⁽¹¹⁸⁾ studied the effect of type of wiremesh and amount of transverse reinforcement on ferrocement folded plate roofing panels. The elastic analysis was done by assuming ferrocement to be homogeneous isotropic material. The membrane and bending actions were assumed to be uncoupled.

The folded plates were designed for uniform live load of 75 kg/m^2 . The above analysis showed that the longitudinal normal force N_x and longitudinal bending moment M_x at mid span governed the design. Assuming that the total tensile force is taken by mesh reinforcement only, the required steel area in the longitudinal direction was provided by two layers of galvanized square welded mesh (12.7 mm x 12.7 mm size with wire diameter of 0.889 mm) in one group of panels and by two layers of galvanized hexagonal mesh (18 mm opening with wire diameter of 0.889 mm) in the second group of panels. The longitudinal skeletal steel provided in all the specimens was the same. Transverse skeletal steel bars of 6 mm diameter were provided at 50 cm, 60 cm and 70 cm spacings along the length of both the group of panels.

The panels were simply supported over a span of 4.5 m and subjected to uniform loading, which was simulated by loading with sand in increments

of 200 kg until maximum permissible deflection was observed. The elastic deflections predicted by the above analysis were marginally higher than the experimental values. This was attributed mainly to ineffective simulation of the loading condition. The panels made of hexagonal mesh yielded larger deflections for the same load as compared to the panels made of welded square mesh. The cracks were initiated at higher loads for panels with square mesh than those with hexagonal mesh. Crack spacing and crack widths were smaller for panels with square mesh than for panels with hexagonal mesh. The effect of transverse reinforcement was more pronounced in the higher load ranges than in the lower load ranges. On comparing the behaviour of folded plate panels with the asbestos panels of same dimensions and profile⁽¹¹⁹⁾, it was seen that for the same load, asbestos panels deflect more than the ferrocement panels made either of hexagonal or square mesh. The unit cost of ferrocement panels was found to be about 35% less than the asbestos panels.

Desayi, Viswanatha and Kanappan⁽¹²⁰⁾ investigated the behaviour of nine folded plates of trapezoidal shape. The span/depth ratio, amount of longitudinal reinforcement and the mesh type were the main variables. The specimens were tested under symmetrical two point loading. Two different methods were tried to determine cracking and ultimate moments. In method I, the cracking moment was determined by the following expression :

$$M_{cr} = \sigma_{mr} \cdot I_e / y_t \quad (2.43)$$

The ultimate moment of resistance was determined using a rectangular stress block for mortar in compression and neglecting its tensile strength. The wire mesh and skeletal steel were assumed to be stressed to their yield stresses in tension or compression. For the purpose of analysis, the trapezoidal cross-section was converted to an equivalent unsymmetrical I-section of the same height.

The method II for determining cracking and ultimate moment is the same as discussed in section 2.4.1 and used in the study of channel sections⁽¹¹⁰⁾. Both the methods gave a satisfactory comparison with the experimental results. However, the method II gave a smaller coefficient of variation of the ratio of theoretical and experimental ultimate moments.

The deflections for trapezoidal sections were calculated in the same way as determined in the case of channel sections⁽¹¹⁰⁾. The agreement between the theoretical and experimental deflections was satisfactory.

Out of the nine specimens, seven failed in flexure and two in shear. The two specimens which failed in shear, were reinforced with thin chicken wire mesh. The thinner chicken wire mesh had offered much less resistance than the square wiremesh towards the load carrying capacity of the specimens. In general, the first crack and ultimate moments/loads increased with an increase in the amount of longitudinal reinforcement.

Paramasivam et. al⁽¹²¹⁾ investigated the elastic behaviour of single and combined unit of folded plates for bus shelter under uniform vertical loads. The single unit was 3 m x 3 m in plan with a rise of 0.7 m and 45° sloping sides. The folded plate was designed for uniform vertical load of 2 kN/m. The elastic analysis was done by finite element method using computer program SAPIV⁽¹²²⁾. The stresses obtained were low and hence a nominal mesh reinforcement with 3 mm cover resulting into an overall thickness of 18 mm was provided. The two units were cast with a provision of 100 mm mesh overlap from the outer edge for joining at a later stage.

The single unit was first tested by applying four layers of sand bags resulting into a total of 2 kN/m. The unit was then unloaded. The deflection and strain readings during loading and unloading showed reasonable agreement.

The second unit was then connected to the first unit by tying the overlapping meshes and subsequently plastering it. The combined unit was also loaded with four layers of sand bags. The load deflection curves of the single and combined unit showed linear behaviour upto the maximum applied load. No distress was observed in any part of the structure including the cast-in-situ connection at maximum loading. The maximum deflections under 2 kN/m were found to be 2.96 mm and 2.62 mm for single and combined unit, respectively. The strain readings were observed to be linear and computed values of membrane stresses from the strain readings were found to be very small. It was observed that the central bay is stronger than the outer bays. The cost of construction of these units including the foundation was found to be about 30% less than the similar type of reinforced concrete bus shelter.

2.4.4 Cylindrical Shells

Paramasiyam and Lee⁽¹²³⁾ investigated the behaviour of single and combined ferrocement cylindrical shell units. The single unit was 3 m x 3 m in plan with a rise of 0.5 m. It was designed for a superimposed load of 1.2 kN/m². The reinforcement consisted of 3 mm diameter mild steel bars at 175 mm centre to centre with one layer of woven wiremesh at top and bottom of the skeletal steel. The shell thickness was 15 mm. The combined unit was obtained by tying the projected mesh reinforcements of the two units with an overlap of 150 mm. The mortar was applied by hand pressing and cured for five days.

The single and combined shell units were tested under uniformly distributed load. The combined shell unit was found to be more efficient than the single unit. At working load of 1.2 kN/m², the maximum deflection and principal tensile stress were found to be 7 mm and 1.9 MPa and these

values were in close agreement with theoretical predictions using classical membrane theory.

2.4.5 Hyperbolic Paraboloid Shell

Das Gupta, Paramasivam and Lee⁽¹²⁴⁾ investigated the behaviour of a ferrocement hyperbolic paraboloid shell in the shape of an inverted umbrella. The shell was 2.44 m x 2.44 m in plan with the rise from the centre to the exterior edge of 0.37 m. The shell was 16 mm thick and reinforced with two layers of woven wiremesh spaced by 3 mm diameter mild steel bars at 150 mm centres both ways. It was tested under uniformly distributed load upto a load intensity of 4.8 kN/m^2 . The maximum deflection and principal tensile stress at 4.8 kN/m^2 load level were found to be 1.6 mm and 1.25 MPa and no distress was observed in any part of the structure. The shell was analysed by classical membrane theory and the experimental results were found to be in good agreement with theoretical predictions.

2.4.6 Funicular Shells

Elangovan and Santha Kumar⁽¹²⁵⁾ investigated the behaviour of room size ferrocement funicular shell under uniformly distributed loads. The funicular shell roof was 2.7 m x 2.7 m in plan with a rise of 0.5 m and shell thickness of 30 mm. The shell was supported continuously on edge beams of size 250 mm x 250 mm. The funicular shape of the shell was provided by 6 mm diameter skeletal steel bars at 337.5 mm spacing. One layer of chicken wiremesh of 0.711 mm wire diameter was provided on both sides of the skeletal steel. Form work was used only for the edge beams. The shell was cast without the form work.

The shell was tested under uniformly distributed load applied in the form of sand bags over the entire area. A maximum load of 16 kN (2.2 kN/m^2)

was applied in increments of 4 kN. This load is about four times the minimum live load as per I.S. Code⁽¹²⁶⁾. The maximum deflection under the applied load was 0.24 mm. The elastic analysis of funicular shell was done by finite element method. The theoretical maximum deflection compared well with the experimental value. The funicular shell had the compressive stress in most parts of the shell except for a distance of about 10% of span from the edges. The maximum values of compressive and tensile stresses were 0.07 MPa and 0.025 MPa respectively. The maximum moment in the shell was very small (0.09 N mm/mm).

2.4.7 Tension Ribbon

Subrahmanyam et. al⁽¹²⁷⁾ investigated the behaviour of 25.1 m long, 0.93 m wide and 30 mm thick ferrocement tension ribbon under increasing uniformly distributed load. The ferrocement ribbon was designed for a normal working load of 150 kg/m^2 (self weight and finishes) and an occasional live load of 75 kg/m^2 . The main reinforcement consisted of 10 numbers 10 mm diameter high yield strength deformed bars in the longitudinal direction, 5 mm diameter steel bars at 50 cm centres in the transverse direction and two layers of galvanized wiremesh of 10 mm x 10 mm size with wire diameter of 0.889 mm. The ribbon was cast without the form work in one single operation. The initial central dip due to reinforcement was 0.70 m. After 28 days of casting, the central dip was found to be 0.80 m.

The uniformly distributed load on the structure was applied in the form of brick layers. The first visible cracks occurred at a load level of 137 kg/m^2 . Some of the observations were discontinued after a load level of 266 kg/m^2 due to safety reasons. The structure was loaded upto 395 kg/m^2 without the occurrence of the failure.

The ribbon was idealized as cable-beam system. The analysis incorporated the material and geometrical nonlinearity of the structure. An iterative finite difference method was used to solve the problem. The analysis was carried out by considering (i) the composite action of ferrocement, and (ii) the action of reinforcement alone. The horizontal tension was better predicted by the analysis considering the composite action, while the deformation behaviour was better predicted by considering the action of the reinforcement alone. The central deflection due to normal working load of 150 kg/m^2 (1.47 kN/m^2) was only $\text{span}/157$. The maximum crack width at this load level was about 0.06 mm . At occasional working load of 225 kg/m^2 (2.21 kN/m^2), the maximum crack width was 0.185 mm . Against the design load of 150 kg/m^2 (1.47 kN/m^2), the structure withstood a load of 395 kg/m^2 (3.87 kN/m^2) with a deflection of $\text{span}/80$.

2.5 CONCLUDING REMARKS

Research investigations into the behaviour of ferrocement has revealed that its mechanical properties depend on the volume fraction and specific surface of mesh reinforcement, tensile strength of mortar, yield strength of wiremesh, modulus of elasticity of mortar and wiremesh, bond strength between mortar and mesh reinforcement and the mortar cover.

Several researchers have investigated the behaviour of different types of roofing/flooring elements. These include simple channel sections, ribbed slabs and spatial elements like folded plates and shells of various shapes. Based on the test results of ferrocement control specimens, some approximate and quasi-empirical relations have been proposed to predict the load deformation and cracking behaviour of these elements. Simple classical theories such as beam bending theory, plate bending theory and the membrane cum bending

theory have been used to predict the behaviour in both the elastic and the post cracking ranges. Invariably most of the researchers have used the modified flexural rigidity (EI_{cr}) in the computations for the prediction in the post cracking range. Such an analysis tends to be approximate as it is unable to cater for the complexities arising due to the changing EI values from section to section in the post cracking range, orthotropy of the composite material and yielding of wiremeshes at the critical sections leading to local redistribution of stresses. Thus, there is a need to develop a rational basis of the analysis of ferrocement structures which can predict their behaviour right upto the ultimate load. This would also need to establish a suitable failure criterion for the constituent materials of the composite under different stress states.

In the present study, the behaviour of a new type of roofing/flooring element in the form of box girder shape has been investigated experimentally and analytically. The above element provides flat top surface and better load deformation and cracking behaviour as compared to channel sections and ribbed slabs which are also flat top due to its larger flexural and torsional rigidity. A rational analysis of the box girder has been carried out through the elastic, cracked and ultimate stages using the finite element method. The details of the analytical method are presented in the following chapter.

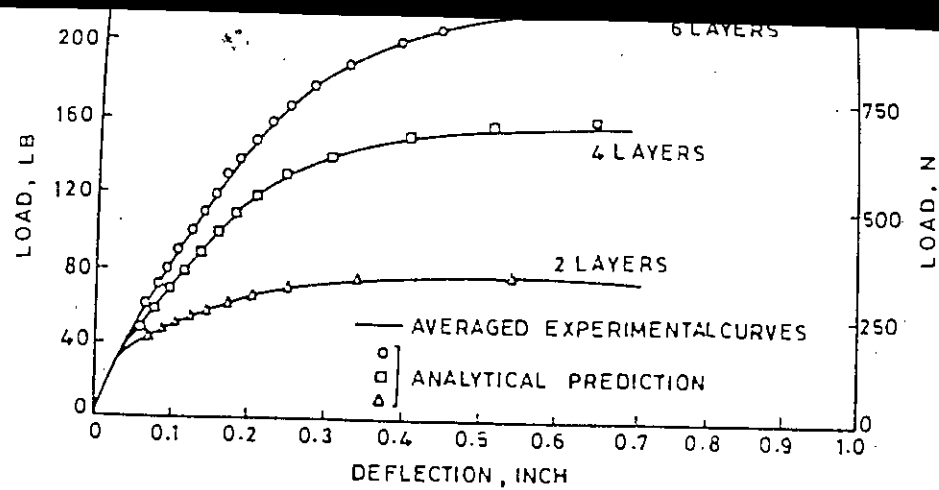


FIG. 2.1 - COMPARISON OF ANALYTICAL AND EXPERIMENTAL LOAD-DEFLECTION CURVES OF THE SPECIMENS WITH 1/2" WELDED MESH⁽⁶²⁾

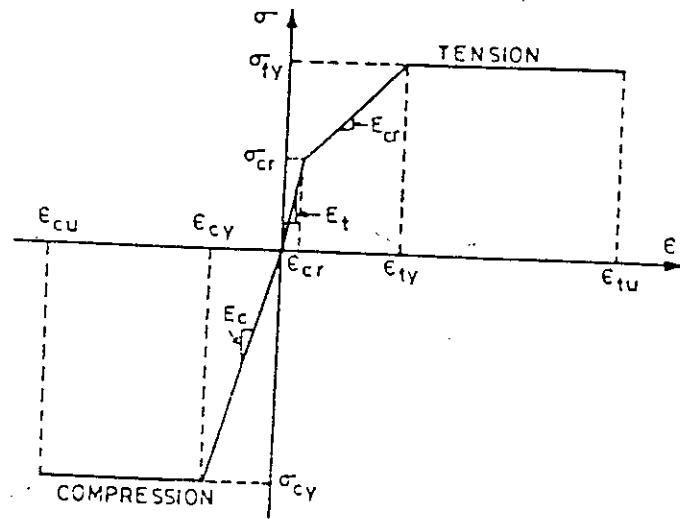


FIG. 2.2 - IDEALIZED STRESS-STRAIN CURVE FOR FERROCEMENT⁽⁶³⁾

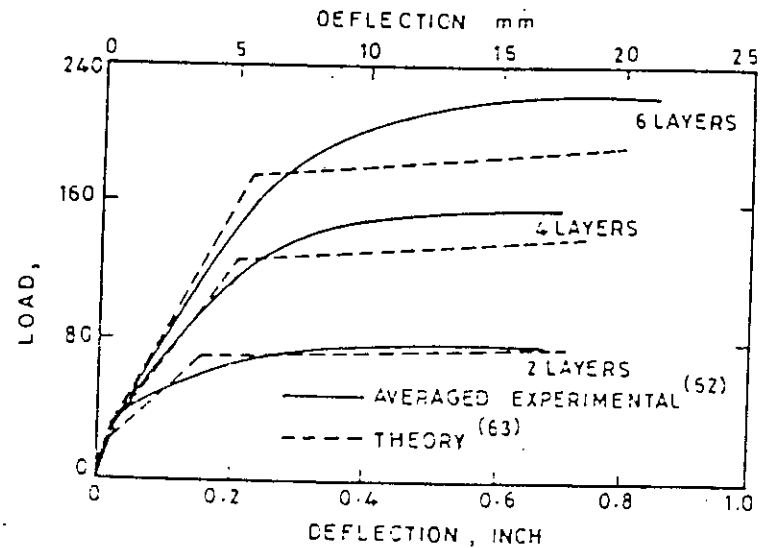


FIG. 2.3 - COMPARISON OF LOAD-DEFLECTION CURVES BY THE THEORY⁽⁶³⁾ WITH THE AVERAGED EXPERIMENTAL CURVES OF BALAGURU *et. al*⁽⁶²⁾

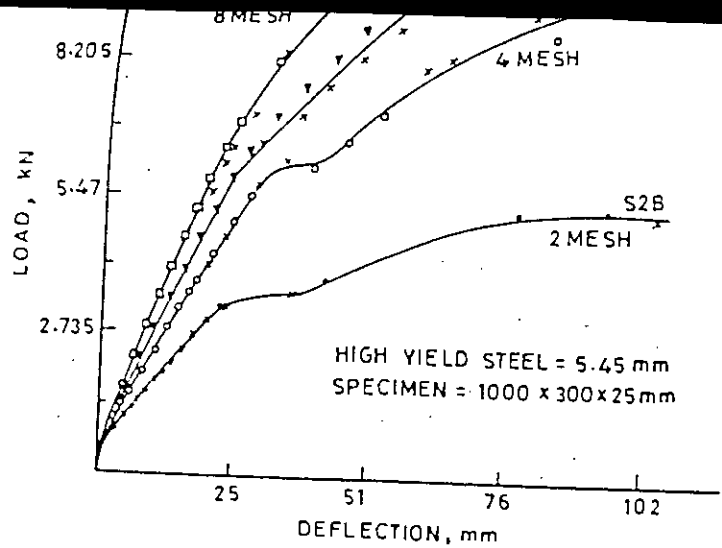


FIG.2.4 -LOAD-DEFLECTION BEHAVIOUR: HIGH YIELD STEEL (66)

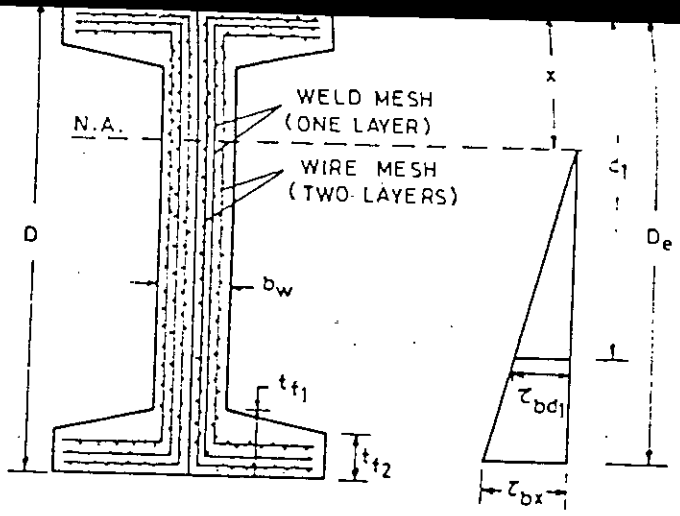


FIG.2.6 -BUILT-UP I-SECTION WITH ASSUMED VARIATION FOR BOND STRESS (70)

57

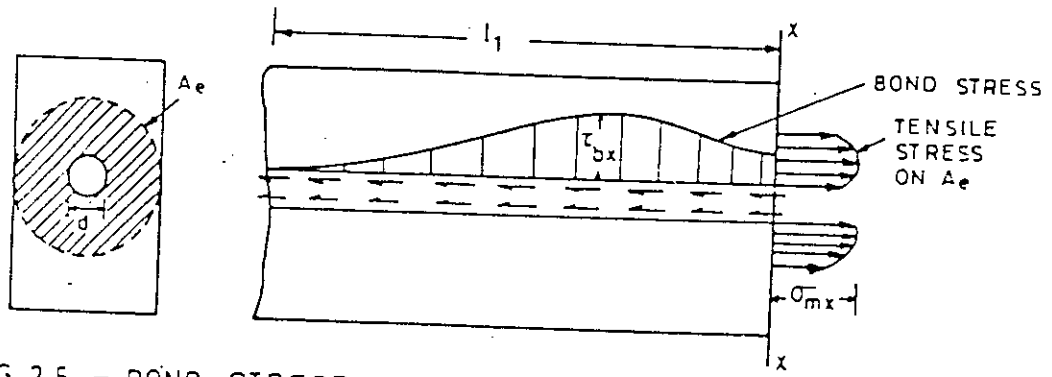


FIG.2.5 - BOND STRESS DISTRIBUTION AND TENSILE STRESS DISTRIBUTION IN CONCRETE AT A DISTANCE l_1 FROM A CRACK FORMED IN A REINFORCED CONCRETE MEMBER (71)

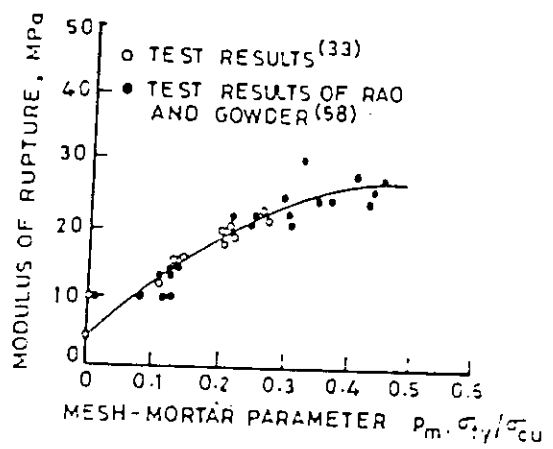


FIG.2.7 -VARIATION OF MODULUS OF RUPTURE OF FERROCEMENT WITH MESH MORTAR PARAMETER (33)

CHAPTER III

METHOD OF ANALYSIS

3.1 GENERAL

For the analysis of ferrocement elements, two approaches have been used. In one approach, conventional reinforced concrete theory has been extended to ferrocement in which suitable idealized stress-strain relations for the component materials, namely, mortar and mesh (or mesh and skeletal steel) reinforcement are assumed. The effect of mortar in tension is neglected or it is included upto the cracking strain of the mortar. Logan and Shah⁽⁵⁹⁾, Rajgopalan and Parameswaran⁽¹²⁸⁾, Balaguru et. al⁽⁶²⁾ and Naaman⁽¹³⁾ have analysed ferrocement beams using this approach. In the second approach, ferrocement composite is treated as a homogeneous material. A suitable stress-strain relation for the composite is assumed in compression and tension. The tensile contribution of the mortar is incorporated in the stress-strain relation of the composite in tension. Huq and Pama^(38, 63) and Kaushik et. al^(74, 116) analysed ferrocement beams and ribbed slabs respectively using this approach. Desayi et. al^(110, 120) also followed this approach. They expressed stress in the composite as a function of the mesh-mortar parameter.

Three dimensional ferrocement plated structures and shells of various shapes have been analysed in the elastic stage by using beam theory^(110, 120), classical membrane theory^(123, 124), membrane and bending theory⁽¹¹⁸⁾ and more recently the finite element method^(122, 125) (described in section 2.4). Classical membrane theory fails to predict even the elastic behaviour in the case of complex shell shapes, i.e. hypped hyper shaped ferrocement shell element as reported by Tatsa et. al⁽¹²⁹⁾ and finally analysed by the finite element method. In the cracked range, the analysis has been reported only in

the case of trapezoidal shaped folded plate using beam theory by Desayi et. al⁽¹²⁰⁾. Even the elastic analysis of folded plates by beam method is an approximate one because it does not take into account the stresses induced due to the distortion and warping of the cross-section.

3.2 BRIEF REVIEW OF VARIOUS METHODS OF ANALYSING THIN WALLED BOX GIRDER ELEMENTS

Thin walled box girder elements carry the applied loads due to membrane and bending actions. These two actions also include the traditionally known distortion and warping of the cross section. Maisel and Roll⁽¹³⁰⁾ reviewed various methods of elastic analysis of thin walled box girders and presented a brief summary of the simpler approximate methods which require only the use of a slide-rule or programmable desk calculator. The methods presented by Richmond⁽¹³¹⁾, Kupfer⁽¹³²⁾ and Steinle⁽¹³³⁾ cover the distortion and warping of the cross-section. These approximate methods however do not cover all the structural actions of the box girder. Folded plate, finite strip and finite element methods can be described as relatively exact methods because they consider all the structural actions involved in the three dimensional plated structures. Folded plate method, also known as elasticity method, was developed by Goldberg and Leve⁽¹³⁴⁾. It was used in the study of simply supported box girder bridges by Scordelis⁽¹³⁵⁾ and Chu and Dudnik⁽¹³⁶⁾. The method however suffers from being fairly complex, and is difficult to apply to orthotropic folded plates or box girders. The finite strip method was first introduced in analysing prismatic folded plate structures and box girder bridges by Cheung^(137, 138). It is a special form of finite element method in which the structure is discretized into a finite number of strips which have constant cross-section and material properties over the entire length. The method can be used for orthotropic materials. The computational

effort required is very small as compared to finite element method⁽¹³⁹⁾.

The folded plate and finite strip methods are suitable only for the elastic analysis of box girder elements. An attempt was made by Kaushik et. al⁽¹⁴⁰⁾ to analysis ferrocement box girder elements in the cracked range by finite strip method. The predicted deflections at mid span in the uncracked and cracked range compared satisfactorily with the experimental results while predicted longitudinal strains at 25 mm above the soffit at mid span compared satisfactorily only in the uncracked range and were about 50 to 65 percent of the experimentally observed strains in the cracked range. The large discrepancy in the cracked range is due to the basic assumption that the entire length of the strip is cracked (due to constant material property assumption in the strip method). While even at ultimate failure, the entire length is never cracked. After cracking at a particular section, the strains increase at a much faster rate as compared to the uncracked sections.

3.3 CHOICE OF THE METHOD OF ANALYSIS

The use of beam or finite strip method leads to the approximate solution in the cracked range. The above methods fail to predict the complete load deformation response and progressive cracking in the structure due to increasing loads.

The finite element method is the most powerful and versatile tool of structural analysis. Nonlinear analysis of reinforced concrete plates and shells by finite element method has been carried out by various researchers using two different approaches i.e. the modified EI approach and the layered approach. In the modified EI approach, a macroscopic view of the problem is taken. An overall moment curvature relation reflecting the various stages of material behaviour is assumed. This approach has been applied to reinforced

concrete plates by Jofrient and McNeice⁽¹⁴¹⁾ and to plates and shells by Bell⁽¹⁴²⁾. The approach is simple but can not accurately reflect the interaction between membrane and bending actions. In the layered approach, the element is assumed to be consisting of suitable number of concrete and steel layers. The variation of material properties across the plate thickness is allowed by assigning different material properties to layers depending upon their strain state. The material properties are assumed to be constant over the each layer thickness. Kirchhoff's assumption is used to relate strain in any layer in terms of strains and curvatures of the reference surface. Idealized stress-strain relations are assumed for the component materials i.e. in the uncracked, cracked, yielded or crushed state for concrete and unyielded or yielded state for steel. The stiffness of the element is obtained by adding the contribution of all the layers. The resulting stiffness matrix contains the stiffness contributions due to membrane, bending and membrane-bending interaction. Recently Prakhya and Adidam⁽¹⁴³⁾ used layered approach in analysing ferrocement slabs.

In the present study, the layered finite element approach is suitably modified and adopted. For thin ferrocement structures, the element is assumed to be consisting of single mortar layer in the uncracked stage, uncracked and cracked mortar layers in the cracked stage and smeared layers of wire mesh and skeletal steel (Fig. 3.1 and 3.16). In the cracked stage, the depth of cracked yielded crushed mortar is determined. Wire mesh and skeletal steel are checked against yielding. The stiffness of the element in the cracked stage is obtained by adding the contributions due to uncracked mortar layer, cracked/yielded mortar layer and unyielded layers of wire mesh and skeletal steel. This results in a saving in the computational effort in the computer program as compared to the conventional layered approach.

3.4 FINITE ELEMENT FORMULATION OF THE PROBLEM

The ferrocement box girders have been analysed by finite element method under dead loads and monotonically increasing live loads. A rectangular flat shell element capable of representing membrane action, bending action and the interaction between membrane and bending action is adopted. Only material nonlinearity due to cracking of mortar, tension stiffening effect of mortar between the cracks and the nonlinear stress-strain relationships for the mortar, wiremesh and skeletal steel is considered. Since the box section provides large flexural and torsional rigidity, the deflections in the cracked range are assumed to be small. Hence, geometrical nonlinearity is not considered. Also not considered in the analysis are bond slip between the reinforcement and mortar, time dependent and thermal effects.

3.4.1 Choice of the Element

For the analysis of prismatic box girders with linear edges, flat shell elements are the most appropriate one. Different flat shell elements are obtained by combining the different membrane and the bending elements. For the analysis of above type of structures, rectangular flat shell elements with 4 nodes^(144, 145) or isoparametric parabolic shell elements with 8 or 9 nodes^(143, 146, 147) have been used. For the same size of element and same degrees of freedom per node, the computational effort required in 8 or 9 noded elements is very large as compared to 4 noded elements. The computational effort increases even more when iterative nonlinear analysis of the structures is carried out. In order to save on computational effort, a simple 4 noded rectangular flat shell element with six degrees of freedom per node is adopted for the present analysis. The chosen element can also be used for the analysis of prismatic folded plates, cylindrical shells and

other three-dimensional structures consisting of rectangular plates. The procedure developed, however, allows the use of any general type of element.

The chosen element is obtained by combining a twelve degrees of freedom membrane element⁽¹⁴⁸⁾ having a linear variation of u_0 and a cubic variation of v_0 with a twelve degrees of freedom nonconforming plate element⁽¹⁴⁹⁾, as shown in Fig. 3.2. Such an element provides a better inter-element compatibility of displacement at fold lines. The six degrees of freedom at each corner node are u_0 , v_0 and $\partial v_0 / \partial x$ representing membrane action and w_0 , $\partial w_0 / \partial y$ and $-\partial w_0 / \partial x$ representing bending action. The efficiency of the chosen element has been established by Gibson and Mitwally⁽¹⁴⁸⁾, Mcleod⁽¹⁵⁰⁾ and Lim⁽¹⁵¹⁾ by analysing different types of reinforced concrete plate structures such as box girders, folded plates and frames with shear walls in the elastic range.

The displacement components u_0 , v_0 , w_0 at any point x , y on the reference plane are described in terms of nodal displacements, listed as $\{\delta_m\}^e = \{u_{01}, v_{01}, \theta_{z1}, u_{02}, v_{02}, \theta_{z2}, \dots\}$ for membrane action and as $\{\delta_b\}^e = \{w_{01}, \theta_{x1}, \theta_{y1}, w_{02}, \theta_{x2}, \theta_{y2}, \dots\}$ for bending action, with the help of shape functions given below:

$$\begin{aligned} u_0 &= A_1 + A_2x + A_3y + A_4xy \\ &= \sum_{i=1}^4 N_j u_{0i} \end{aligned} \quad (3.1)$$

where $j = 3i - 2$ and N_j are the shape functions.

$$\begin{aligned} v_0 &= A_5 + A_6x + A_7y + A_8x^2 + A_9xy + A_{10}x^3 + A_{11}x^2y + A_{12}x^3y \\ &= \sum_{i=1}^4 [N_{j1} v_{0i} + N_{\ell} \cdot \theta_{zi}] \end{aligned} \quad (3.2)$$

where $\ell = 3i$, $j = \ell - 1$ and N_{j1} , N_{ℓ} are the shape functions.

$$\Theta_z = \frac{\partial v_o}{\partial x} = A_6 + 2A_8x + A_9y + 3A_{10}x^2 + 2A_{11}xy + 3A_{12}x^2y \quad (3.3)$$

$$\begin{aligned} w_o &= B_1 + B_2x + B_3y + B_4x^2 + B_5xy + B_6y^2 + B_7x^3 + B_8x^2y + B_9xy^2 \\ &\quad + B_{10}y^3 + B_{11}x^3y + B_{12}xy^3 \\ &= \sum_{i=1}^4 [N'_j w_{oi} + N'_k \Theta_{xi} + N'_l \Theta_{yi}] \end{aligned} \quad (3.4)$$

where $l = 3i$, $j = l-2$, $k = l-1$ and N'_j, N'_k, N'_l are the shape functions.

Choosing a non-dimensionalized coordinate system with $\xi = \frac{x}{a}$ and $\eta = \frac{y}{b}$ (a and b are the sides of the rectangular element), the shape functions are easily determined as given in Table 3.1.

3.4.2 Basic Formulation For Elastic Analysis

A flat continuum subjected to combined action of stretching and bending is essentially a problem of three dimensional elasticity but, however, using Love-Kirchhoff's assumptions for thin flat plates it reduces to a two dimensional one. These assumptions may be stated as follows :

- (1) The straight fibers of a plate which are perpendicular to the reference plane before deformation remain so after deformation and do not change their length.
- (2) The normal stresses acting on planes parallel to the reference plane may be neglected in comparison with the other stresses.

Although the first assumption results in a plane strain condition and the second one in a plane stress condition, these assumptions give reasonably accurate results for thin plates on account of normal strains being very small and having little influence on stresses and strain.

Table 3.1

Shape Functions (N) for Membrane and Bending Elements

Nodal Freedom	Shape Function (N_m) for Membrane Element	Nodal Freedom	Shape Function (N_b) for Bending Element
u_{01}	$-\xi - \eta + \xi\eta + 1$	w_{01}	$1 - 3\xi^2 - \xi\eta - 3\eta^2 + 2\xi^3$ $+ 3\xi^2\eta + 3\xi\eta^2 + 2\eta^3 - 2\xi^3\eta$ $- 2\xi\eta^3$
v_{01}	$1 - \eta - 3\xi^2 + 2\xi^3 + 3\xi^2\eta - 2\xi^3\eta$	θ_{x1}	$b(\eta - \xi\eta - 2\eta^2 + 2\xi\eta^2$ $+ \eta^3 - \xi\eta^3)$
θ_{z1}	$a(\xi - 2\xi^2 - \xi\eta + \xi^3 + 2\xi^2\eta - \xi^3\eta)$	θ_{y1}	$-a(\xi - \xi\eta - 2\xi^2 + 2\xi^2\eta$ $+ \xi^3 - \xi^3\eta)$
u_{02}	$\xi - \xi\eta$	w_{02}	$3\xi^2 + \xi\eta - 2\xi^3 - 3\xi^2\eta$ $- 3\xi\eta^2 + 2\xi^3\eta + 2\xi\eta^3$
v_{02}	$3\xi^2 - 2\xi^3 - 3\xi^2\eta + 2\xi^3\eta$	θ_{x2}	$b(\xi\eta - 2\xi\eta^2 + \xi\eta^3)$
θ_{z2}	$a(-\xi^2 + \xi^3 + \xi^2\eta - \xi^3\eta)$	θ_{y2}	$-a(-\xi^2 + \xi^2\eta + \xi^3 - \xi^2\eta)$
u_{03}	$\xi\eta$	w_{03}	$-\xi\eta + 3\xi^2\eta + 3\xi\eta^2 - 2\xi^3\eta$ $- 2\xi\eta^3$
v_{03}	$3\xi^2\eta - 2\xi^3\eta$	θ_{x3}	$b(-\xi\eta^2 + \xi\eta^3)$
θ_{z3}	$a(-\xi^2\eta + \xi^3\eta)$	θ_{y3}	$-a(-\xi^2\eta + \xi^3\eta)$
u_{04}	$\eta - \xi\eta$	w_{04}	$\xi\eta + 3\eta^2 - 3\xi^2\eta - 3\xi\eta^2 - 2\eta^3$ $+ 2\xi^3\eta + 2\xi\eta^3$
v_{04}	$\eta - 3\xi^2\eta + 2\xi^3\eta$	θ_{x4}	$b(-\eta^2 + \xi\eta^2 + \eta^3 - \xi\eta^3)$
θ_{z4}	$a(\xi\eta - 2\xi^2\eta + \xi^3\eta)$	θ_{y4}	$-a(\xi\eta - 2\xi^2\eta + \xi^3\eta)$

Using Kirchhoff's assumptions, the displacements (u,v,w) at any point 'P' in the shell (Fig. 3.3) at a fiber distance z from the reference plane can be described in terms of the displacements and their derivatives on the reference plane. Thus,

$$\begin{aligned} u &= u_0(x,y) - z \frac{\partial w_0}{\partial x} \\ v &= v_0(x,y) - z \frac{\partial w_0}{\partial y} \\ w &= w_0(x,y) \end{aligned} \quad (3.5)$$

The displacements $\{u_0, v_0, w_0\}$ can be expressed in terms of shape functions and nodal displacements at the reference plane as follows :

$$\begin{Bmatrix} u_0 \\ v_0 \\ w_0 \end{Bmatrix} = \begin{bmatrix} N_m & 0 \\ \hline 0 & N_b \end{bmatrix} \begin{Bmatrix} \delta_m \\ \delta_b \end{Bmatrix} \quad (3.6)$$

where N_m and N_b are the shape functions for membrane and bending actions respectively.

The strains $\{\epsilon\}$ at point 'P' are obtained by differentiating equation (3.5). Thus,

$$\begin{aligned} \{\epsilon\} &= \begin{Bmatrix} \frac{\partial u}{\partial x} \\ \frac{\partial v}{\partial y} \\ \frac{\partial u}{\partial y} + \frac{\partial v}{\partial x} \end{Bmatrix} = \begin{Bmatrix} \frac{\partial u_0}{\partial x} \\ \frac{\partial v_0}{\partial y} \\ \frac{\partial u_0}{\partial y} + \frac{\partial v_0}{\partial x} \end{Bmatrix} + z \begin{Bmatrix} -\frac{\partial^2 w_0}{\partial x^2} \\ -\frac{\partial^2 w_0}{\partial y^2} \\ -2 \frac{\partial^2 w_0}{\partial x \partial y} \end{Bmatrix} \\ &= \{\epsilon_0\} + z \{\chi_0\} \end{aligned} \quad (3.7)$$

where $\{\epsilon_o\}$ and $\{\chi_o\}$ are in plane strains and curvatures at the reference plane. $\{\epsilon_o\}$ and $\{\chi_o\}$ can be expressed in terms of nodal displacements and appropriate derivatives of shape functions as follows :

$$\begin{aligned}\{\epsilon_o\} &= [B_m] \{\delta_m\}^e \\ \{\chi_o\} &= [B_b] \{\delta_b\}^e\end{aligned}\tag{3.8}$$

where $[B_m]$ contains first order derivatives of $[N_m]$ and $[B_b]$ contains the second order derivatives of $[N_b]$.

Writing equation (3.7) in terms of strain derivative matrices $[B_m]$, $[B_b]$ and nodal displacements,

$$\begin{aligned}\{\epsilon\} &= [B_m] \{\delta_m\}^e + z [B_b] \{\delta_b\}^e \\ &= [[B_m] : z[B_b]] \begin{Bmatrix} \{\delta_m\}^e \\ \dots\dots\dots \\ \{\delta_b\}^e \end{Bmatrix} \\ &= [B] \{\delta\}^e\end{aligned}\tag{3.9}$$

where

$$[B] = [[B_m] : z[B_b]]\tag{3.10}$$

and

$$\{\delta\}^e = \begin{Bmatrix} \{\delta_m\}^e \\ \{\delta_b\}^e \end{Bmatrix}\tag{3.11}$$

From the material constructive law, the stresses

$$\{\sigma\} = [D] (\{\epsilon\} - \{\epsilon_o^i\}) + \{\sigma_o^i\}\tag{3.12}$$

where $[D]$, $\{\epsilon_o^i\}$ and $\{\sigma_o^i\}$ are the material property matrix, initial strain vector and the initial stress vector respectively.

Applying the principle of virtual work, it can be shown that the element nodal forces $\{F\}^e$ and element nodal displacements $\{\delta\}^e$ are related through a square symmetric matrix $[K]^e$ called the element stiffness matrix, as follows :

$$\{F\}^e = \int [B]^T [D] [B] dV \{\delta\}^e - \int [B]^T [D] \{\epsilon_0^i\} dV + \int [B]^T \{\sigma_0^i\} dV - \int [N]^T \{p\} dV \quad (3.13)$$

where the element stiffness matrix

$$[K]^e = \int [B]^T [D] [B] dV \quad (3.14)$$

the consistent nodal forces due to initial strain $\{\epsilon_0^i\}$

$$= - \int [B]^T [D] \{\epsilon_0^i\} dV \quad (3.15)$$

the consistent nodal forces due to initial stress $\{\sigma_0^i\}$

$$= \int [B]^T \{\sigma_0^i\} dV \quad (3.16)$$

the consistent nodal forces due to body forces $\{p\}$

$$= - \int [N]^T \{p\} dV \quad (3.17)$$

Substituting for $[B]$ from equation (3.10) in equation (3.14), the element stiffness matrix can be expressed as given below :

$$[K]^e = \int_{\text{vol}} \begin{array}{cc} [B_m]^T [D] [B_m] & \vdots & [B_m]^T z [D] [B_b] \\ \dots\dots\dots & & \dots\dots\dots \\ [B_b]^T z [D] [B_m] & \vdots & [B_b]^T z^2 [D] [B_b] \end{array} dV$$

$$= \int_{\text{Area}} \begin{array}{cc} [B_m]^T \int_0^t [D] dz [B_m] & \vdots & [B_m]^T \int_0^t z [D] dz [B_b] \\ \dots\dots\dots & & \dots\dots\dots \\ [B_b]^T \int_0^t z [D] dz [B_m] & \vdots & [B_b]^T \int_0^t z^2 [D] dz [B_b] \end{array} dA$$

$$\begin{aligned}
 &= \int_{\text{Area}} \begin{array}{c|c} [B_m]^T [D_{mm}] [B_m] & [B_m]^T [D_{mb}] [B_b] \\ \hline [B_b]^T [D_{mb}] [B_m] & [B_b]^T [D_{bb}] [B_b] \end{array} dA \\
 &= \begin{bmatrix} [K_{mm}] & [K_{mb}] \\ [K_{mb}] & [K_{bb}] \end{bmatrix} \quad (3.18)
 \end{aligned}$$

$$\text{where } [K_{mm}] = \int_{\text{Area}} [B_m]^T [D_{mm}] [B_m] dA ,$$

$$[K_{mb}] = \int_{\text{Area}} [B_m]^T [D_{mb}] [B_b] dA = [K_{bm}]^T ,$$

$$[K_{bb}] = \int_{\text{Area}} [B_b]^T [D_{bb}] [B_b] dA ,$$

$$[D_{mm}] = \int_0^t [D] dz ,$$

$$[D_{mb}] = \int_0^t z [D] dz \quad \text{and}$$

$$[D_{bb}] = \int_0^t z^2 [D] dz$$

$[K_{mm}]$, $[K_{mb}]$ and $[K_{bb}]$ are the membrane stiffness, coupling stiffness and bending stiffness respectively. If the material properties are symmetrical with respect to the middle plane, the term $\int z[D]dz$ becomes zero and thus does $[K_{mb}]$. For such materials, the membrane and bending actions are uncoupled.

The element stiffness $[K]^e$ and the consistent nodal forces $\{F\}^e$ have been evaluated by numerically integrating the equations (3.14-3.17) over the element area. A three by three Gauss quadrature has been followed for numerical integration. The element stiffness $[k]^e$ is thus determined by

$$\begin{aligned}
 [K]^e &= \int_{\Lambda} \begin{array}{c} [B_m]^T [D_{mm}] [B_m] \\ \dots\dots\dots [B_m]^T [D_{mb}] [B_b] \\ \dots\dots\dots [B_b]^T [D_{mb}] [B_m] \\ \dots\dots\dots [B_b]^T [D_{bb}] [B_b] \end{array} d\Lambda \\
 &= \sum_{i=1}^n \sum_{j=1}^n \begin{array}{c} [B_m]_{ij}^T [D_{mm}]_{ij} [B_m]_{ij} \\ \dots\dots\dots [B_m]_{ij}^T [D_{mb}]_{ij} [B_b]_{ij} \\ \dots\dots\dots [B_b]_{ij}^T [D_{mb}]_{ij} [B_m]_{ij} \\ \dots\dots\dots [B_b]_{ij}^T [D_{bb}]_{ij} [B_b]_{ij} \end{array} C_i C_j \quad \text{ab} \\
 &\quad \quad \quad (3.19)
 \end{aligned}$$

where $[B_m]_{ij}$, $[B_b]_{ij}$, $[D_{mm}]_{ij}$, $[D_{mb}]_{ij}$ and $[D_{bb}]_{ij}$ are the appropriate strain matrices and the material matrices as defined earlier at Gauss points (i,j) , C_i , C_j are the appropriate weighting coefficients, and n is the order of Gauss quadrature used. Thus the element area is divided into n^2 number of areas which can have different $[D_{mm}]_{ij}$, $[D_{mb}]_{ij}$, $[D_{bb}]_{ij}$. Figure 3.4 shows the typical sampling (Gauss) points and areas under their command for three point integration rule. The position of sampling points and the weighting coefficients are given in Table 3.2. Since in the present study, the highest power in defining displacement function is three, the highest power expected in the integration for element stiffness is six. The three points Gauss integration rule can exactly integrate functions only upto fifth order (one order less). Going in for a higher order i.e. fourth order increases the computation effort almost by double. The reduced integration has a favourable feature that it yields better behaviour as pointed by Zienkiewicz et. al⁽¹⁵²⁾.

Table 3.2 Gauss Integration Constants for Three Point Integration ($n = 3$)

S.No.	Position of Sampling Point	Weighting Coefficient
1	$Z_1 = 0.11270, 0.16653, 0.79253$	0.27777, 0.77778, 0.77778
2	$Z_2 = 0.5$	0.44444, 0.44444, 0.44444
3	$Z_3 = 0.88729, 0.83346, 0.20742$	0.77777, 0.77778, 0.77778

The consistent nodal forces due to body forces can be determined by

$$\begin{aligned} \{F\}_b^e &= \int_{\text{Area}} [N]^T \{p\} dA \\ &= \sum_{i=1}^n \sum_{j=1}^n [N_{ij}]^T \{p\}_{ij} \cdot C_i \cdot C_j \cdot a \cdot b \end{aligned} \quad (3.20)$$

where $\{p_{ij}\}$ are the pressure intensities at the Gauss points i, j .

Similarly, the consistent nodal forces due to initial stress $\{\sigma_o^i\}$ can be determined by

$$\begin{aligned} \{F\}^e &= \int_V [B]^T \{\sigma_o^i\} dV \\ &= \sum_{i=1}^n \sum_{j=1}^n \begin{matrix} [B_m]_{ij}^T \{F_{om}\}_{ij} \\ \dots\dots\dots \\ [B_b]_{ij}^T \{M_o\}_{ij} \end{matrix} C_i \cdot C_j \cdot ab \end{aligned} \quad (3.21)$$

where $\{F_{om}\}_{ij}$ and $\{M_o\}_{ij}$ are the membrane forces and bending moments due to initial stress $\{\sigma_o^i\}$ at the Gauss point i, j .

The element stiffnesses and nodal forces which may be in a local coordinate system, are to be transformed to a global coordinate system. To make the transformation simple, all the three displacement components (u_o, v_o, w_o) along x, y, z directions are arranged together followed by the three rotations $(\theta_x, \theta_y, \theta_z)$ about x, y, z directions. If (u_o, v_o, w_o) and $(\theta_x, \theta_y, \theta_z)$ are the deformations in the local coordinate system and $(\bar{u}_o, \bar{v}_o, \bar{w}_o)$ and $(\bar{\theta}_x, \bar{\theta}_y, \bar{\theta}_z)$ are the deformations in the global coordinate system as shown in Fig. 3.5(a), then these are related by a transformation matrix $[T]$ as given below :

$$\begin{Bmatrix} u_o \\ v_o \\ w_o \\ \dots \\ \theta_x \\ \theta_y \\ \theta_z \end{Bmatrix} = \begin{bmatrix} [T] & & 0 \\ & \dots & \\ 0 & & [T] \end{bmatrix} \begin{Bmatrix} \bar{u}_o \\ \bar{v}_o \\ \bar{w}_o \\ \dots \\ \bar{\theta}_x \\ \bar{\theta}_y \\ \bar{\theta}_z \end{Bmatrix} \quad (3.22)$$

where $[T]$ is a 3×3 transformation matrix consisting of direction cosines of the local axes x, y, z with respect to the global axes X, Y, Z . In general

$$[T] = \begin{bmatrix} l_x & m_x & n_x \\ l_y & m_y & n_y \\ l_z & m_z & n_z \end{bmatrix} \quad (3.23)$$

where (l_x, m_x, n_x) , (l_y, m_y, n_y) and (l_z, m_z, n_z) are the direction cosines of the local axes x, y, z with respect to the global axes X, Y, Z respectively.

The complete transformation matrix $\tilde{[T]}$ for an element nodal deformation vector $\{\delta\}^e$, consisting of the six displacements at each of the four nodes of the element is obtained as ;

$$\{\delta\}^e = \begin{bmatrix} [T] & & & & & 0 \\ & [T] & & & & \\ & & [T] & & & \\ & & & [T] & & \\ & & & & [T] & \\ 0 & & & & & [T] \end{bmatrix} \{\bar{\delta}\}^e$$

(24x1) (24x1) (24x1)

$$= [\tilde{T}] \{\bar{\delta}\}^e \quad (3.24)$$

Similarly, the nodal forces are transformed as :

$$\{F\}^e = [\tilde{T}] \{\bar{F}\}^e \quad (3.25)$$

Using principle of virtual work or minimum potential energy theorem, it can be shown that the element stiffness matrix in local coordinate system $[K]^e$ is related to the element stiffness matrix in global coordinate system $[\bar{K}]^e$ by

$$[\bar{K}]^e = [\tilde{T}]^T [K]^e [\tilde{T}] \quad (3.26)$$

For prismatic box girders, the transformations are further simplified as only two types of transformations are necessary. Taking the X axis oriented in the span-wise direction and the Z axis downwards, as shown in Fig. 5(b), the two transformations are as follows :

- (i) elements rotated about the X axis, i.e. the web elements of the box girder ;
- (ii) elements rotated about the Y axis, i.e. the diaphragm elements.

The transformation matrices for the two cases are :

Case 1 : Rotation about the X-axis (Fig. 3.5 (c)).

$$\begin{Bmatrix} u_o \\ v_o \\ w_o \end{Bmatrix} = \begin{bmatrix} 1 & 0 & 0 \\ 0 & \cos \Theta_x & \sin \Theta_x \\ 0 & -\sin \Theta_x & \cos \Theta_x \end{bmatrix} \begin{Bmatrix} \bar{u}_o \\ \bar{v}_o \\ \bar{w}_o \end{Bmatrix} \quad (3.27)$$

Case 2 : Rotation about the Y-axis (Fig. 3.5(d)).

$$\begin{Bmatrix} u_o \\ v_o \\ w_o \end{Bmatrix} = \begin{bmatrix} \cos \Theta_y & 0 & -\sin \Theta_y \\ 0 & 1 & 0 \\ \sin \Theta_y & 0 & \cos \Theta_y \end{bmatrix} \begin{Bmatrix} \bar{u}_o \\ \bar{v}_o \\ \bar{w}_o \end{Bmatrix} \quad (3.28)$$

The transformed element stiffnesses and nodal forces in global coordinate system are assembled to give the structure stiffness $[K]$ and the nodal force vector $\{F\}$ on the structure. These two are related by a set of linear simultaneous equations defining the equilibrium of the structure under the applied loads as given below :

$$\text{or } [K]\{\delta\} = \{F\} \quad (3.29)$$

where $\{\delta\}$ is the nodal displacement vector of the structure.

After substituting the appropriate boundary conditions, equation (3.29) is solved to yield nodal displacements in global coordinate system. These displacements are transformed into local coordinate system for each element. From nodal displacements in the local coordinate system, the in-plane strains $\{\epsilon_o\}$ and curvatures $\{\chi_o\}$ at reference plane are determined at Gauss points of each element. The strain and stress distribution across the thickness at Gauss points are determined by equations (3.7) and (3.12). The resultant membrane forces $\{F_m\}$ at Gauss points are determined by integrating the stresses $\{\sigma\}$ over the plate thickness :

$$\{F_m\} = \begin{Bmatrix} F_{mx} \\ F_{my} \\ F_{mxy} \end{Bmatrix} = \int_t \{\sigma\} dz \quad (3.30)$$

Similarly, the resultant bending moments $\{M\}$ at Gauss points are determined by integrating the moments of the stresses $\{\sigma\}$ about the reference plane:

$$\{M\} = \begin{Bmatrix} M_x \\ M_y \\ M_{xy} \end{Bmatrix} = \int_t \{\sigma\} z \, dz \quad (3.31)$$

3.4.3 Material Modelling and Failure Criteria

A realistic model for the analysis of thin walled ferrocement structures has to incorporate the characteristic properties of its constituent materials, namely, the mortar, the wiremesh and the skeletal steel reinforcement. The material properties of mortar and reinforcement depend on the stress or strain state of the material. In the present study, the use of Kirchhoff's second assumption in neglecting the transverse normal stress allows the element to be in a state of plane stress. The plane stress constitutive relations assumed for the constituent materials are given below :

3.4.3.1 Mortar

The stress-strain relation for mortar in uniaxial compression has been investigated by many researchers as part of their investigation on mechanical properties of ferrocement. A typical uniaxial stress-strain relation for mortar is shown in Fig. 3.6. On the tension side, the curve is nearly linear upto the tensile strength where the mortar cracks and the stress drops to zero. On the compression side, the curve is nearly linear upto about 30 percent of its ultimate stress, then deviates gradually from linearity till the slope becomes zero and reaches the ultimate stress. A descending tail follows the peak and finally ends with a complete crushing. In analytical form, the stress-strain curve of a mortar was represented by Fourier series (equation 2.18) by Balaguru et. al.⁽⁶²⁾ in analysing ferrocement beams. Rajgopalan and Parameswaran⁽¹²⁸⁾ analysed ferrocement beams by using the following parabolic stress-strain

(σ - ϵ) relation for mortar (Fig. 3.7) in compression.

$$\sigma = \sigma_{cc} \left[2 \left(\frac{\epsilon}{\epsilon_{co}} \right) - \left(\frac{\epsilon}{\epsilon_{co}} \right)^2 \right] \quad (3.32)$$

where σ_{cc} and ϵ_{co} are the peak compressive stress and the corresponding strain respectively. The stress-strain relation in tension was assumed to be a semi-parabola without a descending portion, the peak stress and the strain corresponding to the tensile strength and the cracking strain of the mortar respectively.

No investigation on mortar under biaxial or multiaxial stress state has been reported, whereas for concrete, several such investigations have been reported by researchers^(153, 154). In the absence of such an information for mortar, necessary guidance from the reported concrete results has been suitably adopted.

In ferrocement structures, the failure is normally governed by tensile cracking of the mortar and yielding of wiremeshes and rarely by crushing of the mortar. Hence an elaborate stress-strain law in compression zone is not justified. In the present study, the mortar is idealized to be linearly elastic-perfectly plastic in biaxial compression, and linearly elastic in biaxial tension and tension-compression (Fig. 3.8).

Failure Criteria for Mortar :

Prakhya and Adidam⁽¹⁴³⁾ assumed the yield surface for mortar based on the test results of Kupfer et. al⁽¹⁵³⁾ (Fig. 3.9). Considering strain hardening, the initial yield surface was assumed when the principal compressive stress attained a value of 30 percent of uniaxial ultimate compressive strength (Fig. 3.10). The classical normality flow rule was considered for the yielded mortar. In addition, a crushing surface, analogous to the yield surface but

in terms of strains was used in defining the complete collapse or crushing of the yielded mortar. The mortar was assumed to have crushed when the principal compressive strain reached a value equal to the crushing strain of mortar in uniaxial compression. In tension, the mortar was assumed to be cracked when the principal tensile stress reached a value equal to the mortar tensile strength.

Instead of correlating failure with the stresses, the failure of the constituent materials in the present study is correlated with the strains. Strain based failure criteria in finite element analysis has one advantage that the strains are first calculated by multiplying nodal deformations with the strain derivative matrix. Stresses are obtained by multiplying the strain vector with the material matrix. Hence in calculating stresses, an approximation creeps in due to the assumed material property matrix, while in adopting strain based failure criteria, this problem does not occur.

In the present study, the mortar is assumed to be yielded when the principal compressive strain reaches a value equal to ϵ_{cy} i.e. corresponding to stress σ_{cy} (Fig. 3.8). The crushing of the mortar is assumed when the principal compressive strain attains a value equal to the ultimate crushing strain ϵ_{cu} . In tension, the mortar is assumed to be cracked when the principal tensile strain reaches a value equal to the mortar cracking strain ϵ_{cr} . The adopted failure criteria is shown in Fig. 3.11.

Uncracked Elastic Stiffness :

In the elastic region, the mortar is assumed to be homogeneous, isotropic and linearly elastic. Thus the stress-strain relations are

$$\left. \begin{matrix} \sigma_x \\ \sigma_y \\ \tau_{xy} \end{matrix} \right\} = \frac{E_m}{(1-\nu^2)} \begin{bmatrix} 1 & \nu & 0 \\ \nu & 1 & 0 \\ 0 & 0 & \frac{1-\nu}{2} \end{bmatrix} \left\{ \begin{matrix} \epsilon_x \\ \epsilon_y \\ \gamma_{xy} \end{matrix} \right\} \quad \text{or } \{\sigma\} = [D]\{\epsilon\} \quad (3.33)$$

Cracked Stiffness

When any of the principal strains exceed or equal the cracking strain ϵ_{cr} , the mortar will crack in a direction perpendicular to the strain. The modulus of elasticity E_m and Poisson's ratio ν are assumed to be zero in a direction perpendicular to the crack. A reduced shear modulus equal to $0.4G$ has been assumed for the cracked section (155) where G is the shear modulus of the uncracked mortar.

Let the co-ordinate axes x' , y' be perpendicular and parallel respectively to the crack (Fig. 3.12), then the stress-strain relations referring to $x'y'$ coordinate system are

$$\left. \begin{matrix} \sigma'_{x'} \\ \sigma'_{y'} \\ \tau'_{xy} \end{matrix} \right\} = \begin{bmatrix} 0 & 0 & 0 \\ 0 & E_m & 0 \\ 0 & 0 & 0.4G \end{bmatrix} \left\{ \begin{matrix} \epsilon'_{x'} \\ \epsilon'_{y'} \\ \gamma'_{xy} \end{matrix} \right\} \quad \text{or } \{\sigma'\} = [D']\{\epsilon'\} \quad (3.34)$$

The strain vector in the $x'y'$ system transforms in the following manner:

$$\left. \begin{matrix} \epsilon'_{x'} \\ \epsilon'_{y'} \\ \gamma'_{xy} \end{matrix} \right\} = \begin{bmatrix} c^2 & s^2 & sc \\ s^2 & c^2 & -sc \\ -2sc & 2sc & c^2 - s^2 \end{bmatrix} \left\{ \begin{matrix} \epsilon_x \\ \epsilon_y \\ \epsilon_{xy} \end{matrix} \right\} \quad \text{or } \{\epsilon'\} = [T_c]\{\epsilon\} \quad (3.35)$$

where $c = \cos \beta$, $s = \sin \beta$ and β is the angle between x axis and x' axis.

The stress vector transforms as follows :

$$\begin{Bmatrix} \sigma_x \\ \sigma_y \\ \tau_{xy} \end{Bmatrix} = \begin{bmatrix} c^2 & s^2 & -2sc \\ s^2 & c^2 & 2sc \\ sc & -sc & c^2 - s^2 \end{bmatrix} \begin{Bmatrix} \sigma'_x \\ \sigma'_y \\ \tau'_{xy} \end{Bmatrix} \quad \text{or } \{\sigma\} = [T_c]^T \{\sigma'\} \quad (3.36)$$

Equation (3.34) can be transformed to xy coordinate system as follows :

$$\{\sigma\} = [D]_{cr} \{\epsilon\} \quad (3.37)$$

where

$$[D]_{cr} = [T_c]^T [D'] [T_c] \quad (3.38)$$

If both the principal strains exceed the cracking strain ϵ_{cr} , the mortar will crack in both the principal directions. The stress strain relations in $x'y'$ coordinate system then reduce to :

$$\begin{Bmatrix} \sigma'_x \\ \sigma'_y \\ \tau'_{xy} \end{Bmatrix} = \begin{bmatrix} 0 & 0 & 0 \\ 0 & 0 & 0 \\ 0 & 0 & 0.4G \end{bmatrix} \begin{Bmatrix} \epsilon'_x \\ \epsilon'_y \\ \gamma'_{xy} \end{Bmatrix} \quad (3.39)$$

Equation (3.39) can be transformed to xy coordinate system using equation (3.38).

If the mortar cracks in one direction, and the strain parallel to the crack reaches yield strain ϵ_{yc} , then the stress-strain relations can be expressed as follows :

$$\begin{Bmatrix} \sigma'_x \\ d\sigma'_y \\ \tau'_{xy} \end{Bmatrix} = \begin{bmatrix} 0 & 0 & 0 \\ 0 & 0 & 0 \\ 0 & 0 & 0.4G \end{bmatrix} \begin{Bmatrix} \epsilon'_x \\ d\epsilon'_y \\ \gamma'_{xy} \end{Bmatrix} \quad (3.40)$$

The second equation of (3.40) indicates that the material retains the yield stress and does not require any increase in stress with the further increase in strain.

Tension Stiffening Effect :

Cracking in a composite material like ferrocement is complicated by the presence of the wiremesh and the skeletal steel reinforcement. Figure 3.13 shows a reinforced mortar element under uniaxial tensile stress. When strain in the mortar reaches its cracking strain ϵ_{cr} , primary cracks form at random critical sections. A slip occurs between the mortar and the reinforcing bar at the primary crack section. The mortar surfaces at the cracked sections are free of stress and the force in the reinforcement equals the external load. But the mortar between primary cracks is still capable of carrying stresses because of the bond between the mortar and reinforcing bar. This phenomena is called the 'tension stiffening effect'. The mortar stress is zero at the cracks but is not zero if averaged over the length. As the load increases, more cracks form and the amount of tension carried by the mortar progressively decreases. Thus the average mortar stress vs. strain curve for the element may be considered to have an unloading portion (Fig. 3.14). The concept of working with average stress and strain over a relatively longer gauge length to account for the tension stiffening effect was first introduced by Scanlon⁽¹⁵⁶⁾. In the present study, the elastic modulus of the mortar is assumed to be zero once the mortar cracks, but the unbalanced stress is gradually released according to an assumed unloading curve (Fig. 3.14). If the first solution gives principal strain ϵ_1 (Fig. 3.14) greater than the mortar cracking strain ϵ_{cr} , the mortar cracks, and zero modulus is used for the following solution. Let the stress corresponding to ϵ_1 be σ_1 , then σ_{01} instead of σ_1 is considered as the unbalanced stress. For the second solution σ_{02} is the unbalanced

stress etc. For the sake of simplicity, the unloading curve is assumed to be a straight line. The average tensile stress is assumed to be zero when the tensile strain in the extreme fiber is equal to the failure strain of the wiremesh.

Stiffness at Yielding and Crushing of Mortar :

When one of the principal strains of the mortar exceeds the value ϵ_{yc} (Fig. 3.8), the mortar is assumed to be yielded. The stiffness in the yielded direction is zero. As in the case of cracked mortar, here also a reduced shear modulus equal to $0.4G$ is assumed for the yielded mortar to account for the dowel action of reinforcement. The stress-strain relations can be expressed as follows :

$$\begin{Bmatrix} d\sigma'_x \\ \sigma'_y \\ \tau'_{xy} \end{Bmatrix} = \begin{bmatrix} 0 & 0 & 0 \\ 0 & E_m & 0 \\ 0 & 0 & 0.4G \end{bmatrix} \begin{Bmatrix} d\epsilon'_x \\ \epsilon'_y \\ \gamma'_{xy} \end{Bmatrix} \quad (3.41)$$

When both the principal strains exceed the yield strain ϵ_{yc} , the mortar is assumed to be yielded along both the directions. The stress-strain relation can then be expressed as

$$\begin{Bmatrix} d\sigma'_x \\ d\sigma'_y \\ \tau'_{xy} \end{Bmatrix} = \begin{bmatrix} 0 & 0 & 0 \\ 0 & 0 & 0 \\ 0 & 0 & 0.4G \end{bmatrix} \begin{Bmatrix} d\epsilon'_x \\ d\epsilon'_y \\ \gamma'_{xy} \end{Bmatrix} \quad (3.42)$$

When any of the principal strains reaches the crushing strain ϵ_{cu} , the mortar is assumed to be crushed. The crushed mortar is assumed to lose all its stiffness. Therefore, the stress-strain relation can be expressed as :

$$\begin{Bmatrix} \sigma'_x \\ \sigma'_y \\ \tau'_{xy} \end{Bmatrix} = \begin{bmatrix} 0 & 0 & 0 \\ 0 & 0 & 0 \\ 0 & 0 & 0 \end{bmatrix} \begin{Bmatrix} \epsilon'_x \\ \epsilon'_y \\ \gamma'_{xy} \end{Bmatrix} \quad (3.43)$$

3.4.3.2 Wiremeshes and skeletal steel

The wiremesh and skeletal steel reinforcement are assumed to be distributed in the form of smeared layers of equivalent effective area (Fig. 3.1). The centres of the smeared layers are assumed to be the same as that of the corresponding wiremesh layers and skeletal steel bars.

The stress-strain relations for the wiremesh and the skeletal steel are assumed to be linearly elastic-perfectly plastic (Fig. 3.15) with the same yield stress and elastic modulus in tension and compression. It is further assumed that the smeared layers carry only uniaxial stress. When stress in the reinforcement remains in the elastic range, the stress-strain relation can be expressed as

$$\begin{Bmatrix} \sigma_x \\ \sigma_y \\ \tau_{xy} \end{Bmatrix} = \begin{bmatrix} E_s \text{ or } E_f & 0 & 0 \\ 0 & 0 & 0 \\ 0 & 0 & 0 \end{bmatrix} \begin{Bmatrix} \epsilon_x \\ \epsilon_y \\ \gamma_{xy} \end{Bmatrix} \quad (3.44)$$

When the wiremesh or the skeletal steel yield, they are assumed to have zero incremental stiffness. The stress-strain relations, therefore, become :

$$d\{\sigma\} = [0] d\{\epsilon\} \quad (3.45)$$

3.4.4 Rigidities of the Composite Material

In a plane stress problem, membrane forces $\{F_{in}\}$ at Gauss points can be obtained by integrating the stress vector $\{\sigma\}$ over the plate thickness. Thus

$$\begin{aligned}
 \{F_m\} &= \begin{Bmatrix} F_{mx} \\ F_{my} \\ F_{mxy} \end{Bmatrix} = \int \sigma \, dz \\
 &= \int [D] \{\epsilon\} \, dz = \int [D] \{ \{\epsilon_o\} + z \{\chi_o\} \} \, dz \\
 &= [\int [D] \, dz] \{\epsilon_o\} + [\int [D] z \, dz] \{\chi_o\} \\
 &= [D_{mm}] \{\epsilon_o\} + [D_{mb}] \{\chi_o\}
 \end{aligned} \tag{3.46}$$

Defining the rigidities as the derivative of membrane force with respect to membrane strains $\{\epsilon_o\}$ or curvatures $\{\chi_o\}$ at reference plane, $[D_{mm}]$ and $[D_{mb}]$ become the tangent rigidities for membrane action and membrane bending interaction respectively.

Similarly, the internal moments at Gauss points are the sum of the moments due to stresses $\{\sigma\}$ about the reference plane. Thus

$$\begin{aligned}
 \{M\} &= \begin{Bmatrix} M_x \\ M_y \\ M_{xy} \end{Bmatrix} = \int \{\sigma\} z \, dz \\
 &= \int [D] \{\epsilon\} z \, dz = \int [D] \{ \{\epsilon_o\} + z \{\chi_o\} \} z \, dz \\
 &= [\int [D] z \, dz] \{\epsilon_o\} + [\int [D] z^2 \, dz] \{\chi_o\} \\
 &= [D_{mb}] \{\epsilon_o\} + [D_{bb}] \{\chi_o\}
 \end{aligned} \tag{3.47}$$

Taking the derivative of moments $\{M\}$ with respect to the membrane strains $\{\epsilon_o\}$ and curvatures $\{\chi_o\}$ at the reference plane, $[D_{mb}]$ and $[D_{bb}]$ become the tangent rigidities due to membrane-bending interaction and bending action respectively. Rigidities of ferrocement are then obtained by summing up

the rigidities of the component materials, namely, mortar, wiremesh and skeletal steel.

Rigidities in the Elastic Stage :

Referring to Figure 3.1, A_{ftxl} , $A_{f tyl}$, A_{fbxl} , $A_{f byl}$ etc. are the area of wiremeshes per unit width along x and y directions. Similarly, A_{stx} , A_{sty} , A_{sbx} and A_{sby} are the areas of skeletal steel per unit width along x and y directions. D_{txl} , D_{tyl} , D_{stx} , D_{sty} , D_{bxl} , D_{byl} , D_{sbx} , D_{sby} etc. are the distances of wiremeshes or skeletal steel bars from the reference plane. Subscripts t and b correspond to the location of wiremeshes or skeletal steel bars above and below the reference plane respectively. For the sake of convenience, the middle plane of the element is taken as the reference plane.

Membrane rigidity $[D_{mm}]$ of ferrocement is the sum of the membrane rigidities due to mortar, wiremesh and skeletal steel. Thus

$$[D_{mm}] = [D_{mm}]_m + [D_{mm}]_{wm} + [D_{mm}]_{ss} \quad (3.48)$$

where subscripts m , wm , and ss correspond to the mortar, wiremesh and skeletal steel respectively, and

$$[D_{mm}]_m = \int_{-t/2}^{t/2} [D]_m dz = \frac{E_m t}{(1 - \nu^2)} \begin{bmatrix} 1 & \nu & 0 \\ \nu & 1 & 0 \\ 0 & 0 & \frac{1 - \nu}{2} \end{bmatrix} \quad (3.49)$$

$$[D_{mm}]_{wm} = E_f \begin{bmatrix} \Sigma(A_{ftx})_i + \Sigma(A_{fbx})_i & 0 & 0 \\ 0 & \Sigma(A_{f ty})_i + \Sigma(A_{f by})_i & 0 \\ 0 & 0 & 0 \end{bmatrix} \quad (3.50)$$

$$[D_{mb}]_{ss} = E_s \begin{bmatrix} (A_{stx} + A_{sbx}) & 0 & 0 \\ 0 & (\Lambda_{sty} + \Lambda_{sby}) & 0 \\ 0 & 0 & 0 \end{bmatrix} \quad (3.51)$$

Similarly, membrane-bending interaction rigidity $[D_{mb}]$ of ferrocement is equal to

$$[D_{mb}] = [B_{mb}]_m + [D_{mb}]_{wm} + [D_{mb}]_{ss} \quad (3.52)$$

where

$$[D_{mb}]_m = \int_{-t/2}^{t/2} [D]_z dz = [0] \quad (3.53)$$

$$[D_{mb}]_{wm} = E_f \begin{bmatrix} \Sigma(A_{ftx} \cdot D_{tx})_i + \Sigma(\Lambda_{fbx} \cdot D_{bx})_i & 0 & 0 \\ 0 & \Sigma(\Lambda_{fty} \cdot D_{ty})_i + \Sigma(\Lambda_{fby} \cdot D_{by})_i & 0 \\ 0 & 0 & 0 \end{bmatrix} \quad (3.54)$$

and

$$[D_{mb}]_{ss} = E_s \begin{bmatrix} (A_{stx} \cdot D_{stx} + \Lambda_{sbx} \cdot D_{sbx}) & 0 & 0 \\ 0 & (\Lambda_{sty} \cdot D_{sty} + \Lambda_{sby} \cdot D_{sby}) & 0 \\ 0 & 0 & 0 \end{bmatrix} \quad (3.55)$$

The bending rigidity $[D_{bb}]$ of ferrocement is equal to

$$[D_{bb}] = [D_{bb}]_m + [D_{bb}]_{wm} + [D_{bb}]_{ss} \quad (3.56)$$

here

$$[D_{bb}]_m = \int_{-t/2}^{t/2} [D]z^2 dz = \frac{E_m t^3}{12(1-\nu^2)} \begin{bmatrix} 1 & \nu & 0 \\ \nu & 1 & 0 \\ 0 & 0 & \frac{1-\nu}{2} \end{bmatrix} \quad (3.57)$$

$$[D_{bb}]_{wm} = E_f \begin{bmatrix} (\Lambda_{ftx} \cdot D_{tx}^2)_i + (\Lambda_{fbx} \cdot D_{bx}^2)_i & 0 & 0 \\ 0 & (\Lambda_{fty} \cdot D_{ty}^2)_i + (\Lambda_{fby} \cdot D_{by}^2)_i & 0 \\ 0 & 0 & 0 \end{bmatrix} \quad (3.58)$$

and

$$[D_{bb}]_{ss} = E_s \begin{bmatrix} (\Lambda_{stx} \cdot D_{stx}^2 + \Lambda_{sbx} \cdot D_{sbx}^2) & 0 & 0 \\ 0 & (\Lambda_{sty} \cdot D_{sty}^2 + \Lambda_{sby} \cdot D_{sby}^2) & 0 \\ 0 & 0 & 0 \end{bmatrix} \quad (3.59)$$

Rigidities in the Cracked Stage :

For determining the rigidities in the cracked stage, the principal strains are calculated at the top and bottom surfaces at Gauss points. These are checked against the cracking strain ϵ_{cr} or yielding and crushing strains ϵ_{cy} and ϵ_{cu} of the mortar. The strains in the wiremesh and skeletal steel are checked against yielding. If the principal strains are less than ϵ_{cr} and ϵ_{cy} , then the composite remains in the elastic stage and the expressions for rigidities are given by equations (3.48 to 3.59). If the principal strains exceed ϵ_{cr} or ϵ_{cy} , the mortar cracks or yields in a direction perpendicular to the principal strains. If the principal compressive strain exceeds ϵ_{cu} , the mortar gets crushed. The depth of cracked or yielded/crushed mortar is determined by assuming a linear distribution of principal strains across the element thickness. If the mortar cracks or yielded/crushed along both the principal directions,

then the maximum cracked or yielded/crushed depth is adopted for determining the rigidities of the cracked or yielded/crushed mortar layer. The rigidities of such a section are determined by adding the rigidities of the uncracked mortar depth, cracked or yielded mortar depth and unyielded layers of wiremesh and skeletal steel. Since these rigidities are based on the latest strain-state of the composite and determined by taking the derivative of the resisting membrane forces and moments, these are called tangent rigidities of the material for a given strain state.

Let t_{top} and t_{bot} be the depths of the mortar cracked or yielded/crushed (Fig. 3.16) measured from the top and bottom surfaces respectively. The rigidities of the uncracked-unyielded mortar core can be determined as follows :

$$\begin{aligned} \text{Membrane rigidity } [D_{mm}]_{uc} &= \int_{-t/2 + t_{top}}^{t/2 - t_{bot}} [D] dz = \int_{-t_{tp}}^{t_{bt}} [D] dz \\ &= \frac{E_m (t_{bt} + t_{tp})}{(1 - \nu^2)} \begin{bmatrix} 1 & \nu & 0 \\ \nu & 1 & 0 \\ 0 & 0 & \frac{(1 - \nu)}{2} \end{bmatrix} \end{aligned} \quad (3.60)$$

where $t_{tp} = t/2 - t_{top}$ and $t_{bt} = t/2 - t_{bot}$

Membrane-bending interaction rigidity

$$\begin{aligned} [D_{mb}]_{uc} &= \int_{-t_{tp}}^{t_{bt}} [D] z dz \\ &= \frac{E_m (t_{bt}^2 - t_{tp}^2)}{(1 - \nu^2)} \begin{bmatrix} 1 & \nu & 0 \\ \nu & 1 & 0 \\ 0 & 0 & \frac{(1 - \nu)}{2} \end{bmatrix} \end{aligned} \quad (3.61)$$

Bending rigidity

$$\begin{aligned}
 [D_{bb}]_{uc} &= \int_{-t_{tp}}^{t_{bt}} [D] z^2 dz \\
 &= \frac{E_m (t_{bt}^3 + t_{tp}^3)}{3(1 - \nu^2)} \begin{bmatrix} 1 & \nu & 0 \\ \nu & 1 & 0 \\ 0 & 0 & \frac{(1 - \nu)}{2} \end{bmatrix} \quad (3.61)
 \end{aligned}$$

Rigidities of the Top Cracked or Yielded Mortar :

For the sake of generality, let the depth of top crushed mortar layer (Fig. 3.16) be t_{cul} , then the depth of cracked or yielded mortar layer is $t_{top} - t_{cul}$. $[D']$ matrices for various cracking and yielding cases of the mortar are given in equations (3.34 and 3.39 to 3.43). These matrices can be transformed from the principal cracked/yielded directions to the local coordinate system of the element by equation (3.38). Let this transformed material matrix be $[D'_t]$. The various rigidities are as follows :

$$\begin{aligned}
 \text{Membrane rigidity } [D_{mm}]_{tc} &= \int_{-t/2 + t_{cul}}^{-t/2 + t_{top}} [D'_t] dz \\
 &= (t_{top} - t_{cul}) [D'_t] \quad (3.63)
 \end{aligned}$$

Membrane-bending rigidity

$$\begin{aligned}
 [D_{mb}]_{tc} &= \int_{-t/2 + t_{cul}}^{-t/2 + t_{top}} [D'_t] z dz = \int_{-t'_{cul}}^{-t'_{tp}} [D'_t] z dz \\
 &= \frac{(t_{tp}^2 - t'_{cul}{}^2)}{2} [D'_t] \quad (3.64)
 \end{aligned}$$

where $t'_{cul} = t/2 - t_{cul}$

$$\begin{aligned} \text{Bending rigidity } [D_{bb}]_{tc} &= \int_{-t'_{cul}}^{-t_{tp}} [D'_t] z^2 dz \\ &= \frac{1}{3} \cdot (t'^3_{cul} - t^3_{tp}) [D'_t] \end{aligned} \quad (3.65)$$

Rigidities of the Bottom Cracked or Yielded Mortar :

Let the depth of bottom crushed mortar layer be t_{cu2} . The depth of bottom cracked or yielded mortar layer is $t_{bot} - t_{cu2}$. Let the transformed material matrix in the local coordinate system of the element be $[D'_b]$. The various rigidities are obtained as follows :

$$\begin{aligned} \text{Membrane rigidity } [D_{mm}]_{bc} &= \int_{t/2 - t_{bot}}^{t/2 - t_{cu2}} [D'_b] dz = \int_{t_{bt}}^{t'_{cu2}} [D'_b] dz \\ &= (t'_{cu2} - t_{bt}) [D'_b] \end{aligned} \quad (3.66)$$

where $t'_{cu2} = t/2 - t_{cu2}$

$$\begin{aligned} \text{Membrane-bending rigidity } [D_{mb}]_{bc} &= \int_{t_{bt}}^{t'_{cu2}} [D'_b] z dz \\ &= \frac{(t'^2_{cu2} - t^2_{bt})}{2} [D'_b] \end{aligned} \quad (3.67)$$

$$\begin{aligned} \text{Bending rigidity } [D_{bb}]_{bc} &= \int_{t_{bt}}^{t'_{cu2}} [D'_b] z^2 dz \\ &= \frac{(t'^3_{cu2} - t^3_{bt})}{3} [D'_b] \end{aligned} \quad (3.68)$$

Therefore, the rigidities of the mortar corresponding to membrane action, membrane-bending interaction and bending action are obtained by adding up the rigidities of the uncracked/unyielded mortar core, the top depth cracked/yielded if any and the bottom depth cracked/yielded if any. Thus,

$$\text{Membrane rigidity } [D_{mm}]'_m = [D_{mm}]_{uc} + [D_{mm}]_{tc} + [D_{mm}]_{bc} \quad (3.69)$$

Membrane-bending rigidity

$$[D_{mb}]'_m = [D_{mb}]_{uc} + [D_{mb}]_{tc} + [D_{mb}]_{bc} \quad (3.70)$$

Bending rigidity

$$[D_{bb}]'_m = [D_{bb}]_{uc} + [D_{bb}]_{tc} + [D_{bb}]_{bc} \quad (3.71)$$

Rigidities of the Mortar when Full Depth is Cracked :

When the principal strains at the top and bottom surfaces exceed the cracking strain ϵ_{cr} , the full depth of the element is cracked which is quite common in the bottom soffit slab of a box girder in the mid-span region. The principal strains at the top and bottom surfaces may have different orientations due to variation of strains across the depth. Hence the orientation of cracks at top and bottom surfaces may be marginally different. Let the material matrix $[D']$ transformed with respect to the crack orientations at top and bottom surfaces be $[D'_{ft}]$ and $[D'_{fb}]$. In this case, the transformed material matrix for full depth cracked is assumed to be the average of $[D'_{ft}]$ and $[D'_{fb}]$. Let the average transformed material matrix be $[D'_f]$. Thus, the various rigidities of the mortar can be expressed as

$$\begin{aligned} \text{Membrane rigidity } [D_{mm}]'_m &= \int_{-t/2}^{t/2} [D'_f] dz \\ &= t [D'_f] \end{aligned} \quad (3.72)$$

$$\text{Membrane-bending rigidity } [D_{mb}]'_m = \int_{-t/2}^{t/2} [D'_f] \cdot z \, dz = [0] \quad (3.73)$$

$$\begin{aligned} \text{Bending rigidity } [D_{bb}]'_m &= \int_{-t/2}^{t/2} [D'_f] \cdot z^2 \, dz \\ &= \frac{t^3}{12} [D'_f] \end{aligned} \quad (3.74)$$

Rigidities Due to Wiremesh and Skeletal Steel :

In the cracked stage, the strains in the wiremesh and skeletal steel layers are checked against their yield strains. If the strains are less than the yielding strains, the wiremesh and skeletal steel are unyielded and their rigidities are given by equations (3.50, 3.51, 3.54, 3.55, 3.58 and 3.59). If the strains in wiremesh and skeletal steel layers exceed their respective yield strains, then their rigidities are taken as zero.

As in the elastic stage, the rigidities of ferrocement in the cracked stage are taken as the sum of the corresponding rigidities due to the mortar, wiremesh and skeletal steel. The stiffness matrix of the cracked element can then be determined by substituting cracked rigidities $[D_{mm}]'$, $[D_{mb}]'$ and $[D_{bb}]'$ of the composite in equation (3.19).

3.4.5 Nonlinear Analysis

3.4.5.1 Method of nonlinear analysis

An incremental iterative method has been used to carry out the nonlinear analysis. The total load on the structure is applied in a suitable number of load increments. Iterations within each load increment have been carried out using the Initial Stiffness Method (Modified Newton-Raphson Method) until the equilibrium and constitutive relations are satisfied within a certain allowable limit. The Initial Stiffness Method uses the tangent stiffness based

on the stress-strain state at the beginning of the load increment, for all iterations in the current load increment.

Consider a structure whose load deformation relationship is nonlinear as shown in Fig. 3.17. Let the nodal deformations, strains and stresses corresponding to load $\{F\}$ be $\{\delta\}$, $\{\epsilon\}$ and $\{\sigma\}$ respectively. Assuming a linear elastic behaviour during a small load increment $d\{F\}$, the increments $d\{\delta'\}$, $d\{\epsilon'\}$ and $d\{\sigma'\}$ in deformations, strains and stresses may be obtained using equations (3.29, 3.9 and 3.12) as follows :

The anticipated increment $d\{\delta'\}$ in the nodal deformations of the structure corresponding to the load increment $d\{F\}$ is

$$d\{\delta'\} = [K_T]^{-1} d\{F\} \quad (3.75)$$

where $[K_T]$ is the tangent stiffness matrix of the structure assembled from the tangent stiffnesses of individual elements $[K_T]^e$, defined by

$$[K_T]^e = \int [B]^T [D_T] [B] dV \quad (3.76)$$

where $[D_T]$ represents the tangent material matrix at strain level $\{\epsilon\}$ as shown in Fig. 3.18.

$$\text{Incremental strain } d\{\epsilon'\} = [B] d\{\delta'\} \quad (3.77)$$

$$\text{Incremental stress } d\{\sigma'\} = [D_T] d\{\epsilon'\} \quad (3.78)$$

The anticipated incremental stress $d\{\sigma'\}$ will not be equal to the actual incremental stress $d\{\sigma\}$ due to nonlinear constitutive relation of the material (Fig. 3.18). The unbalanced stress $d\{\sigma_0\}$ at strain level $\{\epsilon\} + d\{\epsilon'\}$ is equal to the anticipated incremental stress $d\{\sigma'\}$ minus the actual incremental stress $d\{\sigma\}$.

Similarly, at $\{\delta\} + d\{\delta'\}$, the load deformation curve corresponds to point B' with an unbalanced force vector $\{R_o\}$ which is related to the unbalanced stress $d\{\sigma_o\}$ at this level by equations (3.16 or 3.21) as follows :

$$\{R_o\} = \int [B^T] d\{\sigma_o\} dV \quad (3.79)$$

This unbalanced force $\{R_o\}$ out of the original load increment $d\{F\}$ is applied on the B' stage of the structure and the structure analysed using $[K_T]$ based on the stress-strain state at the beginning of the current load increment. The incremental deformation $d\{\delta''\}$ due to force $\{R_o\}$ is obtained as

$$d\{\delta''\} = [K_T]^{-1} \{R_o\} \quad (3.80)$$

The corresponding incremental strain $d\{\epsilon''\}$ and stress $d\{\sigma''\}$ are obtained as

$$d\{\epsilon''\} = [B] d\{\delta''\} \quad (3.81)$$

$$d\{\sigma''\} = [D_T] d\{\epsilon''\} \quad (3.82)$$

where $[D_T]$ is the tangent material matrix at strain level $\{\epsilon\} + d\{\epsilon'\}$. Thus the unbalanced stress at strain level $\{\epsilon_o\} + d\{\epsilon'\} + d\{\epsilon''\}$ becomes $d\{\sigma_o\}$ and the corresponding unbalanced force vector as $\{R_o'\}$. Note that the unbalanced stress in the current iteration is determined on the basis of tangent material matrix $[D_T]$ corresponding to strain state at the end of the previous iteration while structure stiffness matrix $[K_T]$ used for the current iteration again corresponds to the strain state at the beginning of current load increment. Next iteration is carried out with unbalanced force vector $\{R_o'\}$ applied on the B'' stage using structure stiffness matrix $[K_T]$. The iterations are continued for successive unbalanced forces till the

specified accuracy as defined by a suitable convergence criteria described in section 3.4.5.2 is achieved. The structure is loaded by the next load increment and the procedure repeated as outlined above till failure is indicated either by a large increase in the unbalanced force or by a large increase in incremental deformation or by the structure stiffness matrix deteriorating to a non-positive definite state.

3.4.5.2 Convergence criteria

For the nonlinear analysis, iterations in each load increment are carried out to satisfy equilibrium and constitutive relations. Theoretically this situation is obtained only after infinite number of iterations, but for engineering solutions, the convergence may be assumed to have reached when certain convergence criteria are satisfied.

In the iterative procedure, the unbalanced nodal force $\{R_o\}$ or the incremental nodal displacements $d\{\delta'\}$ provide a measure of satisfaction of the equilibrium equations. Some of the convergence criteria commonly used are as follows :

- (i) Norm of residual forces

$$\text{The norm } || R_o || = (\{R_o\}^T \{R_o\})^{1/2} \quad (3.83)$$

is specified not to exceed a percentage of the norm of the applied loads, $|| F ||$

$$\text{where } || F || = (\{F\}^T \{F\})^{1/2} \quad (3.84)$$

- (ii) Norm of displacement changes

$$\text{The norm } || d\{\delta'\} || = (d\{\delta'\}^T d\{\delta'\})^{1/2} \quad (3.85)$$

is computed and compared with a percentage of the norm of the total displacements.

(iii) Energy norm due to residual forces

$$\text{The norm } ||E_R|| = ||\{R_o\}^T d\{\delta'\}|| \quad (3.86)$$

is computed and compared with a percentage of the energy norm due to applied loads given by

$$||E_f|| = ||\{F_b\}^T \{\delta\}|| \quad (3.87)$$

where $\{\delta\}$ is the displacement caused by applied loads $\{F\}$.

(iv) Residual forces - Absolute magnitude

The absolute value of the largest term in $\{R_o\}$ is found and checked to see if it exceeds a fraction of the norm of the applied load vector.

The nodal force vector contains forces and moments and the displacement vector contains deflections and rotations. These quantities are not dimensionally homogeneous. Thus the norm of each type of force or displacement has to be obtained separately. Again from amongst forces or displacements, only one type of force or displacement component may depict the structural behaviour in a predominant way. Convergence criteria based on this predominant quantity may also indicate the general behaviour of the structure.

In the proposed procedure, the norm of residual nodal forces in a specified direction is compared with the norm of applied loads in the same direction and the energy norm due to residual forces is compared with the energy norm due to applied loads. The convergence is assumed to be achieved when either of the above norms is satisfied. The computer then stops the iteration and goes on to the next load increment. The residual unbalanced nodal forces are carried over and added to the next load increment.

Usually the failure of a structure is symptomatically indicated by the divergence of the iteration. In order to prevent the computer from wasteful computation, divergence criteria are also specified for the norm of residual forces and the energy norm due to residual forces. Whenever the norm of residual forces or energy norm due to residual forces exceed their respective divergence norms, the computer stops the solution. To save on computer time, a limit on maximum number of iterations in each load increment is also imposed. The solution goes on to the next load increment if the number of iterations for a particular load increment exceeds this limit.

3.5 COMPUTER PROGRAM

A general computer program has been developed to carry out nonlinear analysis of three dimensional plated structures of prismatic cross-section under dead loads and monotonically increasing live loads. Ferrocement structures and thin reinforcement concrete structures can be analysed by this program. As a particular case, ferrocement plates and thin reinforced concrete slabs can also be analysed. A brief description of the solution algorithm is as follows:

- (i) Total load on the structure is divided into suitable number of load increments.
- (ii) For the first load increment and for the first iteration, the structure stiffness matrix is generated based on the uncracked rigidities of the element given by equations (3.49 to 3.59).
- (iii) The equations of equilibrium are solved for the incremental deformations under the load increment. The incremental strains and stresses at each Gauss point are obtained as described in section 3.4.5.1.
- (iv) At each Gauss point, the total strains are obtained by adding incremental strains to the accumulated strains. The total anticipated stresses are

then obtained by adding the incremental stresses based on the latest rigidities of the previous iteration (using equation 3.78) to the actual stresses at the end of previous iteration.

- (v) The actual stresses, at each Gauss point are calculated using latest rigidities (given by equations 3.49 to 3.74) corresponding to the total strains and incorporating the tension stiffening effect described in section 3.4.3.1.
- (vi) Unbalanced stresses at each Gauss point are converted into unbalanced nodal forces using equation (3.21).
- (vii) Norm of unbalanced nodal forces and energy norm due to unbalanced nodal forces are checked for convergence and divergence. If they have converged or maximum number of prescribed iterations have been carried out, the analysis is continued to step (viii). If they have diverged, then solution is stopped.
- (viii) The residuals are added to the next load increment and the structure stiffness matrix is assembled based on the latest rigidities of the last iteration. If the structure stiffness matrix $[K]$ becomes non-positive definite, the analysis is stopped, otherwise the analysis is resumed from step (iii).

The flow diagram for the incremental iterative procedure is also explained in Fig. 3.19.

The computer program for the incremental iterative procedure, written in FORTRAN IV, consists of a number of modules as shown in a block diagram (Fig. 3.20). The main module calls and controls various modules required for the solution of the problem. A brief description of various modules is given below :

- GAUSS :** This subroutine reads in the information as regards the location and the corresponding weighting constants for integration points.
- SHAPE1 :** This subroutine generates the shape functions and the elements of the strain derivative matrix at Gauss points in terms of nondimensionalized parameters ξ and η of the 24 degrees of freedom flat shell element.
- GDATA :** It reads and prints the vital information about the problem, such as the title, general control data of the problem, material properties, elements, their nodal connections and material identification number, boundary nodes and the boundary conditions and the number and the size of the load increments.
- LOAD :** It reads and prints the nodal load vector in global co-ordinate system. It also generates the consistent nodal load vector for dead loads and uniformly distributed loads on the element, if any and transforms the same to global coordinate system by calling subroutine TFORM. Finally it assembles the nodal load vector for the structure in global coordinate system.
- SHAPE2 :** It generates shape functions $[N]$ and strain derivative matrix $[B]$ at a Gauss point of an element from the generalized values obtained in SHAPE1.
- STIFGP :** This subroutine calculates the contribution of the given Gauss point of an element towards local $[K_{mm}]$, $[K_{mb}]$ and $[K_{bb}]$ of the element.
- STIFN :** This subroutine numerically evaluates the element stiffness matrix from $[K_{mm}]$, $[K_{mb}]$ and $[K_{bb}]$ submatrices generated at Gauss points in subroutine STIFGP. The element stiffness matrix is rearranged by calling subroutine REARNG for the convenience of transformation. The element stiffness matrix is then transformed to global coordinate system by calling subroutine TFORM. Finally it writes the element connection information and the transformed element stiffness matrix on a scratch tape.

TFORM : This subroutine transforms the element stiffness, the load vector and the nodal deformation vector from the local to the global system or vice-versa.

REARNG : This subroutine rearranges the elements of the stiffness matrix of the finite element in the order of the six degrees of freedom per node for the convenience of transformation as described in section 3.4.2.

SOLVE : This subroutine reads the element nodal connections and stiffness from the scratch tape and assembles the structure stiffness, introduces boundary conditions and reduces the structure stiffness to an upper triangular form by the Gaussian elimination process. It stores the reduced equations on another peripheral storage device to be used for other load cases, if any, and for back substitution for getting the solution in the form of nodal deformations.

RESOLV : This subroutine is useful when the structure with the same stiffness and boundary conditions is to be solved for a number of load cases. In such cases, the structure stiffness need not be assembled and reduced to a triangular form again.

BSUB : This subroutine finds out the unknown nodal deformations or reactions by back substitution. It also calculates the vectorial norm of incremental and total nodal deformations.

STRESS : This subroutine picks up the nodal deformations for each element and calculates the strains and their principal values and directions at the Gauss integration points and/or at nodes of the element. It also calculates the anticipated stresses at the Gauss points assuming material characteristics as at the beginning of the iteration. Further knowing the latest total strains at the Gauss points, the actual stresses as per the assumed material model are evaluated. Lastly it determines the stresses released as the difference of

anticipated total stresses minus the actual stresses and the contribution towards unbalanced nodal forces from each Gauss point.

CHECK : This subroutine checks the mortar for cracking, yielding or crushing and wire mesh and skeletal steel for yielding. It also determines the forces resisted and develops the tangent rigidities as per strain distribution at each Gauss point.

3.6 TEST PROBLEMS

3.6.1 Test Problem for Elastic Analysis

An aluminium model of North light folded plate was tested by Scordelis, Croy and Stubbs⁽¹⁵⁷⁾ to verify the theoretical results obtained by the folded plate theory and elementary beam theory with the experimental results. The model was 1219.2 mm x 914.4 mm in size and made from bent aluminium sheets 1.6 mm thick and rested on 4.83 mm thick end traverses. The form and the loading are shown in Fig. 3.21.

Taking advantage of the symmetry, only half of the folded plate has been analysed using a finite element discretization, as shown in Fig. 3.21, with appropriate boundary conditions. The number of the elements and the nodes used in the discretization are 18 and 28 respectively. The total computer time required for complete analysis is 14.30 seconds on DEC 2050 computer system.

The reported results of analysis⁽¹⁵⁷⁾ based on Goldberg and Leve's method⁽¹³⁴⁾ consist of longitudinal stresses and transverse moments at mid, quarter and one eighth span. The mid span and the quarter span results are compared with those obtained by the present formulation in Fig. 3.22.

The computed results compare favourably at mid and quarter span sections. The maximum variation at mid span section in longitudinal stresses is 8.9 percent at nodes 'c' and 'd' and in transverse moments 5.4 percent at free edges 'a' and 'f'. This shows that even with a coarse mesh as adopted in the present analysis, satisfactory results are obtained.

The mid span vertical deflections as obtained by Scordelis et al.⁽¹⁵⁷⁾ using Goldberg and Leve's method and by the present finite element method are compared in Table 3.3. At nodes 'a' and 'f' where the deflection is maximum, the computed results are less by only 0.7%. The maximum variation of 6.0 % is at nodes 'c' and 'd' where the deflections are just 2.1 percent of the maximum deflections at nodes 'a' and 'f'.

Table 3.3 Comparison of Vertical Deflections at Mid Span of Aluminium North Light Folded Plate

Method	Mid-span deflection (mm) at					
	a	b	c	d	e	f
Goldberg and Leve ⁽¹³⁴⁾	2.885	1.755	0.0597	0.0597	1.755	2.885
Present FEM	2.867	1.744	0.0561	0.0561	1.744	2.865
% variation between the two methods	0.624	0.627	6.03	6.03	0.627	0.693
Experimental	-	1.379	0.0025	-0.015	1.382	-

3.6.2 Test Problems for Nonlinear Analysis

(1) Folded Plates Tested by Scordelis and Gerasimenko⁽¹⁵⁸⁾

Two models of folded plates having a butterfly type of cross-section and of approximately one-sixth geometrical scale of a prototype canopy over a school walkway were tested under simply supported end conditions by Scordelis

and Gerasimenko. The two models as shown in Fig. 3.23 were of identical geometrical dimensions but differed in the provision of reinforcement. The reinforcement requirement for model 'A' was determined by the folded plate elastic analysis, whereas for model 'B', the reinforcement was determined by the elementary beam theory. The purpose of the study was to compare the behaviour through the elastic, inelastic and ultimate stages of the two models reinforced differently.

The overall plan dimensions of the models were 762 mm x 1778 mm, and the plates were 12.7 mm thick cast with 38.1 mm thick diaphragms. The concrete cylinder (152.4 mm x 304.8 mm) compressive strength for model 'A' after 16 days was 20.69 MPa and that for model 'B' after 14 days was 25.03 MPa. The Poisson's ratio for concrete was assumed to be 0.18. The values of the modulus of elasticity for concrete determined by the ACI code formula, were 22754.0 MPa and 25029.0 MPa for models 'A' and 'B' respectively. In both the models, 14 gauge 2.032 mm diameter annealed tie wire was used as reinforcement. The yield stress, ultimate strength and modulus of elasticity for the wire were 227.54 MPa, 358.54 MPa and 196508.0 MPa respectively. For the nonlinear analysis, the cracking, yielding and crushing strains of the concrete are assumed as 0.000170, 0.002 and 0.0035 respectively. The unit weight of the models is assumed as 25 kN/m³.

In the model tests, line loads equal to the joint reactions produced by a uniform design load of 2.753 kN/m² were applied at a number of points on the fold lines. The vertical displacement of the joints and strains in the longitudinal reinforcement over a gauge length of 152.4 mm were measured at the mid span. Both the models were initially subjected to 8 cycles of loading and unloading upto the design load. The models were finally tested under increasing loads upto the failure.

One quarter of the folded plate is discretized as shown in Fig. 3.23(a) by twenty elements and thirty nodes with appropriate boundary conditions. The actual reinforcement as shown in Figs. 3.23(b), (c) is discretized into eight types of plate materials with steel bars assumed to be placed at the middle of the thickness of the plates. A total load equal to 4.0 times the design load is applied on the models in seven load increments. The first load increment is taken equal to the design load and the rest six load increments taken equal to half the design load. A maximum of four iterations are permitted in each load increment. The failure of both the models at the seventh load increment is indicated by the divergence in the residual load vectorial norm and the energy norm due to residual loads. This is also indicated by the large increase in the deflections. The total computer time taken for the analysis of models 'A' and 'B' with complete displacement and stress output is nearly 2 minutes and 25 seconds each.

The elastic longitudinal stresses and transverse moments at mid span under the design load for model 'A' as obtained by the folded plate theory⁽¹³⁴⁾ are compared with the results of the present analysis in Figs. 3.24(b) and (c). The predicted longitudinal stresses (Fig. 3.24(b)) by the present analysis are in good agreement with those obtained by the folded plate theory at the intermediate nodes 'b', 'c' and 'd'. The maximum variation is at the free edge node 'a' where the predicted stress is more by about 18 percent. The predicted transverse moments (Fig. 3.24(c)) are in good agreement with the folded plate theory at nodes 'a' and 'b' and are less by about 12 percent at nodes 'c' and 'd'. The variation is probably due to the modulus of elasticity for the composite being taken equal to that of the concrete in the folded plate analysis, whereas in the finite element analysis, the modulus of elasticity of the concrete and steel along with the variation in the amount of steel for the different regions is properly taken into account.

The predicted mid span deflections at the fold lines for model 'A' under increasingly applied loads are compared with the experimental deflections in Fig. 3.25. The predicted deflections compare well with the experimental deflections upto 2.5 times the design load. At higher loads, the predicted deflections are more than the experimental deflections. At 3.5 times the design load, the experimental load-deflection curve at the free edge node 'a' becomes almost horizontal. Beyond this load, the slope of the load-deflection curve increases and gradually changes sign. At the reported test failure load of four times the design load, a reversal in the experimental load-deflection curve takes place. At failure load, the diagonal tension cracks in the shell near the supports and the cracks in the diaphragm had become excessively large. In the present analysis, the diaphragms have not been modelled due to the rectangular shape of the finite element chosen.

The longitudinal strains in the steel at various points on the cross-section at mid span are compared in Fig. 3.26. The predicted tensile strains compare well with the experimental values upto two times the design load. Beyond this load, the predicted tensile strains are more than the experimental strains and increase at a fast rate. This is because the yield strain of steel is predicted at 2.5 times the design load. Beyond this load, the stiffness contribution of steel is zero due to the assumed linearly elastic-perfectly plastic stress-strain curve of the steel. The predicted compressive strains compare well with the experimental strains upto 3.5 times the design load and only at the failure load, the predicted compressive strains become large as compared to the experimental strains.

The first crack load for model 'A' is theoretically obtained at 0.85 times the design load while the experimental value from the load-deflection curves is also less than the design load as evinced by the point of nonlinearity on the load-deflection curves. The predicted crack-patterns at failure load (Fig. 3.27)

compare well with the reported experimental one except near the supports which is due to the noninclusion of the diaphragms in the analysis as mentioned above.

For model 'B', the predicted mid span deflections at various points are compared with the experimental ones in Fig. 3.28. The predicted deflections compare well upto three times the design load and beyond this load, the predicted deflections become more than the experimental ones. In this model also, the experimental load-deflection curves become stiffer beyond 3.5 times the design load. This model had also failed at four times the design load due to widening of cracks in the shell near the supports and in the diaphragms.

The predicted mid span longitudinal strains in steel at different load levels are compared with the experimental strains in Fig. 3.29. The predicted tensile strains are on the stiffer side of the experimental strains upto two times the design load and are on the flexible side at 2.5 times the design load. The steel is predicted to yield at about 2.25 times the design load. The reported load-tensile strain curve is only upto 2.75 times the design load. The predicted compressive strains continue to be on the stiffer side upto three times the design load and beyond this load these are on the flexible side.

The theoretical first crack load for model 'B' is obtained as 0.98 times the design load. The experimental first crack load is also approximately equal to the design load as apparent from the nonlinearity of the load-deflection curves. The predicted crack-patterns (Fig. 3.30) at failure load compare well with the reported experimental one in the major portion and differ only near the supports due to noninclusion of the diaphragms in the analysis.

(2) Corner Supported Square Slab Under a Concentrated Load at Centre

An isotropically reinforced square concrete slab, simply supported at the four corners was tested by McNeice⁽¹⁵⁹⁾ under a central load. The slab was 914.4 mm x 914.4 mm x 44.45 mm in size isotropically reinforced with 0.85 percent steel in the two perpendicular directions. The compressive strength, modulus of elasticity and Poisson's ratio of the concrete were 37.923 MPa, 28614 MPa and 0.15, respectively. The modulus of elasticity of the steel was 199955 MPa. For nonlinear analysis the cracking, yielding and crushing strains of the concrete and yield strain of the steel are assumed as 0.00015, 0.002, 0.0035 and 0.0022 respectively. The unit weight of the slab is assumed as 25 kN/m³.

Taking advantage of the symmetry of the geometry and the load, a quarter of the slab is discretized as shown in Fig. 3.31(a) by 36 elements and 49 nodes. The total load of 14 kN is applied in six load increments of 4 kN, 2 kN, 2 kN, 2 kN, 2 kN and 2 kN each. The failure of the slab is indicated at 14 kN load due to large increase in deflection and the residual vector norm ratio. The total computer time taken for only displacement output at various load levels is 3 minutes and 13 seconds. Nonlinear analysis of the above slab using layered technique and incorporating tension stiffening effect has also been reported by Lin and Scordelis⁽¹⁶⁰⁾. They also discretized a quarter of the slab by the same number of elements and nodes as done in the present analysis. They divided the concrete thickness in 10 layers. The results of the present method are compared with the analytical results of Lin and the experimental results in Fig. 3.31(b). The predicted mid span deflections are comparable with the experimental deflections in the elastic stage but are on the stiffer side in the cracked range upto about 11.6 kN and thereafter are on the flexible side. The deflections predicted by the proposed method are more close to the experimental values and are also

comparable with the analytical results of Lin except near the ultimate failure load. The predicted deflections at ultimate load of 14 kN are large as compared to the experimental results and those of Lin, but the present method has shown better comparison in the major portion of the cracked range as compared to the results of Lin. The discrepancy at near ultimate load is due to modelling of the concrete thickness by 10 layers by Lin and by two layers (uncracked and cracked layers) in the present method. Since ferrocement elements are usually 15 mm to 25 mm thick, the results of this example also justify the present approach of considering the element to be consisting of single matrix layer in uncracked range and of uncracked and cracked layers in the cracked range. There is also a saving in computational effort as compared to layered approach in which the matrix thickness is divided in about 8 to 10 layers.

The theoretical first crack load is obtained as 4.03 kN and the experimental first crack load as evident from the non-linearity of the load-deflection curve is about 4.0 kN.

(3) Ferrocement Box Beams Tested by Al-Sulaimani and Ahmad⁽¹⁶¹⁾

Al-Sulaimani and Ahmad carried out flexural tests on ferrocement box beams reinforced with or without skeletal steel. The box beams had an overall length 2500 mm, effective span 2400 mm, overall depth 207 mm, overall width 156 mm and thickness of webs and flanges as 20 mm. The beams were provided with two layers of galvanized square woven wire mesh having opening size 6.35 mm and wire diameter 0.90 mm. Yield strength of wire mesh was 414 MPa. In one box beam, three skeletal steel bars of diameter 4.3 mm having yield strength of 707 MPa were provided in the compression and tension flange. The value of ferrocement elastic modulus under flexure was 9500 MPa.

The modulus of elasticity of mortar, wire mesh and skeletal steel have not been reported. For analysis, the modulus of elasticity of wire mesh and skeletal steel have been assumed as 150000 MPa and 200000 MPa respectively. The modulus of elasticity of mortar as determined from the law of mixtures (neglecting the contribution of skeletal steel) comes out to be 18000 MPa. Poisson's ratio for the mortar has been assumed as 0.20. The two layers of wire mesh have been assumed to be placed at a distance of 5 mm from the centre to the plate thickness, thus providing a cover of 5 mm to the centre of the mesh layer. The cracking, yielding and crushing strains of the mortar have been assumed as 0.00015, 0.002 and 0.0035 respectively. The unit weight of the ferrocement has been assumed as 25 kN/m^3 .

Taking advantage of symmetry of cross-section and loading, a quarter of the box beam has been discretized as shown in Fig. 3.32 by 24 elements and thirty five nodes. For the box beam without skeletal steel, marked C-i-1, a total load of 12 kN has been applied in five load increments of 4 kN, 2 kN, 2 kN, 2 kN and 2 kN each. The failure of the box beam at 12 kN is indicated by a large increase in deflection and energy norm ratio due to residual forces. The total computer time taken for only displacement output is 1 minute and 29 seconds.

Deflections of the box beam C-i-1 at mid span are compared in Fig. 3.33(a). The predicted deflections compare well in the elastic range but are on the stiffer side upto about 9 kN and thereafter on the flexible side of the experimental deflections. At ultimate load of 12 kN, the predicted deflections are more by about 60 percent. The theoretical first crack load is obtained as 4.33 kN whereas the experimental first crack load as evident from the nonlinearity of the load deflection curve is about 4.5 kN.

For the box beam with skeletal steel, marked C-ii-1, a total load of 20 kN has been applied in seven load increments of 5 kN, 2.5 kN, 2.5 kN, 2.5 kN, 2.5 kN, 2.5 kN and 2.5 kN each. The failure of the box beam at 20 kN load is indicated by large increase in deflection, residual load vector norm ratio and energy norm ratio due to residual forces. The total computer time taken for only displacement output is 2 minutes and 8 seconds.

Deflections of the box beam C-ii-1 at mid span are compared in Fig. 3.33(b). The predicted deflections compare well in the elastic range; are on the stiffer side upto about 12 kN and thereafter on the flexible side of the experimental deflections. The predicted deflections in the major portion of cracked range compare well with the experimental ones. The predicted deflections can be considered satisfactory in view of the actual modulus of elasticity of the mortar, wire mesh and skeletal steel being unknown. The theoretical first crack load is obtained as 4.89 kN. The experimental first crack load as evident from the nonlinearity of the load deflection curve is about 4.5 kN.

3.7 CONCLUDING REMARKS

For three dimensional ferrocement structures involving membrane and bending actions, classical membrane and bending theories have been used. These theories can predict the behaviour only in the elastic range for some simple shapes, loading and boundary conditions. For complete analysis through elastic, cracked and ultimate stages, finite element method has been used by several researchers to analyse reinforced concrete plates and shells of various shapes. In the case of ferrocement, nonlinear analysis using finite element method has been reported only in the case of two way slabs. The method can incorporate the material and geometrical nonlinearity of the problem. The method predicts the complete load-deformation response, internal

stresses and strains in the constituent materials and propagation of cracks under increasingly applied loads.

In the present investigation, finite element method in conjunction with the modified layered approach has been adopted for the nonlinear analysis of thin ferrocement plated structures. Instead of considering the element to be consisting of suitable number of layers of mortar and reinforcement as in the conventional layered approach, the element is assumed to be consisting of single mortar layer in the uncracked stage, uncracked and cracked mortar layers in the cracked stage and smeared layers of wire mesh and skeletal steel. In the cracked stage, the depth of cracked/yielded/crushed mortar is determined. The stiffness of the element in the cracked stage is obtained by adding the contributions due to uncracked mortar layer, cracked/yielded mortar layer and unyielded layers of wire mesh and skeletal steel. This results in a saving in the computational effort as compared to the layered approach.

The validity of the proposed formulation for the nonlinear analysis of thin ferrocement structures has been established with the help of three different test problems chosen for the investigation whose test results were known. It is seen from the comparison of the results that the predicted values are generally in good agreement with the test results except near the ultimate failure load where predicted values are on flexible side. The proposed formulation is quite economical and yet capable of predicting the complete behaviour of structures in uncracked and cracked stages including the crack propagation and the distressed zones.

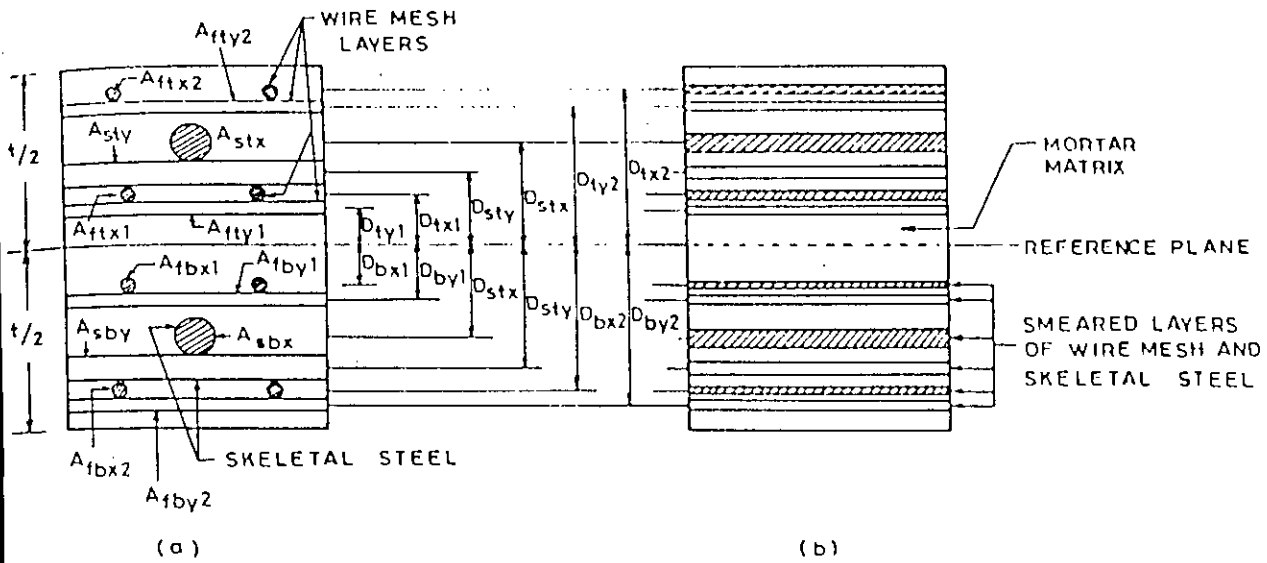


FIG. 3.1 (a) TYPICAL FERROCEMENT SECTION AND (b) EQUIVALENT IDEALIZED SECTION WITH SMEARED LAYERS OF WIRE MESH AND SKELETAL STEEL

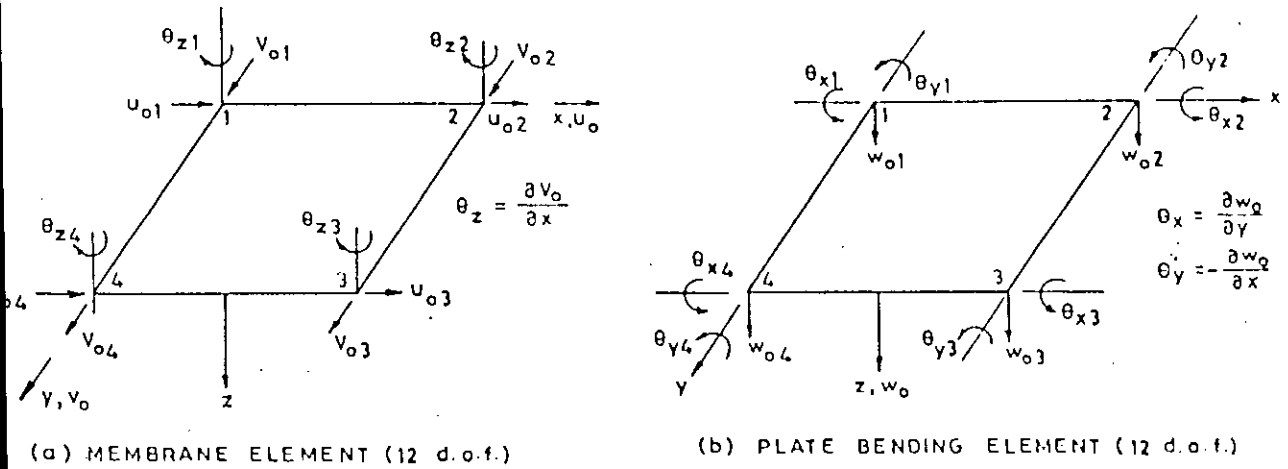


FIG. 3.2 RECTANGULAR FLAT SHELL ELEMENT (24 d.o.f.)

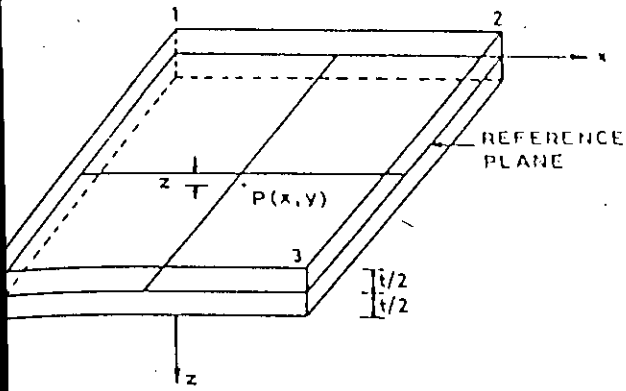


FIG. 3.3 - RECTANGULAR FLAT SHELL ELEMENT

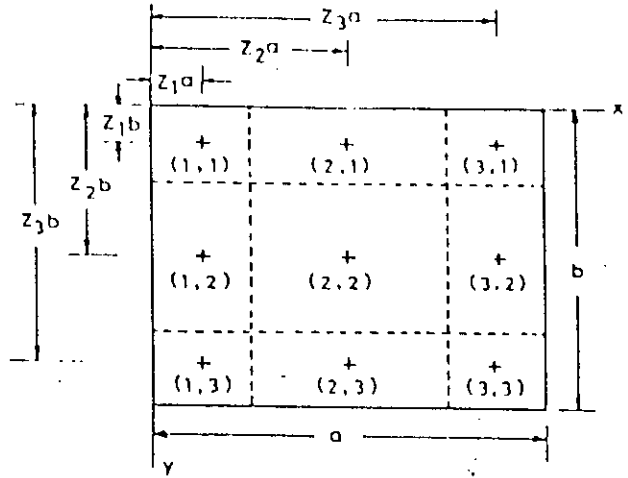


FIG. 3.4 - GAUSS INTEGRATION POINTS AND AREAS UNDER THEIR COMMAND

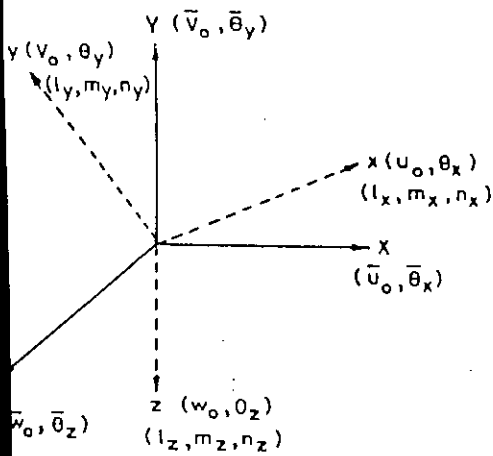


FIG. 3.5 (a) TRANSFORMATION BETWEEN LOCAL COORDINATE SYSTEM (x, y, z) AND GLOBAL COORDINATE SYSTEM (X, Y, Z)

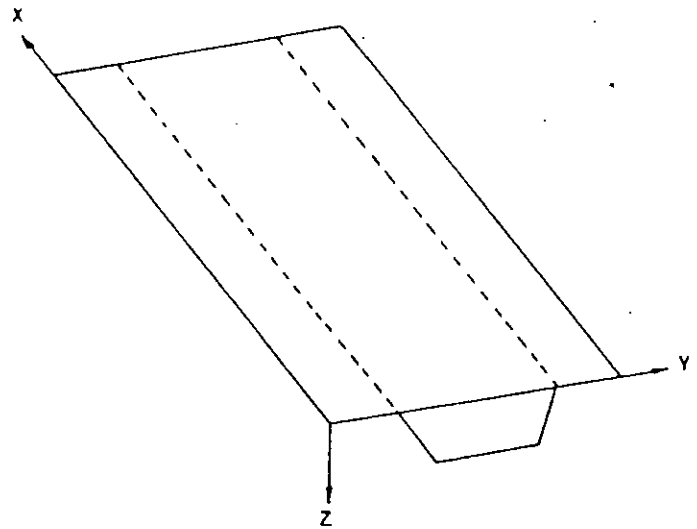


FIG. 3.5 (b) A TYPICAL PRISMATIC BOX GIRDER

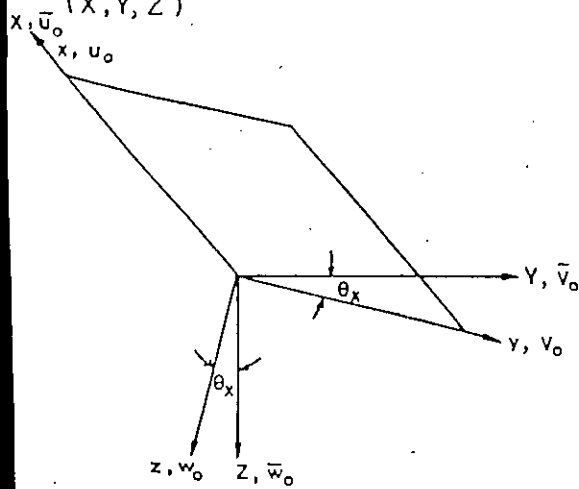


FIG. 3.5 (c) ROTATION OF ELEMENT ABOUT X-AXIS

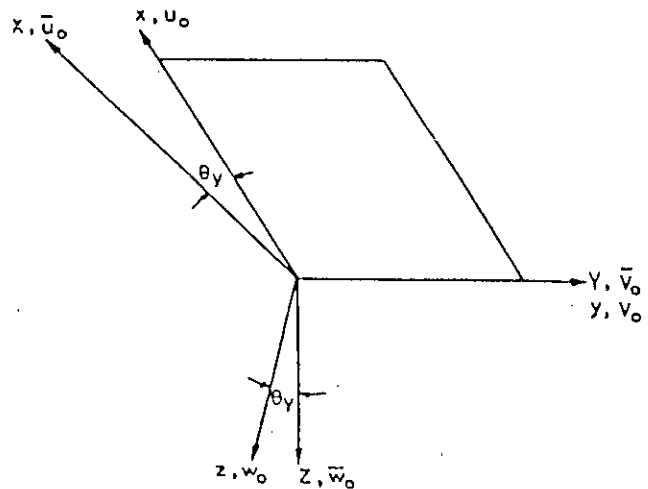
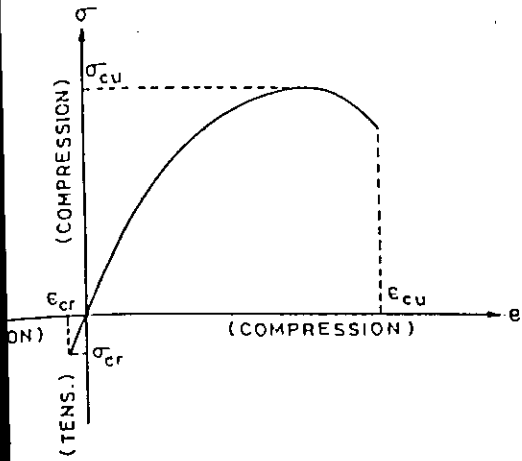


FIG. 3.5 (d) ROTATION OF ELEMENT ABOUT Y-AXIS

FIG. 3.5 - TRANSFORMATION AND SELECTION OF AXIS



6 - A TYPICAL UNIAXIAL STRESS-STRAIN CURVE FOR MORTAR

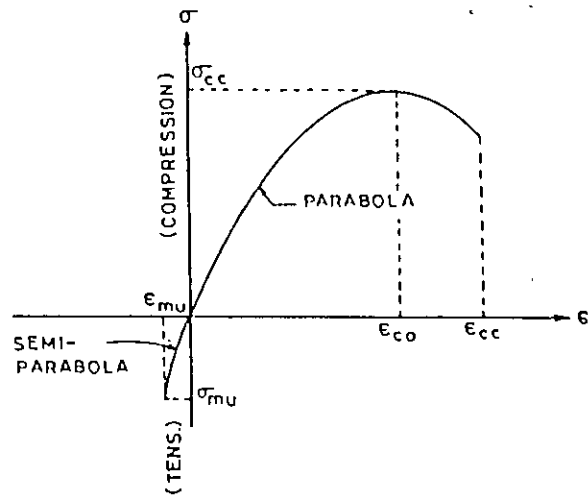
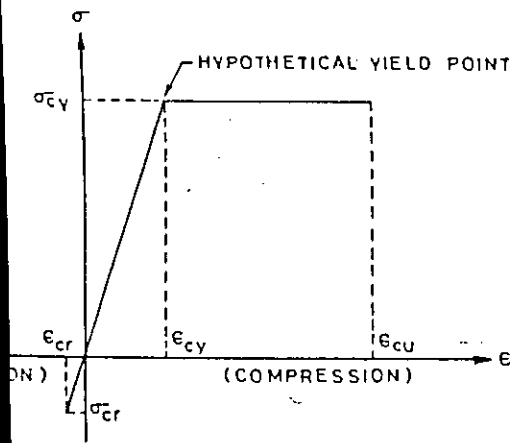


FIG.3.7 -THEORETICAL UNIAXIAL STRESS-STRAIN CURVE OF MORTAR USED BY RAJGOPALAN et.al.(128)



- IDEALIZED UNIAXIAL STRESS-STRAIN CURVE FOR MORTAR (PRESENT STUDY)

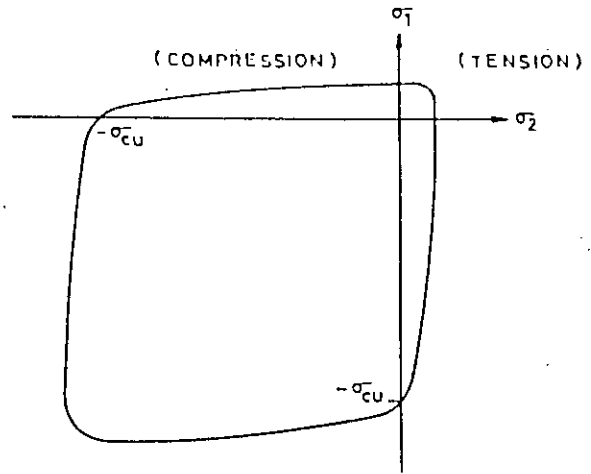
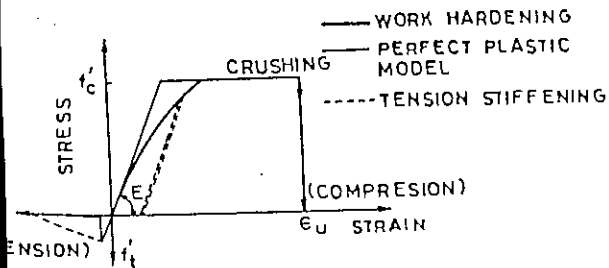


FIG.3.9 - FAILURE SURFACE OF CONCRETE UNDER BIAxIAL STRESS STATE BY KUPFER et al.(153)



- ONE DIMENSIONAL REPRESENTATION OF MORTAR CONSTITUTIVE MODEL

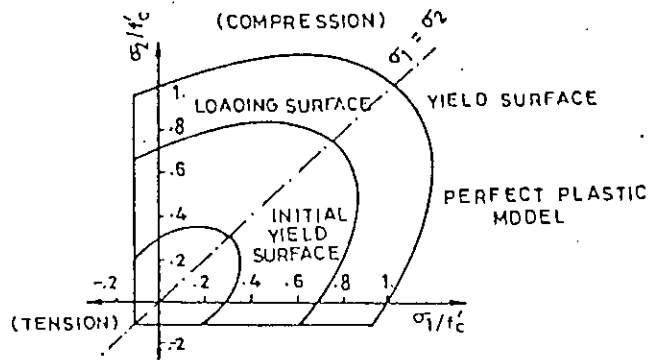
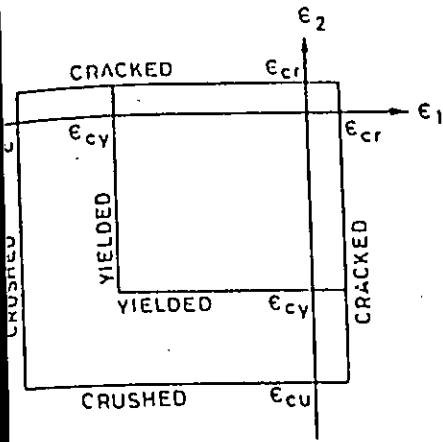


FIG.3.10(b) - TWO DIMENSIONAL SPACE REPRESENTATION OF MORTAR CONSTITUTIVE MODEL BY PRAKHYA et.al.(143)



3.11 - ASSUMED LIMITING STRAIN FAILURE CRITERIA

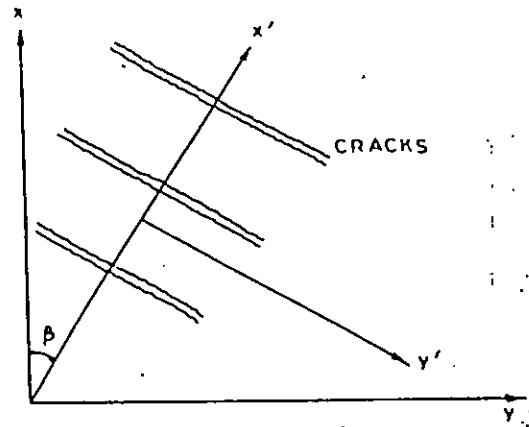
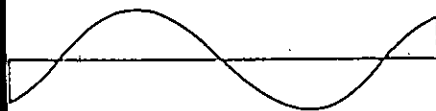
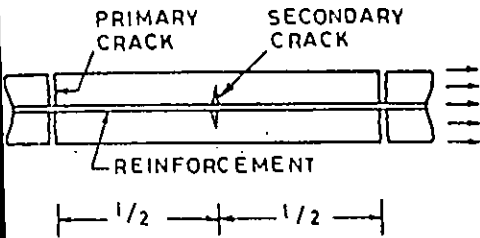


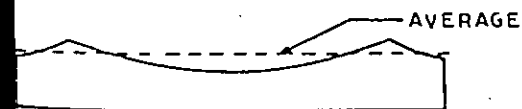
FIG. 3.12 - COORDINATE TRANSFORMATION FOR A CRACKED ELEMENT



BOND STRESS DISTRIBUTION



MORTAR STRESS DISTRIBUTION



STRESS IN REINFORCEMENT

3.13 - STRESS DISTRIBUTION IN A CRACKED FERROCEMENT ELEMENT

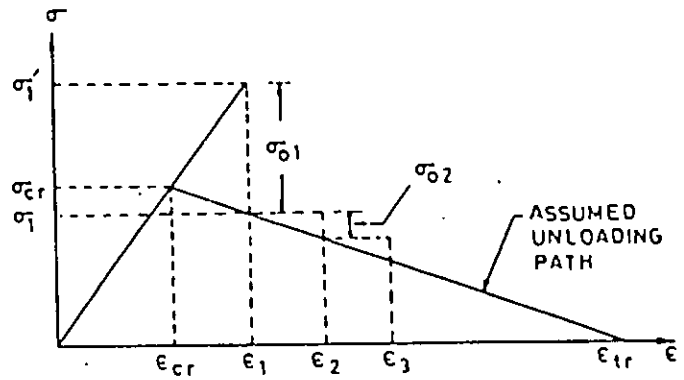


FIG. 3.14 - GRADUAL UNLOADING FOR CRACKED MORTAR

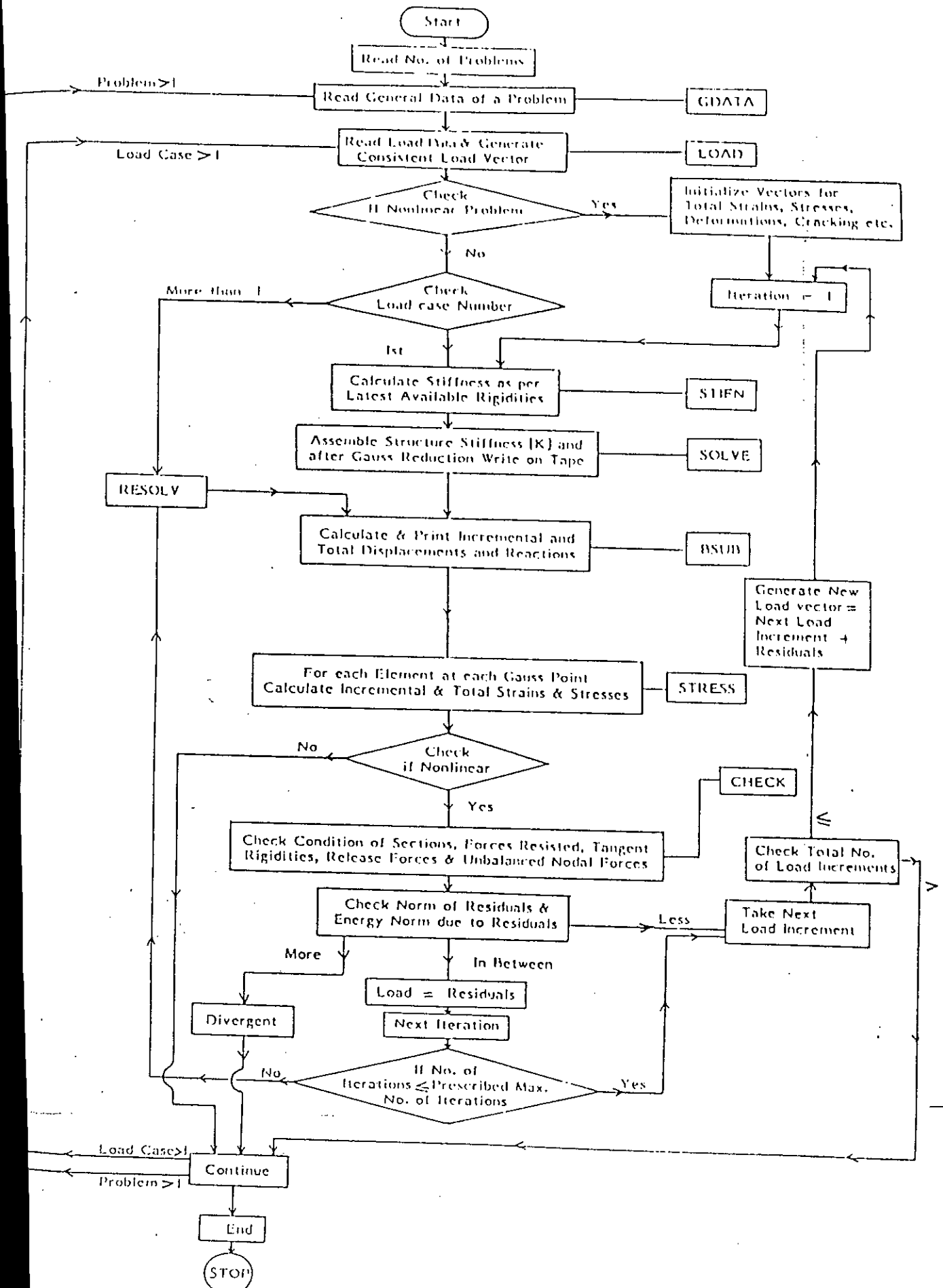
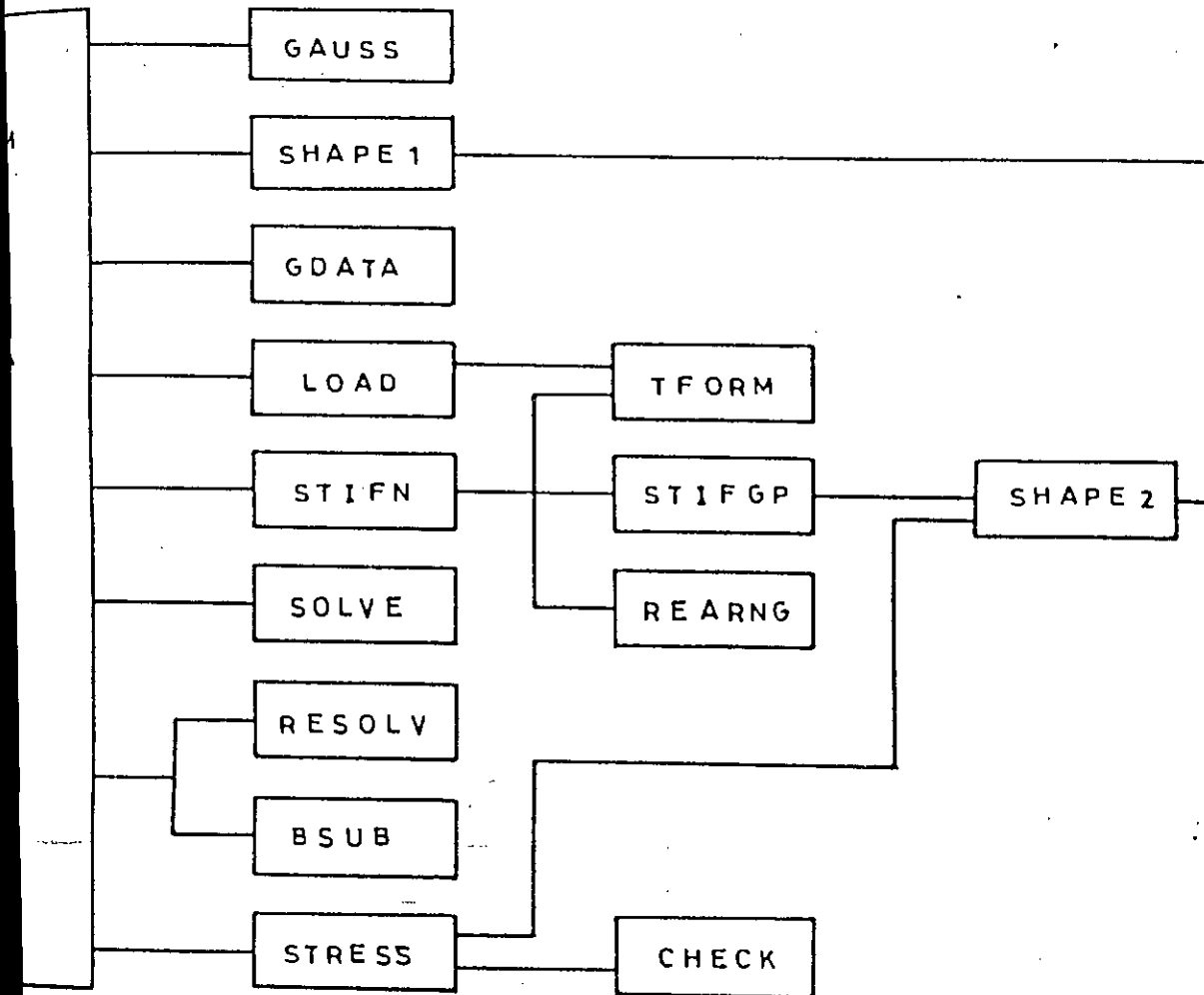


Fig. 3.19 Flow Diagram for Incremental Iterative Procedure



3-20

- ARRANGEMENT OF DEFFERENT MODULES USED
FOR ANALYSING 3-D PLATED STRUCTURES.

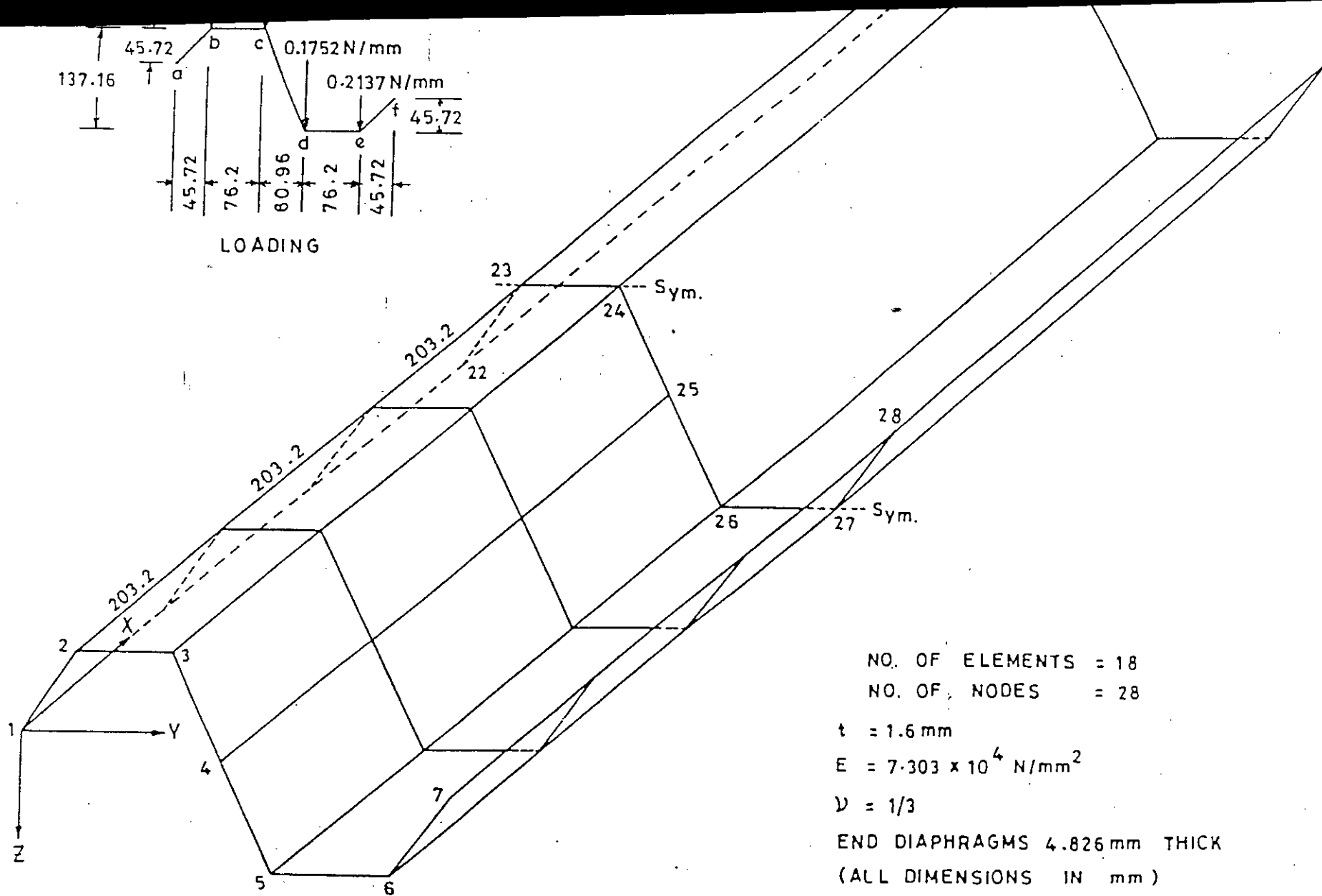
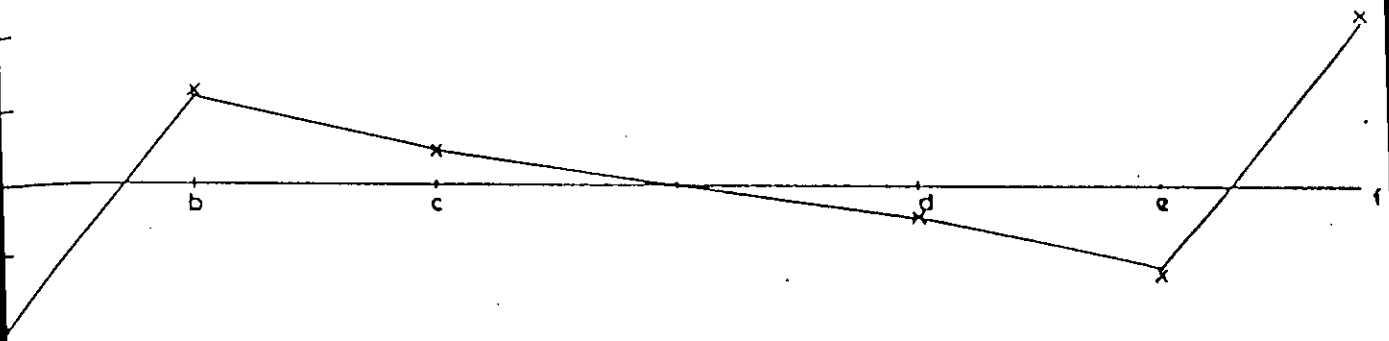
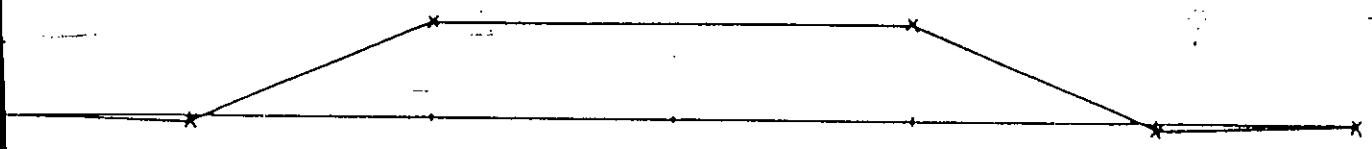


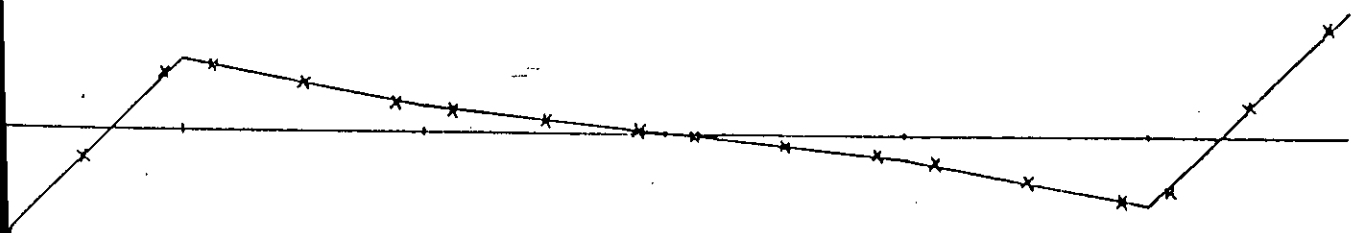
FIG. 3-21 - ALUMINIUM NORTH-LIGHT FOLDED PLATE TESTED BY SCORDELIS (FINITE ELEMENT DISCRETIZATION)



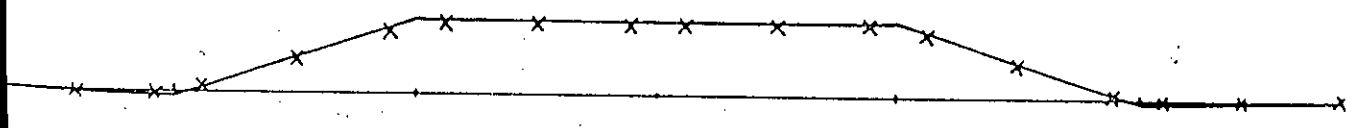
(a) MID SPAN LONGITUDINAL STRESS (N/mm²)



(b) MID SPAN TRANSVERSE MOMENT (mm.N/mm)



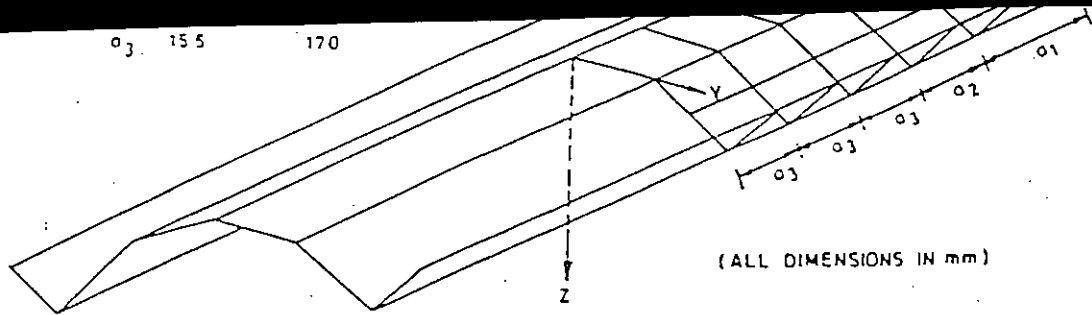
(c) QUARTER SPAN LONGITUDINAL STRESS (N/mm²)



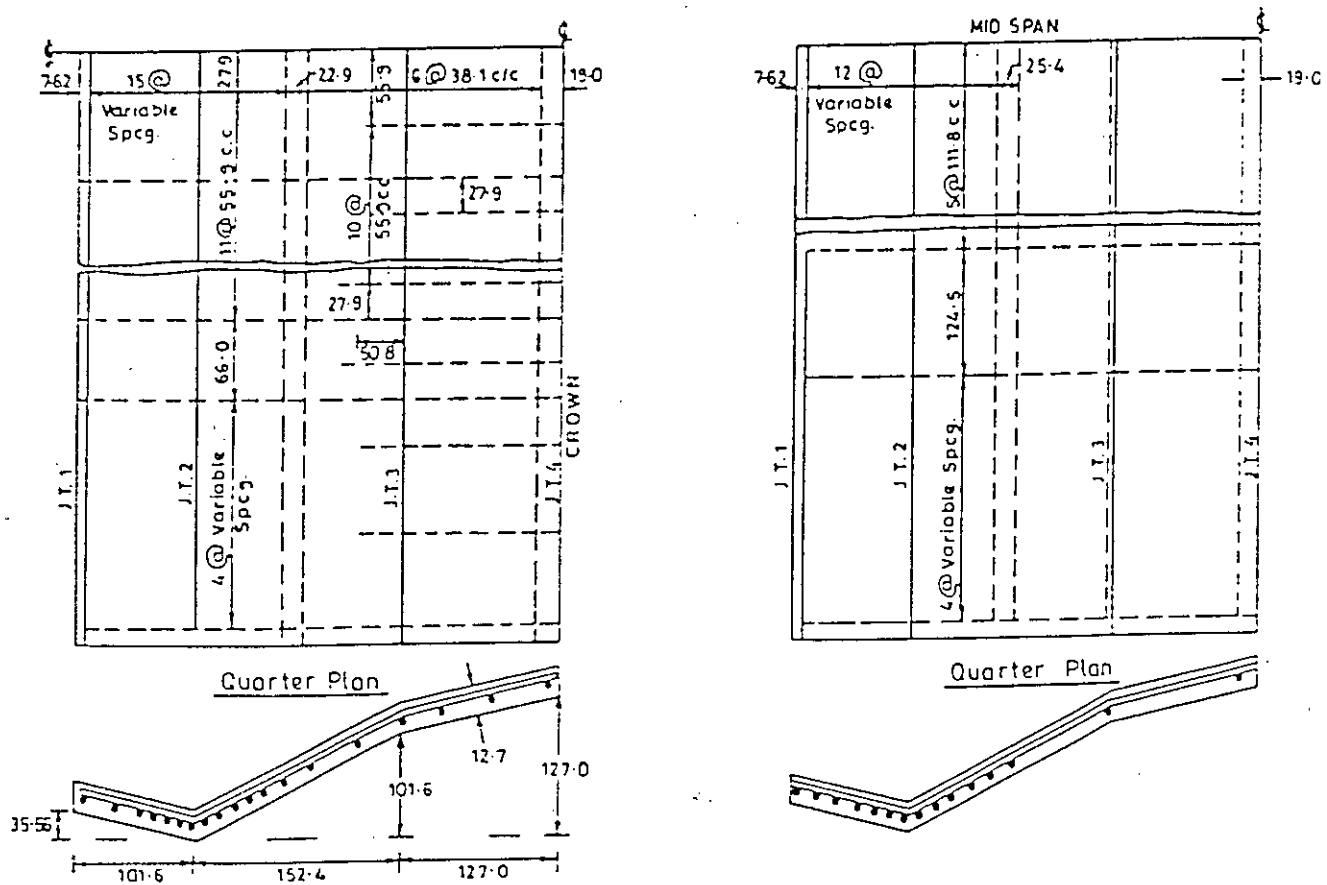
(d) QUARTER SPAN TRANSVERSE MOMENT (mm.N/mm)

— CLASSICAL METHOD (134) RESULTS
 x FEM RESULTS (AUTHOR)

G.3.22 - COMPARISON OF RESULTS FOR NORTH LIGHT FOLDED PLATE (157)



(a) Finite Element Idealization of a Quarter of the Folded Plate

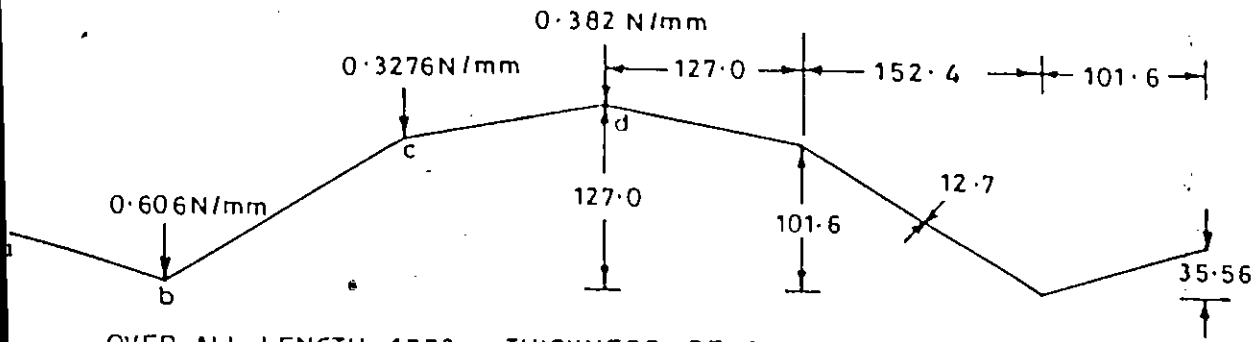


(b) Reinforcement Scheme For Model 'A'

(c) Reinforcement Scheme For Model 'B'

(ALL BARS ARE OF 2.032 mm DIAMETER)

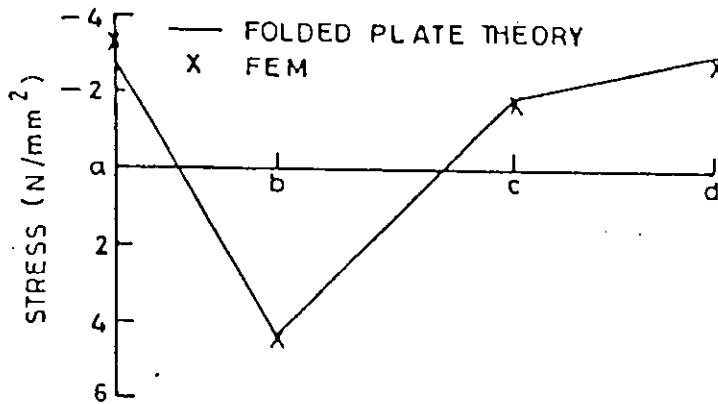
FIG. 3-23 - DETAILS OF FOLDED PLATES TESTED BY SCORDELIS AND GERASIMENKO (152)



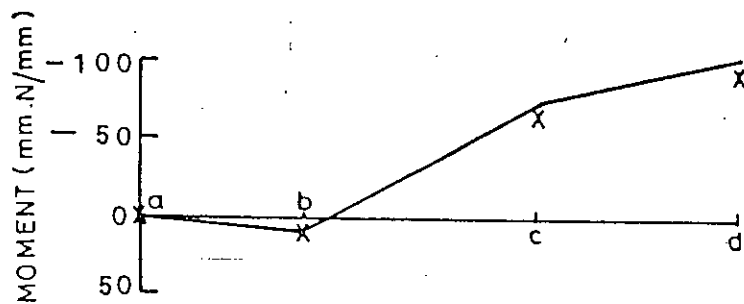
OVER ALL LENGTH=1778 , THICKNESS OF DIAPHRAGMS = 38.1

(All Dimensions in mm)

(a) Design Line Load and Basic Dimensions of Models



(b) Mid Span Longitudinal Stress (N/mm^2) Under Design Load (Elastic Analysis)



(c) Mid Span Transverse Moment ($mm.N/mm$) Under Design Load (Elastic Analysis)

S. 3.24 — ELASTIC ANALYSIS AT DESIGN LOAD FOR FOLDED PLATE 'A'

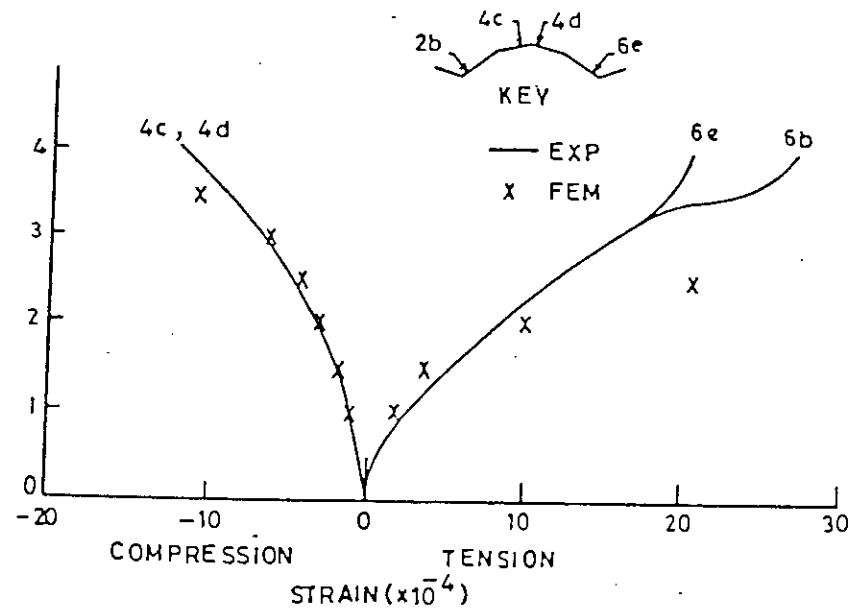
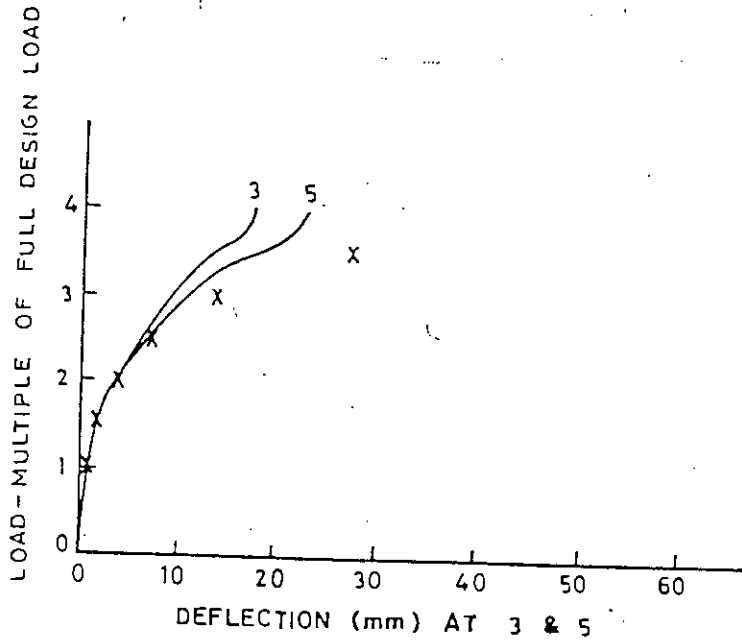
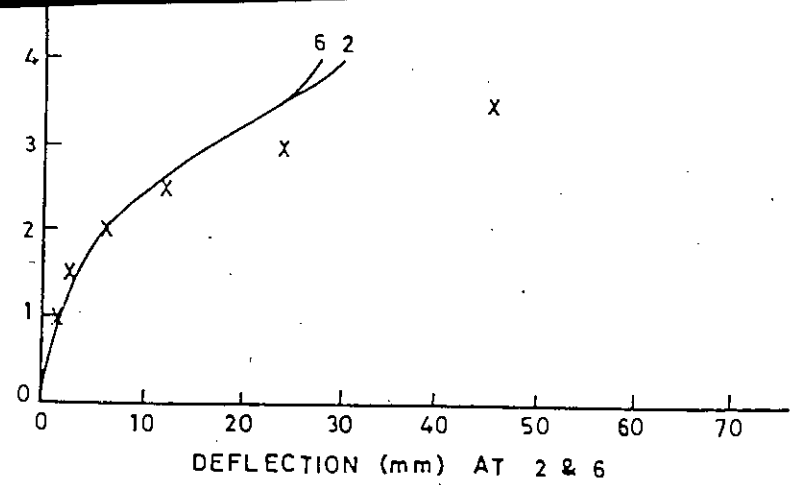
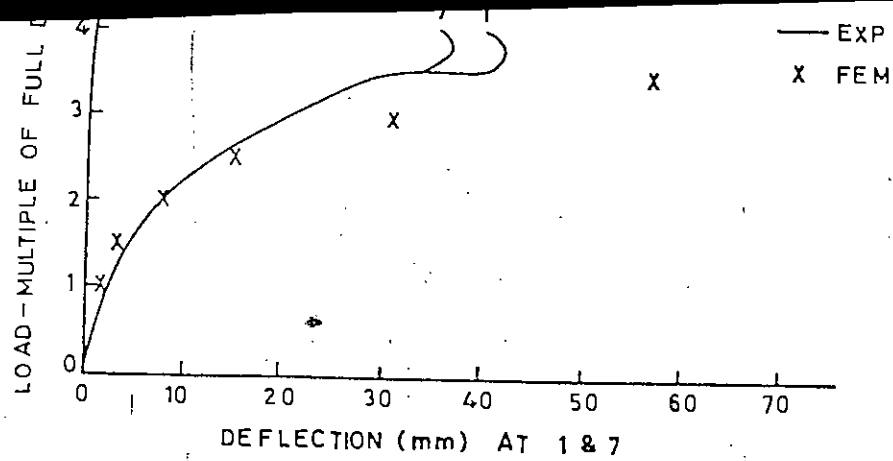


FIG. 3.25 -LOAD VS. MID SPAN LONGITUDINAL DEFLECTIONS OF MODEL 'A'

FIG. 3.26 -LOAD VS. MID SPAN LONGITUDINAL STRAINS IN STEEL OF MODEL 'A'

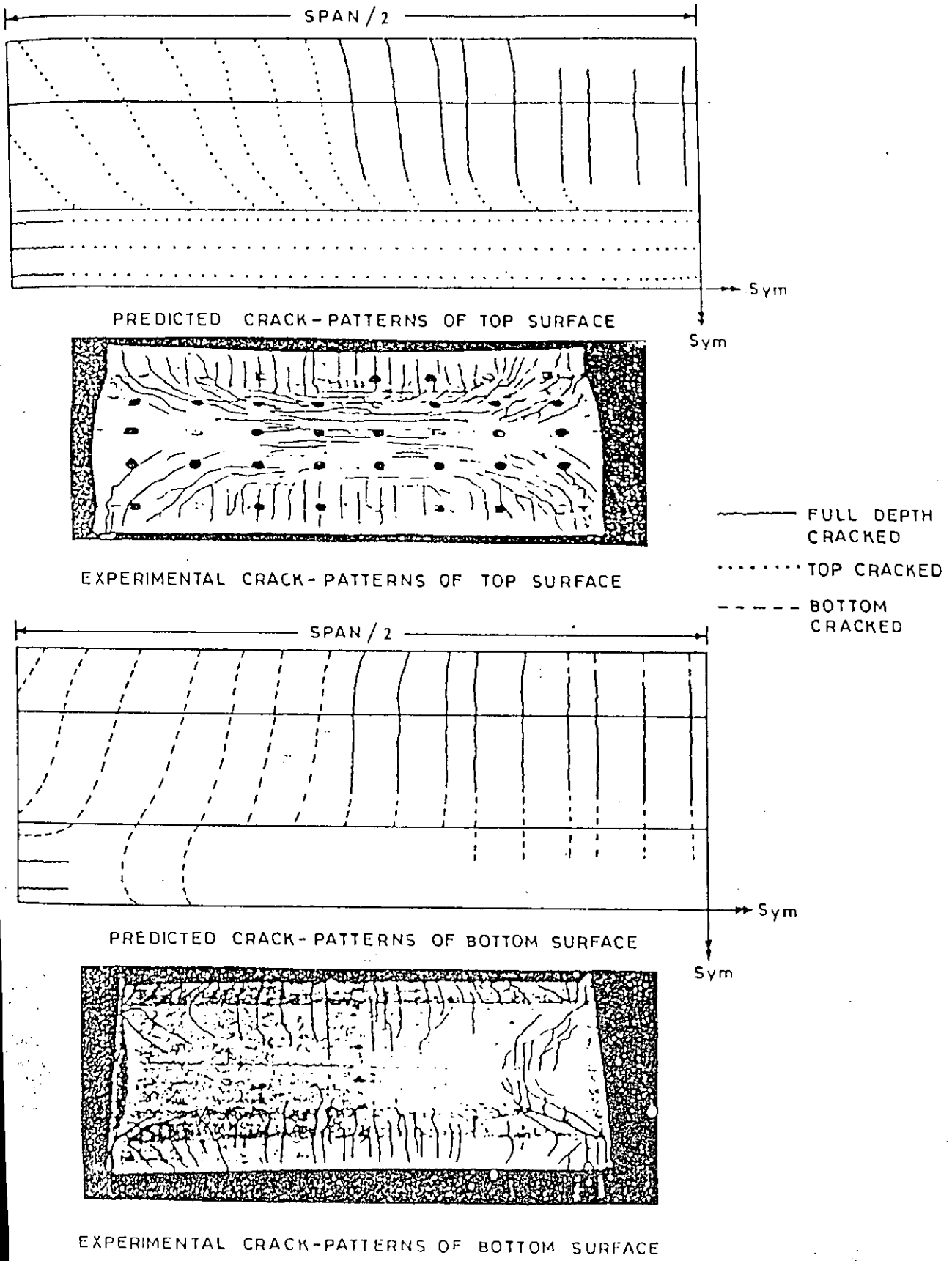


FIG. 3.27 - COMPARISON OF PREDICTED AND EXPERIMENTAL CRACK - PATTERNS OF MODEL 'A'

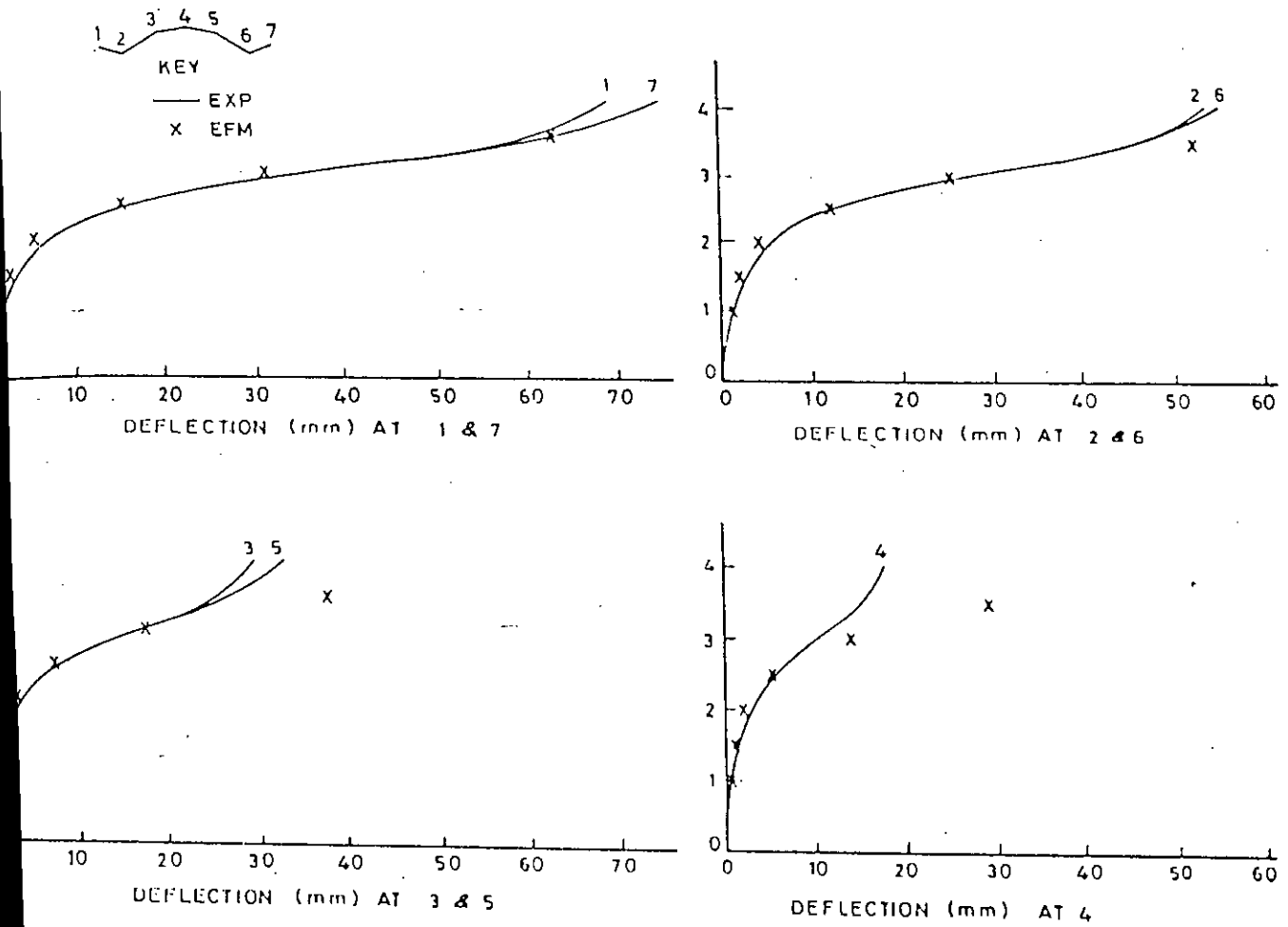


FIG.3.28 - LOAD VS. MID SPAN DEFLECTIONS OF MODEL 'B'

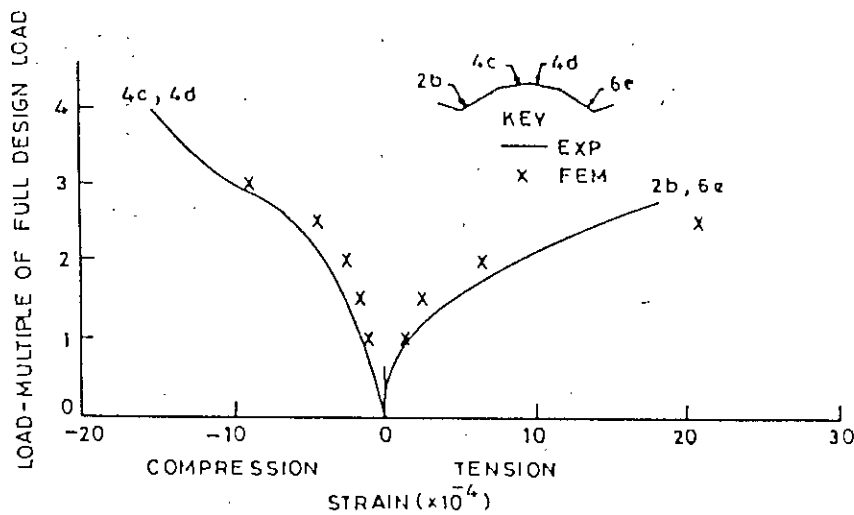
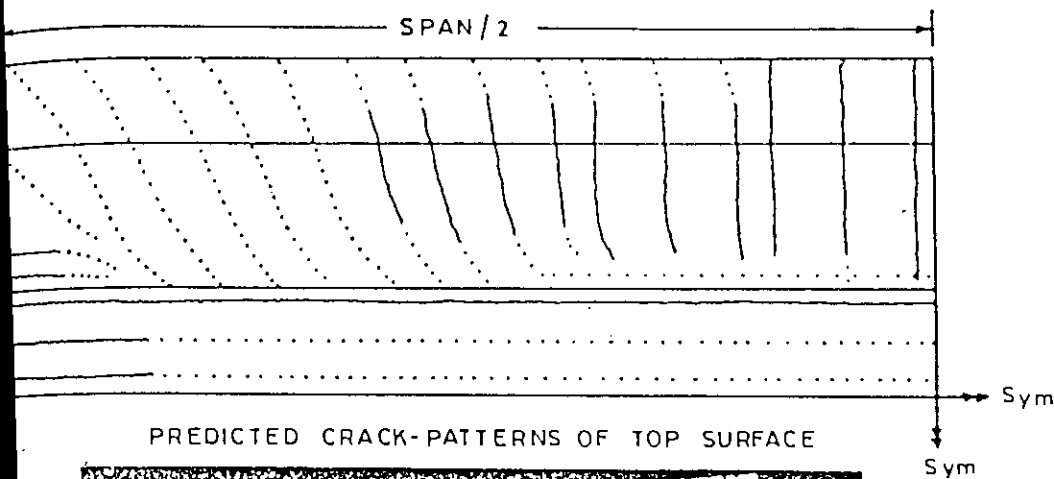
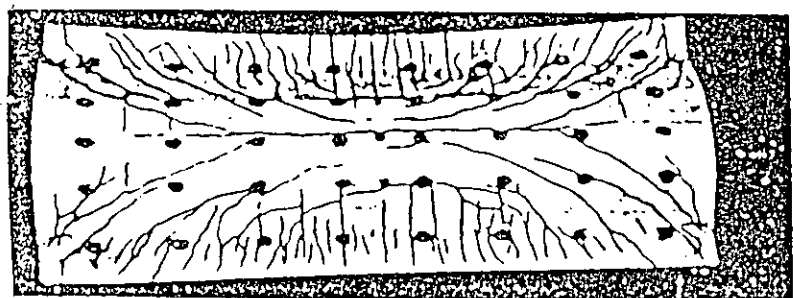


FIG. 3.29 - LOAD VS. MID SPAN LONGITUDINAL STRAINS IN STEEL OF MODEL 'B'

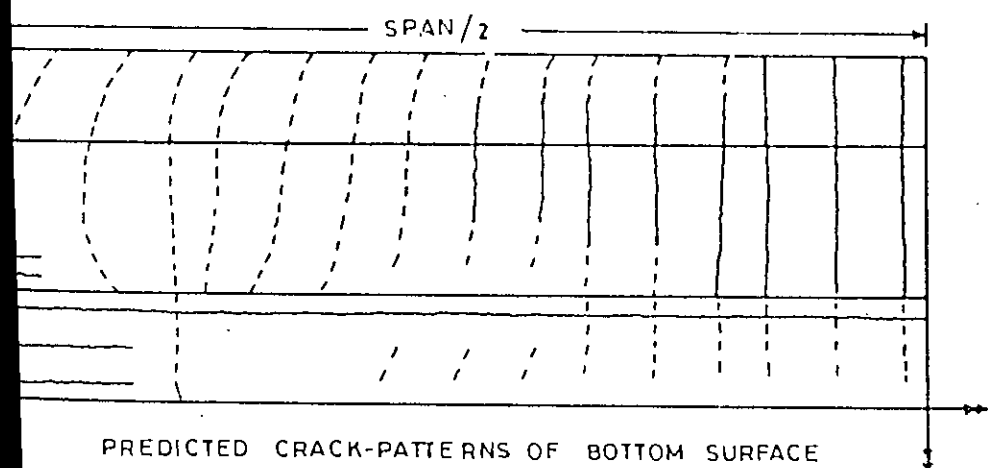


PREDICTED CRACK-PATTERNS OF TOP SURFACE

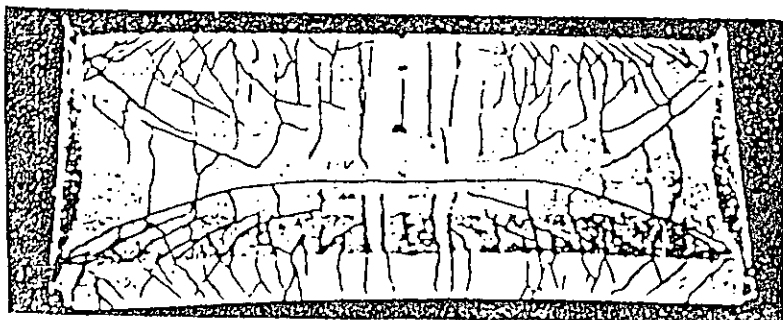


EXPERIMENTAL CRACK-PATTERNS OF TOP SURFACE

- FULL DEPTH CRACKED
- TOP CRACKED
- BOTTOM CRACKED



PREDICTED CRACK-PATTERNS OF BOTTOM SURFACE



EXPERIMENTAL CRACK-PATTERNS OF BOTTOM SURFACE

3.30 — COMPARISON OF PREDICTED AND EXPERIMENTAL CRACK-PATTERNS OF MODEL 'B'

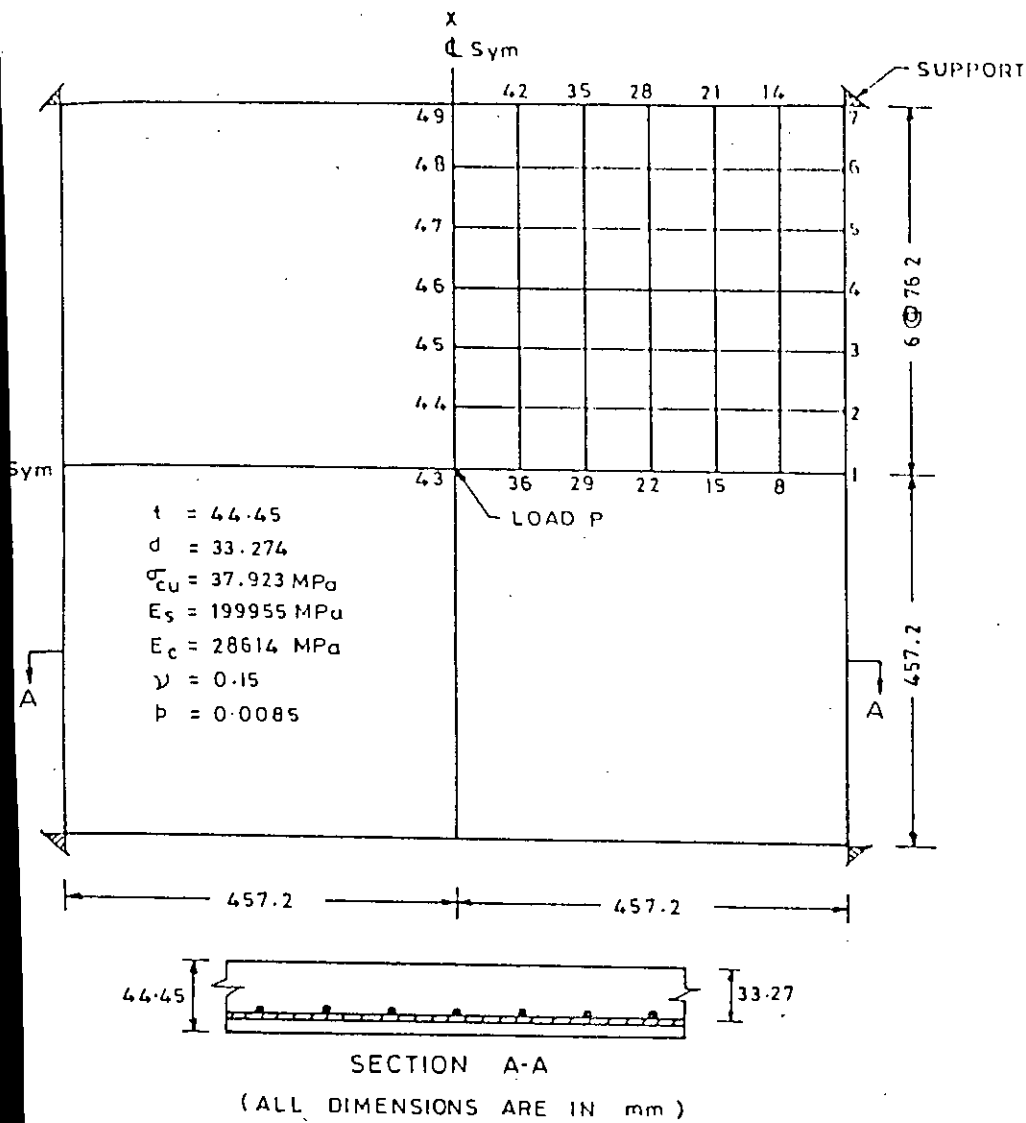
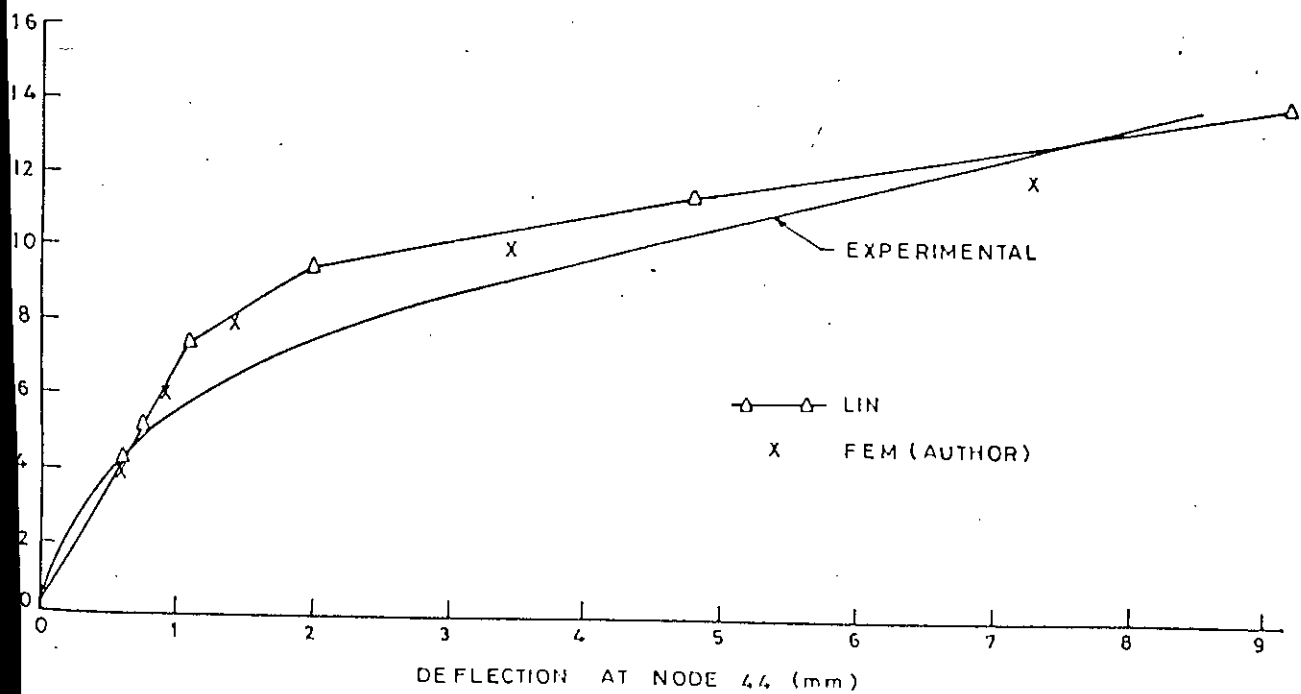
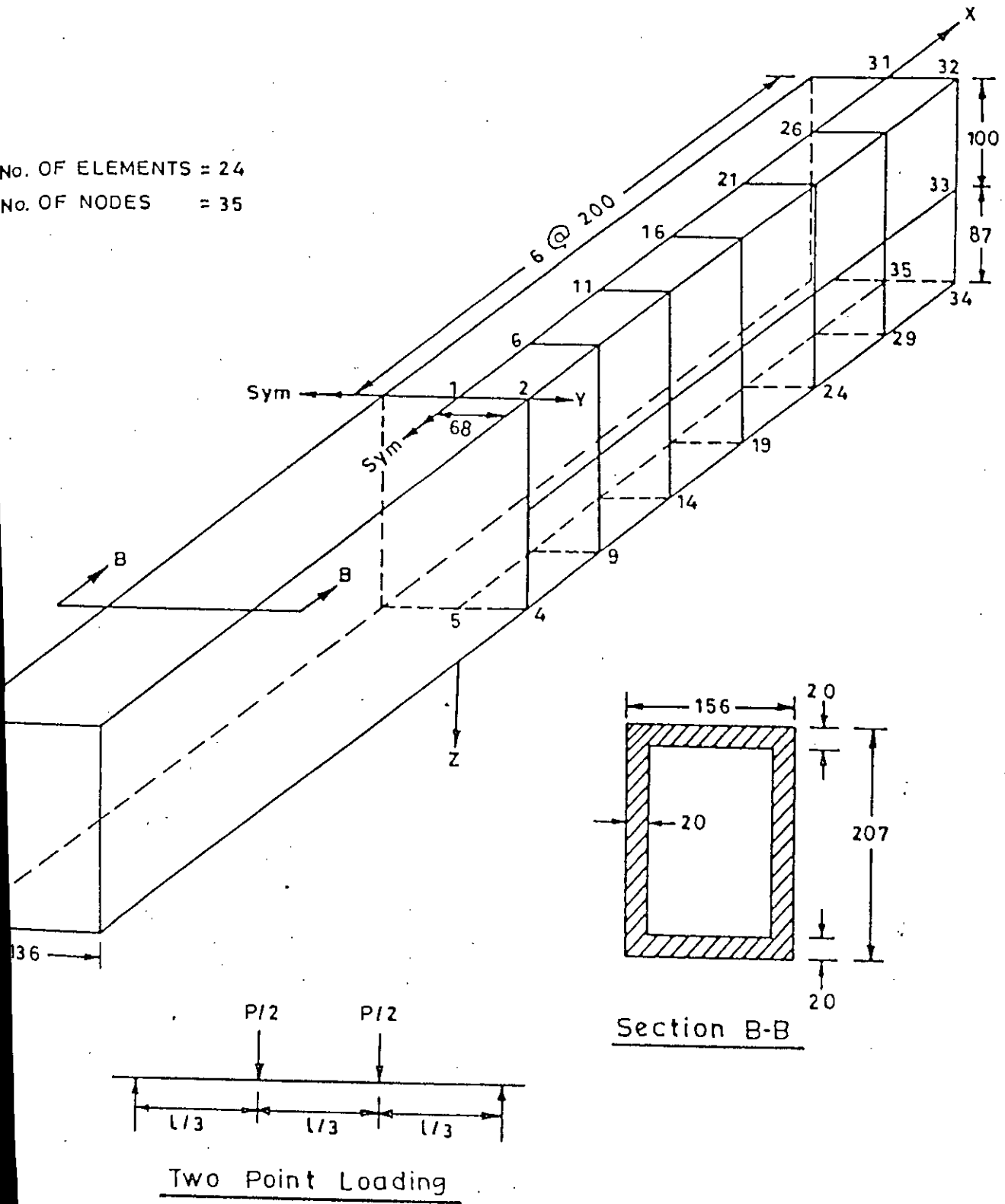


FIG. 3.31(a) - DISCRETIZATION OF McNEICE SLAB⁽¹⁵⁹⁾



G.3.31(b) - LOAD-DEFLECTION CURVE AT NODE 44 OF TWO WAY SLAB

No. OF ELEMENTS = 24
 No. OF NODES = 35



DISCRETIZATION OF FERROCEMENT BOX BEAM TESTED BY AL-SULAIMANI AND AHMAD⁽¹⁶¹⁾

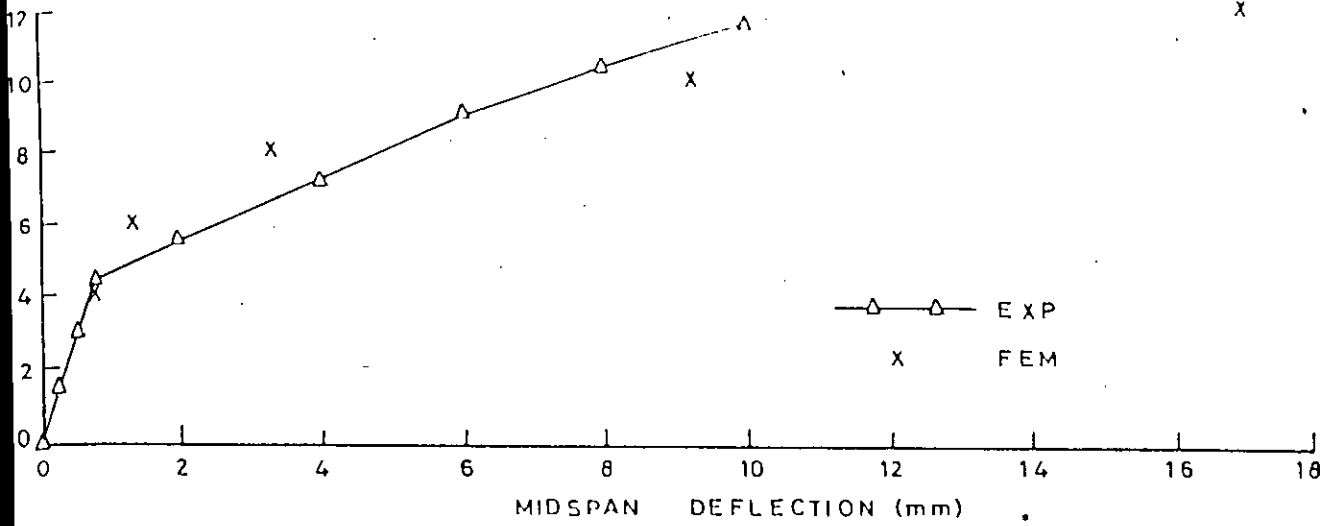


FIG. 3.33(a) -LOAD VS. MIDSPAN DEFLECTION FOR BEAM C-i-1

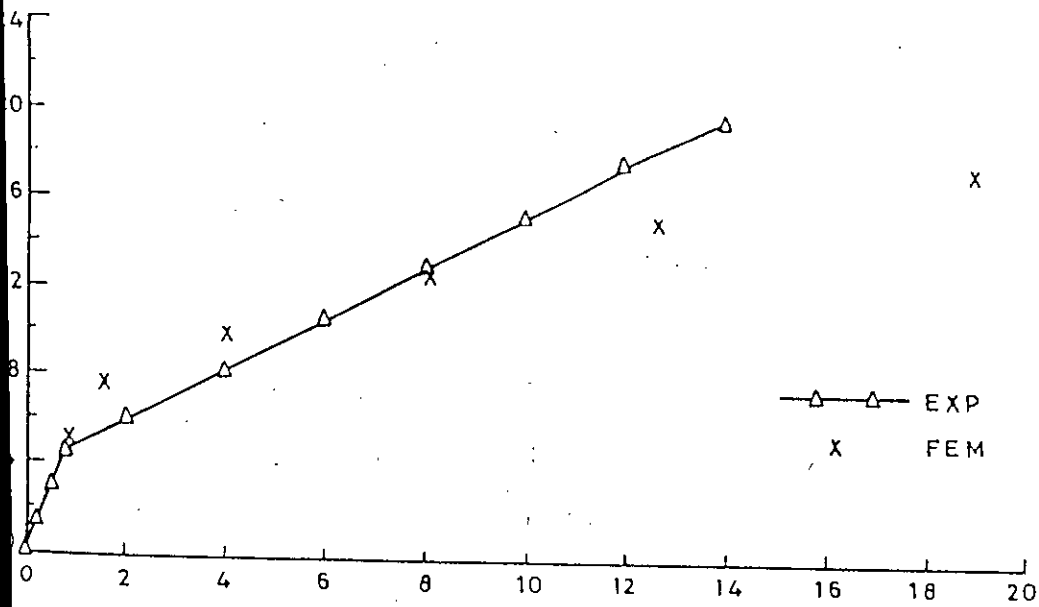


FIG. 3.33(b) -LOAD VS. MIDSPAN DEFLECTION FOR BEAM C-ii-1

CHAPTER IV

EXPERIMENTAL PROGRAMME

4.1 INTRODUCTION

In order to investigate the behaviour of ferrocement box girder elements, four single cell box girders, one double cell box girder and one composite single cell box girder having bottom flange and side webs of ferrocement and top flange of reinforced concrete were cast. All the box girders had the same span, depth and size of the cells. To eliminate the scale effect, a medium size room span of 4.58 m was chosen. A span to depth ratio of 20 was chosen for limiting the deflections under service loads as per IS 456⁽¹⁶²⁾. All the single cell box girders had two layers of wire mesh and skeletal steel reinforcement. The double cell box girder was obtained by joining two single cell box girders, as above, at the level of the top flange. The distance between the inner webs of the two cells was kept equal to the width of bottom flange. The bottom flange of the two cells was provided and extra third layer of wire mesh in the middle half portion. The composite single cell box girder had same wire mesh and skeletal steel reinforcement in the bottom flange and side webs as provided in the single cell ferrocement box girders. The thickness of the top reinforced concrete flange was kept 40 mm as compared to 25 mm in ferrocement box girders. The reinforced concrete flange had nominal skeletal steel reinforcement.

Two single cell box girders were tested under uniformly distributed load (udl) over the entire top flange. To study the behaviour under unsymmetrical loads, two single cell box girders were tested under udl over half the flange width and full span. The double cell box girder was investigated to study the behaviour of a combined unit under various combinations of loads applied on

one cell, both the cells and also between the two cells in the elastic stage. The double cell box girder was finally tested under monotonically increasing sustained loads of short durations applied over the entire top flange. The composite box girder was tested with a view to replace the top compression flange by reinforced concrete having nominal reinforcement. The webs and the bottom flange were kept of ferroceement as they have better tensile behaviour as compared to reinforced concrete. Adopting a compression flange of reinforced concrete results in economy because wire mesh reinforcement is several times costlier than ordinary reinforcing bars and also only nominal reinforcement is sufficient in the compression zone. The only drawback is that the weight of the reinforced concrete flange increases due to increase in thickness as compared to a ferroceement compression flange.

4.2 MATERIALS

Cement, sand, aggregate, wire mesh, skeletal steel bars, water, super-plasticizer and chromium trioxide were used in casting ferroceement box girders, reinforced concrete diaphragms and reinforced concrete top flange of the composite box girder. The specifications and properties of these materials are given below:

4.2.1 Cement

Ordinary portland cement conforming to Indian Standard Specifications I.S. :269-1976⁽⁷⁾ was used throughout the investigation. The cement was obtained in one lot and stored in an air tight silo. The physical test results of the cement used are given in Table 4.1.

4.2.2 Sand

Sand from Badarpur (near Delhi) was used for preparing the mortar and concrete. The grading and fineness modulus of the sand are given in Table 4.2.

TABLE 4.1
Physical Properties of Cement

Sl.No.	Characteristics	Result	Value specified by IS:269-1976 ⁽⁷⁾
1.	Fineness-determined by sieving the cement through IS-90 micron sieve	9.5%	10%
2.	Normal consistency	25%	-
3.	Setting time in minutes		
	a) Initial	85	30
	b) Final	190	600
4.	Compressive strength (MPa)		
	a) at 3 days	180	160
	b) at 7 days	240	220
5.	Specific gravity	3.15	-

TABLE 4.2
Siege Analysis and Physical Properties of Sand

IS Sieve Designation	Percentage weight retained on individual sieve
4.75 mm	nil
2.36 mm	4.59
1.18 mm	25.27
600 micron	22.97
300 micron	40.28
150 micron	6.13
Fineness Modulus	= 2.80
Specific gravity	= 2.54
Density (Loose), kN/m ³	= 12.86
Density (compacted), kN/m ³	= 13.97

Clumps of clay and other foreign matter were separated out from the sand.

4.2.3 Aggregate

10 mm size crushed stone aggregate was used in preparing the concrete mix. It was obtained by passing the crushed stone through 10 mm size sieve and taking out the material retained on 4.75 mm sieve.

4.2.4 Wire Mesh

Machine woven square galvanized steel wire mesh of opening size 6.35 mm x 6.35 mm with an average wire diameter of 0.80 mm was used. Wire mesh rolls of 0.92 m x 15.0 m were procured in one single lot. Tensile tests on wires taken out from different rolls were carried out on Monsanto tensometer (made in U.K.). The stress-strain curves showed a large variation. This was probably due to slippage of wire from the anchoring disc. Thus tests on wire mesh samples were carried out in a manner similar to the one reported by Balaguru et al.⁽⁶²⁾. In this case a 40 mm wide strip of mesh was embedded in a mortar pad at each end, leaving a free mesh length of 85 mm (Fig. 4.1). Each mortar pad was about 13 mm thick, 40 mm wide and 110 mm long. The mortar pads were provided extra layers of mesh - one above and one below leaving central 100 mm length of the test piece. For measuring strains, demec points were fixed on the mortar pads providing gauge length of 100 mm including embedded 7.5 mm length of wire mesh at each end. The effect of the embedded length of the wire mesh at each end is ignored in determining the modulus of elasticity of the wire mesh.

Tension tests on the specimens were carried out on an universal testing machine. 100 mm gauge length extensometer was used to measure the extension between the demec points. Load was applied in increments of 20 kg (196.2N). Photograph of the specimen and test setup is shown in Plate 4.1.

The average stress-strain curve obtained from six wire mesh specimens is shown in Fig. 4.3. The modulus of elasticity, proof stress corresponding to 0.2% proof strain and the ultimate tensile stress of the wire mesh are given in Table 4.3.

4.2.5 Skeletal Steel Bars

Skeletal steel bars of 5.91 mm and 3.23 mm diameter were used in longitudinal and transverse direction in casting the box girders. 5.91 mm diameter bars were also used as reinforcement for diaphragms. The mechanical properties of these bars are given in Table 4.3 and their stress-strain curves are shown in Fig. 4.3.

4.2.6 Water

Potable tap water was used for preparing mortar and concrete mixes and also for curing purposes.

4.2.7 Superplasticizer

Locally available superplasticizer containing synthetic sulphonated naphthaline/formaldehyde condensates was used to improve the workability of the mortar. As specified by the manufacturer, the superplasticizer had a specific gravity of 1.14 and pH value of 7.61. It did not contain chlorides and sulphates.

4.2.8 Chromium Trioxide

Chromium trioxide supplied in granular form for laboratory purposes was used to effectively reduce the hydrogen gas problem. The compound had instant solubility in water.

4.2.9 Cement-Sand Mortar and Concrete Mix

The mix proportion for the cement sand mortar was 1 : 2.5 by weight with a water cement ratio of 0.45. To improve the workability of mortar, a locally available superplasticizer (as described in section 4.2.7) equal to one percent by weight of cement was added to the mixing water. Chromium trioxide equal to 200 parts per million by weight of water was also added to the mixing water. The average compressive strength, direct tensile strength, modulus of rupture, modulus of elasticity and Poisson's ratio for the mortar are given in Table 4.4. The stress-strain curve for the mortar in uniaxial compression is shown in Fig. 4.4.

The concrete mix had cement, sand and 10 mm size aggregate in the ratio of 1 : 1.8 : 2.4 by weight. Water cement ratio was kept at 0.50. The average compressive strength, direct tensile strength, modulus of rupture, modulus of elasticity and Poisson's ratio for the concrete are given in Table 4.4. The stress-strain curve of the concrete in uniaxial compression is shown in Fig. 4.4.

4.3 CASTING OF BOX GIRDERS

For casting box girder elements, a brick masonry mould as shown in Fig. 4.5 was made. The mould was plastered from inside. The vertical sides of the mould were given a slight tapering (1 in 20) to facilitate easy lifting of the girder. The bottom corners were also made round. Plastered surface was given a smooth finish by applying rich cement water slurry with a steel trowel. The mould was cured for two weeks and then allowed to dry for about three weeks before the first girder was cast.

The casting of the girders was carried out in three stages. In the first stage, the bottom U-part of the girder consisting of side webs and bottom

TABLE 4.3
Strength Properties of Wire Mesh and Skeletal Steel Bars

S.No.	Particulars	Yield strength or 0.2% Proof stress (MPa)	Ultimate strength (MPa)	Modulus of Elasticity (MPa)
	Machine woven square GI mesh with opening size 6.35 mm x 6.35 mm and average wire diameter of 0.8 mm	440	520	146,200.0
	Plain mild steel bar of 5.91 mm diameter	440	605	200,000.0
	Plain mild steel bar of 3.23 mm diameter	380	490	210,000.0

TABLE 4.4
Strength Properties of Mortar and Concrete at 28 Days

Mortar

Cement : Sand : Water = 1 : 2.5 : 0.45
(by weight)

Average compressive strength of 100 mm size cubes = 21.70 MPa

Average direct tensile strength of briquettes having minimum cross-section of 100 mm x 100 mm = 2.30 MPa

Average modulus of rupture from 100 mm x 100 mm x 500 mm size prisms = 3.46 MPa

Average modulus of elasticity (from 75 mm x 150 mm cylinders) = 14000 MPa

Average Poisson's ratio = 0.20

Average cracking strain = tensile strength/modulus of elasticity = 164 microns

Average unit weight of ferrocement (from plates) = 25 kN/m³

Concrete

Cement : Sand : 10 mm size aggregate : Water (by weight) = 1 : 1.8 : 2.4 : 0.5

Average compressive strength of 100 mm size cubes = 24.7 MPa

Average direct tensile strength of briquettes having minimum cross-section of 100 mm x 100 mm = 3.30 MPa

Average modulus of rupture from 100 mm x 100 mm x 500 mm size prisms = 3.82 MPa

Average modulus of elasticity (from 150 mm x 300 mm size cylinders) = 21600 MPa

Average Poisson's ratio = 0.16

Average cracking strain = 153 microns

Average unit weight of reinforced concrete = 25 kN/m³

flange was cast. For casting the U-part, wire mesh pieces of required size were cut, straightened and given the mould shape. Utmost care was taken to remove any undulations in the mesh. The width of the wiremesh was insufficient to cover the entire perimeter of the mould. Hence an overlap of 100 mm was provided in the end portion of the bottom flange. The overlapped portion was properly tied at a large number of points along the length. Transverse skeletal steel bars of 3.23 mm diameter were tied to the mesh at 150 mm centre to centre. Two hooks made of 10 mm diameter plain mild steel bars (Fig. 4.6) passing through the bottom flange and side webs were also tied at 1.20 m from the two ends. Longitudinal skeletal steel bars of 5.91 mm diameter for the U-part were tied at this stage. Before tying the second layer of wiremesh, about 10 mm thick cover blocks made of rich cement-sand mortar and of about 25 mm x 25 mm size were placed at a large number of points. These were provided to maintain uniform distance between the two wire mesh layers. The second layer of wire mesh was then tied to the skeletal steel. The mesh overlap in the second layer was staggered. About 100-120 mm length of both the mesh layers and 3.23 mm diameter bars were projected beyond the mould top to ensure monolithicity at the top joints of the girder. Before casting the U-part, the mould was thoroughly cleaned and water was sprinkled. About 0.1 mm thick bitumen paper of one single length was placed along the mould surface. Wetting of the mould surface helped in sticking of the bitumen paper to it. Air pockets between the mould surface and the bitumen paper were removed by gently pressing the paper. First mortar layer of about 5-7 mm thickness was laid on the prepared surface. Reinforcement was now placed on the mortar layer and properly aligned. Further mortar was placed on the reinforcement and pressed through the meshes with a trowel. The mortar was compacted by a portable surface vibrator (Plate 4.2a). After compacting the bottom flange, mortar was pressed

through the web reinforcement. The webs were also compacted with the portable surface vibrator. The cast surface was given a smooth finish. The thicknesses of the bottom flange and side webs were maintained to 25 mm as far as possible all along the length. About 60-70 mm wide grooves at 150 mm from both the ends were made in the bottom flange for fixing diaphragms. At these grooves, the mortar was removed upto the level of top mesh layer. The mortar in the end 150 mm length of the webs was also removed upto this mesh layer.

In the second stage, the top flange of the girder was cast after 4-5 days of casting the bottom U-part. For casting of the top flange, temporary formwork consisting of brick pedestals and plane wooden planks as shown in Fig. 4.7 was made. The planks were levelled and the gaps between the planks and between the planks and the webs were filled with waste cotton fibers. The top of the cast webs was thoroughly chipped and cleaned. Chipping was done to obtain rough mortar surface which could provide better bond between the already cast webs and the top flange. Bitumen paper was spread over the planks. The projected inner wire mesh layers were bent inwards and the outer mesh layers outwards while the 3.23 mm bars were alternately bent inward and outward. About 5 mm thick and 25 mm x 25 mm size cover blocks made of rich cement-sand mortar were placed below the projected wire mesh layers and at various points on the formwork. The wire mesh and skeletal steel reinforcement of the top flange was then tied with the projecting web reinforcement. Again between the two layers of wire mesh of the top flange, 10 mm thick cover blocks were placed at sufficient points. The mortar was then placed over the reinforcement, pressed into the mesh layers by trowel and finally compacted with the portable surface vibrator (Plate 4.2b). Only 150 mm x 630 mm end portions between the webs were not cast. The required thickness of 25 mm was checked at the various points. The

top surface and longitudinal edges were given a smooth finish.

After two days of casting the top flange, the temporary formwork consisting of wooden planks and brick pedestals were removed from inside the cell. Inside of the cell was cleaned with a water jet. For curing the bottom and top flanges, mortar bunds were made and water stored. For curing the webs, water was regularly sprayed through a hose pipe. The girders were wet cured for 28 days. At the end of the curing period, the mortar bunds were broken and the water was removed. The grooves kept for the diaphragms were cleaned with a wire brush.

In the third stage, precast reinforced concrete diaphragms as shown in Fig. 4.8 were placed in the grooves and their projecting reinforcement was bent and tied with the reinforcement of the webs and top flange. The remaining portions of the webs and top flange beyond the end diaphragms were finally cast. The curing of the diaphragm region was done using wet gunny bags. The diaphragms had three centrally located holes of 40 mm diameter. The holes were provided to allow circulation of air through the cell and keeping the inside temperature as close as possible to the outside temperature. After about one week of providing the diaphragms, the girders were lifted from the mould using a 10 ton capacity chain operated overhead crane and placed on the supports.

Four single cell ferrocement box girders having reinforcement and sectional details as shown in Fig. 4.9a, were cast in the above manner.

The double cell box girder having reinforcement and sectional details as shown in Fig. 4.9b, was obtained by first casting two single cell box girders as above and then joining the two at the level of the top flange. In the bottom flange of the girders, an extra outermost third layer of wire mesh of 3.20 m

length was centrally provided. The two single cell box girders were cast in the above manner with the difference that both the wire mesh layers and transverse skeletal steel bars from one edge of the top flange were projecting beyond the cast portion. The girders were lifted from the mould and placed on the supports in such a way that the distance between the inner webs of the two girders was kept equal to the width of the bottom flange of each cell. After placing the girders in the required position, the mortar of the cast edges was chipped and the loose mortar particles removed. The two wire mesh layers and transverse skeletal steel bars of the girders were lapped. One additional longitudinal skeletal steel bar was also provided in the lapped portion. The overlaps of the top mesh layer, bottom mesh layer and transverse skeletal steel were staggered. The average width of the top joint was about 240 mm and the average overlap length of the top and bottom wire mesh layers was about 110 mm. The joint of the double cell box girder prior to casting is shown in Plate 4.3. For casting the joint, two wooden planks with adequate support from the bottom were placed below the joint. The gaps between the cast edges and the planks were closed with waste cotton fibers. The mortar was placed over the joint portion, pressed through the mesh reinforcement and finally compacted using a portable surface vibrator. The wooden planks were removed from the bottom next day and the soffit of the joint was given smooth finish. The precast reinforced concrete diaphragms as described above were also provided at the ends between the two cells. The joint portion was also cured for 28 days.

For casting the composite single cell box girder having bottom flange and side webs of ferrocement and top flange of reinforced concrete, depth of the mould was reduced from 200 mm to 185 mm. This was done to keep the overall depth of the composite box girder the same as for other box girders.

The bottom plaster of the mould was broken and fresh mortar layer laid to obtain the required mould depth. The corners of the mould were made round. The mould was cured for two weeks and then allowed to dry for about three weeks.

The bottom U-part of the composite box girder was cast in a manner described above. For casting the top reinforced concrete flange of 40 mm thickness, the reinforcement of the top flange was tied and placed in position while the mesh and skeletal steel reinforcement of the webs was kept vertical. About 15 mm thick mortar cover blocks were placed below the reinforcement. The concrete mix was poured and compacted upto the level of skeletal steel reinforcement. The projecting wire mesh layers and skeletal steel of the webs were then bent inward and outward and tied to the flange reinforcement. It was ensured that the mesh did not remain free. The balance depth of the top flange was cast and compacted subsequently. Fixing of the diaphragms etc. was done as described above. The reinforcement and sectional details of the composite box girder are shown in Fig. 4.9c.

The casting of the bottom U-part/top flange of the girders was completed in one single operation. In each casting six 100 mm size cubes, six 75 mm x 150 mm size cylinders, three briquettes of 100 mm x 100 mm neck cross-section and three 100 mm x 100 mm x 500 mm size prisms were cast to determine the compressive strength, modulus of elasticity, Poisson's ratio, direct tensile strength and modulus of rupture of the mortar. For concrete instead of 75 mm x 150 mm size cylinders, 150 mm x 300 mm size cylinders were cast to determine the modulus of elasticity and Poisson's ratio.

4.4 TESTING ARRANGEMENT

To achieve simply supported end conditions, supports made of mild steel plates with roller type arrangement were fabricated. Structural details of the

two supports are shown in Fig. 4.2. The support marked 'A' consisted of a 28 mm diameter mild steel rod centrally welded to the bottom plate. The top grooved plate provided free rotation about the rod. This arrangement provided fixity to the reaction but free rotation to the test specimen. Support marked 'B' had two 8 mm diameter rods welded to the bottom plate at a distance of 25 mm from the plate edges. This provided a central 100 mm distance for movement of the 28 mm dia rod. The top grooved plate rested on the rod. This support provided translation to the reaction as well as free rotation to the test specimen. Thus simply supported end conditions were achieved by these supports. The mild steel rods and the grooves were thoroughly lubricated before testing each box girder.

After placing the box girder on the simple supports, the layout for the demec points was marked on the edges of top flange and along the depth of the web in the central half span on both sides of the girder. These demec points were marked to obtain strains at mid span, ± 203.2 mm, ± 406.4 , ± 609.6 mm, ± 812.8 mm and ± 1145.0 mm distance on both sides of the mid span. Along the girder depth, the demec points were marked at 5 mm, 20 mm, 100 mm, 150 mm and 200 mm from the extreme edge of the top flange for ferrocement box girders and at 5 mm, 35 mm, 100 mm, 150 mm and 200 mm for the composite box girders. The demec points were obtained by fixing 8 mm diameter and 3 mm thick brass studs with a punch mark at the centre. The brass studs were fixed to the cast surface with the help of araldite. The strain between the demec points was measured with the help of 203.2 mm gauge length Huggenberger deformeter of 0.00254 mm least count.

For measuring strains on the top surface of the top flange and bottom surface of the bottom flange at the mid and quarter span sections, electrical

resistance strain gauges were used. The bakelite based electrical resistance strain gauges of gauge length 20 mm, resistance 120 ohms and gauges factor 2.0 ± 0.02 were used. All the strain gauges were from one single lot. For fixing the strain gauges, the layout was marked. The mortar/concrete surface was cleaned with emery paper and the fine dust particles were removed with acetone. The strain gauges were also cleaned with acetone and pasted on the mortar/concrete surface with araldite. The strain gauges were connected to the switching unit and strain indicator.

After fixing the demec points and strain gauges, the webs, bottom flange and edges of the top flange were given a coat of white-wash. This was done for ease in detecting the cracks and finally marking them on the girder surface.

The deflections at various points along the span were measured with dial gauges. The crack widths at various load levels were measured with the help of a crack measuring instrument having a least count of 0.02 mm.

The reaction below one of the supports was measured for the single cell box girders with the help of two 5 ton capacity load cells. The strain from the load cells was measured with a SR-4 Strain Indicator. The load cells and SR-4 strain indicator were calibrated on a 10 ton capacity universal testing machine. The general arrangement of the simply supported box girder is shown in Fig. 4.10.

4.5 TESTING OF GIRDERS

The girders were tested under uniformly distributed load applied over the top flange. Uniformly distributed load was applied in the form of brick layers. The strain gauges fixed on the top surface of the compression flange

were completely sealed by pasting a thick paper over them. This was done to protect them from brick dust. At the location of the strain gauges, bricks were cut to appropriate sizes in the first two layers. The strain gauges were also protected from any direct contact with the bricks. Placing of each brick layer was started from the two ends simultaneously and progressed towards the centre. Bricks in the subsequent layers were placed one on top of the other to avoid any arching action. Unloading of the brick layers was started from the centre and progressed towards the two ends simultaneously. Same lot of bricks was used for testing box girders.

To determine the unit weight of bricks, ten samples each containing twenty bricks were weighed and the average was taken for determining the load due to each brick layer.

The testing programme for various girders is as follows :

- (1) Two single cell box girders marked G-1 and G-2 were tested under udl over the entire top flange (Fig. 4.11i).
- (2) Two single cell box girders marked G-3 and G-4 were tested under udl over half flange width and full span (Fig. 4.11ii).
- (3) The double cell box girder marked G-5 was loaded and unloaded under following load conditions in the uncracked stage :
 - (i) three brick layers (3.08 kN/m^2) over half width of the top flange and full span (Fig. 4.11iii).
 - (ii) six brick layers (5.43 kN/m^2) from one free end of cantilever to the centre of the box cell (Fig. 4.11iv).
 - (iii) five brick layers (4.53 kN/m^2) from both free ends of the cantilever to the centres of the two box cells (Fig. 4.11v).

- (iv) four brick layers (4.51 kN/m^2) on the two cells (Fig. 4.11vi).
- (v) seven brick layers (7.89 kN/m^2) in the central part of the top flange i.e. spanning between the inner webs of the two cells (Fig. 4.11vii).

After a rest of about one month, the girder was tested under monotonically increasing sustained loads of short durations applied over the entire top flange (Fig. 4.11viii). Each brick layer was allowed to remain on the girder for a few days till the deflections stabilized. The girder was loaded upto six brick layers (6.16 kN/m^2) and then unloaded.

- (4) One composite single cell box girder marked 'G-6' having bottom flange and side webs of ferrocement and top flange of reinforced concrete was tested under udl over the entire top flange (Fig. 4.11i) upto six brick layers (6.19 kN/m^2) and then unloaded. After a rest of about three months, the girder was again subjected to sustained loads of short durations in a manner similar to the double cell box girder.

Deflections and strains were measured at the selected points before the start of loading, after the application of each brick layer and also after the unloading of each brick layer. After the application of each brick layer, the bottom flange and side webs of the girders were checked for cracking if any. After detecting the cracks, crack widths of only some prominent cracks (i.e. having maximum crackwidth) were measured. The position of the cracks were marked on the girder surface.

4.6 PRESENTATION OF TEST RESULTS

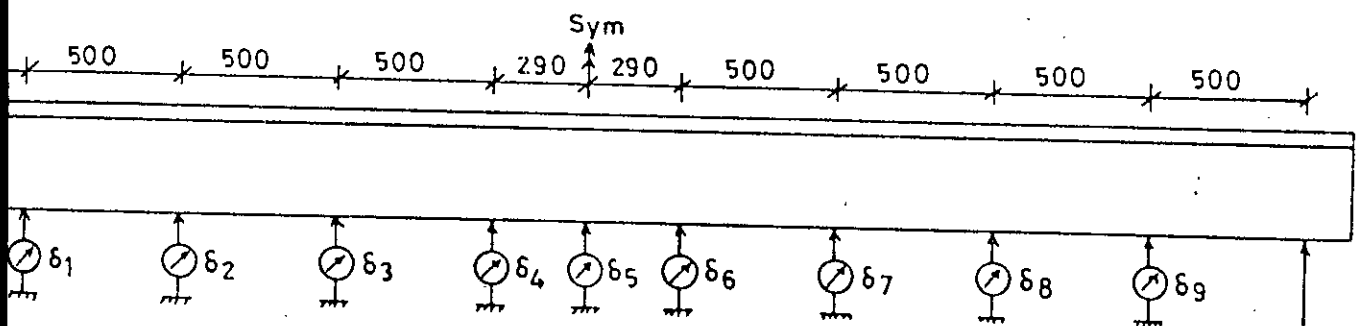
The three different types of box girders casted above namely the single cell (marked G-1 to G-4), the double cell (marked G-5) and the composite box girder (marked G-6) were tested for the different loading conditions as described

above. The load-deflection and the load-strain characteristics were observed under both symmetrically and unsymmetrically applied loads. The details of the observed test results are given one by one for the three cases.

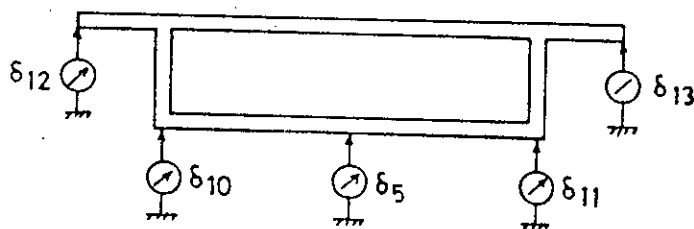
4.6.1 Single Cell Box Girders

4.6.1.1 Girders subjected to udl over the entire top flange

Table 4.5 : Average deflections (mm) at various points along the span of the box girder



DEFLECTIONS ALONG THE CENTRE LINE OF BOTTOM FLANGE



DEFLECTIONS ACROSS THE CROSS-SECTION AT MID SPAN
LAYOUT OF DEFLECTIONS FOR GIRDERS G1 AND G2

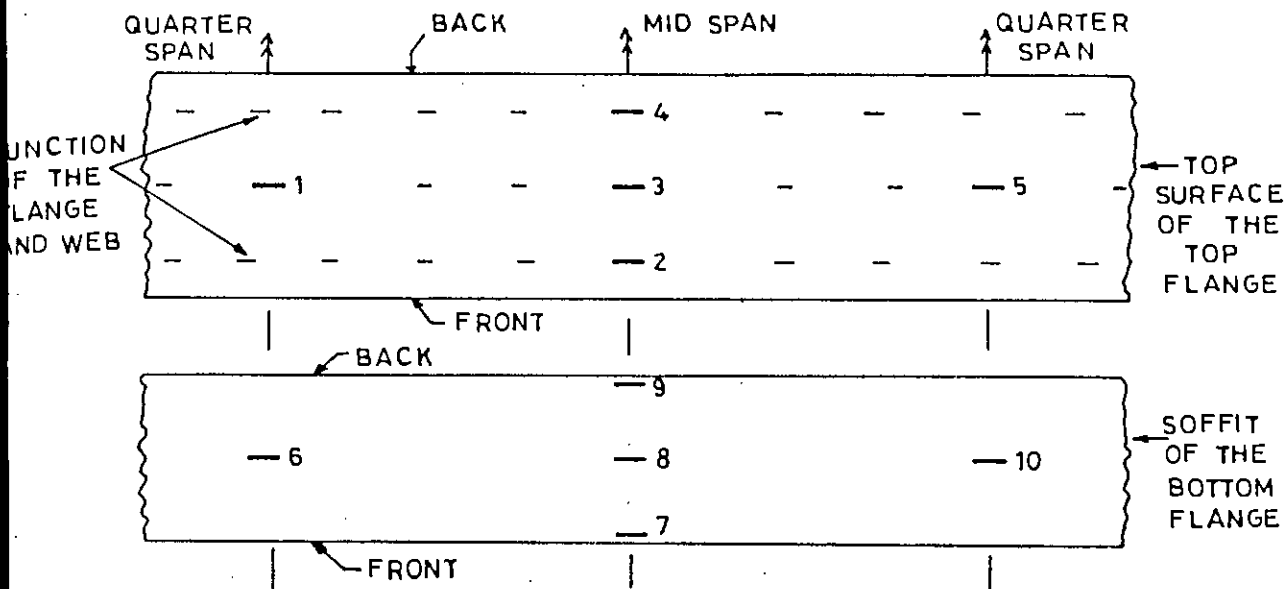
Girder G-1

Deflection + Load (kN) ↓	δ_1, δ_9	δ_2, δ_8	δ_3, δ_7	δ_4, δ_6	$\delta_{10}, \delta_5, \delta_{11}$	δ_{12}, δ_{13}
4.438	0.46	0.84	1.13	1.30	1.36	1.37
8.876	0.99	1.95	2.30	2.59	2.75	2.81
13.314	1.85	2.95	4.18	4.42	4.59	4.82
17.752	3.64	5.43	7.22	9.05	9.20	9.38
22.190	5.08	8.63	11.75	13.82	14.16	14.19
26.628	6.74	12.09	16.46	19.20	19.61	19.56
31.066	8.49	15.36	20.85	23.95	24.43	23.97

Girder G-2

Deflection + Load (kN) ↓	δ_1, δ_9	δ_2, δ_8	δ_3, δ_7	δ_4, δ_6	$\delta_{10}, \delta_5, \delta_{11}$	δ_{12}, δ_{13}
4.438	0.54	0.82	1.01	1.22	1.33	1.31
8.876	1.05	1.66	1.98	2.32	2.39	2.35
13.314	1.98	3.26	4.18	4.80	4.93	4.88
17.752	4.12	6.53	9.35	11.11	11.24	11.30
22.190	5.85	9.60	13.50	15.88	16.04	16.02
26.628	8.05	13.56	18.92	21.82	22.20	22.03
31.066	10.61	18.21	24.72	28.44	29.07	28.72

Table 4.6 : Average strains ($\times 10^{-6}$) on the top surface of the top flange and the soffit of the bottom flange



LAYOUT OF STRAIN GAUGES FOR GIRDERS G1, G2, G3, G4 & G6

Girder G-1

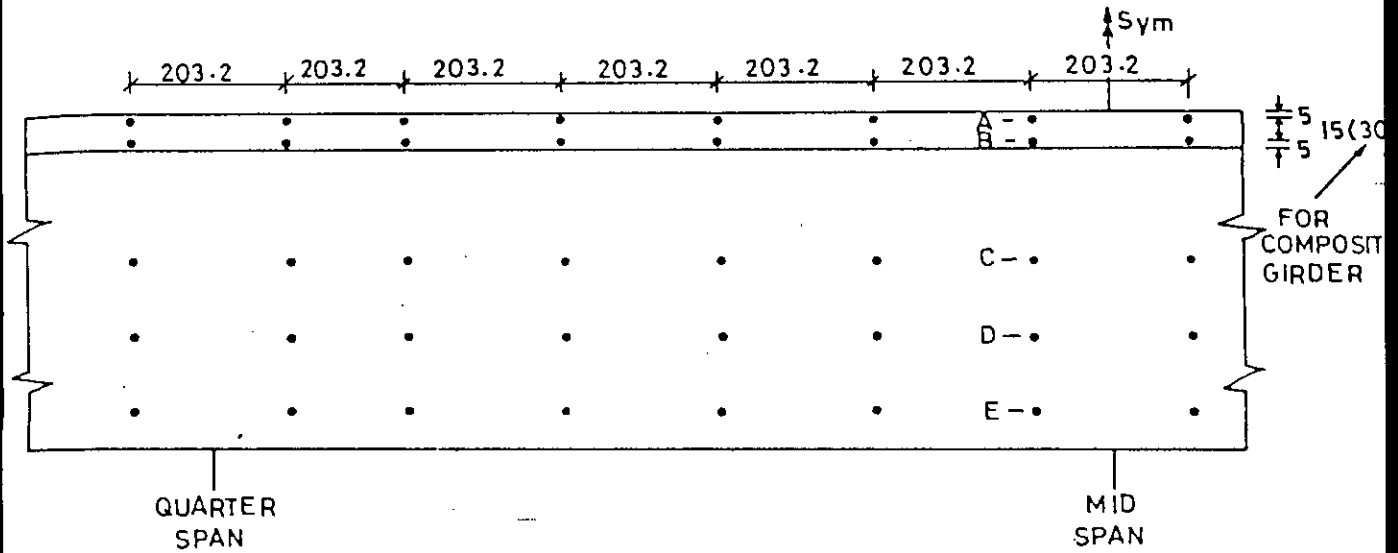
Load (kN) +	4.438	8.876	13.134	17.752	22.190	26.628	31.066
Gauge No. ↓							
1,5	-28	-58	-87	-113	-155	-210	-269
2,4	-37	-83	-131	-178	-237	-346	-480
3	-32	-66	-121	-175	-225	-323	-445
6,10	31	67	108	-	-	-	-
7,9	49	104	-	-	-	-	-
8	44	98	-	-	-	-	-

Girder G-2

1,5	-32	-68	-100	-137	-181	-231	-306
2,4	-45	-92	-145	-208	-286	-395	-562
3	-34	-79	-127	-188	-264	-362	-490
6,10	29	60	110	-	-	-	-
7,9	52	110	-	-	-	-	-
8	47	104	-	-	-	-	-

Note : Negative sign indicates compressive strain.

Table 4.7 : Average longitudinal strains ($\times 10^{-6}$) across the girder depth at various sections



DEMEC POINTS ON THE CANTILIVER FLANGE AND THE WEBS FOR GIRDERS G1 TO G6

Girder G-1

Section	Strain at Level	Load (kN)					
		8.876	13.314	17.752	22.190	26.628	31.066
At mid span	A	-85	-147	-181	-238	-328	-450
	B	-63	-112	-125	-134	-159	-163
	C	13	125	244	500	938	1250
	D	75	275	450	875	1338	1738
	E	113	431	713	1238	1806	2313
At ± 406.4 mm from mid span	A	-75	-125	-163	-213	-294	-388
	B	-56	-88	-100	-125	-150	-150
	C	13	88	175	400	725	1025
	D	56	163	344	688	1088	1500
	E	94	338	513	975	1463	1988
At quarter span	A	-56	-88	-100	-144	-219	-256
	B	-38	-63	-75	-109	-125	-131
	C	0	13	25	125	325	538
	D	38	50	100	269	550	963
	E	63	113	181	400	756	1350

Girder G-2

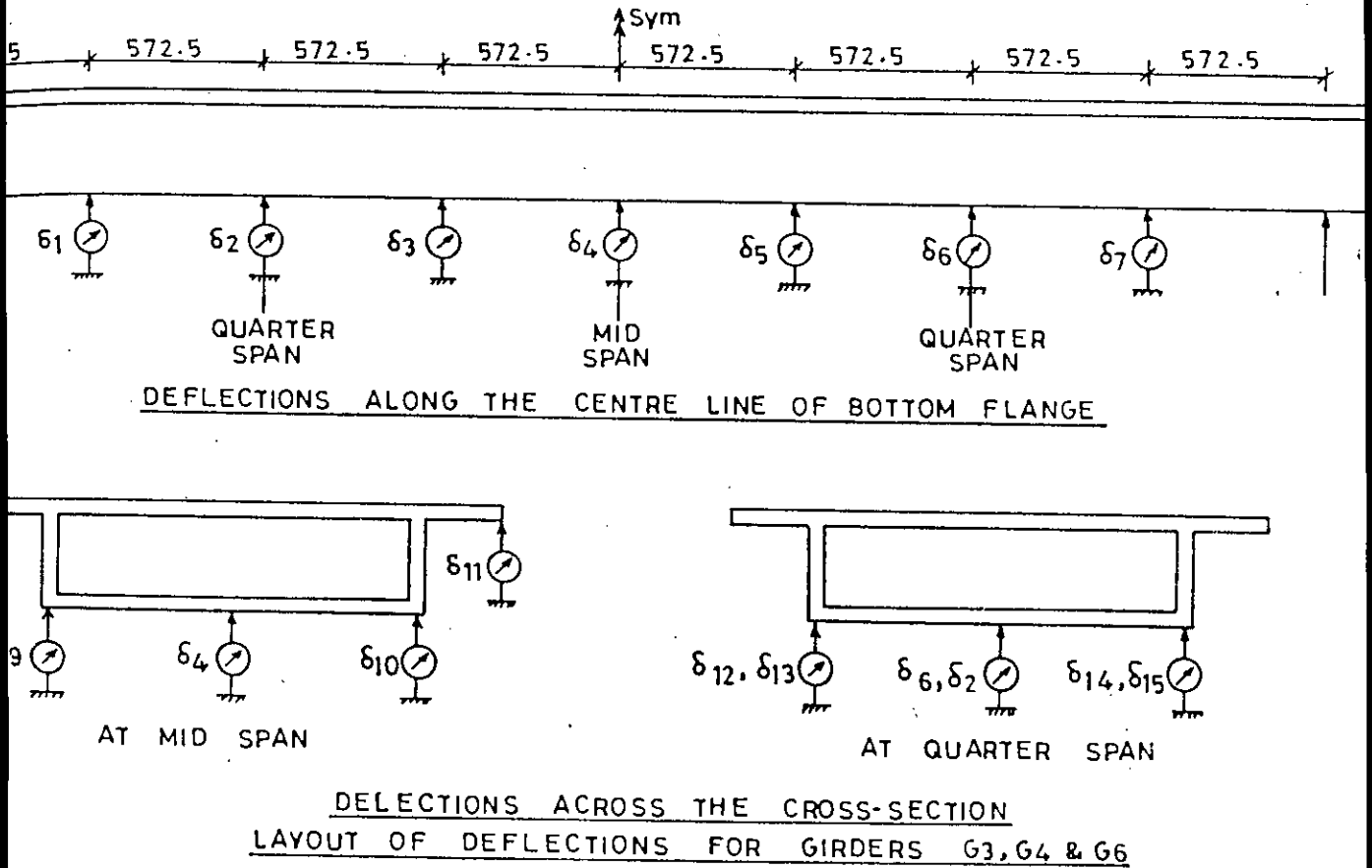
Section	Strain at Level	Load (kN)					
		8.876	13.314	17.752	22.190	26.628	31.066
At mid span	A	-100	-134	-206	-256	-363	-513
	B	-75	-100	-131	-147	-172	-188
	C	19	113	306	550	1025	1488
	D	88	200	550	925	1475	2225
	E	122	335	875	1406	2000	3163
At ± 406.4 mm from mid span	A	-75	-125	-175	-225	-313	-438
	B	-56	-88	-106	-131	-150	-169
	C	13	81	213	413	750	1088
	D	63	150	438	750	1150	1825
	E	100	275	688	1088	1625	2588
At quarter span	A	-63	-100	-125	-163	-231	-281
	B	-44	-75	-75	-125	-134	-150
	C	0	13	31	175	388	600
	D	38	63	125	331	650	1075
	E	75	125	225	513	919	1538

Table 4.8 : Average and maximum crack widths at various load levels for Girders G-1 and G-2

Load (kN)	Average Crack Width, ω_{avg} (mm)		Max. Crack Width ω_{max} (mm)		$\omega_{max}/\omega_{avg}$	
	girder G-1	girder G-2	girder G-1	girder G-2	girder G-1	girder G-2
13.314	0.06	0.06	0.10	0.10	1.67	1.67
17.752	0.09	0.11	0.15	0.20	1.67	1.82
22.190	0.14	0.17	0.25	0.30	1.79	1.77
26.628	0.20	0.26	0.40	0.50	2.00	1.92
31.066	0.35	0.41	0.60	0.80	1.71	1.95

4.6.1.2 Girders subjected to udl over half flange width and full span

Table 4.9 : Average deflections under udl over half flange width and full span



Girder G-3

(mm) \rightarrow (kN) \downarrow	δ_1, δ_7	δ_{12}, δ_{13}	δ_2, δ_6	δ_{14}, δ_{15}	δ_3, δ_5	δ_8	δ_9	δ_4	δ_{10}	δ_{11}
19	0.23	0.24	0.36	0.41	0.40	0.30	0.34	0.46	0.55	0.66
88	0.44	0.48	0.71	0.86	0.81	0.58	0.66	0.89	1.10	1.33
57	0.68	0.73	1.07	1.32	1.24	0.90	0.99	1.32	1.71	1.99
76	0.88	0.97	1.44	1.74	1.66	1.18	1.33	1.77	2.27	2.66
95	1.11	1.22	1.81	2.16	2.09	1.46	1.67	2.24	2.78	3.34
14	1.40	1.53	2.25	2.56	2.60	1.91	2.12	2.74	3.25	3.94
33	2.11	2.93	3.46	4.18	3.72	3.20	3.52	4.18	4.76	5.47
52	3.15	4.48	5.24	6.00	6.22	5.74	6.24	7.06	8.04	8.76
71	4.74	7.25	8.31	9.25	10.36	9.80	10.21	11.44	12.63	12.38

Girder G-4

9	0.24	0.32	0.40	0.51	0.50	0.40	0.43	0.58	0.74	0.80
8	0.46	0.63	0.77	1.02	0.98	0.74	0.81	1.13	1.36	1.52
7	0.66	0.88	1.14	1.52	1.41	1.12	1.20	1.62	2.05	2.29
6	0.88	1.17	1.51	2.16	1.93	1.29	1.59	2.18	2.97	3.20
5	1.10	1.48	1.89	2.65	2.42	1.73	1.98	2.73	3.58	4.05
4	1.76	2.46	3.05	3.50	3.39	2.45	2.87	3.76	4.75	5.28
3	2.44	3.75	4.36	5.04	5.38	4.54	5.06	5.93	7.04	7.65
2	3.21	5.12	5.73	6.50	6.66	5.81	6.32	7.37	8.53	9.14
1	4.20	6.90	7.77	8.65	9.77	8.86	9.52	10.70	11.53	12.30

Table 4.10 : Average strains ($\times 10^{-6}$) on the top surface of the top flange and the soffit of the bottom flange

Girder G-4								
Load (kN) +	4.438	6.657	8.876	11.095	13.314	15.533	17.752	19.971
Gauge No. ↓								
1,5	-34	-50	-65	-88	-109	-132	-161	-198
2	-38	-55	-74	-92	-127	-171	-214	-267
3	-41	-60	-78	-102	-131	-162	-218	-283
4	-48	-69	-94	-124	-158	-195	-256	-340
6,10	34	50	68	89	-	-	-	-
7	40	70	93	129	-	-	-	-
8	45	65	91	115	-	-	-	-
9	46	73	104	-	-	-	-	-

Table 4.11: Average longitudinal strains ($\times 10^{-6}$) across the girder depth on the loaded side

		Girder G-3						
Section	Strain at level	Load (kN)						
		6.657	8.876	11.095	13.314	15.533	17.752	19.971
At mid span	A	-63	-88	-113	-138	-150	-200	-281
	B	-38	-63	-88	-100	-100	-125	-150
	C	0	13	38	63	181	231	625
	D	38	75	100	150	294	413	1000
	E	63	109	169	213	419	769	1400
At ± 406.4 mm from mid span	A	-50	-81	-100	-125	-138	-175	-244
	B	-25	-56	-75	-85	-88	-113	-138
	C	0	6	13	38	100	163	475
	D	31	63	81	125	225	375	800
	E	56	100	138	194	338	613	1175
At quarter span	A	-50	-75	-85	-100	-109	-138	-194
	B	-25	-50	-63	-75	-85	-113	-135
	C	0	6	0	19	38	75	244
	D	25	50	63	75	125	194	475
	E	50	85	109	131	194	356	731
		Girder G-4						
Section	Strain at level	Load (kN)						
		6.657	8.876	11.095	13.314	15.533	17.752	19.971
At mid span	A	-75	-100	-122	-150	-172	-225	-256
	B	-50	-63	-88	-113	-113	-131	-138
	C	13	25	63	88	256	269	563
	D	50	88	150	206	425	525	900
	E	88	144	244	381	638	950	1263
At ± 406.4 mm from mid span	A	-69	-94	-113	-138	-150	-194	-225
	B	-50	-75	-75	-100	-100	-125	-125
	C	0	12	50	75	188	200	413
	D	50	75	125	188	350	425	725
	E	75	125	206	338	525	775	1050

(Contd.....)

Girder G-4 (Contd.....)

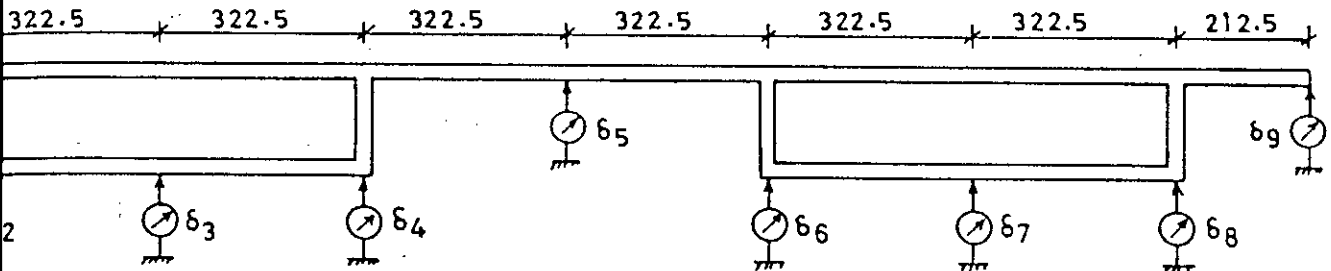
Section	Strain at level	Load (kN)						
		6.657	8.876	11.095	13.134	15.533	17.752	19.971
At quarter span	A	-63	-88	-100	-113	-122	-150	-172
	B	-38	-63	-75	-75	-100	-106	-122
	C	0	6	13	38	63	113	206
	D	38	63	75	106	159	238	391
	E	88	113	134	181	256	413	600

Table 4.12 : Average and maximum crack widths at various load levels

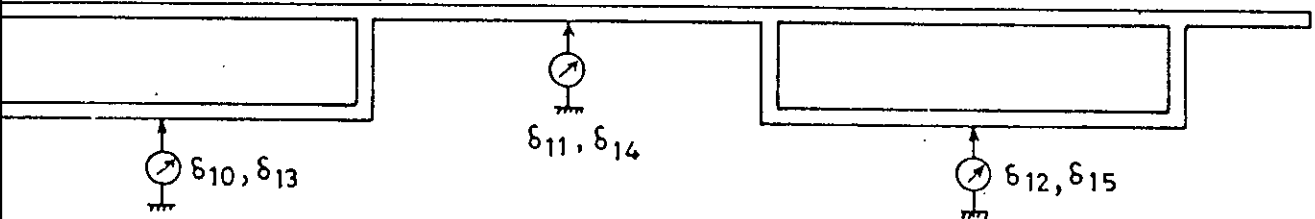
Load (kN)	Average crack width, $\omega_{avg.}$ (mm)		Maximum crack width, $\omega_{max.}$ (mm)		$\omega_{max}/\omega_{avg.}$	
	Girder G-3	Girder G-4	Girder G-3	Girder G-4	Girder G-3	Girder G-4
11.095	-	0.04	-	0.05	-	1.25
13.314	0.03	0.07	0.05	0.10	1.67	1.43
15.533	0.06	0.09	0.10	0.15	1.67	1.67
17.752	0.10	0.12	0.15	0.18	1.50	1.50
19.971	0.14	0.15	0.20	0.22	1.43	1.47

6.2 Double Cell Box Girder

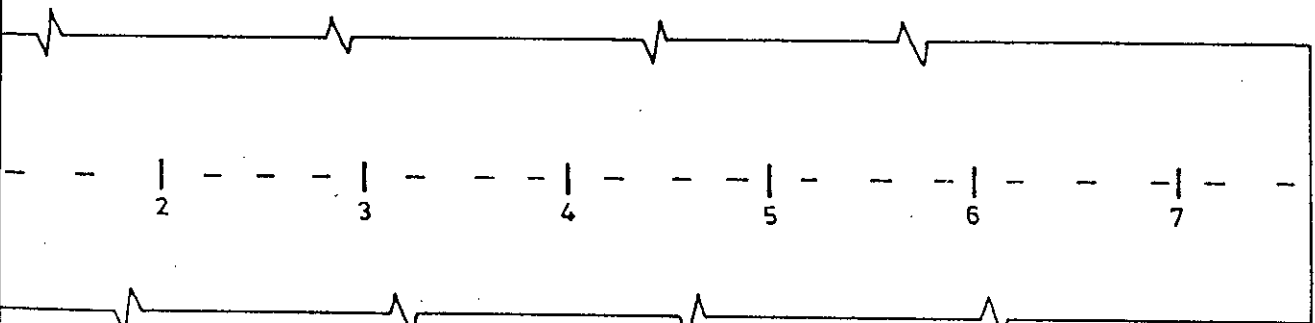
6.2.1 Double cell box girder subjected to various combinations of symmetric and unsymmetric loads in uncracked stage



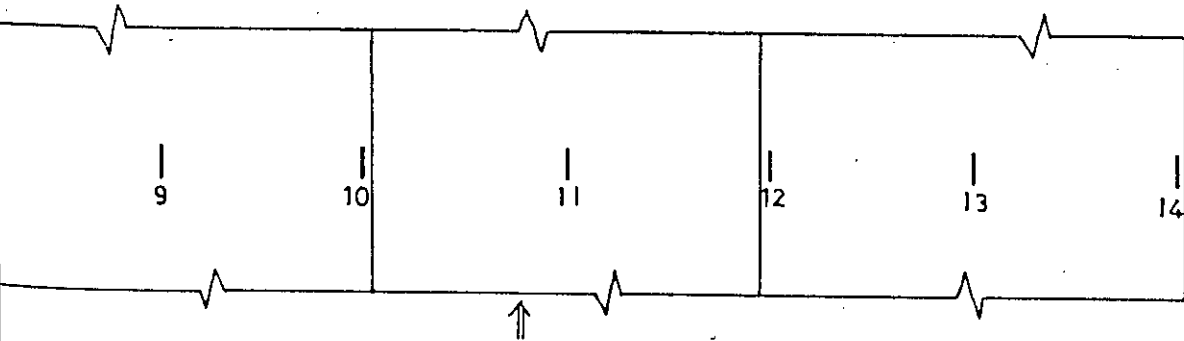
DEFLECTIONS ACROSS THE CROSS-SECTION AT MID SPAN



DEFLECTIONS ACROSS THE CROSS-SECTION AT QUARTER SPANS



TOP SURFACE OF THE TOP FLANGE



SOFFIT OF THE BOTTOM FLANGE

LAYOUT OF STRAIN GAUGES AT MID SPAN

Deflections Across the Girder Cross-section at Mid Span

Table 4.13 : Three bricks layers on half width of top flange and full span (Fig. 4.11 iii)

Deflection(mm) → Load (kN) ↓	δ_1	δ_2	δ_3	δ_4	δ_5	δ_6	δ_7	δ_8	δ_9
5.55	0.08	0.10	0.17	0.22	0.53	0.79	0.84	0.91	0.97
11.10	0.20	0.22	0.37	0.43	1.07	1.61	1.70	1.83	1.95
16.64	0.33	0.35	0.59	0.75	1.69	2.54	2.69	2.87	2.97

Table 4.14 : Six brick layers from free cantilever end to the centre of the nearer girder cell (Fig. 4.11 iv)

Deflection(mm) → Load(kN) ↓	δ_1	δ_2	δ_3	δ_4	δ_5	δ_6	δ_7	δ_8	δ_9
2.22	0.01	0.03	0.02	0.05	0.16	0.30	0.37	0.46	0.48
4.44	0.03	0.05	0.05	0.10	0.33	0.59	0.76	0.91	0.96
6.66	0.05	0.07	0.09	0.15	0.49	0.88	1.11	1.32	1.44
8.88	0.07	0.10	0.12	0.22	0.66	1.15	1.48	1.74	1.89
11.10	0.09	0.13	0.16	0.30	0.85	1.45	1.83	2.19	2.37
13.31	0.12	0.16	0.20	0.35	1.03	1.78	2.24	2.66	2.89

Table 4.15 : Five brick layers from free cantilever ends to the centres of the girder cells (Fig. 4.11 v)

Deflection(mm) → Load (kN) ↓	δ_1	δ_2	δ_3	δ_4	δ_5	δ_6	δ_7	δ_8	δ_9
4.438	0.43	0.44	0.39	0.36	0.36	0.40	0.49	0.64	0.61
8.876	0.88	0.85	0.77	0.71	0.72	0.82	0.98	1.20	1.23
13.314	1.36	1.30	1.18	1.08	1.10	1.21	1.46	1.74	1.79
17.752	1.83	1.77	1.59	1.46	1.47	1.63	1.94	2.27	2.36
22.190	2.31	2.22	2.00	1.84	1.83	2.02	2.37	2.70	2.89

Table 4.16 : Four brick layers over the girder cells (Fig. 4.11 vi)

Deflection(mm) \rightarrow	δ_1	δ_2	δ_3	δ_4	δ_5	δ_6	δ_7	δ_8	δ_9
Load (kN) \downarrow									
6.657	0.59	0.63	0.61	0.60	0.62	0.68	0.72	0.75	0.79
13.314	1.18	1.24	1.21	1.20	1.22	1.33	1.40	1.46	1.52
19.971	1.78	1.87	1.84	1.80	1.83	1.94	2.05	2.18	2.27
26.628	2.39	2.50	2.46	2.42	2.45	2.60	2.76	2.91	3.00

Table 4.17 : Seven brick layers between the girder cells (Fig. 4.11 vii)

Deflection(mm) \rightarrow	δ_1	δ_2	δ_3	δ_4	δ_5	δ_6	δ_7	δ_8	δ_9
Load (kN) \downarrow									
3.329	0.23	0.25	0.31	0.34	0.38	0.36	0.33	0.28	0.28
6.657	0.45	0.49	0.60	0.69	0.77	0.71	0.66	0.57	0.56
9.986	0.66	0.73	0.90	1.04	1.16	1.07	0.98	0.85	0.84
13.314	0.88	0.98	1.21	1.40	1.55	1.43	1.31	1.14	1.11
16.643	1.11	1.23	1.52	1.77	1.94	1.80	1.64	1.43	1.38
19.971	1.34	1.49	1.84	2.14	2.34	2.19	1.99	1.73	1.66
23.300	1.57	1.76	2.16	2.54	2.78	2.62	2.36	2.04	1.95

Strains ($\times 10^{-6}$) on the Top Surface of the Top Flange and
Soffits of the Bottom Flanges

Table 4.18 : Three brick layers on half width of
top flange and full span (Fig. 4.11 iii)

Load (kN) Gauge No.	5.55	11.10	16.64
	-07	-15	-26
	-09	-21	-35
	-12	-25	-39
	-14	-30	-46
	-23	-48	-77
	-25	-49	-77
	-34	-72	-108
	10	22	34
	11	24	36
	11	21	30
	-12	-26	-42
	45	94	147
	41	92	141
	48	98	150

Table 4.19 : Six brick layers from
free cantilever end of
the nearer girder cell
(Fig. 4.11 v)

Load (kN) Gauge No.	4.44	8.88	13.31
1	-02	-03	-06
2	-02	-07	-13
3	-04	-12	-20
4	-14	-30	-49
5	-20	-41	-63
6	-25	-52	-78
7	-28	-57	-88
8	04	07	10
9	01	03	06
10	03	08	12
11	-05	-10	-17
12	32	67	104
13	35	74	116
14	38	82	129

Table 4.20 : Five brick layers from free cantilever ends to the centres of the girder cells (Fig. 4.11 v)

Load (kN) + Gauge No. †	8.876	17.752	22.190
-28	-57	-78	
-25	-49	-63	
-25	-51	-65	
-27	-55	-68	
48	100	132	
45	93	124	
44	90	117	
-06	-14	-18	

Table 4.21 : Four brick layers over the girder cells (Fig. 4.11 vi)

Load (kN) + gauge No. †	13.314	26.628
1,7	-47	-102
2,6	-42	-82
3,5	-43	-85
4	-37	-78
8,14	60	132
9,13	54	113
10,12	59	122
11	-25	-53

Table 4.22 : Seven brick layers between the girder cells

Load (kN) + Gauge No. †	9.986	23.30
1,7	-32	-71
2,6	-35	-86
3,5	-40	-101
4	-30	-77
8,14	40	104
9,13	42	103
10,12	52	134
11	-18	-49

ns ($\times 10^{-6}$) Across the Girder Depth at Mid Span

Table 4.23 : Three brick layers on half width of top flange and full span (Fig. 4.11 iii)

Strain at Level	Front Face	Back Face
A	-38	-100
B	-25	-75
C	13	25
D	25	63
E	50	134

Table 4.24 : Six brick layers from free cantilever end to the centre of the nearer girder cell (Fig. 4.11 iv)

Load (kN)	Strain at Level	Front Face	Back Face
13.31	A	-13	-100
	B	0	-75
	C	0	-13
	D	25	50
	E	25	100

Table 4.25 : Five brick layers from free cantilever ends to the centres of the girder cells (Fig. 4.11 v)

Strain at Level	Front Face	Back Face
A	-85	-85
B	-63	-50
C	06	0
D	63	50
E	119	100

Table 4.26 : Four brick layers over the girder cells (Fig. 4.11 vi)

Load (kN)	Strain at Level	Front Face	Back Face
26.628	A	-100	-88
	B	-75	-63
	C	25	13
	D	63	56
	E	134	125

Table 4.27 : Seven brick layers between the girder cells (Fig. 4.11 vii)

Load (kN)	Strain at Level	Front Face	Back Face
23.30	A	-75	-69
	B	-50	-50
	C	06	0
	D	69	50
	E	125	88

2.2 Double cell box girder subjected to monotonically increasing sustained loads of short durations

Table 4.28 : Deflections (mm) across the girder cross-section at mid span and quarter span

Time (hrs)	Load (kN)	δ_1, δ_9	δ_2, δ_8	δ_3, δ_7	δ_4, δ_6	δ_5	$\delta_{10}, \delta_{12}, \delta_{13}, \delta_{15}$	δ_{11}, δ_{14}
*		1.29	1.22	1.18	1.13	1.14	0.84	0.91
		1.42	1.41	1.40	1.38	1.37	0.96	1.06
	11.095	1.51	1.50	1.47	1.45	1.45	1.04	1.14
		1.55	1.53	1.51	1.47	1.49	1.06	1.17
		3.00	2.92	2.88	2.84	2.88	2.10	2.22
		3.16	3.12	3.08	3.03	3.07	2.20	2.33
		3.36	3.30	3.25	3.21	3.28	2.34	2.48
	22.190	3.44	3.36	3.32	3.28	3.36	2.40	2.55
		3.62	3.57	3.54	3.49	3.55	2.52	2.67
		3.70	3.65	3.62	3.55	3.62	2.57	2.72
		7.51	7.43	7.40	7.32	7.41	5.15	5.40
		8.33	8.23	8.19	8.12	8.20	5.69	5.95
		8.53	8.42	8.37	8.30	8.38	5.82	6.08
	33.285	8.88	8.77	8.72	8.65	8.73	6.07	6.32
		9.25	9.12	9.06	9.01	9.09	6.32	6.57
		9.93	9.80	9.73	9.67	9.80	6.79	7.06
		10.34	10.22	10.15	10.09	10.16	7.18	7.49
		10.42	10.31	10.26	10.21	10.28	7.28	7.60
		14.57	14.50	14.46	14.41	14.52	10.22	10.58
		14.98	14.92	14.83	14.79	14.93	10.52	10.86
		15.41	15.35	15.28	15.21	15.36	10.80	11.18
	44.380	15.57	15.51	15.43	15.35	15.52	10.92	11.30
		15.73	15.69	15.62	15.55	15.73	11.05	11.42
		15.93	15.89	15.80	15.70	15.90	11.13	11.50
		16.06	16.03	15.94	15.84	16.02	11.22	11.60

stantaneous deflections
ours

Contd.....

Table 4.28 (Contd.....)

e s)	Load (kN)	δ_1, δ_9	δ_2, δ_8	δ_3, δ_7	δ_4, δ_6	δ_5	$\delta_{10}, \delta_{12},$ δ_{13}, δ_{15}	δ_{11}, δ_{14}
		20.82	20.77	20.69	20.56	20.78	14.57	15.09
		21.33	21.29	21.23	21.07	21.30	14.89	15.44
		21.75	21.70	21.60	21.44	21.68	15.13	15.67
		22.02	21.95	21.85	21.70	21.92	15.30	15.88
	55.476	22.22	22.18	22.07	21.93	22.15	15.45	15.98
		22.47	22.42	22.27	22.10	22.33	15.59	16.11
		22.70	22.65	22.51	22.35	22.60	15.76	16.28
		22.77	22.74	22.59	22.43	22.69	15.86	16.39
		28.09	28.04	27.85	27.77	28.07	19.58	19.85
		28.75	28.72	28.51	28.42	28.73	20.05	20.69
		29.22	29.18	28.97	28.85	29.17	20.40	21.03
		29.47	29.43	29.22	29.11	29.43	20.57	21.19
	66.570	29.77	29.78	29.56	29.42	29.80	20.84	21.46
		29.96	29.98	29.77	29.65	30.02	20.98	21.62
		30.16	30.15	29.92	29.80	30.19	21.09	21.71
		30.36	30.35	30.13	30.01	30.40	21.24	21.86
		30.40	30.38	30.15	30.03	30.42	21.25	21.88

Table 4.29 : Strains ($\times 10^{-6}$) on the top surface of the top flange and soffits of the bottom flanges

Load (kN) →	11.095		22.190		33.285		44.380		55.476		66.57	
	inst.	after 3 days	inst.	after 11 days	inst.	after 23 days	inst.	after 10 days	inst.	after 13 days	inst.	after 15 days
-35	-43	-92	-120	-174	-232	-280	-347	-418	-485	-550	-684	
-30	-40	-85	-107	-156	-221	-275	-338	-422	-492	-588	-744	
-32	-40	-92	-116	-170	-240	-272	-345	-408	-469	-576	-732	
-27	-38	-79	-96	-141	-198	-260	-327	-382	-445	-530	-672	
45	53	103	120	-	-	-	-	-	-	-	-	
50	60	115	-	-	-	-	-	-	-	-	-	
57	68	-	-	-	-	-	-	-	-	-	-	
-25	-34	-57	-68	-84	-93	-87	-121	-114	-99	-87	-93	

Table 4.30 : Average longitudinal strains ($\times 10^{-6}$) across the girder depth at various sections

Section	Strain at level	Load (kN)									
		22.190		33.285		44.380		55.476		66.57	
		inst.	after	inst.	after	inst.	after	inst.	after	inst.	after
		11	23	10	13	15					
		days	days	days	days	days					
At mid span	A	-75	-113	-150	-181	-219	-256	-306	-344	-413	-475
	B	-50	-75	-113	-125	-113	-125	-100	-100	-113	-138
	C	25	50	138	225	563	688	1013	1200	1563	1825
	D	75	125	294	500	1000	1175	1638	1900	2450	2788
	E	125	208	463	750	1475	1738	2356	2688	3475	3888
At ± 406.4 mm from mid span	A	-69	-100	-138	-175	-188	-238	-263	-313	-388	-425
	B	-50	-75	-100	-113	-113	-113	-106	-113	-113	-125
	C	13	25	100	200	450	563	775	888	1213	1325
	D	63	94	225	400	788	950	1263	1450	1975	2225
	E	113	163	363	613	1150	1388	1825	2063	2825	3213
At Quarter span	A	-56	-75	-94	-113	-138	-163	-200	-225	-275	-325
	B	-38	-50	-69	-75	-88	-100	-113	-125	-125	-150
	C	13	19	38	63	150	213	338	413	588	675
	D	50	63	100	163	288	375	613	725	1063	1263
	E	88	100	175	275	450	563	888	1063	1525	1788

Table 4.31 : Average and maximum crack widths at various load levels

Load (kN)	Time	Average Crack Width, w_{avg} (mm)	Maximum Crack Width, w_{max} (mm)	w_{max}/w_{avg}
22.190	Instantaneous	0.03	0.05	1.67
	After sustained loading of 11 days	0.04	0.06	1.50
33.285	Instantaneous	0.06	0.10	1.67
	After sustained loading of 23 days	0.07	0.12	1.71
44.380	Instantaneous	0.12	0.20	1.67
	After sustained loading of 10 days	0.13	0.22	1.69
55.476	Instantaneous	0.16	0.25	1.56
	After sustained loading of 13 days	0.20	0.30	1.50
66.571	Instantaneous	0.21	0.35	1.67
	After sustained loading of 15 days	0.26	0.40	1.54

4.6.3 Composite Box Girder

4.6.3.1 Composite box girder subjected to udl over the entire top flange

Table 4.32 : Average deflections at various points along the span of the girder

Deflection (mm) + Load (kN) ↓	δ_1, δ_7	δ_2, δ_6	δ_3, δ_5	$\delta_9, \delta_4, \delta_{10}$	δ_8, δ_{11}
4.438	0.30	0.58	0.67	0.77	0.78
8.876	0.76	1.38	1.83	2.02	1.98
13.314	1.76	3.06	4.64	5.02	4.96
17.752	3.57	7.05	9.39	10.45	10.30
22.190	5.66	10.86	14.29	15.92	15.51
26.628	8.62	16.52	21.40	23.80	23.57
22.190	8.21	15.71	20.39	22.70	22.41
17.752	7.66	14.59	18.93	21.13	20.70
13.314	6.98	13.30	17.25	19.32	18.71
8.876	6.23	11.87	15.37	17.29	16.64
4.438	5.43	10.36	13.36	15.09	14.42
Nil	4.35	8.33	10.78	12.17	11.66

Table 4.33 : Average strains ($\times 10^{-6}$) on the top surface of the top flange and the soffit of the bottom flange

Load (kN) + Gauge No. ↓	4.438	8.876	13.314	17.752	22.190	26.628
4	-20	-48	-98	-174	-259	-378
3	-25	-52	-86	-145	-227	-336
10	36	77	-	-	-	-
9	61	124	-	-	-	-
8	40	98	-	-	-	-

Table 4.34 : Average longitudinal strains ($\times 10^{-6}$) across the girder depth at various sections

Section	Strain at level	Load (kN)				
		8.876	13.314	17.752	22.190	26.628
At mid span	A	-63	-100	-156	-256	-344
	B	-31	-44	0	50	100
	C	38	88	331	656	1125
	D	75	194	588	1063	1738
	E	138	331	925	1569	2538
At ± 406.4 mm from mid span	A	-50	-75	-125	-150	-275
	B	-31	-50	-25	0	63
	C	25	75	275	513	875
	D	63	163	513	875	1475
	E	113	250	738	1288	2063
At Quarter span	A	-38	-63	-88	-116	-175
	B	-25	-38	-25	-13	25
	C	13	25	88	231	381
	D	38	88	188	400	650
	E	75	138	294	563	925

Table 4.35 : Average and maximum crack widths at various load levels

Load (kN)	Average Crack Width, w_{avg} (mm)	Maximum Crack Width, w_{max} (mm)	w_{max}/w_{avg}
8.876	0.03	0.05	1.67
13.314	0.06	0.10	1.67
17.752	0.08	0.12	1.50
22.190	0.12	0.16	1.33
26.628	0.14	0.20	1.43

4.6.3.2 Reloading of the composite box girder and subjecting it to sustained loading

Table 4.36 : Deflections (mm) under sustained loading

Time (days)	Load (kN)	δ_2, δ_6	$\delta_9, \delta_4, \delta_{10}$	δ_{11}
Residual	Nil	8.33	12.17	11.66
inst.		1.16	1.67	1.68
2	4.438	1.19	1.71	1.70
3		1.21	1.71	1.71
5		1.21	1.70	1.71
inst.		2.49	3.57	3.58
2		2.53	3.60	3.62
4	8.876	2.56	3.68	3.71
7		2.64	3.80	3.84
11		2.71	3.85	3.89
inst.		3.89	5.70	5.71
1		4.01	5.87	5.87
3		4.12	5.98	5.99
7	13.314	4.25	6.11	6.12
10		4.29	6.25	6.25
14		4.40	6.37	6.38
inst.		5.56	8.08	8.05
1		5.71	8.29	8.29
3		5.84	8.45	8.45
7	17.752	5.91	8.55	8.53
10		5.99	8.69	8.69
14		6.12	8.88	8.89
19		6.26	9.06	9.07
inst.		7.50	10.88	10.90
1		7.66	11.10	11.07
2		7.81	11.27	11.25
3	22.190	7.98	11.46	11.46
4		8.05	11.59	11.58
5		8.19	11.70	11.68
6		8.19	11.80	11.81
7		8.32	11.99	11.99

Table 4.36 (Contd.....)

Time (days)	Load (kN)	δ_2, δ_6	$\delta_9, \delta_4, \delta_{10}$	δ_{11}
Residual	Nil	8.33	12.17	11.66
inst.		9.69	14.09	14.07
2		10.30	14.84	14.85
4		10.49	15.10	15.11
7		10.76	15.50	15.52
11		11.32	16.18	16.18
14	26.628	11.54	16.48	16.48
21		12.28	17.49	17.48
28		12.65	17.96	17.93
35		12.97	18.34	18.34
49		13.68	19.32	19.33
60		14.06	19.86	19.79
109		15.00	21.19	21.14
149		15.28	21.58	21.52
187		15.43	21.66	21.61
249		15.91	22.34	22.30
318		16.05	22.53	22.48

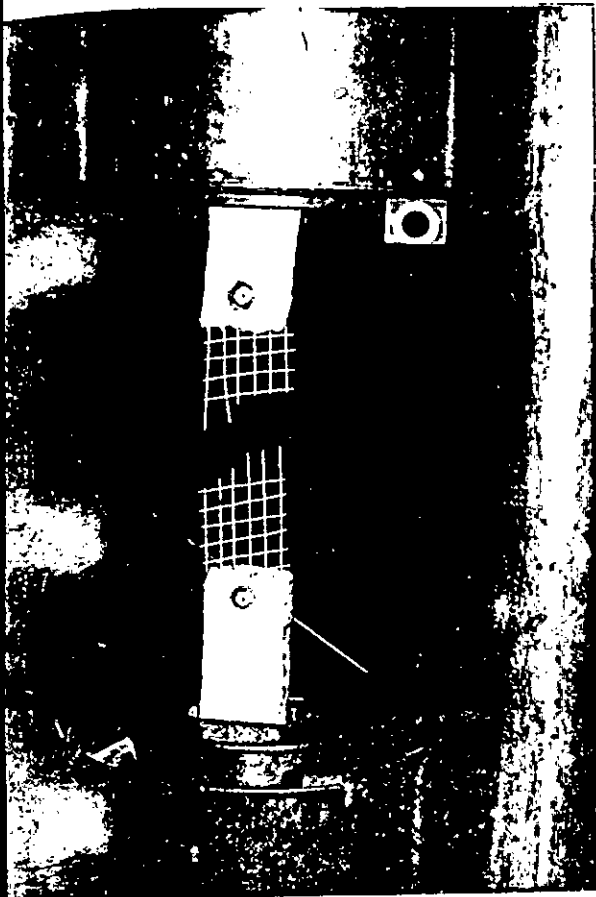


PLATE 4.1 TENSION TESTING OF WIRE MESH SPECIMEN

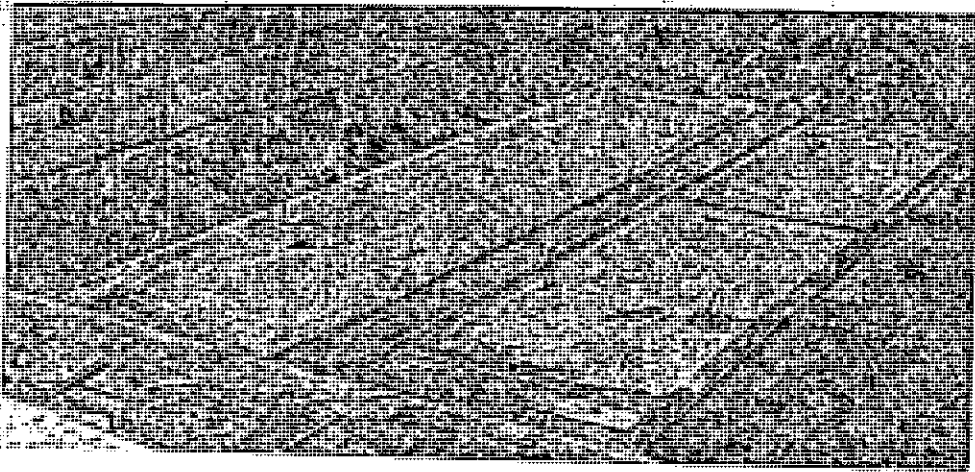


(A)

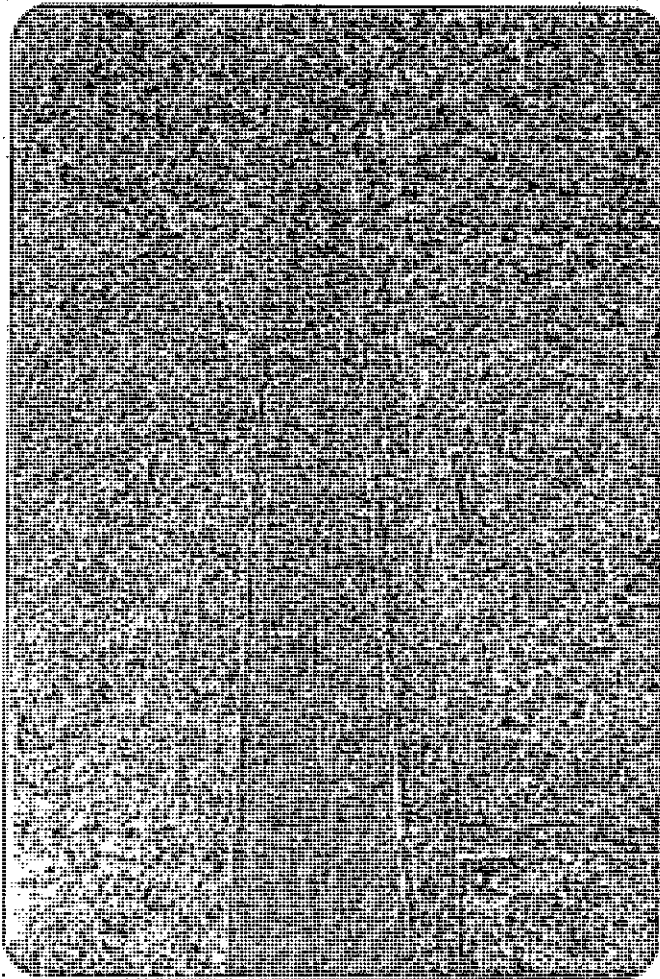


(B)

PLATE 4.2 USE OF PORTABLE SHUTTER VIBRATOR FOR COMPACTING :
(A) BOTTOM FLANGE AND SIDE WEBS, (B) TOP FLANGE



(A)



(B)

ATE 43 JOINT OF THE DOUBLE CELL BOX GIRDER PRIOR
TO CASTING: (A) FULL VIEW (B) CLOSE-UP

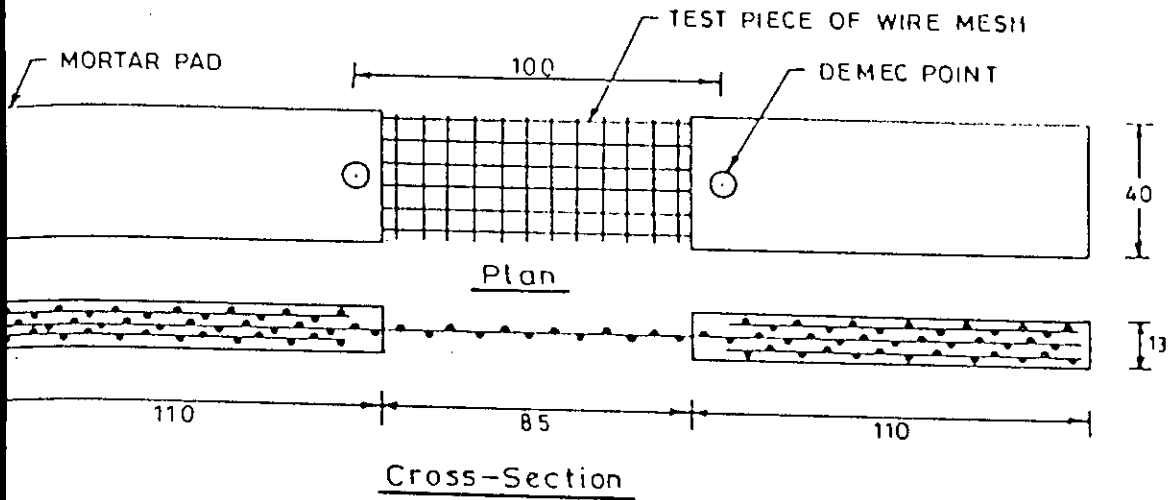
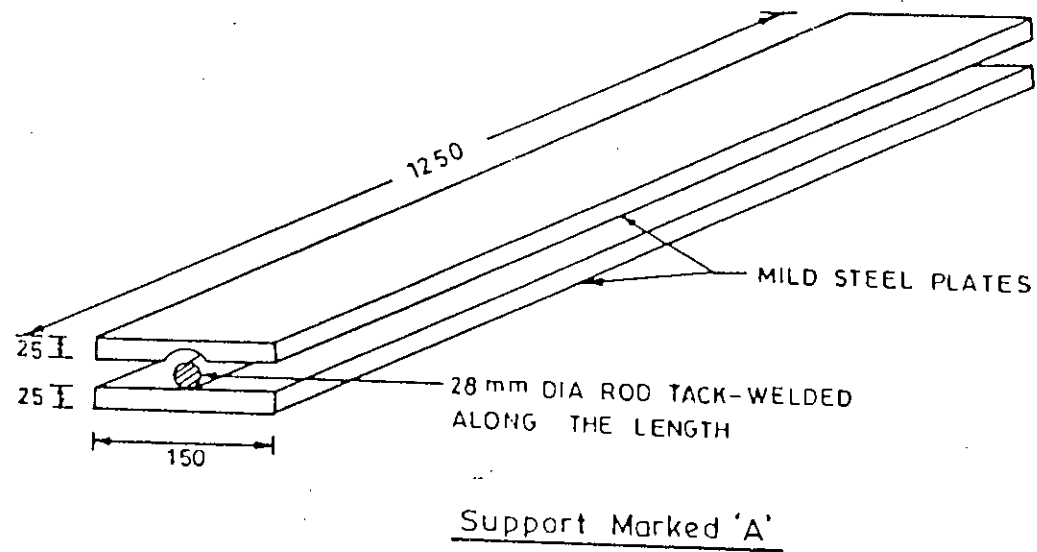
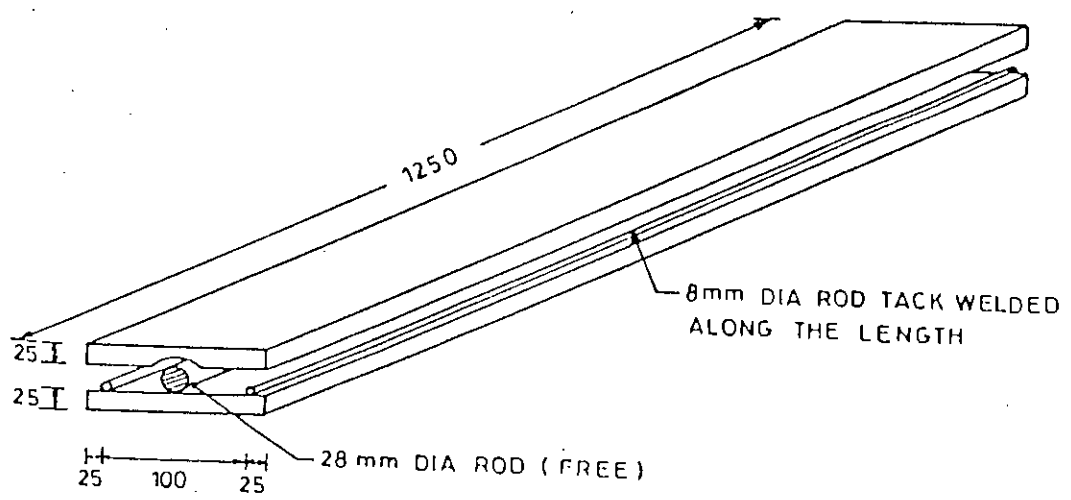


FIG. 4.1—TYPICAL WIREMESH SPECIMEN USED FOR TENSION TEST



Support Marked 'A'



Support Marked 'B'

4.2—STRUCTURAL DETAILS OF MILD STEEL SIMPLE SUPPORTS

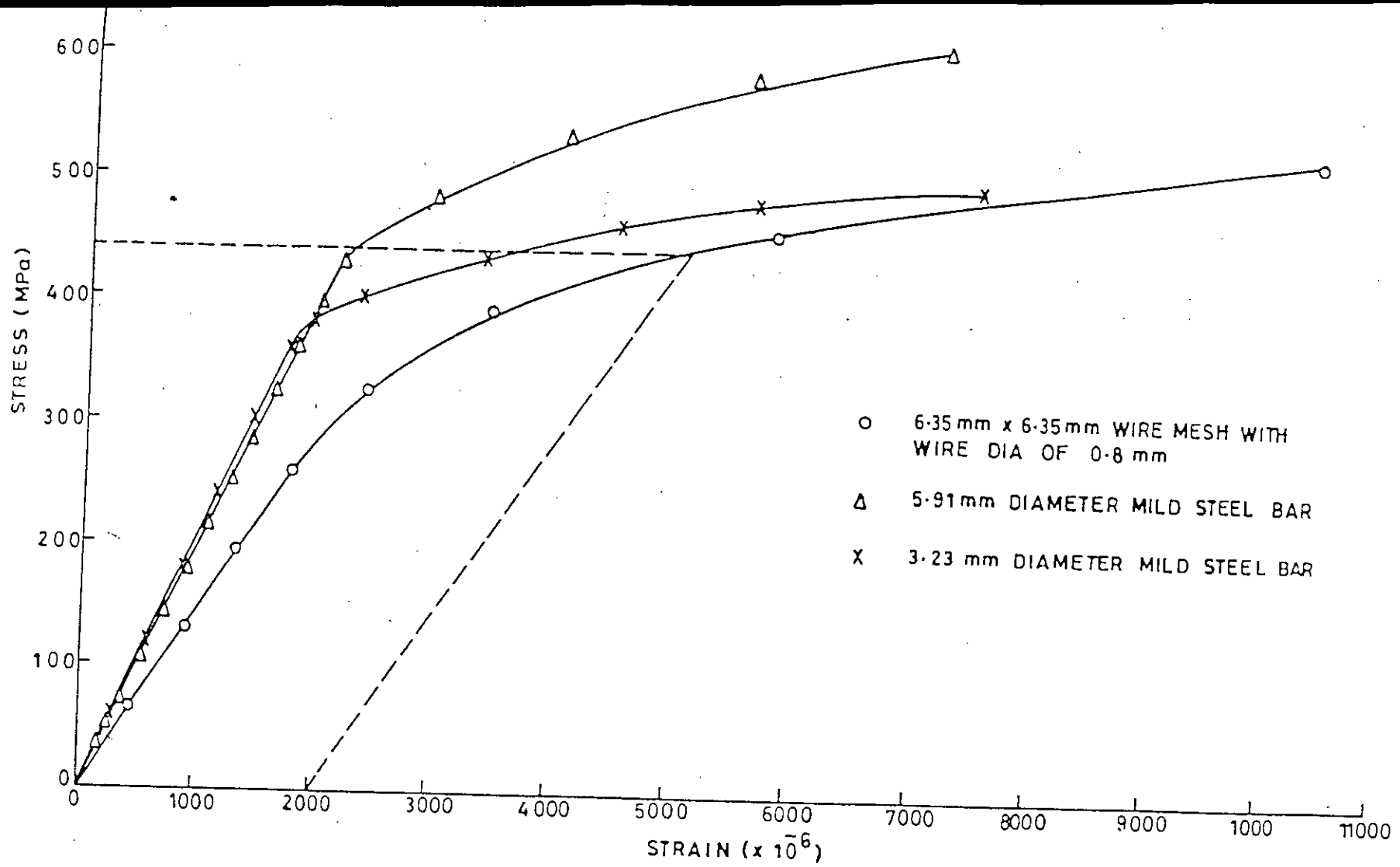


FIG.4.3- STRESS STRAIN CURVES OF WIREMESH, 5.91 mm AND 3.23 mm BARS IN UNIAXIAL TENSION

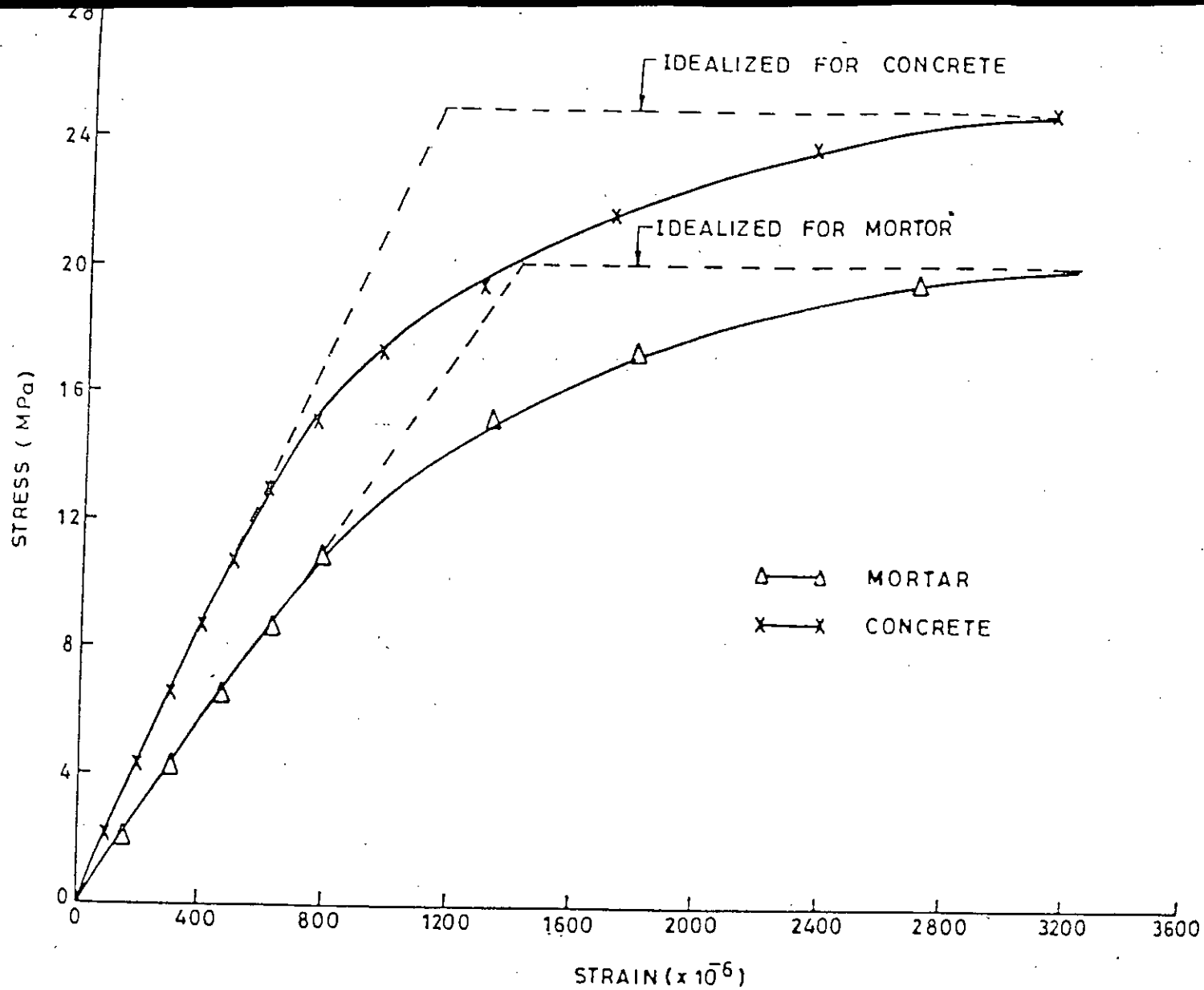
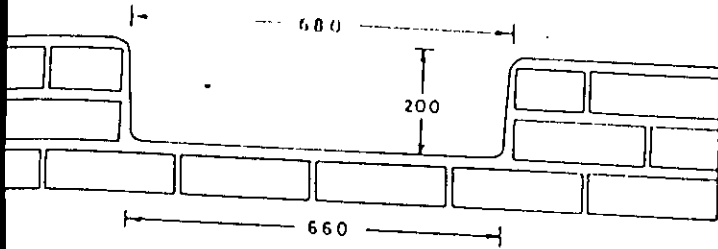


FIG.4.4— STRESS STRAIN CURVES OF MORTAR AND CONCRETE IN UNIAXIAL COMPRESSION



BRICK MASONRY MOULD FOR CASTING BOX GIRDERS

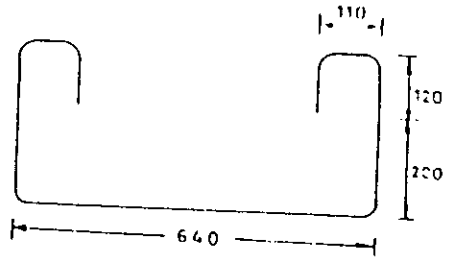
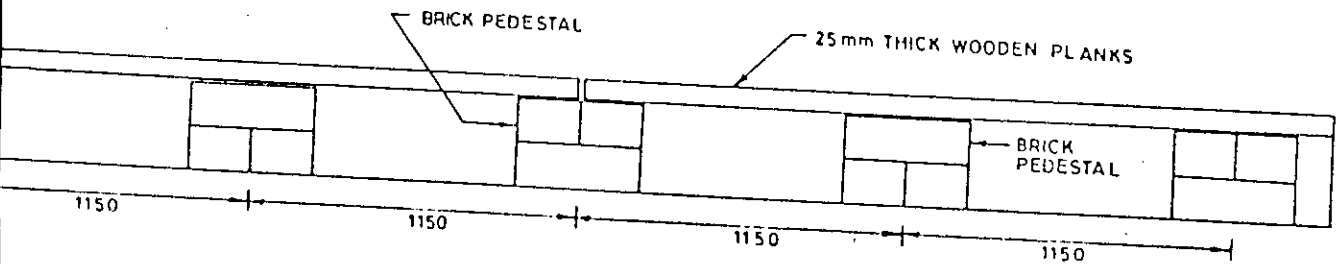
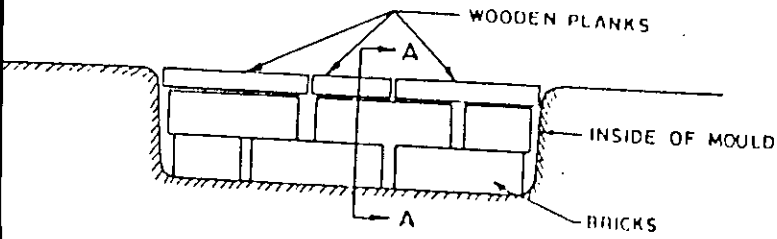


FIG.4.6-10mm DIAMETER HOOK FOR LIFTING OF THE GIRDER



Section A A

FIG. 4.7-TEMPORARY FORMWORK FOR CASTING TOP FLANGE

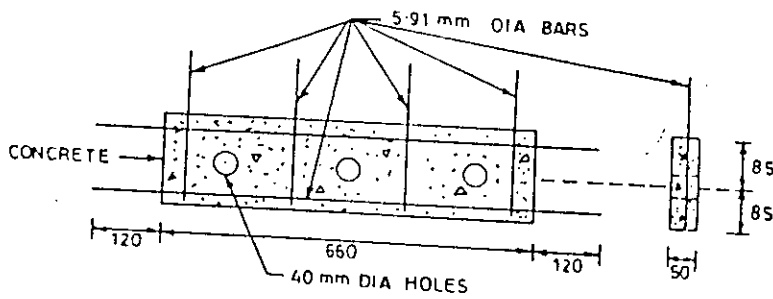
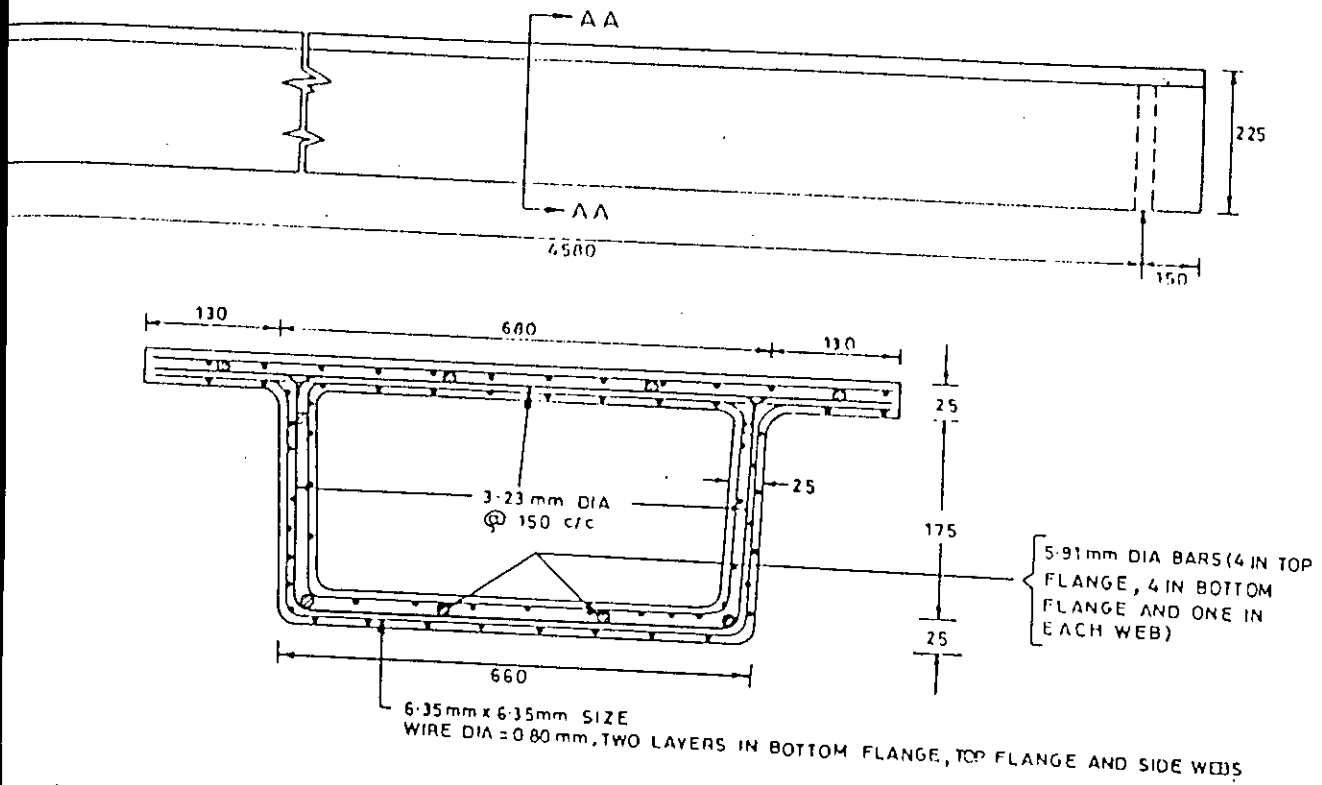
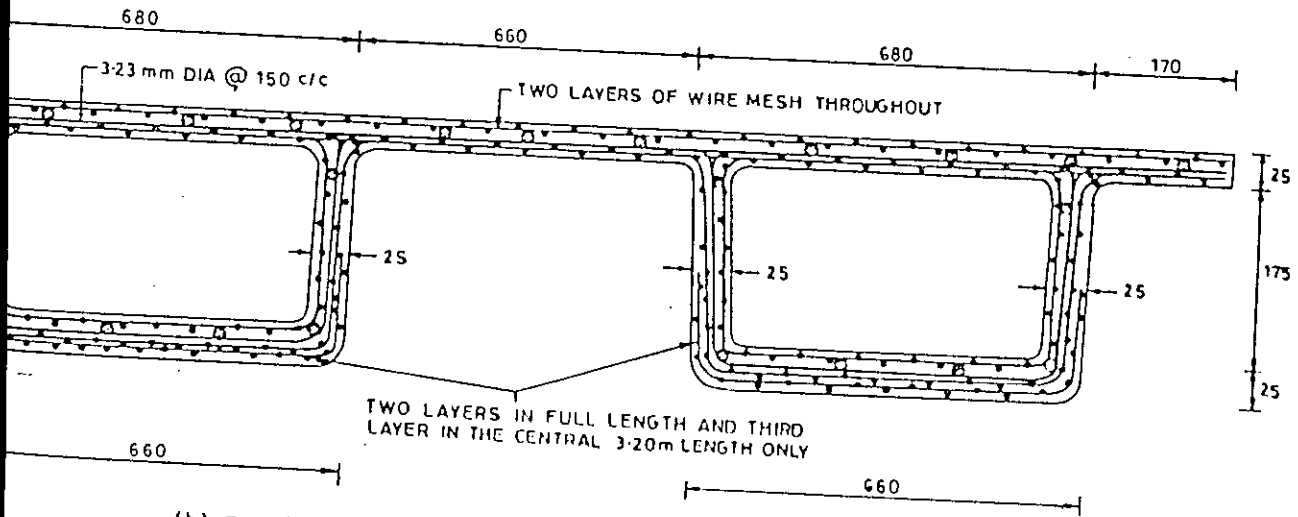


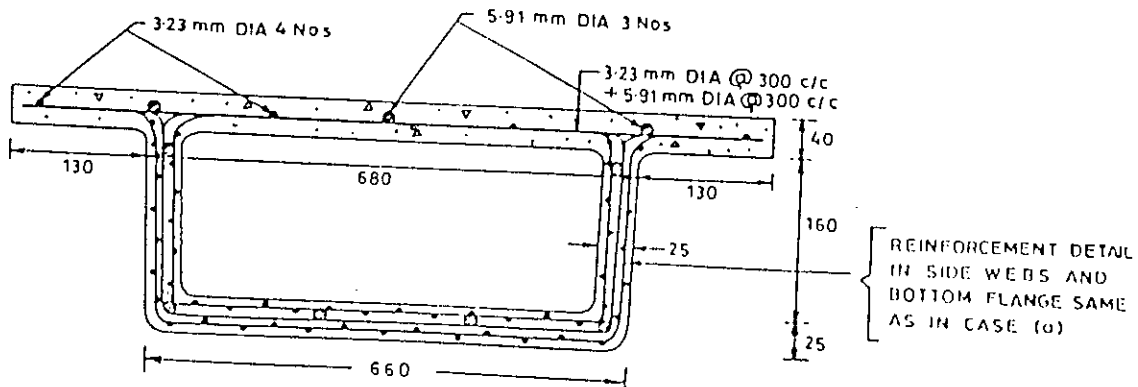
FIG.4.8-STRUCTURAL DETAILS OF PRECAST R.C.C DIAPHRAGM



(a) Section AA For Single Cell Ferrocement Box Girder



(b) Section AA For Double Cell Box Girder



(c) Section AA For Composite Box Girder

FIG. 4.9 - SECTIONAL AND REINFORCEMENT DETAILS OF BOX GIRDERS

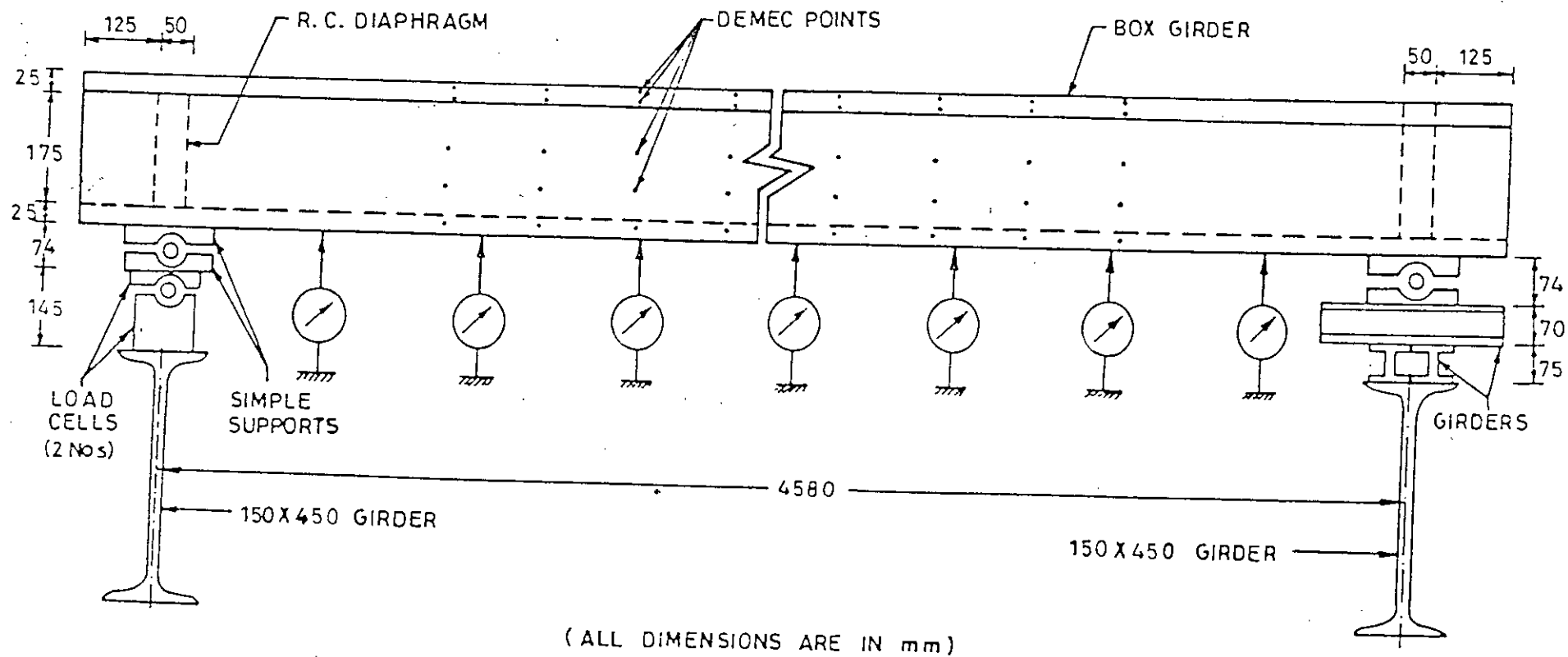
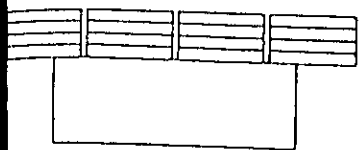
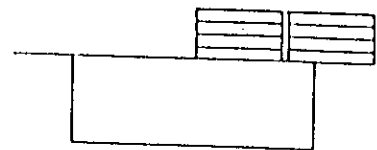


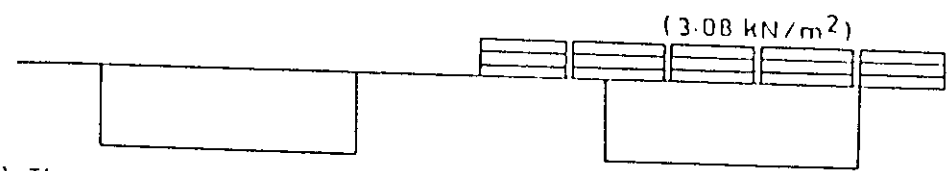
FIG. 4-10 — TEST SET-UP FOR SIMPLY SUPPORTED F. C. BOX GIRDERS



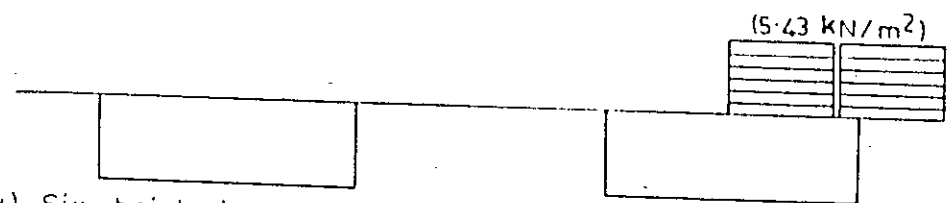
(i) udl over entire top flange



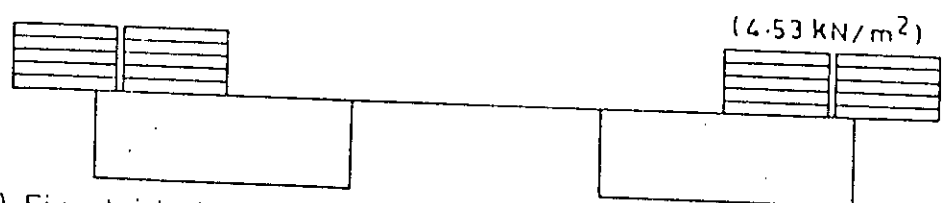
(ii) udl over half flange width and full span



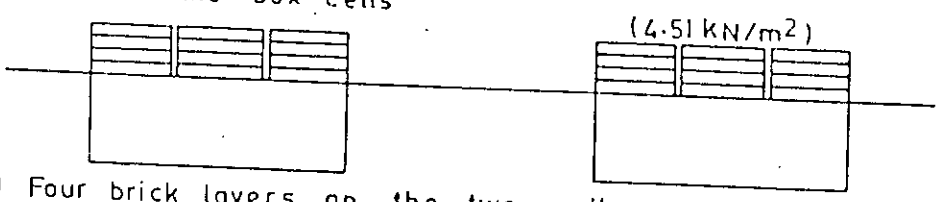
(iii) Three brick layers over half width of top flange and full span



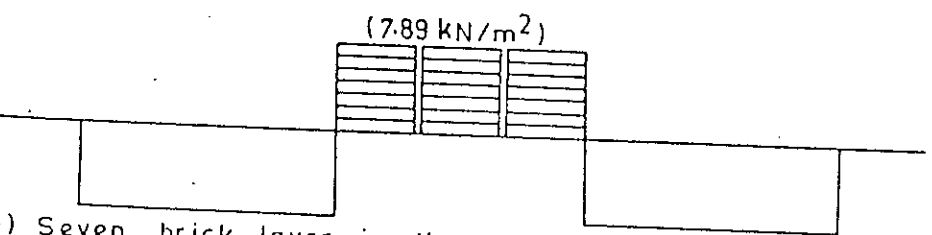
(iv) Six brick layers from one free end of cantilever to the centre of the box cell



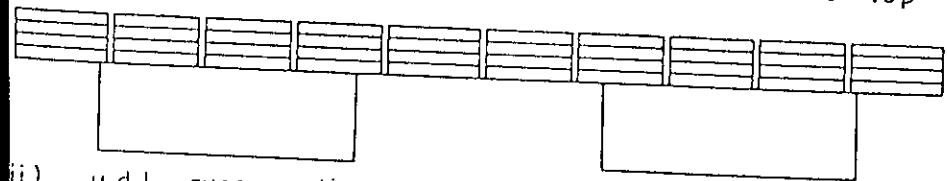
(v) Five brick layers from both free ends of the cantilevers to the centres of the box cells



(vi) Four brick layers on the two cells



(vii) Seven brick layers in the central part of the top flange



(viii) udl over entire top flange

Weight of one brick = 28.449 N

No. of brick rows in the span of the girder = 39

Fig. 4.11 : LOADING ARRANGEMENT ON VARIOUS BOX GIRDERS

CHAPTER - V

TEST RESULTS AND COMPARISON WITH ANALYTICAL PREDICTIONS

5.1 INTRODUCTION

The ferrocement box girders were tested to study their behaviour in the elastic, cracked and ultimate stages. The test results have been compared with the analytical results predicted by the proposed finite element method described in Chapter -III. The proposed analytical method traces the complete response of the girders, i.e., deflections, strains, stresses, propagation of cracks and prediction of ultimate failure under dead loads and monotonically increasing live loads. A detailed comparison of the experimental and analytical results is presented in the following sections. The experimental values reported are average of companion specimens, wherever applicable.

5.2 SINGLE CELL FERROCEMENT BOX GIRDERS SUBJECTED TO udl OVER THE ENTIRE TOP FLANGE

5.2.1 General Test Behaviour

Two single cell ferrocement box girders were tested under uniformly distributed loads (udl) over the entire top flange (Plate 5.1). The experimental results of both the girders were comparable. In both the girders, the first visible cracks appeared in the bottom flange and side webs in the mid span region after the application of three brick layers (corresponding to a udl of 3.09 kN/m^2). The maximum crack width in both the girders at this load level reached 0.1 mm. After the application of four brick layers (4.12 kN/m^2), a large number of cracks appeared. The length and width of cracks formed earlier also increased. Many cracks in the bottom flange traversed the full width of the bottom flange. The maximum crack width in the girders marked G-1 and G-2 reached 0.15 mm and 0.20 mm respectively. With the application of further brick layers new cracks formed, the cracks formed

earlier extended and the width of cracks increased. At seven brick layers (7.22 kN/m^2), the maximum crack width in the two girders reached 0.6 mm and 0.8 mm respectively. The girder marked G-1 was loaded with the eight brick layer (8.25 kN/m^2) also. After about twenty minutes of the loading, the girder failed due to snapping of wire meshes of the bottom flange and side webs (Plates 5.3A, B and C). The average crack spacing at seven brick layers in girder G-2 was about 40 mm in the central part of the bottom flange. At this load level, a few diagonal shear cracks in the web appeared at the support. Longitudinal cracks at the junction of top flange and webs also appeared at this load level in the end portions. On unloading, the recovery in mid span deflection in girder G-2 was about 60 percent. The crack-pattern of the bottom flange and side webs of girder G-2 is shown in Plate 5.2. Chipping of the bottom flange and side webs in girder G-2 was done at several crack locations. Mortar compaction was found to be satisfactory. Mortar cover to the wire mesh varied from 5.15 mm to 7.94 mm with an average of 6.60 mm. This compared well with the theoretical cover of 6.33 mm.

5.2.2 Finite Element Idealization

Taking advantage of the symmetry of the geometry and the loading about both the axes, one quarter of the girder was discretized (Fig. 5.1) by forty four elements with fifty six nodes. The wire mesh and transverse skeletal steel reinforcement was the same in the top flanges, side webs and bottom flange. The variation in the longitudinal skeletal steel in the top flange, side webs and bottom flange was accounted for by taking three different material types for them. Material type for reinforced concrete end diaphragms was accounted for by taking it as a fourth material type. The location of the mesh layers and skeletal steel as considered in the analysis of the girder are shown in Fig. 5.1.

The total superimposed load of 31.07 kN (or 7.22 kN/m²) was applied in six load increments of 8.88, 4.44, 4.44, 4.44, 4.44 and 4.44 kN each. The first load increment comprised of the self weight of the girder plus the superimposed load of 8.88 kN whereas the subsequent load increments were of superimposed load only. The ultimate failure of the girder at 31.07 kN load was indicated by a large increase in the unbalanced force norm ratio. The failure at this load was also indicated by a large increase in deflections in the last load increment. The total computer time taken for complete displacement and stress output was 4 minutes and 40 seconds.

5.2.3 Comparison of Results

The comparison of theoretical and experimental deflections at the mid span and along the span are shown in Figs. 5.2 and 5.3 respectively. Considering the deflections at mid span, the predicted deflections in the elastic stage (i.e. at one and two brick layers) are about 70 percent of the experimental deflections. This difference in the analytical and the experimental deflections may be due to (i) finite element mesh fineness used in the discretization of the girder and (ii) the variation in the modulus of elasticity of the mortar adopted for the theoretical analysis and the actual modulus of elasticity of the mortar in the cast girders. To study the effect of the discretization, the girder was reanalysed by discretizing it with 74 elements and 90 nodes. The mid span deflections at first, second and third load increments (i.e. at two three and four brick layers) increased only marginally by 0.44, 0.34 and 1.96 percent respectively). The mid span deflections at fourth and fifth load increments (i.e. at five and six brick layers) increased by 6.0 and 8.4 percent respectively. The ultimate failure of the girder at sixth load increment (i.e. at seven brick layers corresponding to 31.07 kN load) was indicated by a large increase in the residual vector norm ratio and the energy norm ratio due to residual forces. Thus the

improvement in the deflection values is very small whereas the computer time taken for the analysis increased by about 80 percent. Therefore, the difference in the analytical and the experimental values in the elastic stage and the initial portion of the cracked range may be attributed to the difference in the modulus of elasticity of the mortar adopted for the theoretical analysis and the actual modulus of elasticity of the mortar in the cast girders. The value adopted in the theoretical analysis is from the control mortar cylinders of 75mm x 150mm cast on a vibrating table whereas the mortar in the box girders was compacted using a specially fabricated surface vibrator having a wooden base. Proper compaction of the mortar in casting ferrocement elements is a difficult problem as reported by Gamski⁽¹⁶³⁾ also. At three and four brick layers (3.09 kN/m^2 and 4.12 kN/m^2), the predicted deflections are about 70 percent of the experimental deflections whereas at five and six brick layers (5.15 kN/m^2 and 6.19 kN/m^2) these are about 87 and 98 percent of the experimental deflections. At the ultimate load of seven brick layers (7.22 kN/m^2), the predicted deflections become large thus indicating the failure of the girder.

The theoretical first crack load causing the attainment of cracking strain in the extreme fibre of mortar at the critical Gauss point was obtained as 9.43 kN (or 2.19 kN/m^2) by the linear extrapolation of the result of the first load increment. The experimental first cracks in both the girders were observed after the application of three brick layers. Since all the observations including that of crack detection were made after complete loading of the girder by each brick layers, the appearance of the first crack, even if it happens during the application of any brick layer goes unnoticed and the actual first crack load is, thus, not known. This problem of determining experimental first crack load was overcome by interpolating from the load-deflection curve the point from where non-linear behaviour starts. The first

rack loads so determined for the girders G-1 and G-2 are about 11.50 kN (or 2.67 kN/m^2) and 10.25 kN (or 2.38 kN/m^2) respectively.

A comparison of the predicted and experimental longitudinal tensile strains at 25 mm above the soffit at the mid and quarter span sections is shown in Fig. 5.4. Considering the mid span section, the predicted and the experimental strains are small in the uncracked range and are in good agreement. After cracking of the mortar, the strains increase at a fast rate. At the three and four brick layers, the predicted strains are less than the experimental strains by about 32 and 22 percent respectively. At five brick layers; the predicted strain is more than the experimental strain by about 4 percent. The yielding of the skeletal steel is predicted at six brick layers. The contribution of skeletal steel to the rigidity of the cracked section becomes zero due to the assumed linearly elastic-perfectly plastic stress-strain curve of the material. The contribution of cracked mortar is already small due to its entire depth having cracked. This leads to a large increase in the strain at the section. The predicted strain at six brick layers is thus more than the experimental strain by about 43 percent. At seven brick layers, the yielding of wire mesh is also predicted. Thus the contribution of both the skeletal steel and wire mesh to the rigidity of the cracked composite is zero. The predicted strain at seven brick layers is very large as compared to the experimental strains of the two girders. The actual stress-strain curves of skeletal steel and wire mesh (Fig. 4.3) do not have a well defined yield point. Thus the skeletal steel and wire mesh contribute to the rigidity of the cracked composite beyond their assumed yield strains. The large increase in the predicted deflections at seven brick layers are due to the predicted yielding of the skeletal steel and the wire mesh layers of the bottom flange elements in the mid span region.

On comparing the predicted longitudinal tensile strains at 25 mm above

the soffit with the experimental strains at the quarter span section, the predicted and the experimental strains of the two girders are small upto three brick layers and are in good agreement. At four and five brick layers, the predicted strains are less than the experimental strains by about 29 and 15 percent while at six and seven brick layers these are more by about 20 and 29 percent respectively. Even at seven brick layers, the predicted strains in the skeletal steel and wire mesh layers are less than their respective yield strains.

A comparison of the predicted and the experimental longitudinal compressive strains at the top surface of the top flange at the mid and the quarter span sections is shown in Fig. 5.5. Considering the mid span section, the predicted and the experimental strains are in good agreement upto four brick layers. At five and six brick layers, the predicted strains are more than the experimental strains by about 18 and 30 percent respectively. At seven brick layers the predicted strain becomes large as compared to the experimental strains. The large variation at seven brick layers is due to the predicted yielding of skeletal steel and wire mesh layers of the bottom flange in the theoretical analysis which causes the corresponding increase in the compressive strains of the top flange. Considering quarter span section, the predicted and the experimental strains show a good comparison right upto seven brick layers. At seven brick layers the predicted strain is more than the experimental strain by about 13 percent only. Thus the predicted and the experimental strains have shown good comparison upto the yielding of reinforcement. The predicted strains become large after the yielding of reinforcement due to the reason mentioned above.

The variation of the longitudinal strain across the girder depth at the mid and quarter span sections is shown in Figs. 5.6 and 5.7. On the whole, the variation of the experimental strains across the girder depth is linear.

Considering mid span section (Fig. 5.6) at three and four brick layers, the predicted strains are less than the experimental strains across the entire depth. The maximum variation is at 75 mm above the soffit at three brick layers where predicted strain is less than the experimental strain by about 33 percent. At five brick layers, the predicted and the experimental strains are in good agreement across the entire girder depth. At six brick layers, the predicted strains are more than the experimental strains and the maximum variation is at 25 mm above the soffit where predicted strain is more than the experimental strain by about 43 percent. The large variation at this load level is due to the predicted yielding of skeletal steel. At seven brick layers, the variation becomes quite large due to the predicted yielding of skeletal steel and wire mesh both. Considering quarter span section (Fig. 5.7), the predicted and the experimental strains upto three brick layers are small and are in good agreement. At four and five brick layers, the predicted strains are less than the experimental strains across the entire depth and the maximum variation is at 25 mm above the soffit at four brick layers where predicted strain is less than the experimental strain but about 29 percent. At six brick layers, the predicted and the experimental strains are in good agreement in the cantilever flange and at mid depth while below the mid depth of the girder, the predicted strains are more than the experimental strains. The maximum variation is at 25 mm above the soffit where predicted strain is more than the experimental strain by about 20 percent. At seven brick layers the predicted strains compare well with the experimental strains in the cantilever flange but in the remaining girder depth the predicted strains are more than the experimental strains. The maximum variation is at mid depth of the girder where predicted strain is more by about 33 percent.

The load versus maximum crack width curve for the girders is shown in Fig. 5.8. At the recommended crack width of 0.1 mm for ferrocement structures⁽¹⁾, the load carried by girders G-1 and G-2 both is 3.09 kN/m^2 .

At this load level the average span/deflection ratio is about 960 which is about four times the limiting ratio of 250 as per I.S. Code⁽¹⁶²⁾ from serviceability requirement of limit state of deflection. At a span/deflection ratio of 250, the average load taken by the girders is about 5.70 kN/m^2 which is close to the load at which yielding of the skeletal steel at mid span takes place. Thus the deflections in the box girders even at the yielding of the reinforcement are small. This observation validates the assumption in the proposed finite element model for nonlinear analysis of the ferrocement box girders of neglecting the geometrical nonlinearity. It is also seen from the test results that the maximum compressive strain anywhere in the top flange of the box girder is about 550 micron at the ultimate test load of seven brick layers. This indicates that even for the maximum load on the girder, the stress-strain curve of the mortar (Fig. 4.4) in the compression zone is still within the linear elastic range. This justifies the adopted linearly elastic - perfectly plastic stress-strain curve of the mortar in compression.

The theoretical analysis predicts diagonal shear cracks in the web near the support at seven brick layers. This corroborates well with the appearance of diagonal shear cracks in the web at seven brick layers. The longitudinal cracks at the junction of the top flange and the side webs are predicted at six brick layers between 250 mm to 575 mm from the mid span section. At seven brick layers, the longitudinal cracks spread from 250 mm to 1495 mm from the mid span section. The experimental longitudinal cracks were observed at seven brick layers and they had the average spread from about 500 mm to 1800 mm from the mid span section.

The theoretically predicted crack patterns in the girder at first crack and at three, five, six and seven brick layers are shown in Fig. 5.9. The experimental crack-pattern were photographed after marking the cracks on the girder surface at seven brick layers and painting of the cracks after

completely unloading the girder. The predicted crack-pattern in the bottom flange and side webs of the girder at seven brick layers shows a good comparison with the experimental crack-pattern. The theoretical analysis predicts longitudinal cracks on the bottom surface of the top flange in the mid span region at six brick layers. However, the experimental observation of such cracks is not possible due to the closed cell. At seven brick layers, these longitudinal cracks are predicted to increase along the length and width of the top flange. At seven brick layers, longitudinal cracks on the top surface are predicted at the junction with the side webs in the mid span region. Experimentally, the cracks on the top surface, if any, could not be seen due to the brick loading over its entire surface. If any cracking on the top surface takes place during loading, then these cracks close up after unloading of the girder. On unloading the girder no cracks were visible on the top surface.

No cracking or crushing of the diaphragms is predicted even at the ultimate load. Experimentally also, no cracking or crushing of the diaphragms was observed.

5.3 SINGLE CELL FERROCEMENT BOX GIRDERS SUBJECTED TO udl OVER HALF FLANGE WIDTH AND FULL SPAN

5.3.1 General Test Behaviour

Two single cell box girders marked G-3 and G-4 were tested under udl over half flange width and full span (Plate 5.4). In girder G-3, the first visible cracks appeared in the bottom flange at mid span below the loaded portion after the application of six brick layers (6.19 kN/m^2). The maximum crack width was 0.05 mm. The first visible cracks in girder G-4 appeared in the bottom flange, below the loaded portion after the application of five brick layers (5.15 kN/m^2) and the maximum crack width was 0.05 mm.

With the application of subsequent brick layers, more cracks appeared in the bottom flange and side webs. A total of nine brick layers (9.28 kN/m^2) were applied on both the girders. The maximum crack widths in the two girders at this load level were 0.20 mm and 0.22 mm respectively. The average spacing of cracks in the central part of the bottom flange were about 50 mm and 80 mm respectively. No shear cracks in the webs at the supports and no longitudinal cracks at the junction of the top flange and side webs were observed in the two girders. On unloading, the recoveries in mid span deflection below the loaded web in girders G-3 and G-4 were about 53 and 58 percent respectively. The crack-pattern of the bottom flange and side webs of girder G-3 is shown in Plate 5.5. Chipping of the bottom flange and side webs was done at several crack locations and the mortar compaction was found to be satisfactory. The cover to the wire mesh in girder G-3 varied from 5.60 mm to 7.14 mm with an average of 6.40 mm and in girder G-4 from 5.16 to 7.94 mm with an average of 6.55 mm. This compared well with the theoretical cover of 6.33 mm.

5.3.2 Finite Element Idealization

Nonlinear analysis of the girder was done by discretizing one half of the girder using 72 elements with 80 nodes (Fig. 5.10). A coarser mesh was used for the top flange as it remains in compression well within the elastic range all through the major part of the loading while a finer mesh was used for the bottom flange which cracks under tension. Since the wire mesh and skeletal steel reinforcement in these two girders is the same as provided in girders G-1 and G-2, the number of material types were four in this case also. The total superimposed load of 19.97 kN (or 9.28 kN/m^2) was applied in six load increments of 8.88, 2.22, 2.22, 2.22, 2.22 and 2.22 kN each. At the load of 19.97 kN (or 9.28 kN/m^2), both the residual vector norm

and energy norm ratios increased more rapidly thereby indicating proximity to the ultimate failure. The total computer time taken for complete displacement and stress output was 9 minutes and 13 seconds.

5.3.3 Comparison of Results

A comparison of the theoretical and experimental deflections below the loaded web at mid span is shown in Fig. 5.11. The predicted deflections in the elastic stage (i.e., upto five brick layers) are about 75 percent of the experimental deflections. This discrepancy in the elastic stage may be attributed to the marginally lower value of modulus of elasticity of the mortar in the girder as compared to the value obtained from the control mortar specimens as mentioned in Section 5.2.3. In the cracked stage, the predicted deflections continue to increase at a faster rate as compared to the experimental deflections. At six brick layers (6.19 kN/m^2), the predicted deflection is about 90 percent of the experimental deflection, at seven, eight and nine brick layers ($7.22, 8.25$ and 9.28 kN/m^2) the predicted deflections are about 12, 22 and 33 percent more than the experimental deflections.

The load-deflection curve at quarter span section below the loaded web is shown in Fig. 5.12. In the elastic stage (upto 11.1 KN or 5.15 kN/m^2), the predicted deflections are about 73 percent of the experimental deflections. In the cracked stage, the difference between the predicted and experimental deflections reduces. At six and seven brick layers, the predicted deflections are less than the experimental deflections by about 19 and 7 percent, while at eight and nine brick layers the predicted deflections are more by about 8 and 15 percent.

The variation of deflection across the width of the bottom flange is shown at the mid and quarter span sections in Fig. 5.13. The deflections below the loaded web are more than the deflections below the unloaded web.

A comparison of the predicted and experimental deflections is shown for five, seven and nine brick layers. Considering mid span section, at five brick layers (5.15 kN/m^2), the ratio of the predicted deflection to the experimental deflection varies from 1.13 below the unloaded web to 0.77 below the loaded web. At seven brick layers (7.22 kN/m^2), this ratio varies from 1.00 to 1.17. The maximum variation is at nine brick layers (9.28 kN/m^2) where this ratio varies from 1.52 below the unloaded web to 1.33 below the loaded web. Considering the quarter span section, at five brick layers, the ratio of the predicted to the experimental deflections varies from 1.08 below the unloaded web to 0.73 below the loaded web. At seven brick layer this ratio varies from 1.16 to 0.93 and at nine brick layer from 1.38 to 1.16.

The first crack load as predicted by the analysis is 8.93 kN (or 4.15 kN/m^2). The experimental first crack loads of girders G-3 and G-4 as evident from the nonlinearity of the load-deflection curves are about 12.2 kN (or 6.67 kN/m^2) and 10.0 kN or (4.65 kN/m^2).

The variation of longitudinal tensile strain at 25 mm above the soffit of the loaded web at the mid and the quarter span sections is shown in Figs. 5.14 and 5.15. Considering the mid span section (Fig. 5.14), the predicted strains in the elastic stage (upto five brick layers) are about 65 percent of the experimental strains. In the cracked stage, the predicted strains have increased at a faster rate as compared to the experimental strains. At six brick layers (6.19 kN/m^2), the predicted strain is 98 percent of the experimental strain. At seven, eight and nine brick layers the predicted strains are on the flexible side of the experimental strains. The yielding of the skeletal steel is predicted at nine brick layers thus leading to the large decrease in the slope of the load-strain curve. Considering quarter span section (Fig. 5.15), the predicted strains are about 66 percent of the experimental strains

upto six brick layers. At higher load levels, the predicted strains increase at a faster rate. At seven brick layers, the predicted strain is about 74 percent of the experimental strain while at eight and nine brick layers, the predicted strains are about 26 and 39 percent more than the experimental strains.

The slope of the predicted load-deflection and load-strain curves decreases very fast after cracking of the mortar because the specimens are under-reinforced (two layers of wire mesh giving volume fraction of 0.63 percent in the two principal directions). In the elastic stage, the contribution of the mortar to the rigidity of the ferrocement composite is more than 90 percent while after cracking the major contribution to the rigidity of the composite is through unyielded layers of wire mesh and skeletal steel and uncracked depth of the mortar. The contribution of the cracked mortar is, however, small.

The variation of the longitudinal strain across the girder depth on the loaded web side at the mid and the quarter span sections is shown in Figs. 5.16 and 5.17, respectively. The strain variation is shown at the load levels of five, seven and nine brick layers. The variation of the experimental strain at various load levels is approximately linear. Considering the mid span section (Fig. 5.16), at five brick layers the predicted strains are less than the experimental strains across the entire girder depth. The maximum variation is at 25 mm above the soffit where the predicted strain is about 59 percent of the experimental strain. Here the magnitudes of the strains are small because the girders are still in the uncracked stage. At seven brick layers, the predicted compressive strains in the cantilever flange are in good agreement with the experimental strains whereas in the remaining girder depth, the predicted tensile strains are more than the experimental strains. The maximum variation is at 25 mm above the soffit where predicted strain is about 38

percent more than the experimental strain. At nine brick layers, the predicted strains across the entire girder depth are large as compared to the experimental strains due to the predicted yielding of the skeletal steel of the bottom flange. Considering the quarter span section (Fig. 5.17), the predicted strains at five and seven brick layers are less than the experimental strains across the entire girder depth. The maximum variation is at five brick layers at 25 mm above the soffit where predicted strain is less than the experimental strain by about 32 percent. Here again the magnitude of the strains is small because the girder is in the uncracked stage. At nine brick layers, the predicted strains across the entire girder depth are more than the experimental strains and the maximum variation is at mid depth of the girder where predicted strain is about 47 percent more than the experimental strain.

The variation of longitudinal compressive strain (on the top surface of the top flange) across the width of the top flange at mid span section is shown in Fig. 5.18(a) and (b). The variation of compressive strain from the unloaded side to the loaded side is small in the uncracked stage and in the initial portion of the cracked stage (i.e. upto seven brick layers). In the later portion of the cracked stage, the compressive strains in the loaded portion are more than the compressive strains in the unloaded portion as is seen in both by analytical and the experimental results. The predicted and the experimental strains show a good agreement across the width of the top flange upto seven brick layers. The maximum variation is above the loaded web at nine brick layers where the predicted strain is more than the experimental strain by about 20 percent.

The load versus maximum crack width curves for the two girders are shown in Fig. 5.19. At the recommended crack width of $0.1 \text{ mm}^{(1)}$, the loads taken by girders G-3 and G-4 are 15.53 kN (or 7.22 kN/m^2) and 13.31 kN (or 6.19 kN/m^2), respectively. The girders withstood an average load of

14.42 kN (or 6.70 kN/m²) corresponding to 0.10 mm crack width which compares well with the total load of 13.31 kN (or 3.09 kN/m²) taken by girders G-1 and G-2 subjected to uniformly distributed load over the entire top flange. The average maximum mid span deflection below the loaded web at 0.1 mm crack width is about 5.0 mm. This corresponds to a span/deflection ratio of 916 which compares well with the average span/deflection ratio of 960 of girders G-1 and G-2. Thus the total load taken by ferroce-ment box girders at the recommended crack width of 0.1 mm is nearly the same, i.e., it does not depend on whether the load is applied on full flange or half flange width. Similarly, the maximum mid span deflection at the recommended crack width of 0.1 mm is also about the same. This shows the large inherent load distribution capacity of the box sections. At the maximum applied load of nine brick layers (19.97 kN or 9.28 kN/m²), the maximum crack widths in the bottom flange of the two girders were 0.20 mm and 0.22 mm respectively. At this load level, the average span/deflection ratio was about 380 which is even more than the recommended value of 250 from the serviceability limit state of deflection⁽¹⁶²⁾ criterion. Further, loading on the girders was stopped because of the fear of possible overturning of the girder resulting in likely injury to the personnel and damage to the dial gauges and strain measuring equipment.

The experimental studies did not show any visible longitudinal cracks at the junction of the top flange and the side webs and the same is the predic-tion of the theoretical analysis that there is no longitudinal cracking at the junction of top flange and side webs even at nine brick layers.

The theoretical analysis predicts diagonal shear crack in the loaded web near the support at nine brick layers. The predicted magnitude of the principal tensile strain is 168 micron. However, no visible diagonal tension crack was observed in the loaded web. Secondly, the predicted magnitude of the

tensile strain is about the same as the cracking strain of the mortar. A tensile strain of this order at any point in a structure of this size will cause only microcracking in the composite and the width of the crack will be too small to be observed by the naked eye.

The theoretically predicted crack-patterns in the girder at first crack and at five, seven and nine brick layers are shown in Fig. 5.20. The predicted crack-pattern of the bottom flange and side webs at nine brick layers shows a good agreement with the experimental crack pattern as shown in Plate 5.5. At nine brick layers the theoretical analysis also predicts the longitudinal cracks on the bottom surface of the loaded portion of the top flange at mid span. This part of the girder is invisible and hence the appearance of cracks, if any, could not be confirmed experimentally.

5.4 COMPOSITE SINGLE CELL BOX GIRDER WITH TOP FLANGE OF REINFORCED CONCRETE

5.4.1 General Test Behaviour

The composite single cell box girder was tested under uniformly distributed load over the entire top flange. The first visible cracks appeared in the bottom flange and side webs in the mid span region after the application of two brick layers (2.05 kN/m^2). The maximum crack width was 0.05 mm. At three brick layers (3.09 kN/m^2), a large number of cracks appeared and the maximum crack width increased to 0.10 mm. The girder was loaded upto six brick layers. At this load level the mid span deflection reached about 25 mm and the maximum crack width reached 0.20 mm. Further loading was not done due to the fear of possible failure of the girder and the subsequent damage to the measuring instruments. The average spacing of cracks at this load level was about 35 mm in the central part of the bottom flange. No diagonal shear cracks appeared in the web at the support sections. Also no

longitudinal cracks appeared at the junction of top flange and side webs. The girder was then unloaded. The instantaneous recovery in deflection at mid span was about 50 percent. The loaded girder along with the web cracks is shown in Plate 5.6.

5.4.2 Finite Element Idealization

The nonlinear analysis of the composite box girder subjected to uniformly distributed load over the entire top flange was done by discretizing one quarter of the girder into 44 elements with 56 nodes (Fig. 5.1). The total load of 26.63 kN (or 6.19 kN/m^2) was applied in five load increments of 8.88, 4.44, 4.44, 4.44 and 4.44 kN each. The failure of the girder at 26.63 kN load was indicated by a large increase in the deflections. Total computer time taken for complete displacement and stress output was 3 minutes and 44 seconds.

5.4.3 Comparison of Results

A comparison of the theoretical and experimental deflections at the mid and the quarter span sections is shown in Figs. 5.21(a) and 5.21(b). Considering mid span deflections (Fig. 5.21(a)), the predicted deflections in the elastic stage (i.e. upto two brick layers) are about 82 percent of the experimental deflections. In the cracked stage, the predicted deflections at three and four brick layers are less than the experimental deflections by about 47 and 19 percent while at five and six brick layers, these are more than the experimental deflections by about 7 and 28 percent. Considering quarter span section (Fig. 5.21(b)), the predicted deflections in the uncracked stage (i.e. upto two brick layers) are about 74 percent of the experimental deflections. In the cracked stage, at three and four brick layers the predicted deflections are less than the experimental deflections by about 40 and 22 percent, while at five and six brick layers, the predicted deflections are more than

the experimental deflections by about 3 and 21 percent. A close examination of the load deflection curves at the mid and the quarter span sections shows that the predicted deflections compare well with the experimental deflections over the entire load range except at three brick layers where the predicted deflections are highly on the stiffer side. Again the magnitude of deflections is small.

The theoretical first crack load is predicted at 8.45 kN (or 1.97 kN/m^2). The experimental first crack load as evident from the nonlinearity of the load-deflection results is about 7.80 kN (or 1.81 kN/m^2).

The load versus longitudinal tensile strain curves at the mid and the quarter span sections at 25 mm above the soffit are shown in Fig. 5.22. Considering the mid span section, the predicted strains at two and three brick layers are on the stiffer side of the experimental strains by about 40 percent. Again the magnitudes of the strains at these load levels are small. The predicted strain almost matches with the experimental strain at four brick layers. At five brick layers, the predicted strain is more than the experimental strain by about 14 percent. The yielding of skeletal steel and wire mesh layers of the bottom flange is predicted at six brick layers. The predicted strain at this load level is thus more than the experimental strain by about 10 percent. Considering the quarter span section, the predicted strains have shown a better comparison with experimental values as compared to the mid span section. The predicted strains at three and four brick layers are less than the experimental strains by about 29 and 21 percent while at five and six brick layers, the predicted strains are more than the experimental strains by about 16 and 11 percent.

The variation of longitudinal strain across the girder depth at the mid span section is shown in Fig. 5.23. At three brick layers, the predicted

compressive and tensile strains are less than the experimental strains across the entire girder depth. The maximum variation is at 25 mm above the soffit where predicted strain is less than the experimental strain by about 40 percent. At four brick layers the predicted strains are in good agreement with the experimental strains across the entire girder depth. At five brick layers the predicted compressive strains are in good agreement with the experimental strains whereas predicted tensile strains are more than the experimental strains. The maximum variation is at 75 mm above the soffit where the predicted strain is more than the experimental strain by about 18 percent. At six brick layers, the yielding of skeletal steel and wire mesh layers is predicted. The maximum variation is at 25 mm above the soffit where the predicted tensile strain is more than the experimental strain by about 40 percent.

From the variation of predicted longitudinal strains across the girder depth, it is clear that the neutral axis shifts inside the reinforced concrete flange at four brick layers. This is supported by the measured tensile strains at 35 mm below the top surface of the cantilever flange at five and six brick layers.

The variation of longitudinal strain across the girder depth at quarter span section is shown in Fig. 5.24. At three and four brick layers, the predicted compressive and tensile strains show good agreement with the experimental strains in the cantilever flange and major portion of the girder depth. The maximum variation is at 25 mm above the bottom flange at three brick layers where the predicted strain is less than the experimental strain by about 29 percent. At five and six brick layers also, the predicted strains show good agreement with the experimental strains in the cantilever flange and upto mid depth of the girder. The maximum variation is at 25 mm above the soffit at five brick layers where the predicted tensile strain is more than the experimental strain by about 16 percent.

At the quarter span section the position of the theoretical neutral axis shifts inside the reinforced concrete flange at five brick layers. This is supported by the measured tensile strain at 35 mm below the top surface of the cantilever flange at six brick layers.

The variation of longitudinal compressive strain on the top surface of the reinforced concrete flange at the mid span section is shown in Fig. 5.25. The predicted compressive strains show a good agreement with the experimental strains and the maximum variation is at six brick layers where the predicted strain is more than the experimental strain by about 27 percent.

The maximum experimental compressive strain in the composite box girder is about 400 micron. At this strain level, the stress-strain curve of the concrete is in the linear elastic range. Hence, the assumed linearly elastic-perfectly plastic stress-strain curve of concrete in compression is quite appropriate. In ferrocement structures, the ultimate failure in most of the cases is due to tensile cracking of the mortar and rarely by crushing of the mortar. Hence, a simple stress-strain relationship in compression is adequate to predict the post cracking behaviour satisfactorily.

The longitudinal cracks at the junction of the top flange and side webs of the test girder were absent even at six brick layers and the same is also confirmed by the proposed nonlinear analysis.

The proposed nonlinear analysis predicts diagonal shear cracks in the web at support at six brick layers. The predicted maximum principal tensile strain of 170 micron is of the order of cracking strain of the mortar. The tensile strain of this order will induce microcracking in the mortar and the width of crack will be too small to be observed with the naked eye. However, in the laboratory testing, the diagonal shear cracks were not observed in the webs, possibly due to above reasons.

The load versus maximum crack width curve is shown in Fig. 5.26. At the recommended crack width of 0.1 mm, the load taken by the composite box girder is 13.31 kN (or 3.09 kN/m^2) which is the same as obtained for ferrocement box girders. At this load level, the span/deflection ratio at mid span was about 910 which is about three and half times the recommended ratio of 250 from serviceability limit state of deflection point of view. At six brick layers, the maximum crack width in the bottom flange was 0.20 mm whereas at this load level, the maximum crack widths observed in girders G-1 and G-2 were 0.4 mm and 0.5 mm respectively. In all the box girders, it was noticed that only a few cracks had a crack width more than 0.1 mm and rest of the cracks had crack width less than 0.1 mm.

The load of six brick layers (26.66 kN or 6.19 kN/m^2) can be considered as near ultimate load for the composite box girder. At this load level the span/deflection ratio at mid span was about 190. Hence the deflections at near ultimate load are also small. This also justifies the assumption of neglecting geometrical nonlinearity in the proposed analytical method.

The predicted crack-patterns of the composite box girder at first crack, at three, four, five and six brick layers are shown in Fig. 5.27. The predicted crack-pattern of the bottom flange and side webs at six brick layers compares well with the experimental crack-pattern shown in Plate 6.4. At six brick layers, the theoretical analysis also predicts the transverse cracks on the bottom surface of the top flange in the mid span region. However, no observation could be made of the bottom surface of the top flange due to (i) small depth of the girder and (ii) closing of the cell by diaphragms.

5.5 DOUBLE CELL BOX GIRDER

The double cell box girder was subjected to loading and unloading under various combinations of symmetric and unsymmetric loads to study its behaviour

in the elastic stage. From the performance of the four single cell ferrocement box girders it was observed that the mid span deflection at the appearance of first crack was 4.0 to 5.0 mm. The single cell box girders were provided with two layers of wire mesh in the entire cross-section. In the double cell box girder, a third layer of wire mesh was also provided in the central 3.2 m length in the bottom flanges and upto half the depth of the webs. To be on the safer side, a lower value of 3 mm mid span deflection was assumed for applying maximum load on the girder so that the girder remains crack free. Under various loading conditions, the maximum observed deflection was about 3 mm as planned and no visible cracks appeared on the bottom flanges and side webs. The combined girder behaved as one single unit by undergoing downward deflections along the entire length and width. The loading and unloading paths under various loading conditions were quite close.

5.5.1 Unsymmetrical Loading Cases

The double cell box girder was first subjected to a udl of three brick layers over half the width of the top flange and full span length (Fig. 4.11(iii)). It was then unloaded and again subjected to the same loading but applied on the other half. The deflections in the two cases were comparable.

The girder was next subjected to a udl of six brick layers from one free end of the cantilever to the centre of the nearer box cell (Fig. 4.11(iv)). It was then unloaded. The same load was again applied on the other side of the girder.

The elastic analysis of the double cell box girder subjected to the above two loading cases was done by discretizing one half of the girder by 106 elements with 115 nodes (Fig. 5.28). Due to variation in the mesh and skeletal steel reinforcement six material types i.e. one material type for the top flange, two material types each for the webs and bottom flanges

and one material type for reinforced concrete diaphragms were used. The linear analysis for both the loading cases was done in one single computer run because the inverse of the structure stiffness matrix is required only once and it is used for obtaining the displacements at the nodal points and the stresses and strains at the Gauss points for both the loading cases. Total computer time taken was 3 minutes and 23 seconds.

- (i) For the first loading case of three brick layers (16.64 kN or 3.08 kN/m^2) over half width of top flange and full span, the deflections and strain variation at the mid span section are shown in Fig. 5.29(a) and (b). Considering mid span deflections (Fig. 5.29a), the predicted deflections below the loaded portion are less than the experimental deflections. The maximum difference is below the cantilever end of the loaded portion where the predicted deflection is about 22 percent less than the experimental deflection. The predicted deflection is comparable with the experimental deflection below the right web of the unloaded cell. Towards the cantilever end of the unloaded cell, the predicted deflection continue to be more than the experimental deflections. However, the magnitudes of the deflections in this portion are small. The comparison between the predicted and experimental deflections is reasonably good. The unsymmetrically placed load caused downward deflections only across the entire width.

The variation of the longitudinal strain across the cross-section at mid span is shown in Fig. 5.29(b). Considering the longitudinal compressive strains at the top surface, the predicted strain at the junction of the top flange and right webs of the loaded cell is less than the experimental strain by about 12 percent, while the predicted strain at the centre of the top flange is more than the experimental strain by about 22 percent. At the other points, the predicted strains compare

well with the experimental strains. The predicted longitudinal tensile strains on the soffit of the bottom flanges are less than the experimental strains in the loaded cell and the maximum difference is below the right web of the loaded cell where predicted strain is less by about 17 percent. The predicted strains are more than the experimental strains under the unloaded cell and the maximum variation is below the left web of the unloaded cell where the predicted strain is more by about 40 percent. However, the magnitude of the strains in the unloaded cell is only about one third of that in the loaded cell.

The strain variation across the girder depth is shown only for the front and back faces of the double cell girder. Strain measurements from the demec points was not possible on the inner webs due to practical reasons. Considering the back face of the girder under the loaded portion, the predicted compressive strains are comparable with the experimental strains, while predicted tensile strains are less than the experimental strains. At 25 mm above the soffit, the predicted tensile strains is less than the experimental strain by about 26 percent. At the front face of the girder, the predicted and the experimental strains are small (maximum value 50 microns) and comparable.

- (ii) For the second loading case having six brick layers (13.31 kN or 5.43 kN/m²) applied from the free end of the cantilever to the centre of the nearer cell, the deflections and strains at the mid span section are shown in Figs. 5.30(a) and (b). Considering the mid span deflections (Fig. 5.30a), the predicted deflections below the loaded cell are less than the experimental deflections. The maximum difference is below the cantilever end of the loaded cell where the predicted deflection is less than the experimental deflection by about 20 percent. The predicted

deflection matches the experimental deflection at the centre of the girder. From the right web to the cantilever end of the unloaded cell, the predicted deflections continue to be more than the experimental deflections. However, the magnitudes of the deflection are small. Considering the highly unsymmetric nature of the applied load over the extreme 0.23 times the width of the girder, the predicted deflections can be considered to have a reasonably good comparison with the experimental deflections.

The variation of the longitudinal strains across the cross-section at mid span is shown in Fig. 5.30(b). Considering the longitudinal compressive strains at the top surface, the predicted strains compare well with the experimental strains over the loaded cell while they are more than the experimental strains towards the cantilever end of the unloaded cell. The magnitude of the predicted and experimental strains over the unloaded cell portion is also small. The predicted and the experimental longitudinal tensile strains on the bottom flange of the loaded cell are comparable and the maximum variation is below the right web where the predicted strain is less than the experimental strain by about 13 percent. In the bottom flange of the unloaded cell, the predicted strains are more than the experimental strains. However, the magnitude of the predicted and experimental strains is small (maximum 30 micron). Considering the variation of the longitudinal strain across the girder depth on the back face of the loaded cell, the predicted compressive and tensile strains are comparable with the experimental strains i.e. at 5 mm below the extreme top surface, the predicted compressive strain is less than the experimental strain by about 17 percent while at 25 mm above the soffit, the predicted tensile strain is less than the experimental strain by about 10 percent. On the front face of the unloaded cell,

the predicted and the experimental strains at various depth levels are small. Thus the predicted strains have a reasonably good comparison with the experimental strains from the loaded face to the half width (or centre line) of the girder. Further away from the centre line to the other cantilever end, the predicted strains are more than the experimental strains.

5.5.2 Symmetrical Loading Cases

The double cell box girder was subjected to three symmetrical loading cases as shown in Figs. 4.11(v), (vi) and (vii). For the elastic analysis, one quarter of the double cell box girder was discretized by 53 elements with 61 nodes (Fig. 5.31). The linear elastic analysis for all the three loading cases was done in a single computer run. The total computer time taken for the displacement and stress output was one minute and twenty five seconds.

- (i) Girder subjected to five brick layers (22.19 kN or 4.53 kN/m^2) from free cantilever ends to the centres of the two cells:

Due to the above loading, the deflections and strain variation across the mid span cross-section are shown in Figs. 5.32(a) and (b). The experimental values of the deflections and strains at symmetrical points were close. Therefore, average values of the deflections and strains of symmetric points are plotted on one half of the cross-section. Considering the deflections at mid span (Fig. 5.32a), the predicted deflections are less than the experimental deflections and the difference decreases towards the centre of the girder. The maximum variation is at the cantilever end where the predicted deflection is less than the experimental deflection by about 3 percent.

The variation of the longitudinal strains at the mid span cross-section shown in Fig. 5.32(b). Considering the longitudinal compressive strains

at the top surface, the predicted strains compare well with the experimental strains except at the mid point of the cell where the predicted strain is more than the experimental strain by about 19 percent. Considering the longitudinal tensile strains on the bottom surface of the cell, the predicted strains are less than the experimental strains and the maximum variation is at the mid point of the bottom flange where the predicted strain is less than the experimental strain by about 11 percent. Considering the variation of the longitudinal strains across the girder depth, the predicted compressive and tensile strains compare well upto the mid span of the girder. The maximum variation is at 25 mm above the soffit, where the predicted strain is less than the experimental strain by about 12 percent.

- (ii) Girder subjected to four brick layers (26.63 kN or 4.51 kN/m^2) on the two cells:

Due to the above loading, the variation of average deflections and strains of the symmetric points across the mid span cross-section are shown in Figs. 5.33(a) and (b) respectively. Considering the deflections at mid span (Fig. 5.33a), the predicted deflections are less than the experimental deflections and the maximum variation is at the cantilever end where the predicted deflection is less than the average experimental deflection by about 4 percent.

The variation of longitudinal strain at mid span cross-section is shown in Fig. 5.33(b). Considering longitudinal compressive strains at the top surface, the predicted strains are comparable with the experimental strains and the maximum variation is at the centre of the top flange where predicted strain is more than the experimental strain by about 13 percent. Considering longitudinal tensile strains on the bottom surface of the cell, the predicted strains are more than the average experimental strains and the maximum variation

is at the centre of the bottom flange where predicted strain is more by about 16 percent. Considering variation of the longitudinal strains across the girder depth, the predicted strains are comparable with the experimental strains in the cantilever flange and at mid depth. The maximum variation is at 25 mm above the soffit where the predicted strain is less than the experimental strain by about 17 percent.

- (iii) Girder subjected to seven brick layers (23.3 kN or 7.89 kN/m^2) in the central part of the top flange:

Due to this loading, the deflections and strain variation across the mid span cross-section are shown in Figs. 5.34(a) and (b). The predicted mid span deflections are less than the average experimental deflections and the difference between the two reduces towards the free cantilever end. At the free cantilever end the two deflections almost match. The maximum variation is below the left web of the right cell where the predicted deflection is less than the average experimental deflection by about 11 percent.

The variation of longitudinal strain at mid span cross-section is shown in Fig. 5.34(b). Considering longitudinal compressive strains at the top surface, the predicted strains compare well with the experimental strains. The maximum variation is above the left web of the right cell where predicted strain is less than the average experimental strain by about 11 percent. Considering longitudinal tensile strains on the bottom surface of the right cell, the predicted strain is less than the average experimental strain by about 7 percent below the left web and more than the average experimental strains at the centre of the bottom flange and below the right web by about 12 percent and 11 percent respectively. Considering the variation of longitudinal strains across the girder depth, the predicted strains compare well with the average experimental strains over the entire girder depth.

Thus due to symmetrically placed loads, the predicted vertical deflections and longitudinal strains across the girder cross-section at mid span have shown reasonably good comparison with the average experimental deflections and strains. The predicted deflections have been less than the average experimental deflections by a maximum of 14 percent. The predicted longitudinal strains at the top and bottom surfaces have been within ± 18 percent of the average experimental strains.

5.6 CRACK WIDTH AND CRACK SPACING

In the proposed analytical method, strains at the top and bottom surfaces of the elements are evaluated at the Gauss points (sampling points). If the principal tensile strain at the Gauss points exceeds the cracking strain of the mortar, the mortar is assumed to crack in a direction perpendicular to the principal tensile strain direction. The method also determines the depth of the crack at the Gauss points. With an increase in the applied load, the propagation of the cracks on the surface as well as across the thickness of the elements is predicted. The method does not determine the location of cracks (or spacing of cracks) but rather checks at the Gauss points whether the mortar has cracked or not. The number and positions of the Gauss points depend upon the order of Gauss quadrature used for the numerical integration and the fineness of the mesh (i.e. size of the elements) chosen for discretizing the structure. For the sake of completeness of the study, the experimentally observed average spacing of cracks and maximum crack widths at failure or maximum applied load are compared with the analytical/empirical expressions reported by various researchers.

The experimentally observed average spacing of cracks is compared with the analytical/empirical expressions reported by Naaman and Shah⁽³⁷⁾, Luq and Parna⁽³⁸⁾ and Desayi and Ganesan⁽⁶⁸⁻⁷⁰⁾. Naaman and Shah derived

Eq. 2.5 for the average spacing of cracks for ferrocement in direct tension. The average spacing of cracks was assumed to be 1.5 times the minimum crack spacing. Huq and Pama derived Eq. 2.7 for the maximum spacing of cracks for ferrocement in direct tension and used the same for flexural elements. They assumed the maximum spacing of cracks as twice the minimum crack spacing. Hence for comparing the average spacing of cracks, the Eq. 2.7 given by Huq and Pama is multiplied by $\frac{1}{2} \times 1.5 = 0.75$.

In calculating the average crack spacing by Desayi's method (Eq. 2.24), the box section is idealized into an equivalent I section having unequal flanges and web thickness equal to twice the girder web thickness. From the strain distribution curves (Figs. 5.6, 5.16 & 5.23) across the girder depth by finite element analysis; it is seen that the position of neutral axis at the maximum applied load is close to the junction of the top flange and the web. Therefore, for calculating the average crack spacing at failure, it is assumed that the neutral axis lies at the junction of the top flange and the web. The split tensile strength and ultimate bond strength of the mortar are assumed to be equal and the coefficients K_b , K_t and n are assumed to be $\frac{2}{3}$, $\frac{2}{3}$ and 0.4⁽⁷⁰⁾.

A comparison of the experimentally observed average crack spacing at failure (or at maximum applied load) with the values predicted from the expressions given by Naaman and Shah⁽³²⁾, Huq and Pama⁽³⁸⁾ and Desayi and Ganesan⁽⁶⁸⁻⁷⁰⁾ is shown in Table 5.1. The values predicted by Desayi and Ganesan⁽⁶⁸⁻⁷⁰⁾ show a better agreement with the experimental values, the maximum variation being 19 percent as compared to the values predicted by Naaman and Shah⁽³²⁾ and Huq and Pama⁽³⁸⁾ giving maximum variation of 38 and 37 percent respectively.

	(kN)	Experimental	Huq and Pama ⁽³⁸⁾ (Eq. 2.7)	Naaman and Shah ⁽³²⁾ (Eq. 2.5)	Desayi and Ganesan ⁽⁶⁸⁻⁷⁰⁾ (Eq. 2.24)
1. Girders G-1 and G-2 subjected to udl over entire top flange	31.07	40	48.0	30.8	40.5
2. Girders G-3 and G-4 subjected to udl over half flange width and full span	19.97	50, 80	48.0	30.8	40.5
3. Composite box girder G-6 subjected to udl over entire top flange	26.63	35	48.0	30.8	41.3

The maximum crack widths in all the girders were observed in the mid span region of the bottom flange. A common feature after the appearance of cracks was that a few cracks were distinctly wider than the other cracks. The widths of these cracks were recorded after the application of each brick layer. The maximum and the average widths of these cracks at various load levels for all the girders is shown in Tables 4.8 , 4.12 and 4.35 .

The experimentally observed maximum crack widths are compared with the values obtained from analytical/empirical equations 2.6, 2.8, 2.15 and 2.27 given respectively by Naaman⁽⁴⁴⁾, Huq and Pama⁽³⁸⁾, Logan and Shah⁽⁵⁹⁾ and Desayi and Ganesan⁽⁶⁸⁻⁷⁰⁾ in Table 5.2. The equations 2.6, 2.8 and 2.15 are valid only upto the yielding of the extreme wire mesh layer whereas Eq. 2.27 is independent of the yielding of wire mesh and depends only upon the strain in the extreme mortar fiber. The maximum crack widths predicted by all the equations in the initial portion of the cracked range are far less than the experimental values. The values predicted by Eq. 2.8 (Huq and Pama) even at the yielding of extreme wire mesh layer are far less than the experimental values. The values predicted by Eq. 2.6 (Naaman) compare well with the experimental values of girders G-3, G-4 and G-6 in the later portion of the cracked range and upto the yielding of extreme wire mesh layer. The values predicted by Eq. 2.15 (Logan and Shah) show a better comparison with the experimental values as compared to other equations in the later portion of the cracked range and upto the yielding of extreme wire mesh layer. The values predicted by Eq. 2.27 (Desayi and Ganesan) fall between the values predicted by Eq. 2.8 and Eq. 2.6.

In the experimental investigation, the recommended crack width of 1 mm was reached in one of the cracks soon after the appearance of the first visible crack while the maximum crack width predicted at this load by various equations is quite small. From a limited number of test data on

		Experimental	Naaman (Eq. 2.6)	Huq & Pama (Eq. 2.8)	Logan & Shah (Eq. 2.15)	Desayi & Ganesan (Eq. 2.27)
1. Girders G-1 & G-2 subjected to udl over entire top flange	13.31	0.1, 0.1	0.024	-	0.011	0.013
	22.19	0.25, 0.30	0.078	0.006	0.099	0.065
	26.63	0.40, 0.50	0.188*	0.101*	0.239*	0.129
	31.07	0.60, 0.80	0.193	0.106	0.247*	0.358
2. Girders G-3 & G-4 subjected to udl over half flange width & full span	13.31	0.05, 0.05	0.024	-	0.009	0.014
	15.53	0.10, 0.15	0.027	-	0.040	0.031
	17.75	0.15, 0.18	0.070	-	0.084	0.059
	19.97	0.20, 0.22	0.161	0.078	0.200	0.112
3. Composite box girder G-6 subjected to udl over entire top flange	13.31	0.10	0.024	-	0.007	0.009
	17.75	0.12	0.046	-	0.058	0.043
	22.19	0.16	0.119*	0.041*	0.144*	0.086
	26.63	0.20	0.193	0.106	0.247*	0.178

* predicted values of maximum crack width at yielding of extreme layer of wire mesh which occurs at a load less than the one shown against them.

near prototype box girders, the experimental maximum crack widths at failure have been found to be 1.0 to 3.0 times the predicted maximum crack widths. The ratio of the experimental maximum crack widths to the average crack widths has been found to vary from 1.4 to 2.0. The probable reasons for the experimentally observed maximum crack widths being larger than the predicted maximum crack widths, especially in the initial portion of the cracked range are (i) low volume fraction of the mesh reinforcement, (ii) relatively large mortar cover (≈ 6.3 mm), (iii) the large size of the specimens and (iv) the compaction difficulty in casting ferrocement box girder elements.

The effect of the mesh reinforcement is reflected in the form of well distributed cracks in the bottom flange and side webs in the central 60 to 70 percent of the span length. The girders have shown a high ductility by taking an ultimate load (or maximum applied load) 2.0 to 3.0 times the load at the appearance of the first crack or undergoing deflections at ultimate load of 5.0 to 6.0 times the deflection at the appearance of first cracks.

5.7 CONCLUDING REMARKS

(i) The predicted deflections in the elastic stage vary from 70 to 89 percent of the experimental deflections. This difference may be due to the modulus of elasticity of the mortar in the cast girders being marginally lower than the one obtained from the control mortar specimens. In the cracked stage the difference between the two reduces. The predicted deflections show a reasonably good agreement with the experimental deflections upto the predicted yielding of the reinforcement. Beyond this, the predicted deflections become large as compared to the experimental ones due to the assumed linearly elastic-perfectly plastic stress-strain curves of the reinforcement.

(ii) The predicted strains in the elastic stage are small and in good agreement with the experimental strains. After cracking of the mortar, the strains

increase at a fast rate. The predicted and the experimental strains show a reasonably agreement upto the predicted yielding of the reinforcement. Beyond this the predicted strains become large as compared to the experimental ones due to the assumed linearly elastic-perfectly plastic stress-strain curves of the reinforcement.

(iii) The maximum compressive strains at the ultimate load in single cell ferrocement box girders and the composite box girder are relatively small and lie within the linearly elastic portion of the stress-strain curves of the mortar and concrete. Hence, the assumed linearly elastic-perfectly plastic stress-strain curves of the mortar and concrete in compression are adequate.

(iv) The predicted first crack loads show a good agreement with the experimental first crack loads of the various girders whereas the predicted ultimate loads are on the flexible side of the experimental ultimate loads. This is due to the assumed linearly elastic-perfectly plastic stress-strain curves of skeletal steel and wire mesh.

(v) The predicted crack - patterns of the bottom flange and side webs at the maximum applied load of various girders show a good agreement with the experimental crack-patterns. The added advantage of the analytical method is the prediction of cracks on the soffit of the top flange at ultimate or near ultimate loads. These cracks otherwise can not be observed due to the closed form of the cell.

(vi) The maximum experimental deflection at the ultimate load is about $l/150$ (i.e. relatively small). This justifies the neglecting of the geometrical nonlinearity in the proposed finite element analysis of the box girders.

(vii) At the recommended crack width of 0.1 mm, the total load taken by single cell ferrocement box girders either in the form of udl over the entire

top flange or mid span over half flange width and full span is nearly the same. Also, the maximum mid span deflection in both the loading cases is about the same. This shows the large load distribution capacity of the box section. At this load level an average span/deflection ratio is about 940 which is about four times the limiting ratio of 250 as per I.S. Code⁽¹⁶²⁾ from serviceability requirement of limit state of deflection. At a span/deflection ratio of 250, the average load taken by the girders is about 5.70 kN/m^2 which is close to the load at which yielding of the skeletal steel at mid span takes place.

(viii) Replacing the top flange by reinforced concrete results in the lowering of the first crack load by about 30 percent. However, the load taken by the composite girder at the recommended crack width of 0.1 mm is about the same as taken by ferrocement box girders. The ultimate load taken by the composite girder is also reduced by about 14 percent.

(ix) The average spacing of cracks predicted by Eq. 2.24 given by Desayi and Ganesan⁽⁶⁸⁻⁷⁰⁾ has shown better agreement with the experimental values of the present investigation as compared to the values predicted by Naaman and Shah⁽³²⁾ and Huq and Pama⁽³⁸⁾.

(x) The predicted maximum crack widths in the initial portion of the cracked range by all the equations considered are far less than the experimental values of the girders. The predicted maximum crack widths using Equations 2.6 (Naaman) and 2.15 (Logan and Shah) have shown relatively better agreement with the experimental values in the later portion of the cracked range and upto the yielding of the extreme layer of wire mesh.

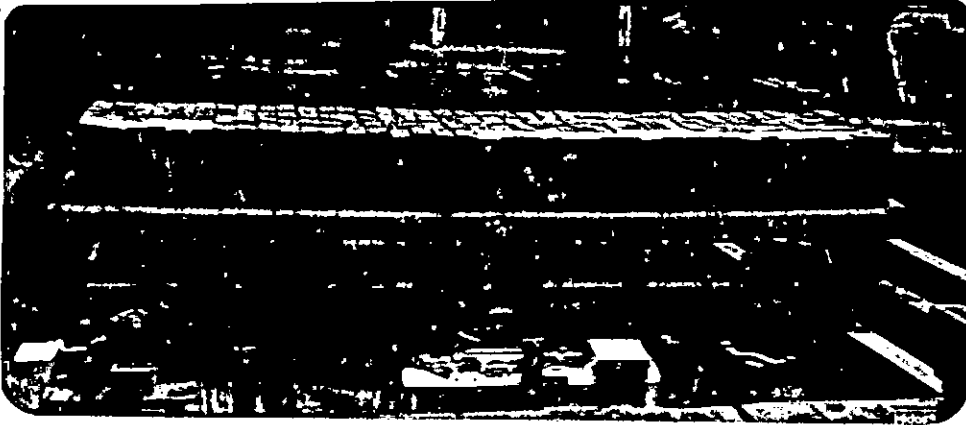


PLATE 5-1 SINGLE CELL BOX GIRDER SUBJECTED TO
UDL OVER THE ENTIRE TOP FLANGE

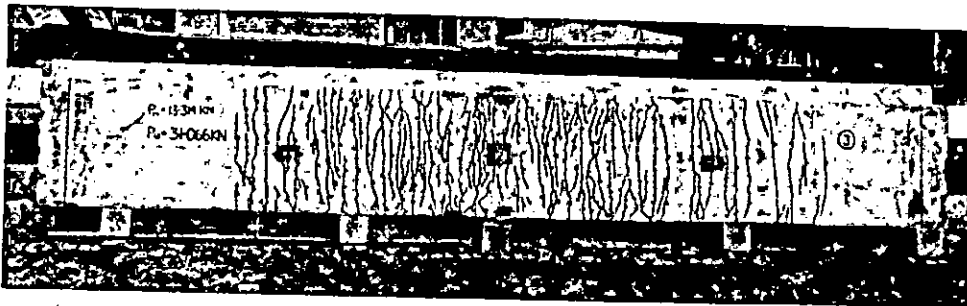
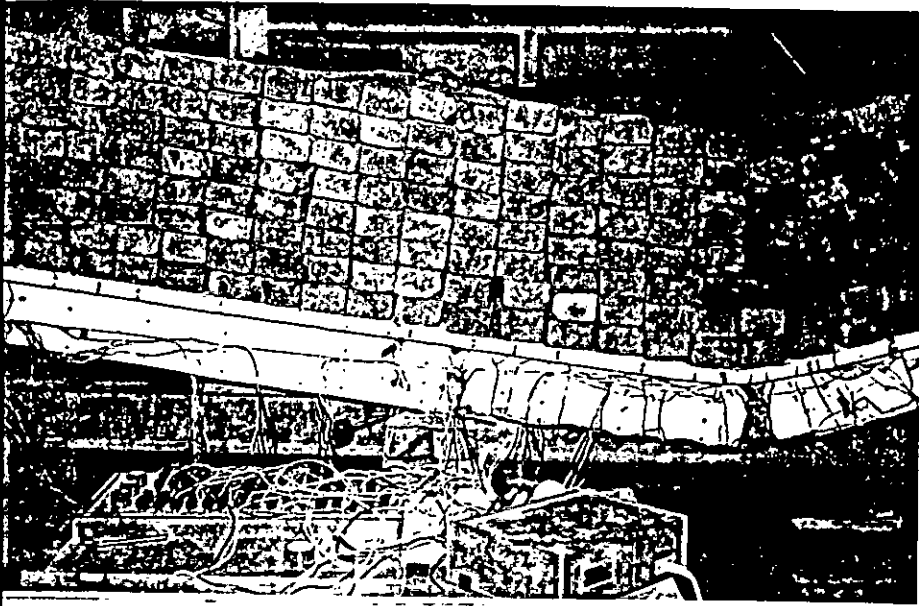
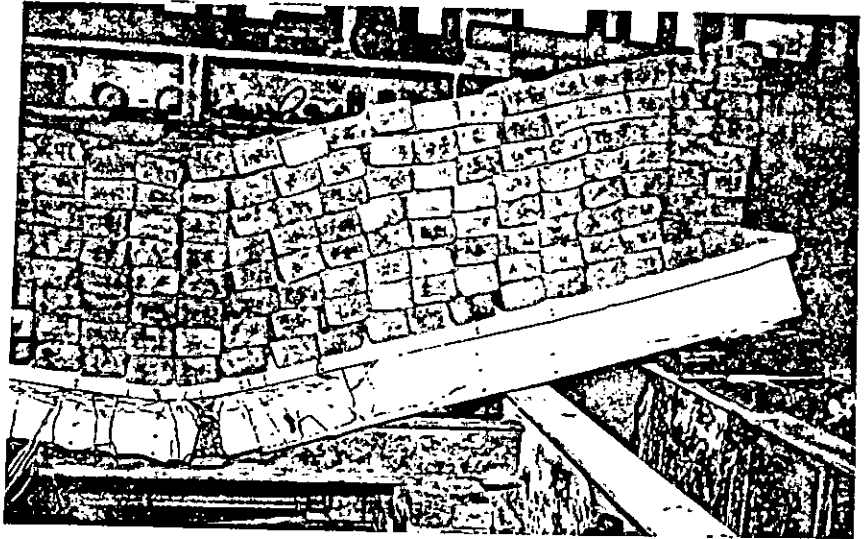


PLATE 5-2 CRACK-PATTERN OF THE BOTTOM FLANGE
AND SIDE WEBS OF THE ABOVE BOX GIRDER



(A)



(B)



(C)

5-3 FAILURE OF THE SINGLE CELL BOX GIRDER DUE TO SNAPPING OF WIRE MESHES OF BOTTOM FLANGE AND SIDE WEBS.

(A) LEFT HALF, (B) RIGHT HALF, (C) CLOSE-UP VIEW



PLATE 5.4 SINGLE CELL BOX GIRDER SUBJECTED TO UDL
OVER HALF FLANGE WIDTH AND FULL SPAN



PLATE 5.5 CRACK PATTERN OF THE BOTTOM FLANGE
AND SIDE WEBS OF THE ABOVE GIRDER



PLATE 5.6 COMPOSITE BOX GIRDER HAVING TOP FLANGE
OF R.C.C. SUBJECTED TO UDL OVER THE
ENTIRE TOP FLANGE

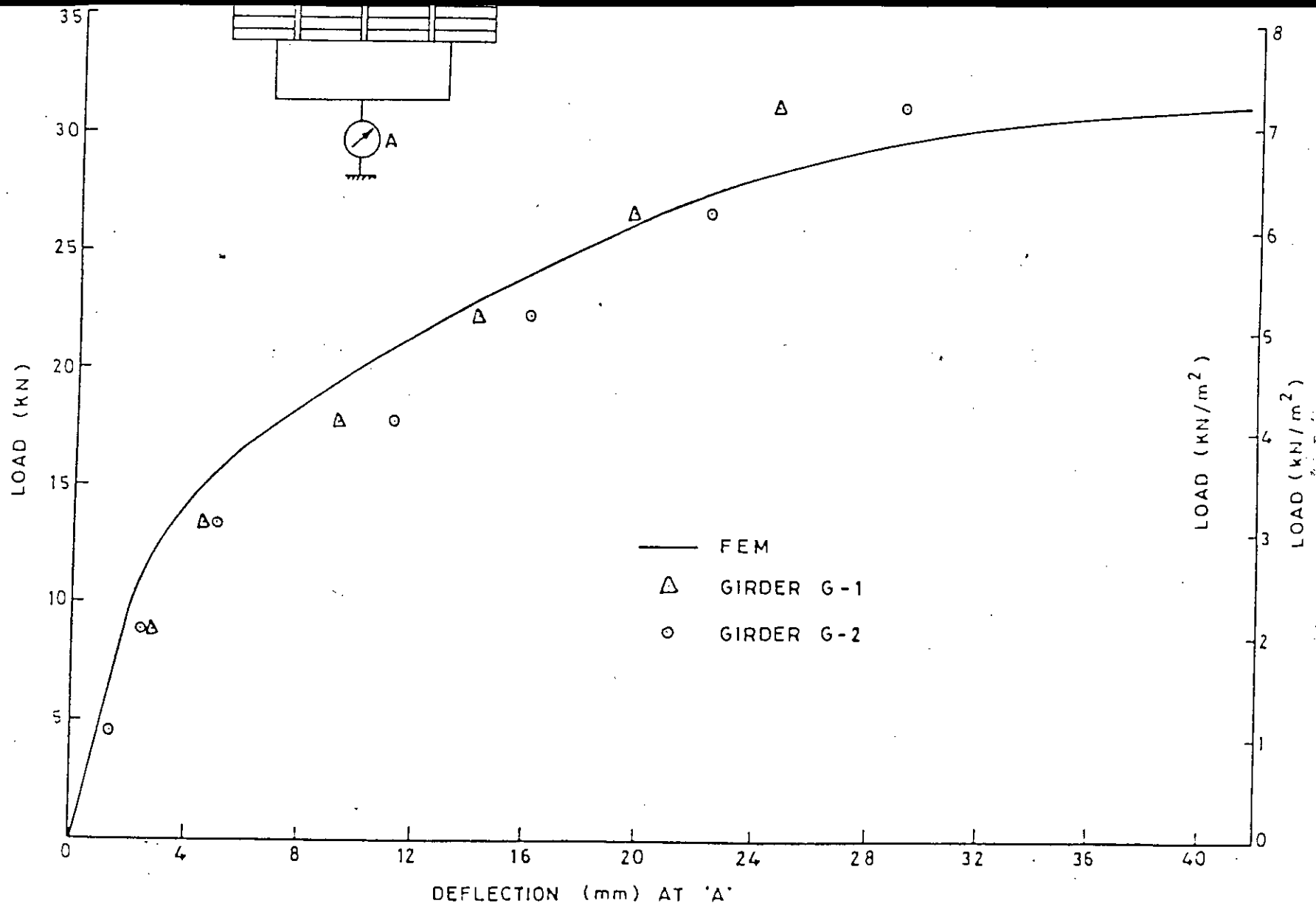


FIG. 5.2 —LOAD VS. MID SPAN DEFLECTION FOR GIRDERS G-1 AND G-2

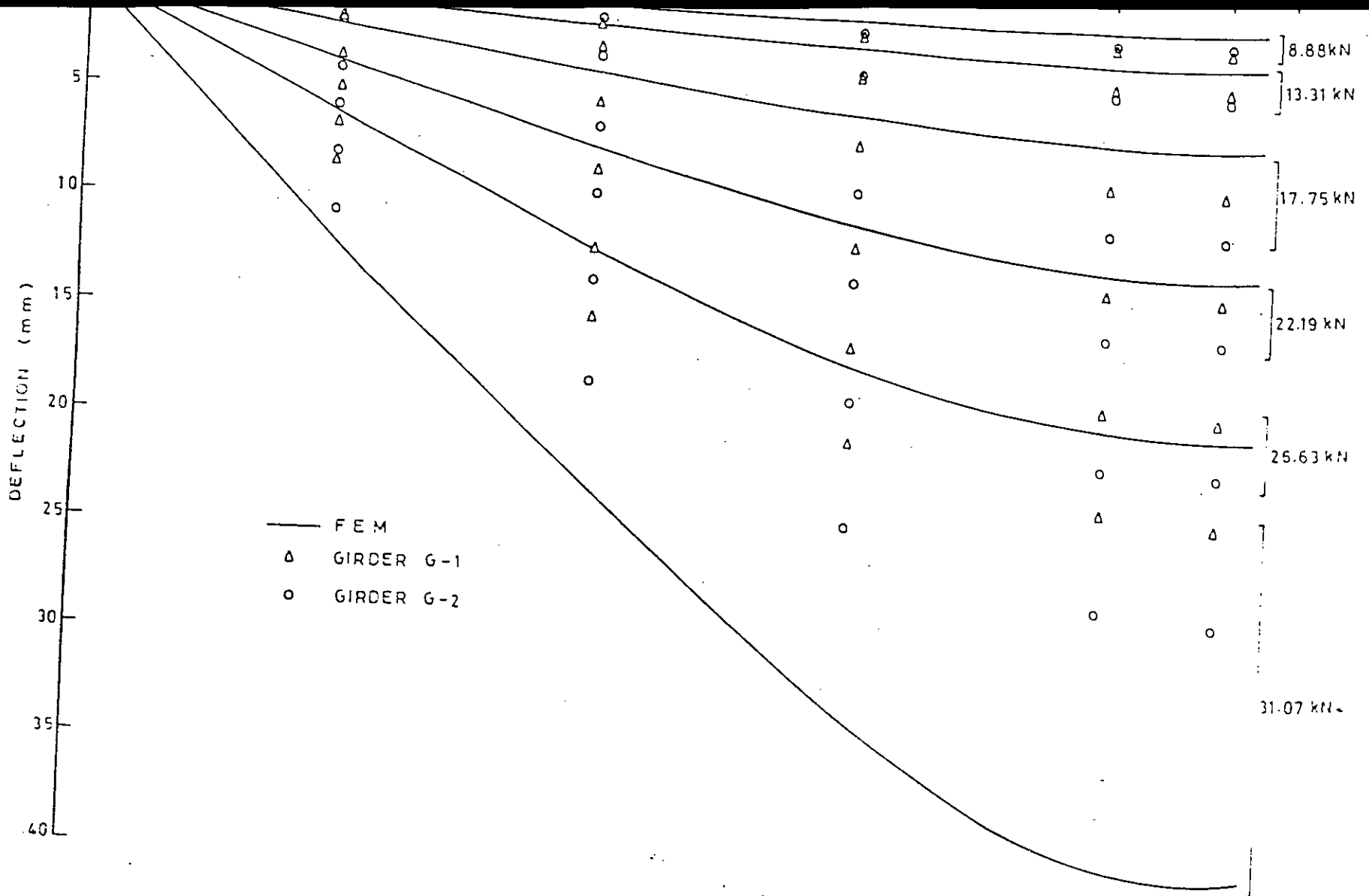


FIG. 5.3 DEFLECTIONS ALONG THE SPAN AT VARIOUS LOAD LEVELS

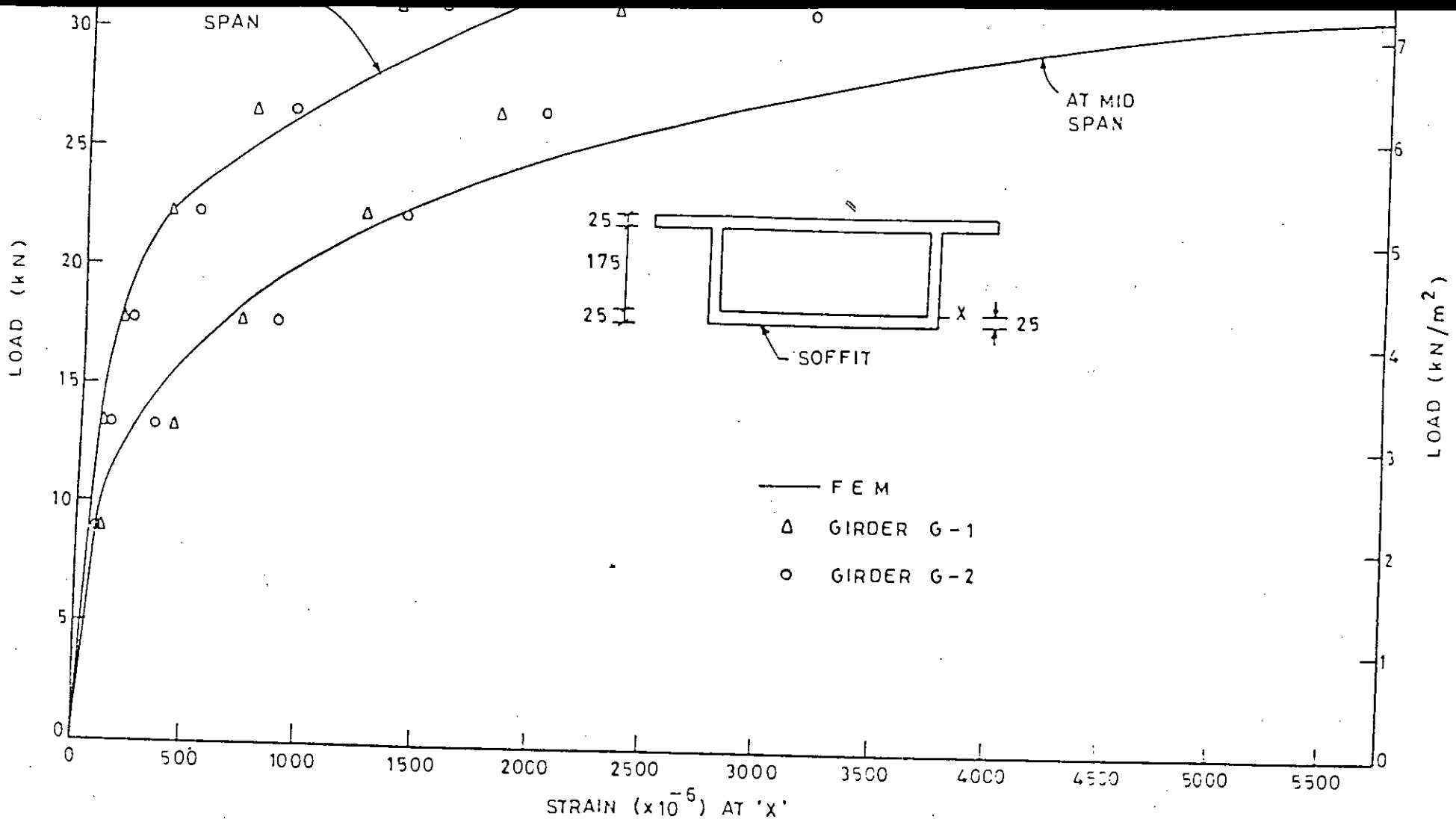


FIG. 5.4 - LOAD VS. LONGITUDINAL TENSILE STRAIN AT 25 mm ABOVE THE SOFFIT

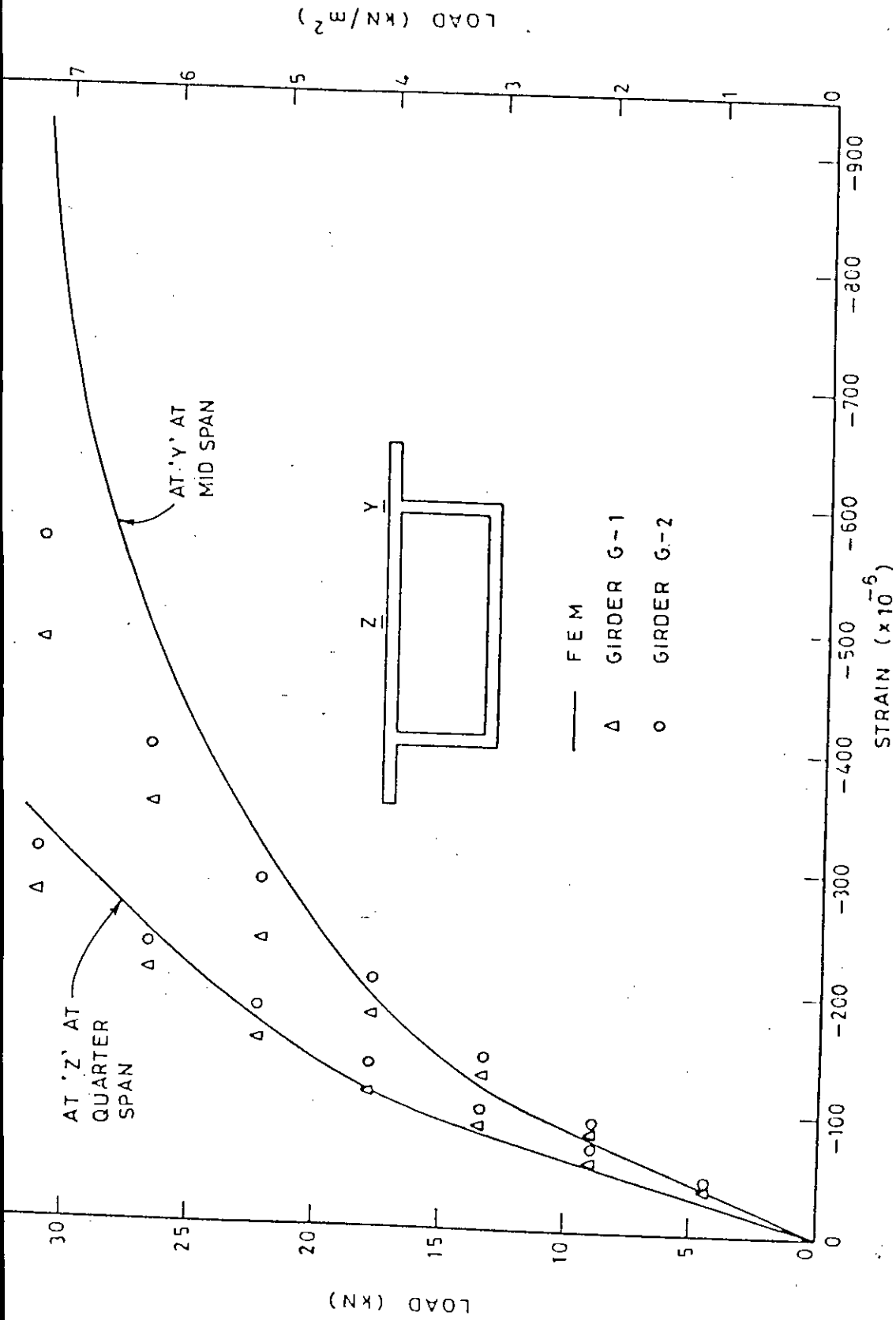


FIG. 5.5 LOAD VS LONGITUDINAL COMPRESSIVE STRAIN AT THE TOP FLANGE

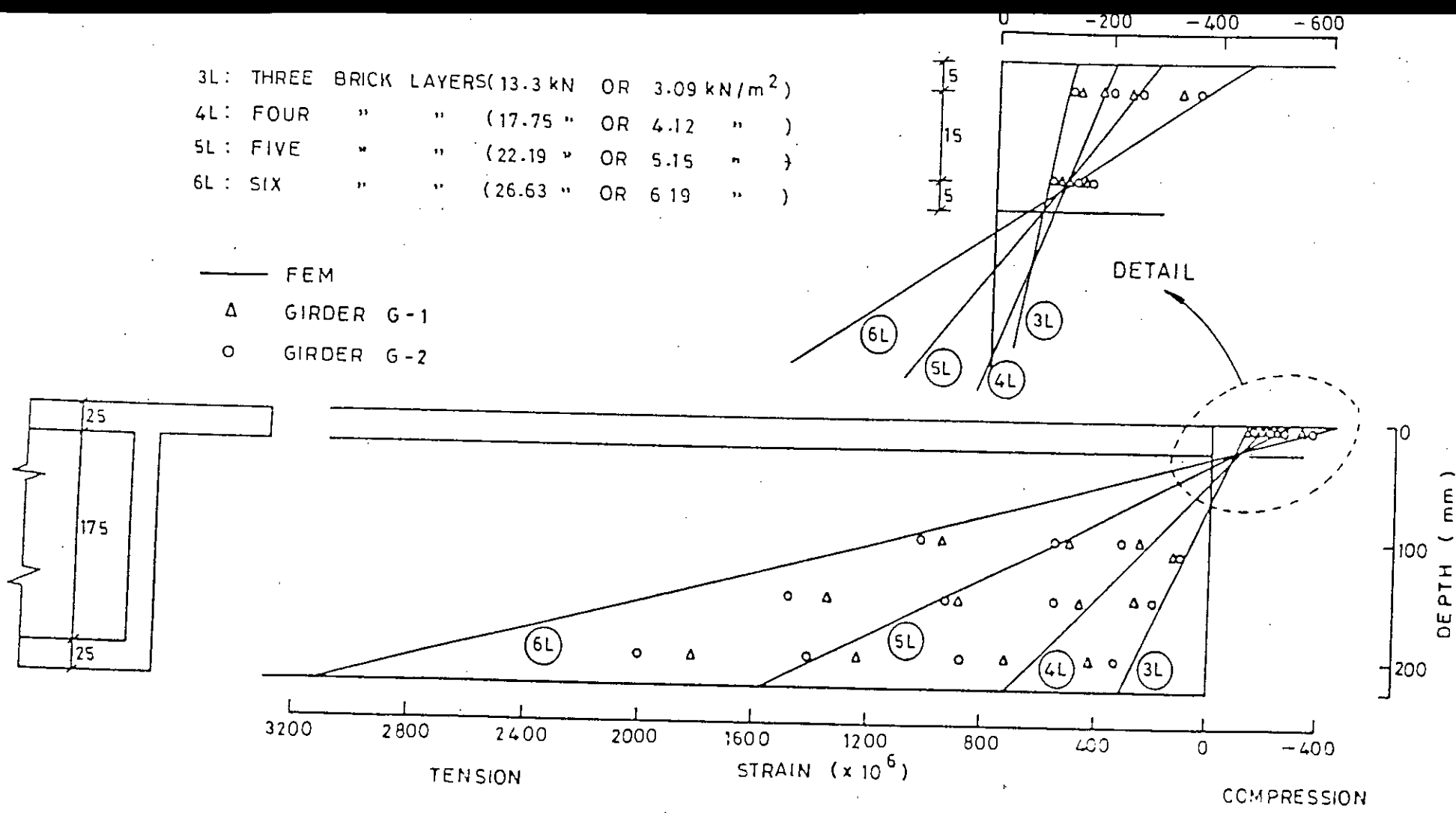


FIG. 5.6 - VARIATION OF LONGITUDINAL STRAIN ACROSS THE GIRDER DEPTH AT MID SPAN

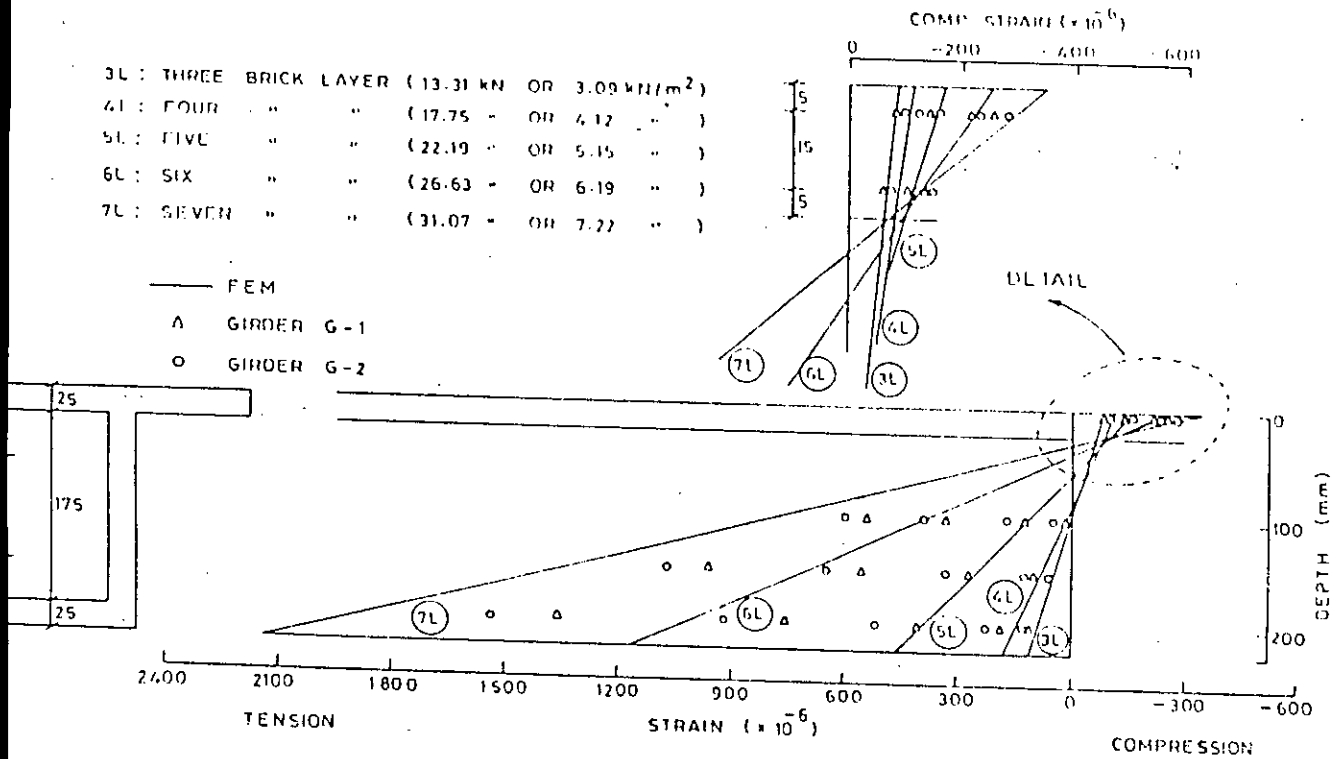


FIG.5.7— VARIATION OF LONGITUDINAL STRAIN ACROSS THE GIRDER DEPTH AT QUARTER SPAN

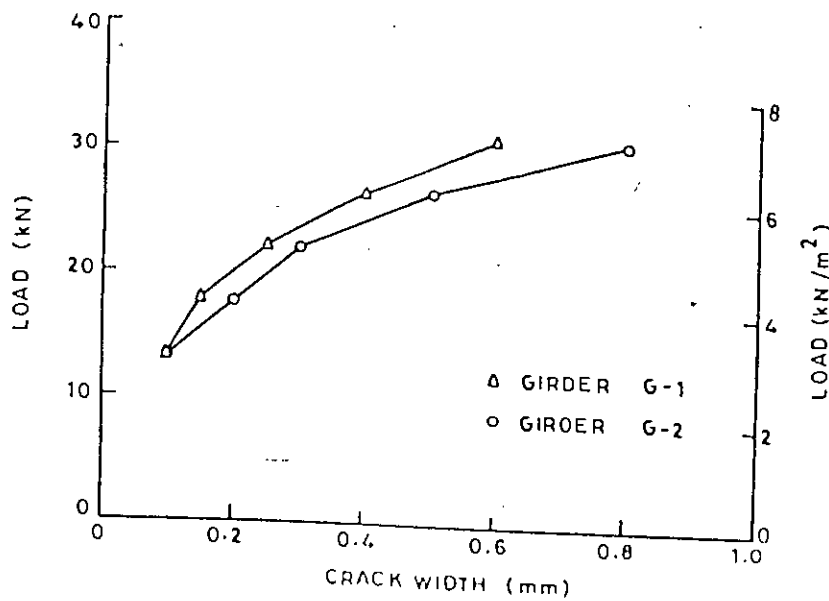
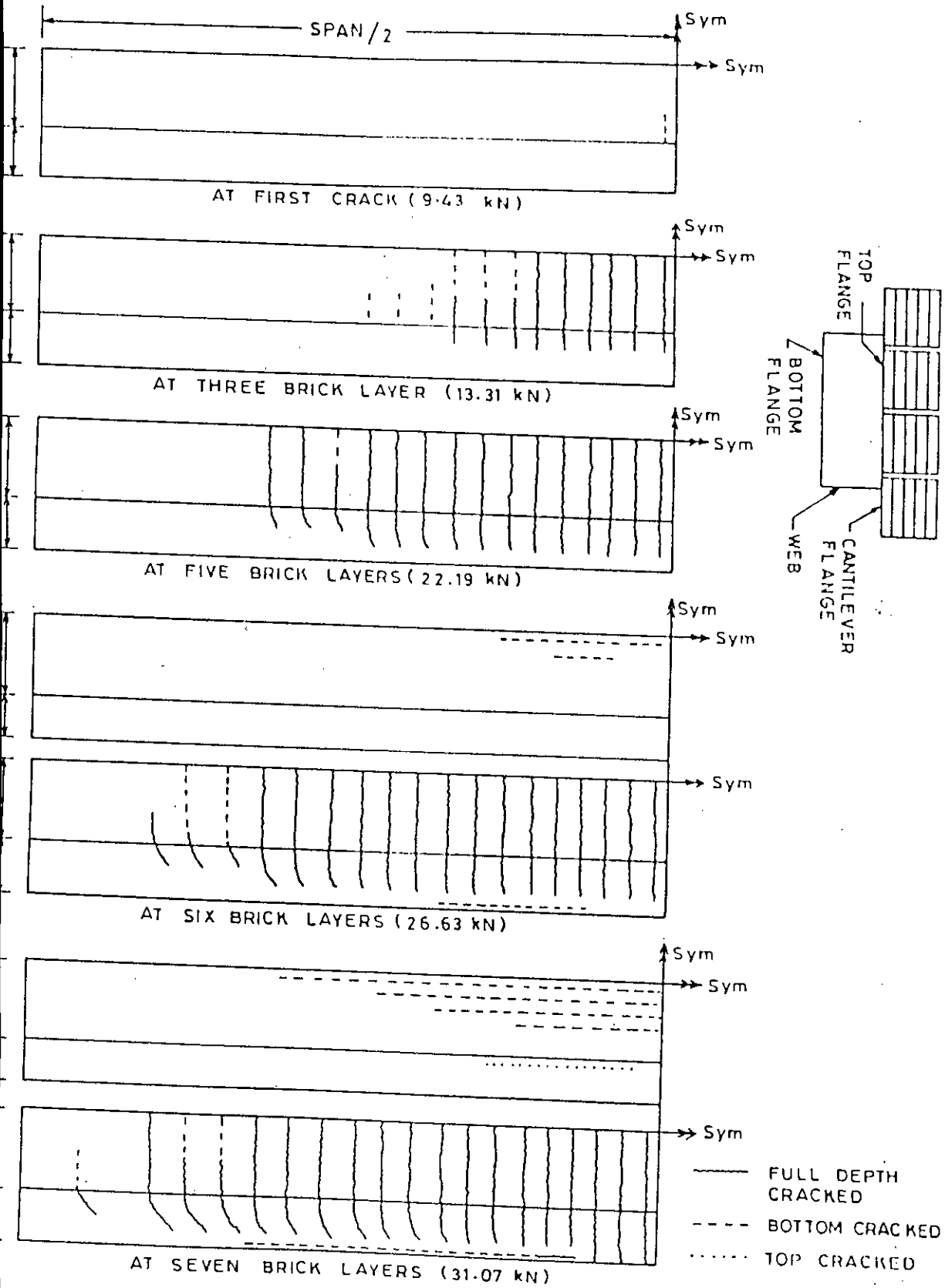


FIG.5.8—LOAD VS MAXIMUM CRACK WIDTH



9— PREDICTED CRACK-PATTERNS OF SINGLE CELL BOX GIRDER SUBJECTED TO UDL OVER ENTIRE TOP FLANGE

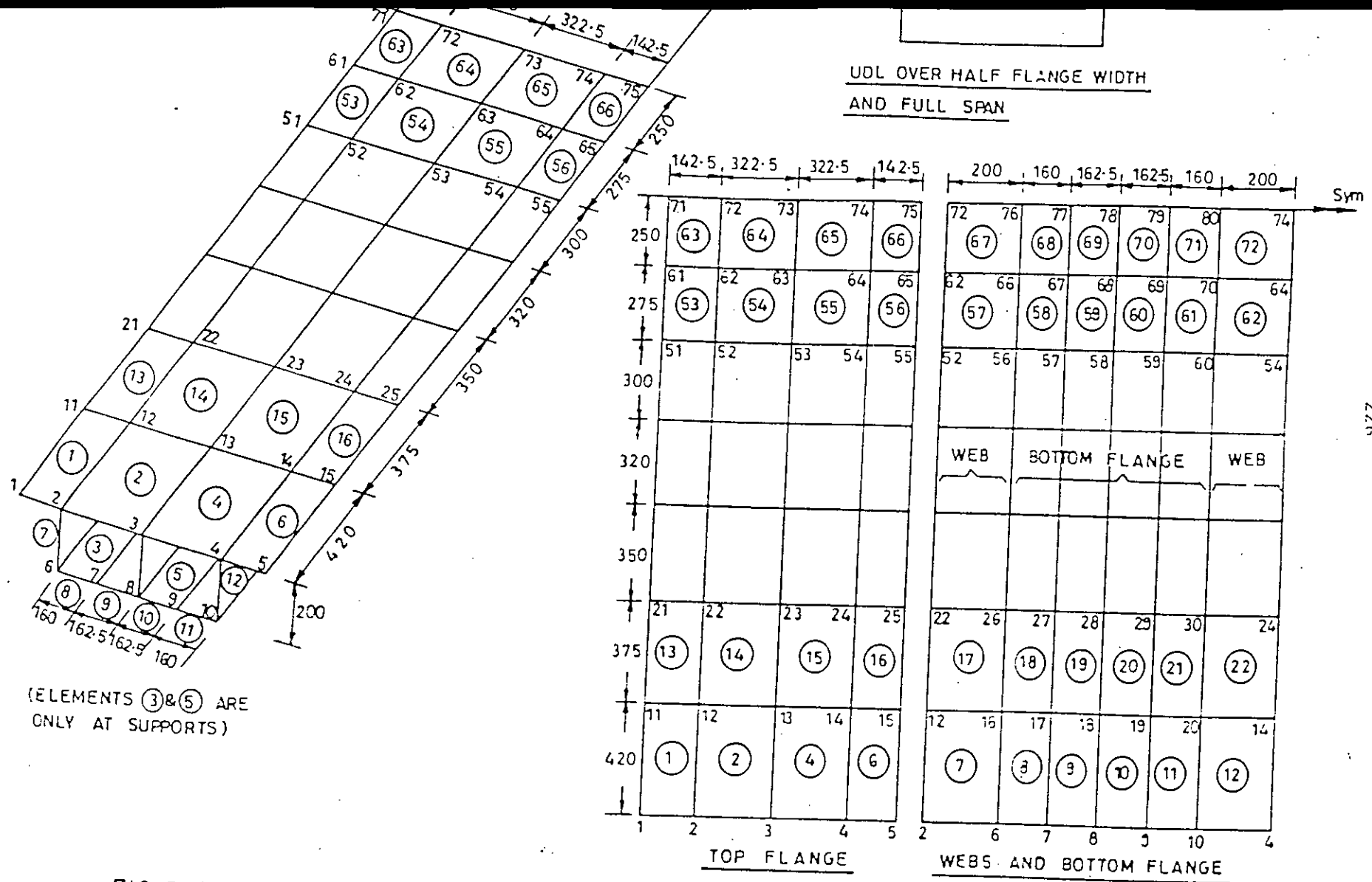


FIG. 5-10— DISCRETIZATION OF BOX GIRDER SUBJECTED TO UDL OVER HALF FLANGE WIDTH AND FULL SPAN

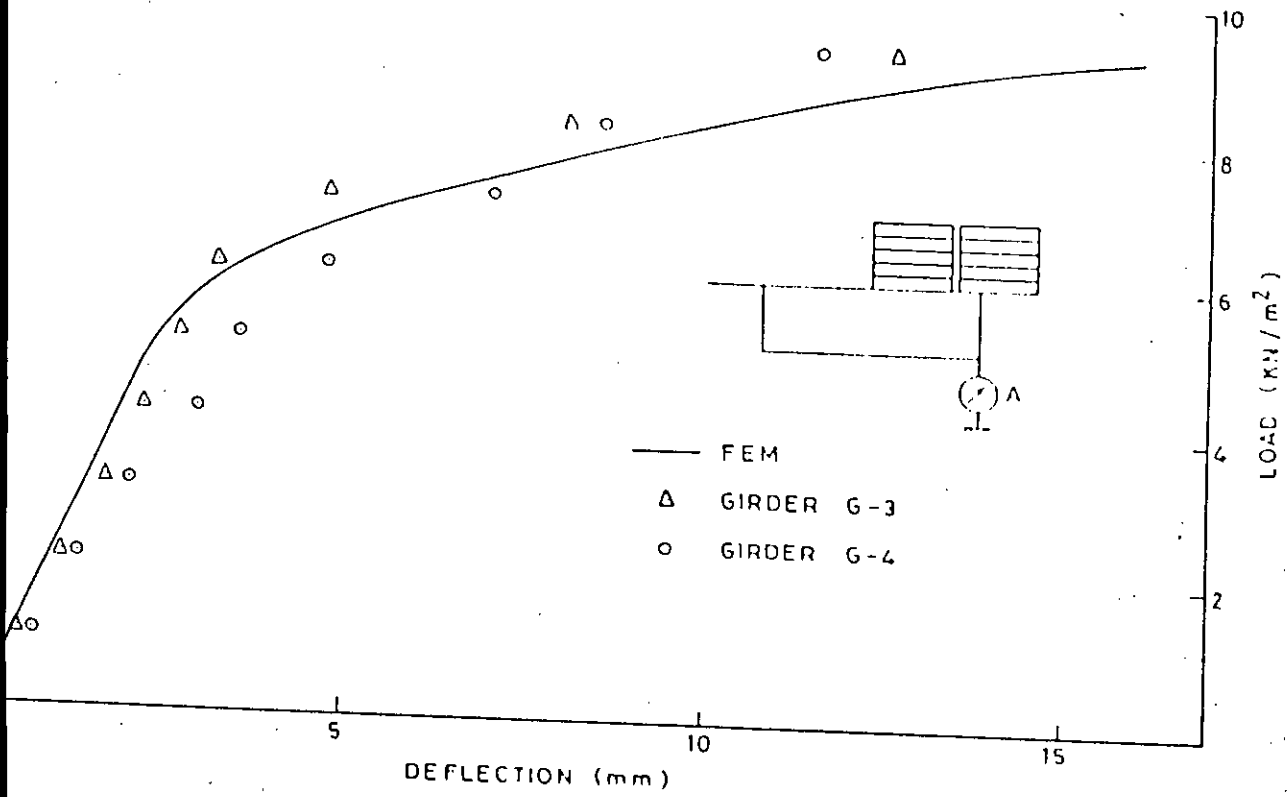


FIG. 5.11. —LOAD VS. MID SPAN DEFLECTION AT 'A'

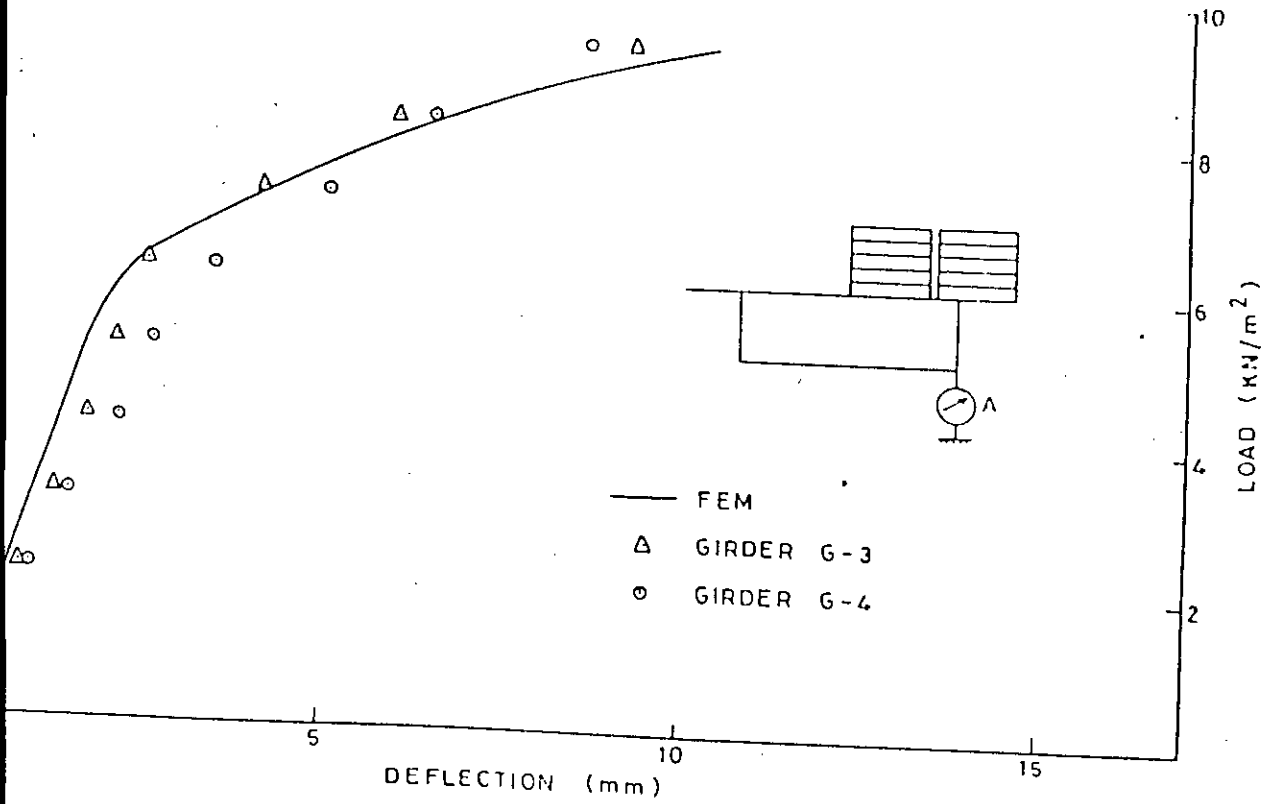
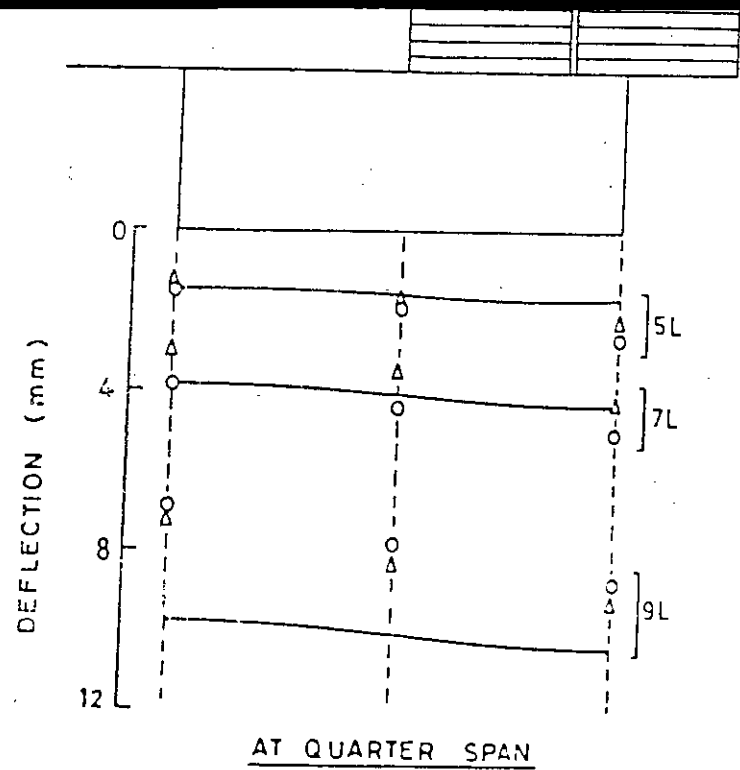
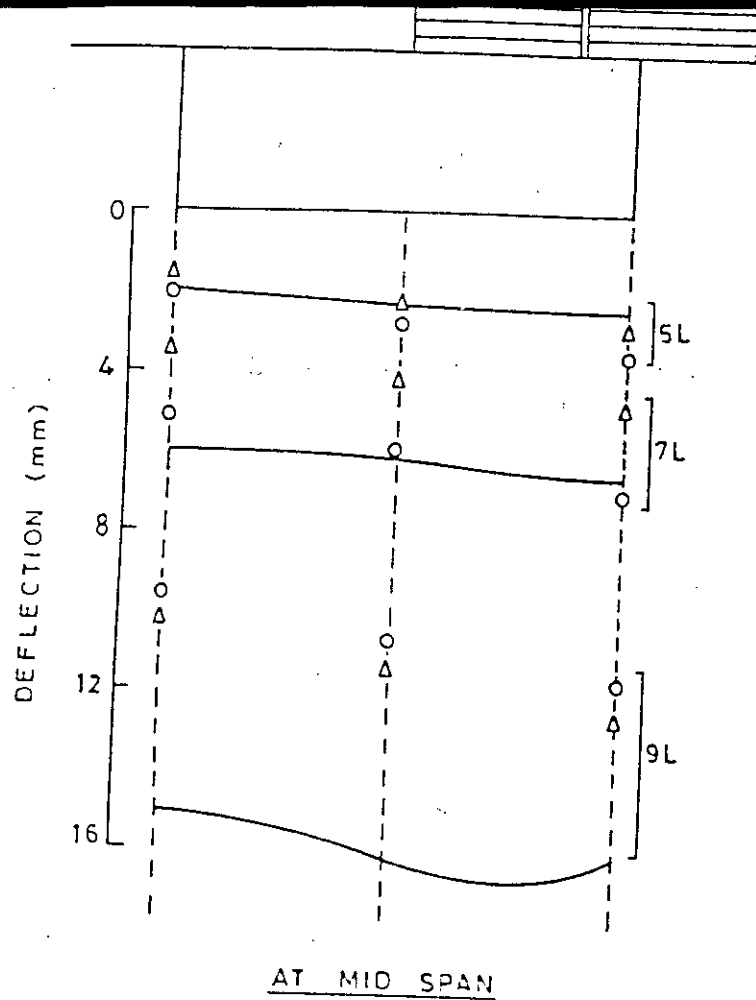


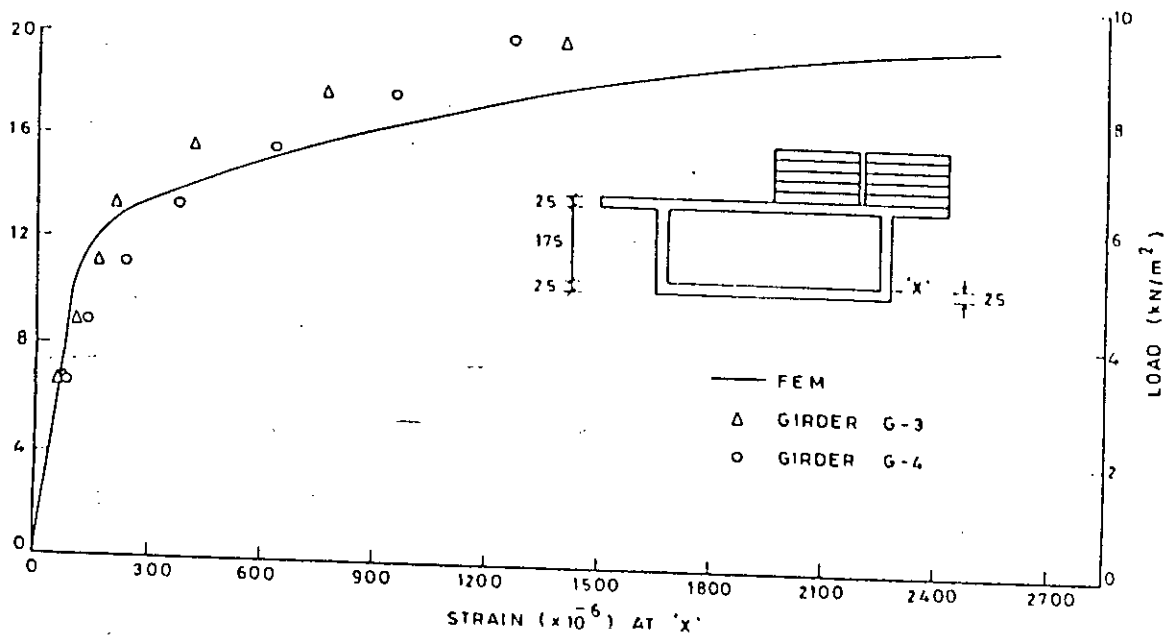
FIG. 5.12 —LOAD VS. QUARTER 'SPAN DEFLECTION AT 'A'



5L: FIVE BRICK LAYERS (11.10 kN OR 5.15 kN/m²)
 7L: SEVEN " " (15.53 " OR 7.22 ")
 9L: NINE " " (19.97 " OR 9.28 ")

— FEM
 Δ GIRDER G-3
 ○ GIRDER G-4

FIG. 5.13 — DEFLECTIONS ACROSS THE CROSS - SECTION



G. 5.14 - LOAD VS. LONGITUDINAL TENSILE STRAIN IN LOADED WEB AT MID SPAN

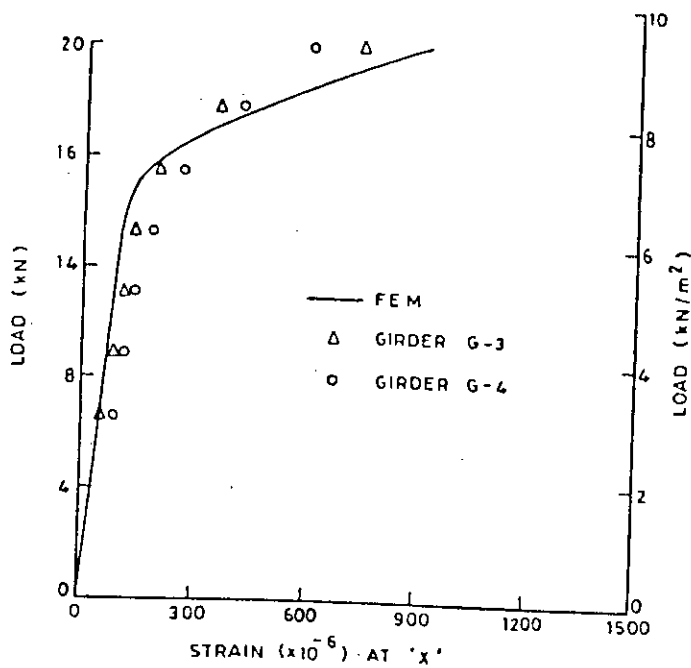


FIG. 5.15 - LOAD VS. LONGITUDINAL TENSILE STRAIN IN LOADED WEB AT QUARTER SPAN

5L: FIVE BRICK LAYERS (11.10 kN OR 5.15 kN/m²)
 7L: SEVEN " " (15.53 " OR 7.22 ")
 9L: NINE " " (19.97 " OR 9.28 ")

— FEM
 Δ GIRDER G-3
 ○ GIRDER G-4

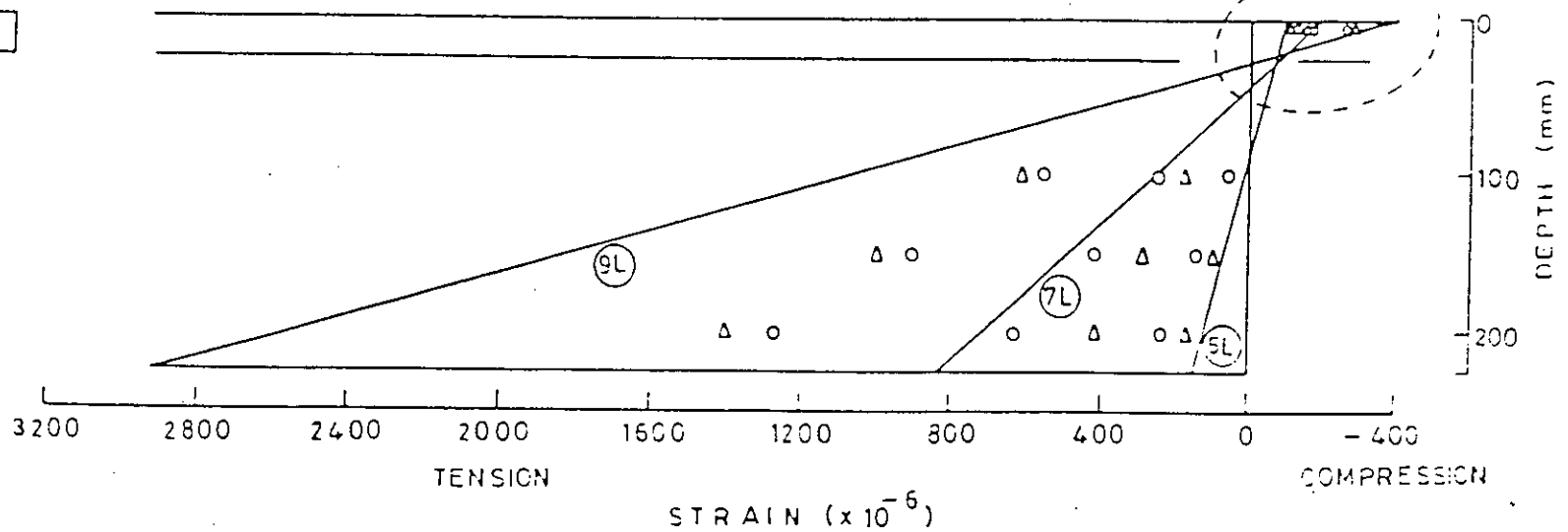
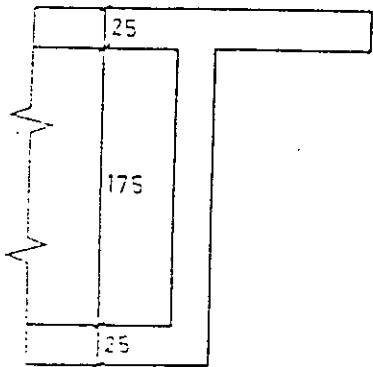
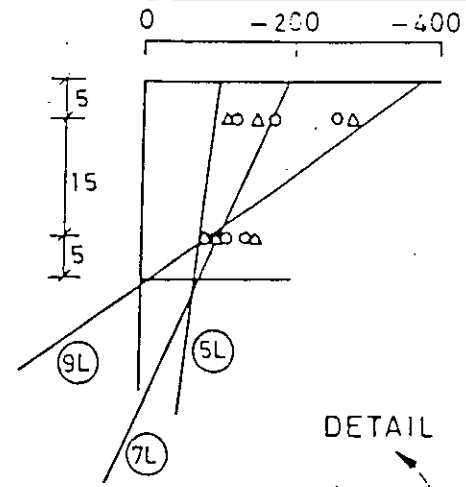


FIG. 5.16 — VARIATION OF LONGITUDINAL STRAIN ACROSS THE GIRDER DEPTH AT MID SPAN (LOADED SIDE)

5L: FIVE BRICK LAYERS (11.10 kN OR 5.15 kN/m²)
 7L: SEVEN " " (15.53 " OR 7.22 ")
 9L: NINE " " (19.97 " OR 9.28 ")

— FEM
 Δ GIRDER G-3
 ○ GIRDER G-4

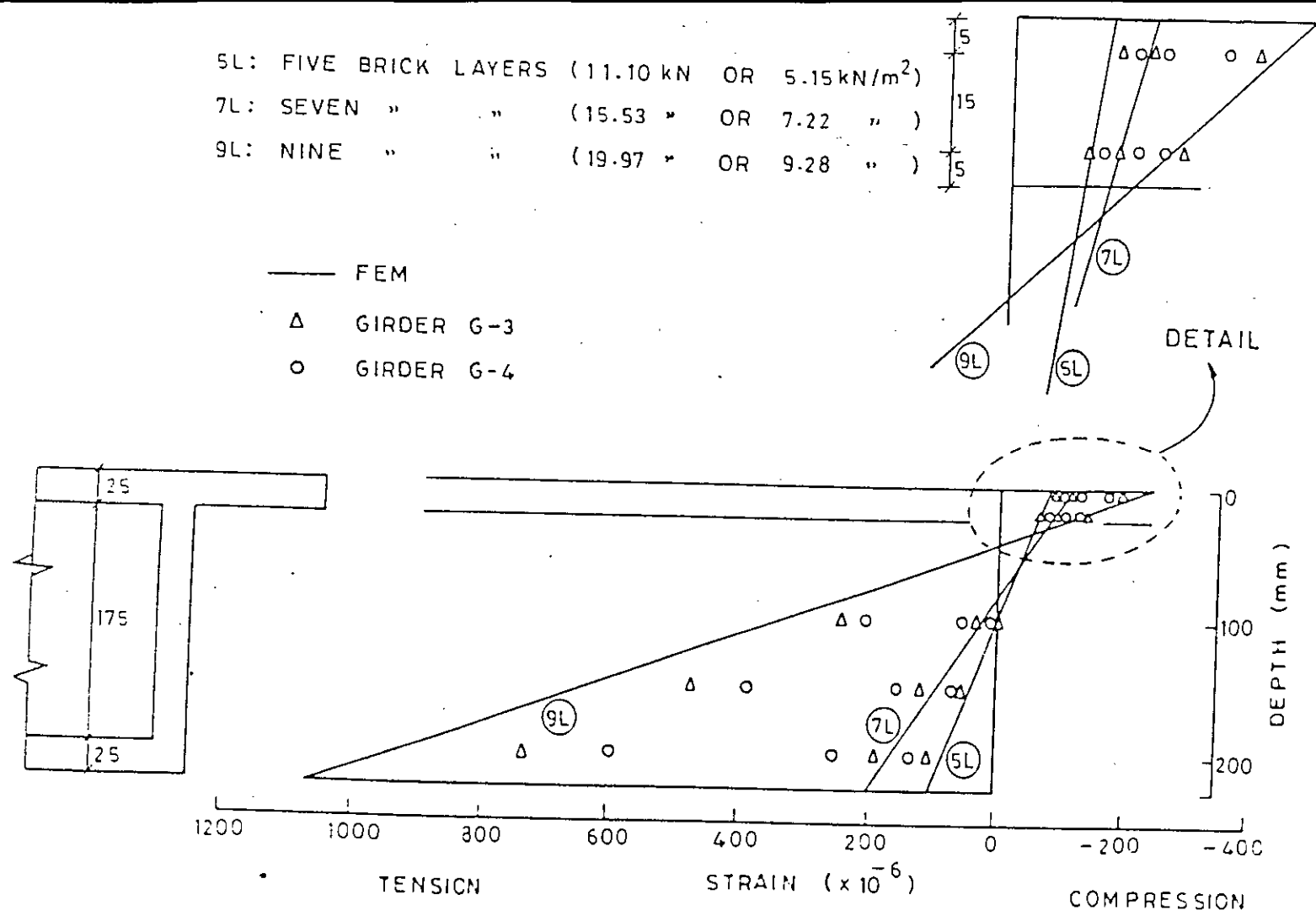


FIG. 5.17— VARIATION OF LONGITUDINAL STRAIN ACROSS THE GIRDER DEPTH AT QUARTER SPAN (LOADED SIDE)

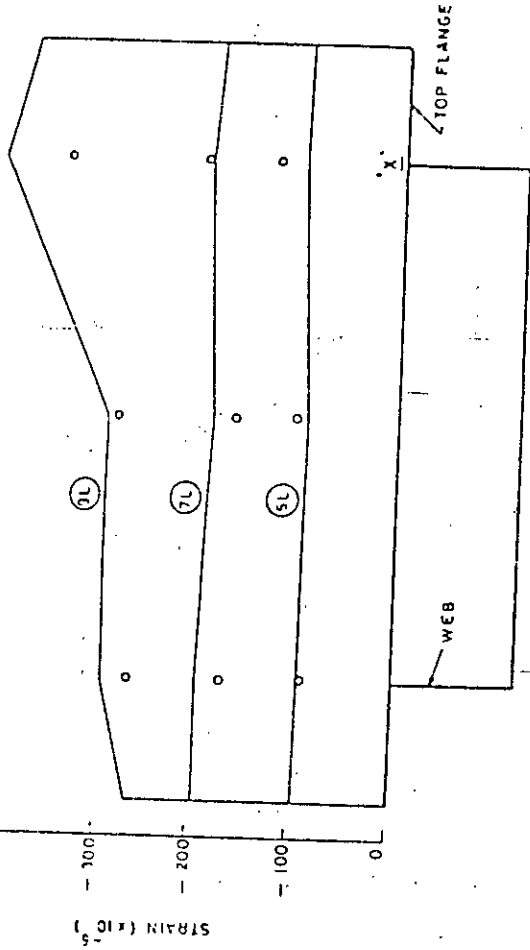


FIG. 5.18(a) -- VARIATION OF LONGITUDINAL COMPRESSIVE STRAIN ACROSS THE WIDTH OF THE TOP FLANGE AT MID SPAN.

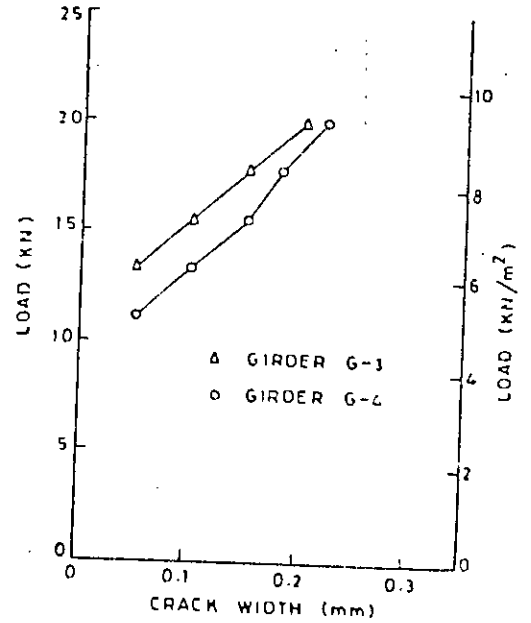
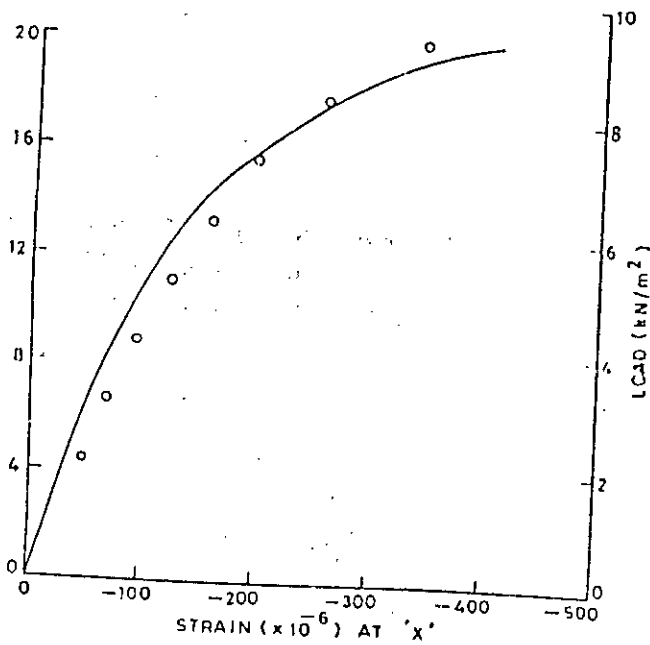


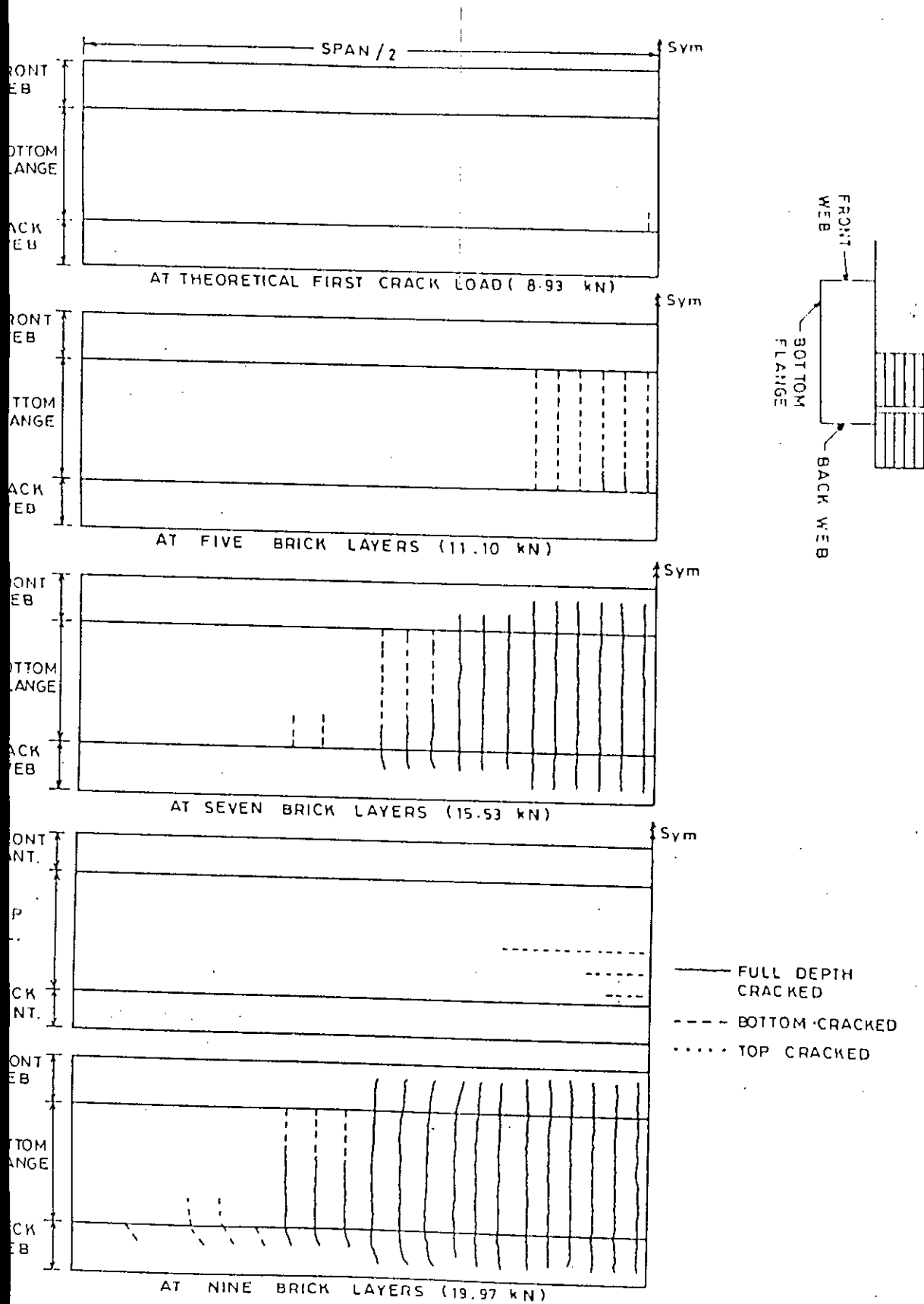
FIG. 5.19-LOAD VS. MAXIMUM CRACK WIDTH



5L: FIVE BRICK LAYERS (11.10 kN OR 5.15 kN/m²)
 7L: SEVEN " " (15.53 " OR 7.22 ")
 9L: NINE " " (19.97 " OR 9.28 ")

— FEM
 ○ GIRDER G-4

FIG. 5.18(b) -- LOAD VS. LONGITUDINAL COMPRESSIVE STRAIN ON TOP FLANGE AT MID SPAN



G. 5.20 - PREDICTED CRACK-PATTERNS OF SINGLE CELL BOX GIRDER
SUBJECTED TO UDL OVER HALF WIDTH AND FULL SPAN

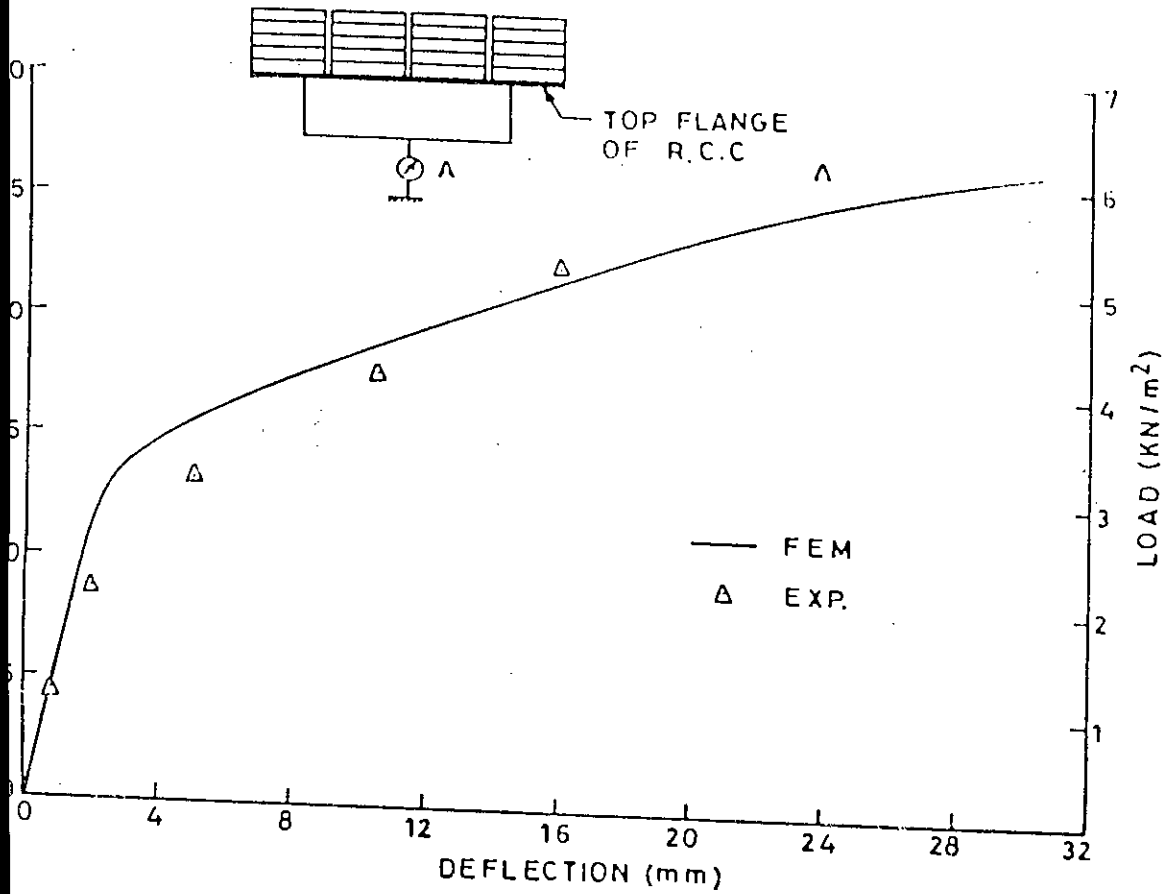


FIG. 5.21 (a) — LOAD Vs MID SPAN DEFLECTION AT 'A'

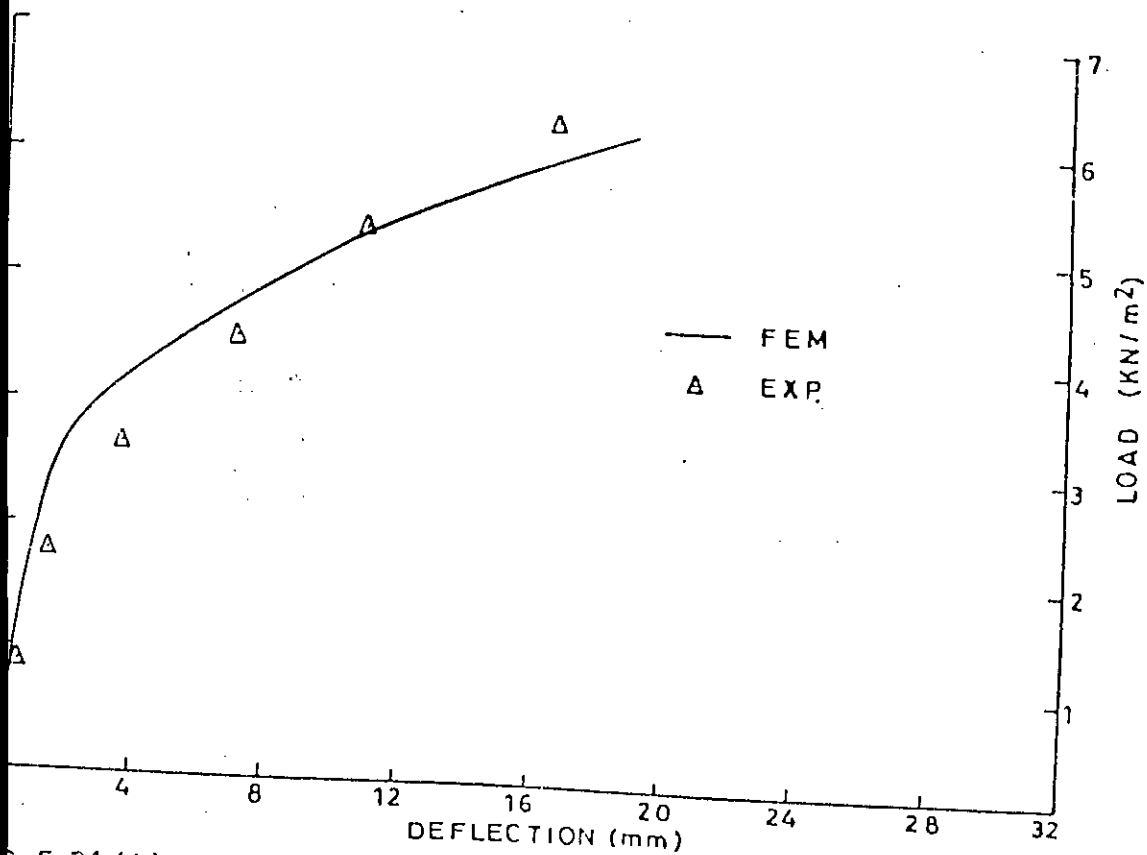


FIG. 5.21 (b) — LOAD Vs QUARTER SPAN DEFLECTION AT 'A'

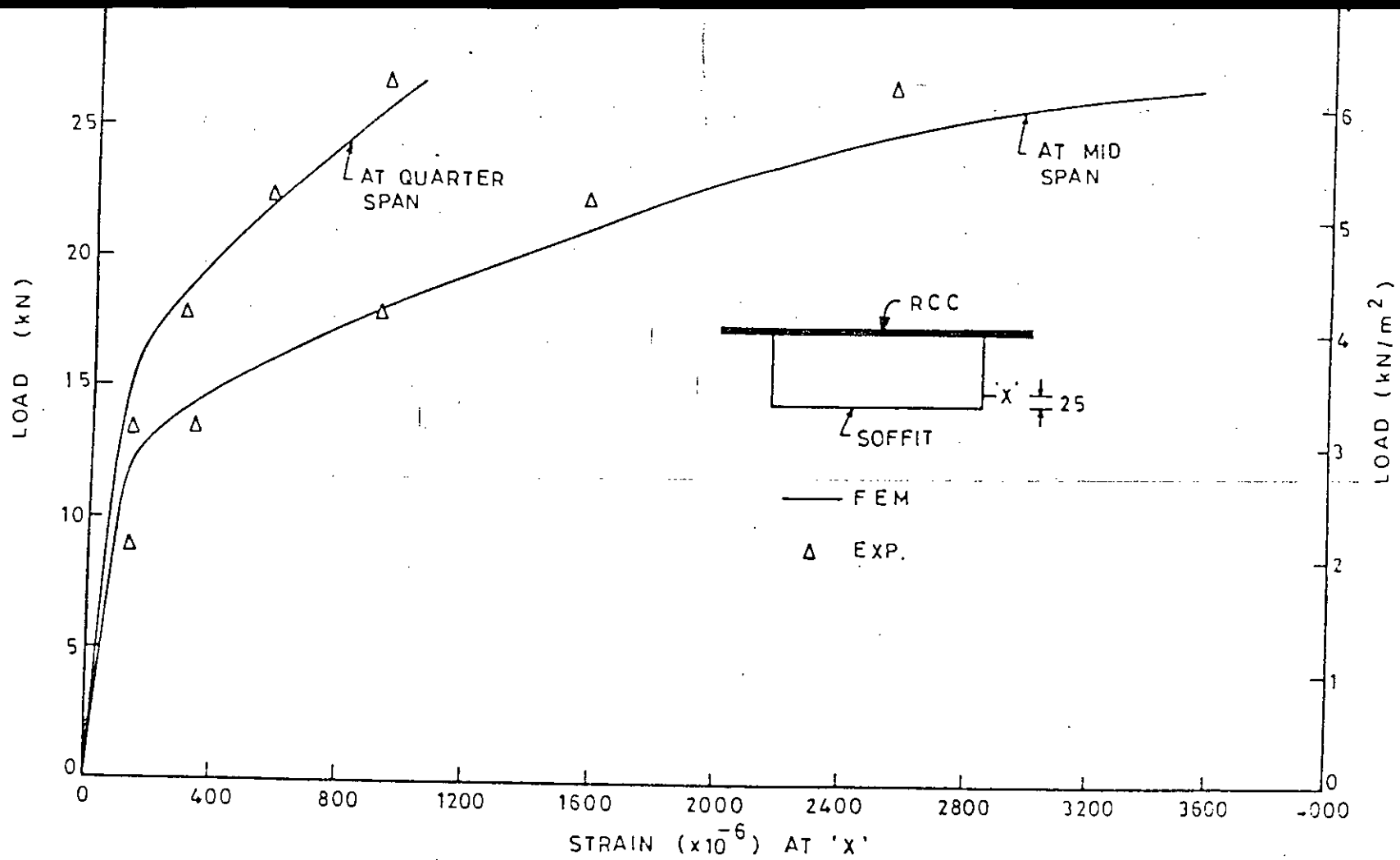
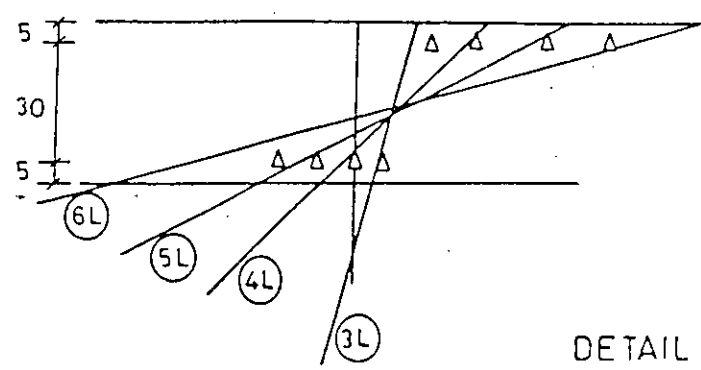


FIG. 5.22 - LOAD VS. LONGITUDINAL TENSILE STRAIN AT 25mm ABOVE THE SOFFIT

3L:	THREE BRICK LAYERS	(13.31 kN	OR	3.09 kN/m ²)
4L:	FOUR " "	(17.75 "	OR	4.12 ")
5L:	FIVE " "	(22.19 "	OR	5.15 ")
6L:	SIX " "	(26.63 "	OR	6.19 ")

— FEM
 Δ EXP.

TENS. STRAIN ($\times 10^{-6}$) COMP. STRAIN ($\times 10^{-6}$)
 400 200 0 -200 -400 -600



DETAIL

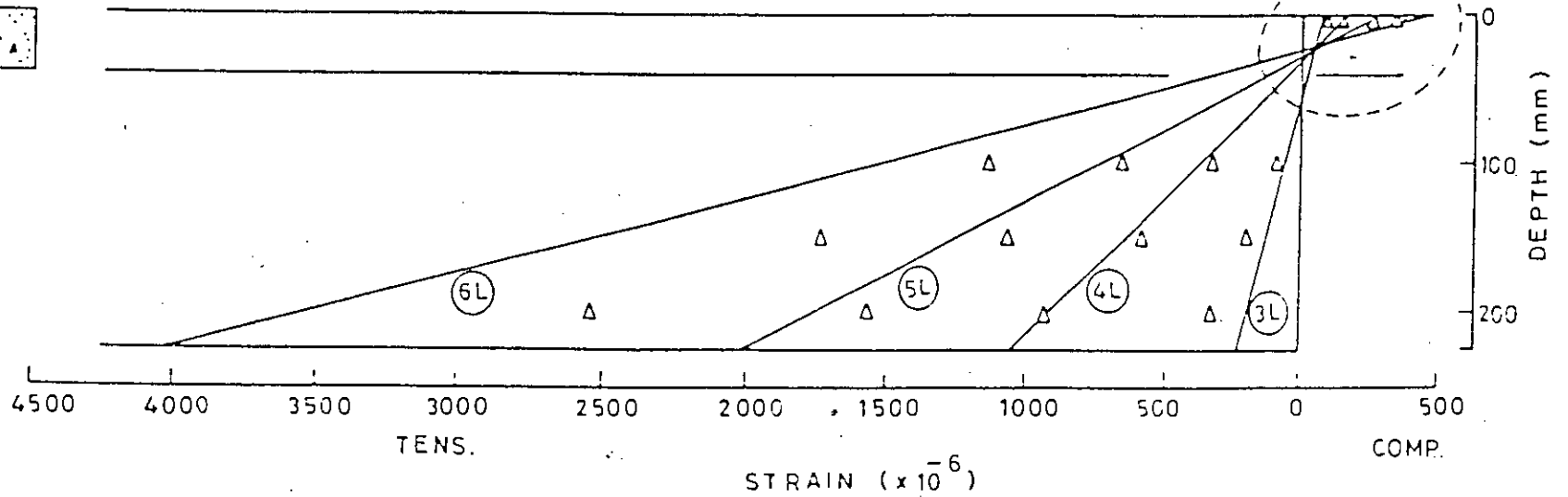
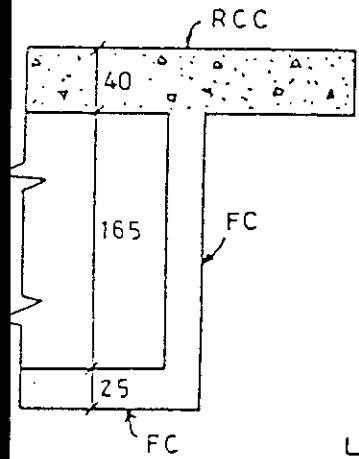
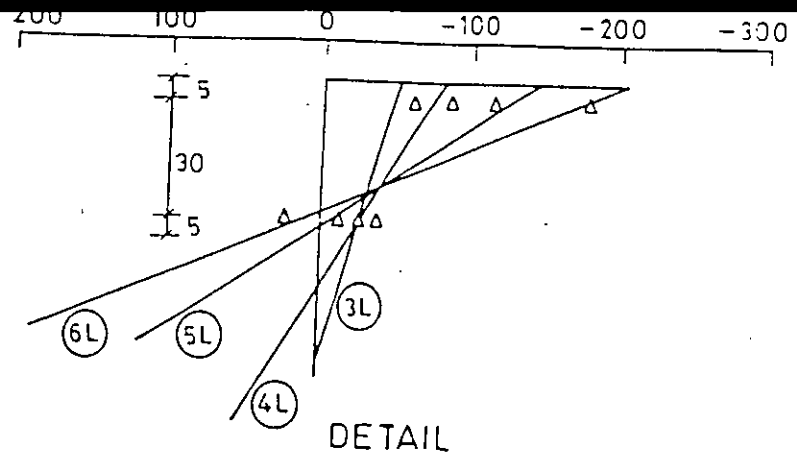


FIG. 5-23 - VARIATION OF LONGITUDINAL STRAIN ACROSS THE GIRDER DEPTH AT MID SPAN

3L:	THREE BRICK LAYERS	(13.31 kN OR 3.09 kN/m ²)
4L:	FOUR "	(17.75 " OR 4.12 ")
5L:	FIVE "	(22.19 " OR 5.15 ")
6L:	SIX "	(26.63 " OR 6.19 ")

— FEM
 Δ EXP.



DETAIL

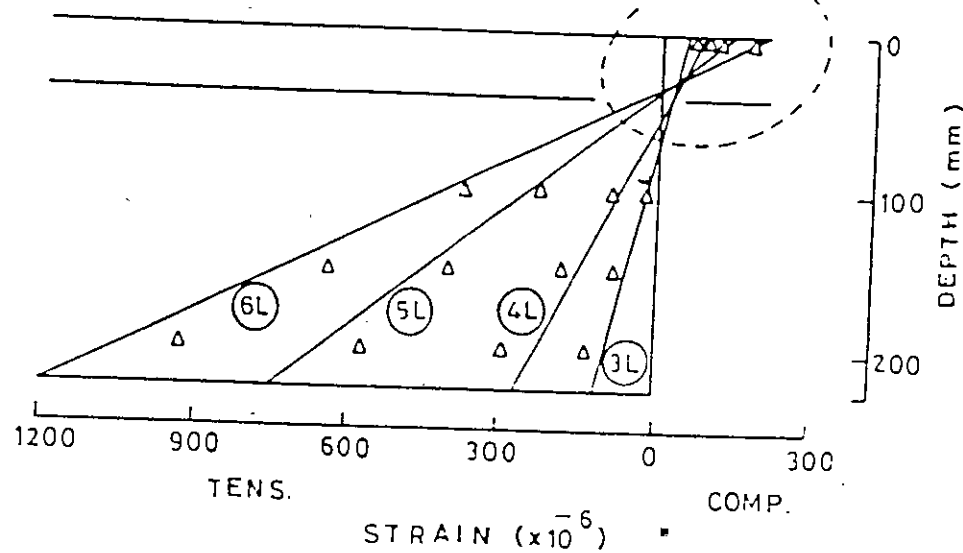
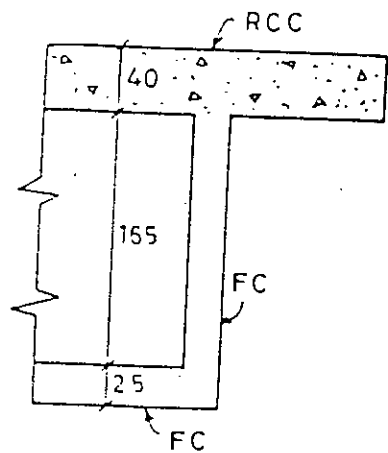


FIG. 5.24 - VARIATION OF LONGITUDINAL STRAIN ACROSS THE GIRDER DEPTH AT QUARTER SPAN

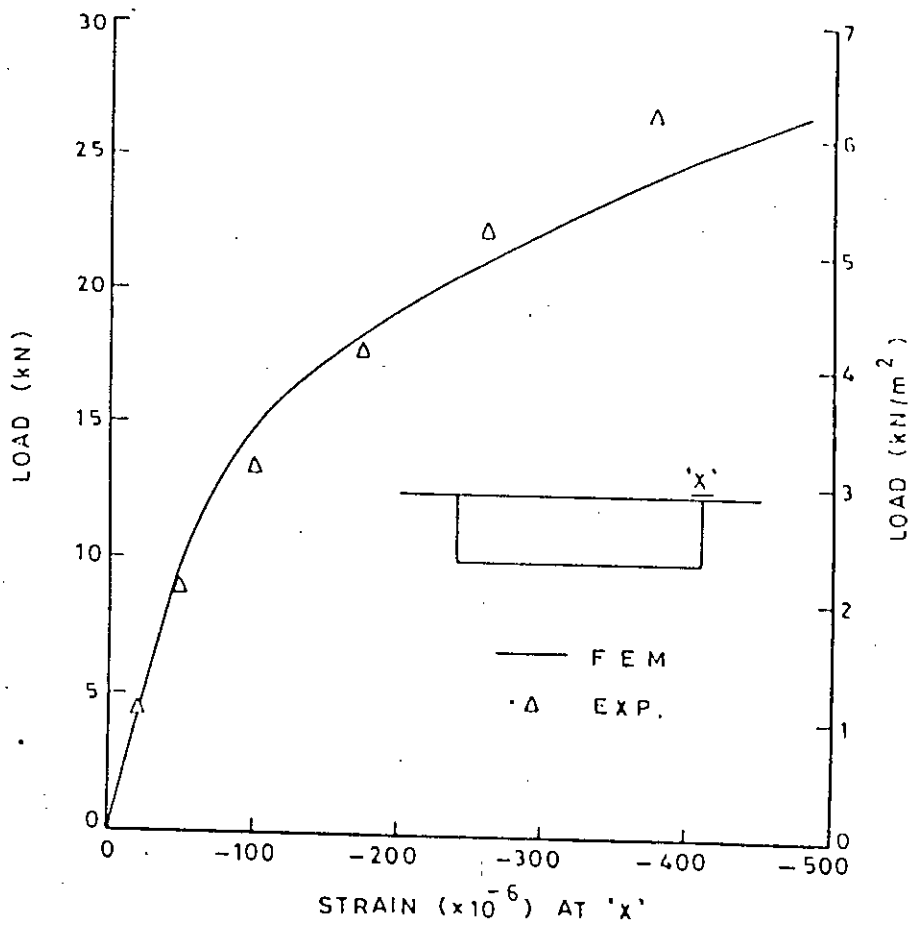


FIG. 5.25—LOAD VS. LONGITUDINAL COMPRESSIVE STRAIN AT MID SPAN

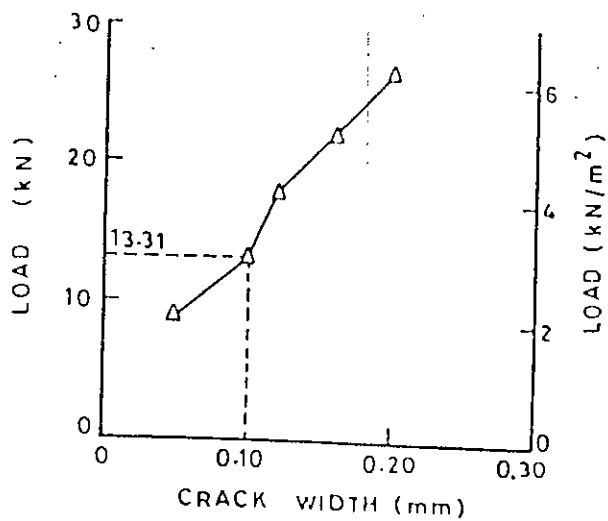


FIG. 5.26—LOAD VS. MAXIMUM CRACK WIDTH FOR COMPOSITE GIRDER

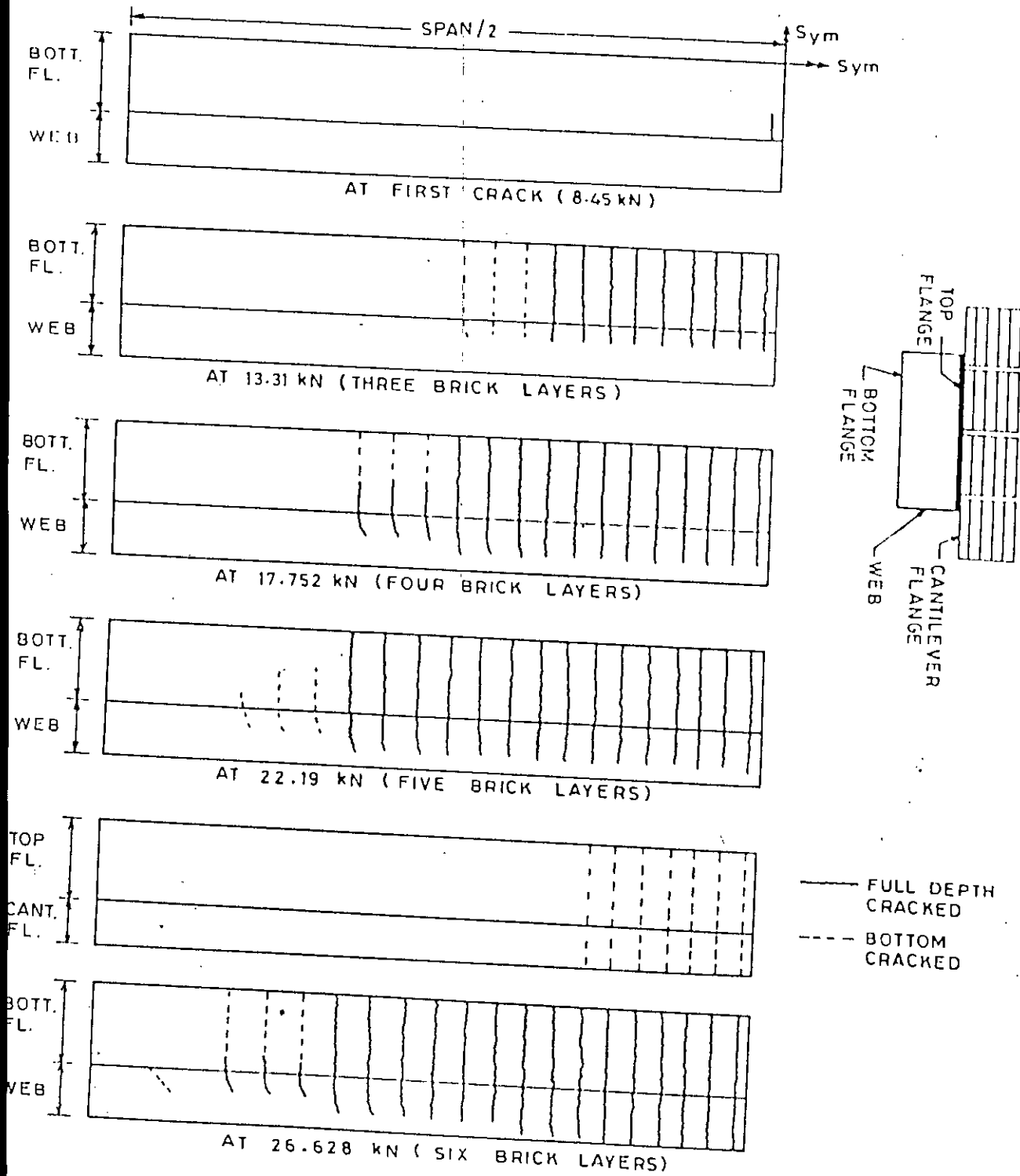
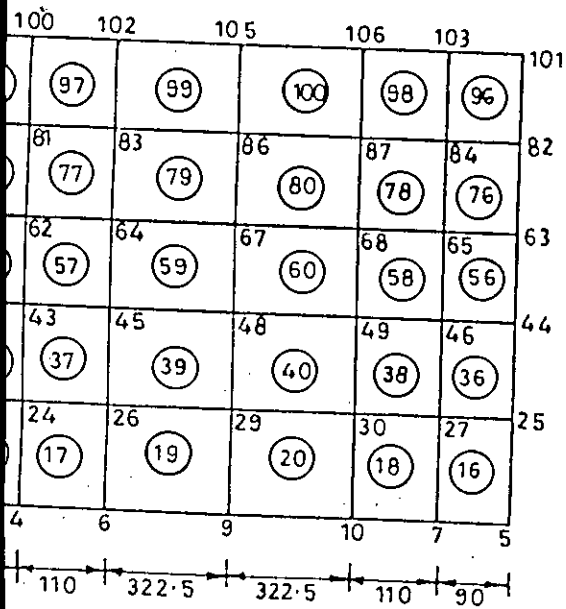
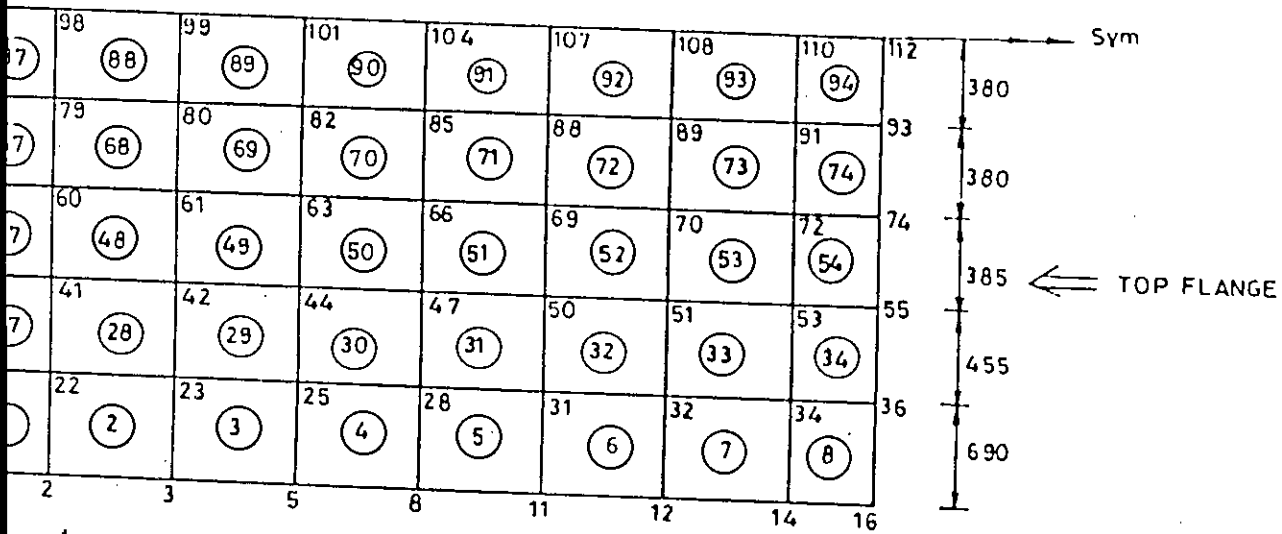
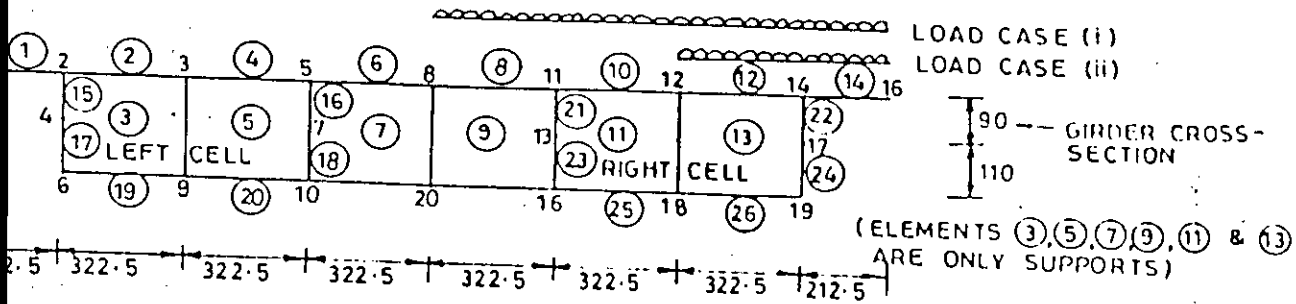
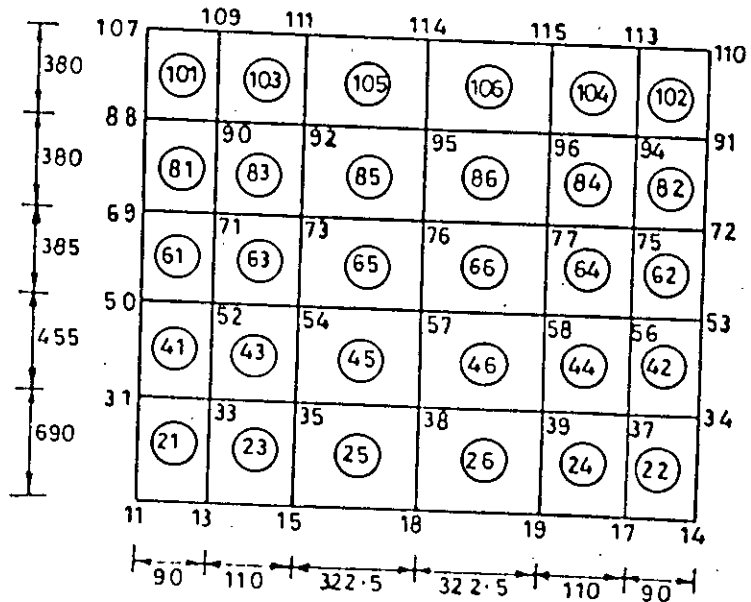


FIG. 5.27- PREDICTED CRACK PATTERNS OF COMPOSITE BOX GIRDER
 SUBJECTED TO UDL OVER THE ENTIRE TOP FLANGE



Left Cell



Right Cell

FIG. 5-28 — DISCRETIZATION OF THE DOUBLE CELL BOX GIRDER
SUBJECTED TO UNSYMMETRIC LOADING CASES

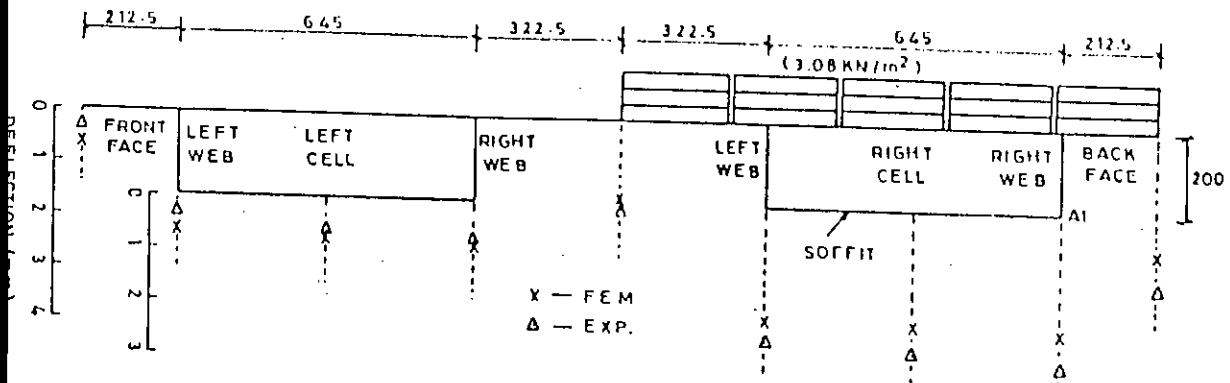
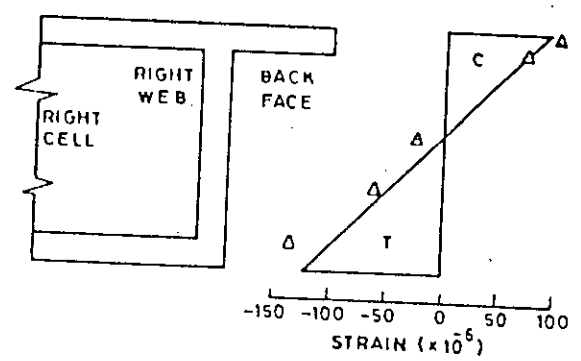
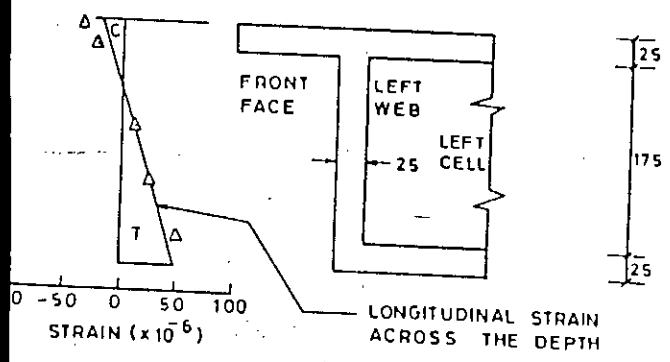
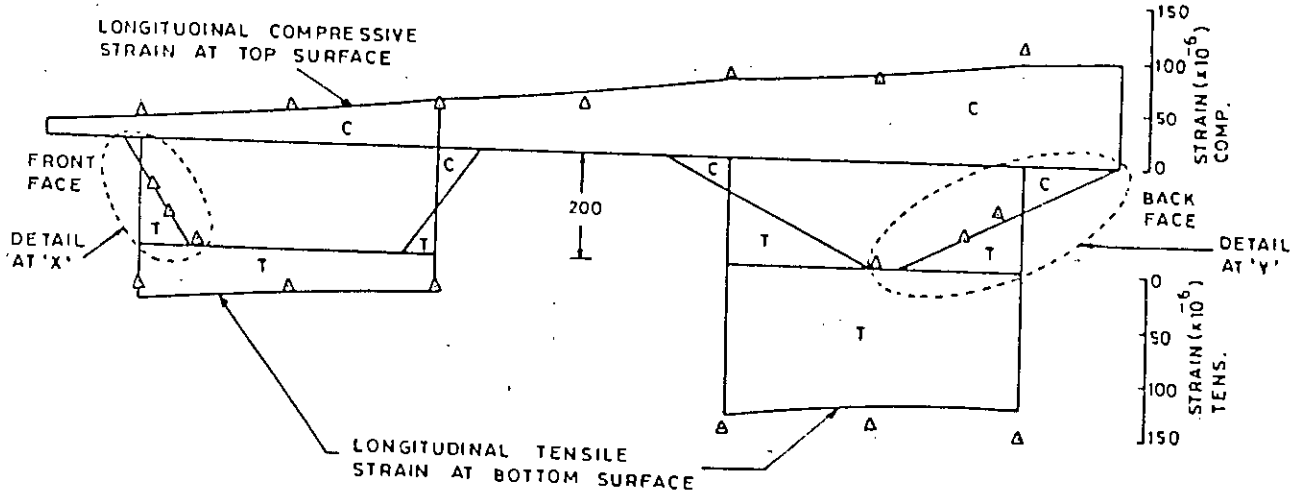


FIG. 5.29(a) - DEFLECTIONS ACROSS THE CROSS-SECTION AT MID SPAN



— FEM
 Δ EXP.
 C: COMPRESSION
 T: TENSION

DETAIL AT 'X'

DETAIL AT 'Y'

FIG. 5.29(b) - STRAIN VARIATION ACROSS THE CROSS-SECTION AT MID SPAN

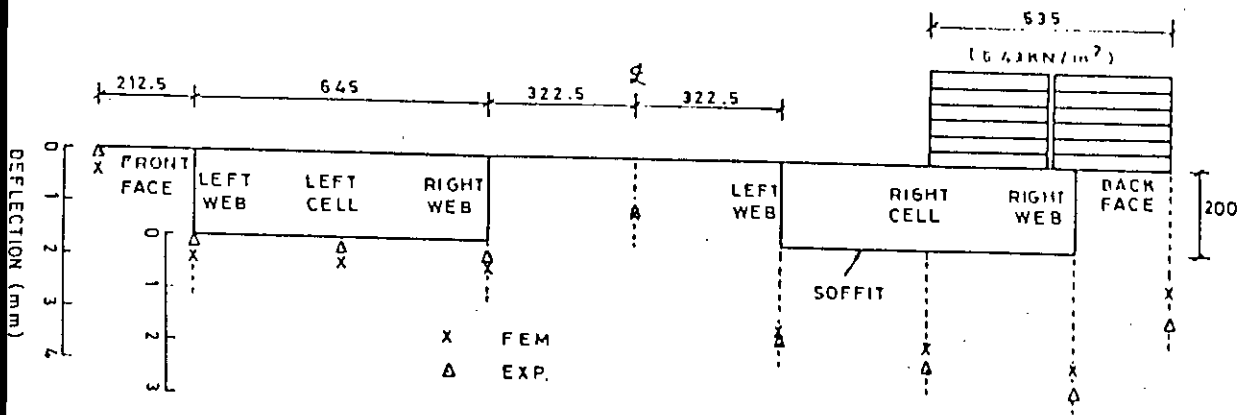


FIG. 5.30(a) - DEFLECTIONS ACROSS THE CROSS-SECTION AT MID SPAN

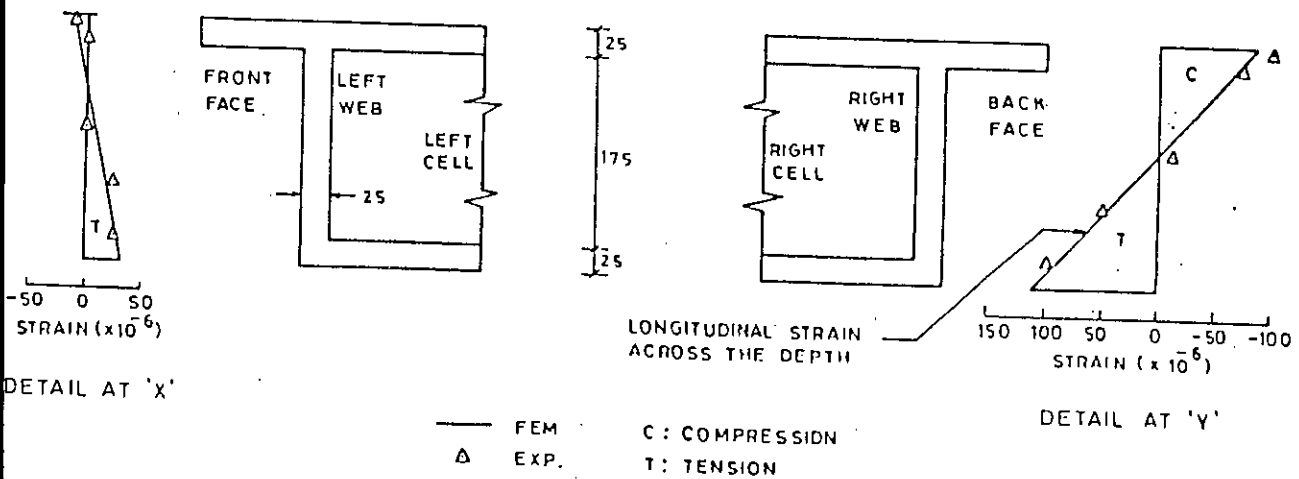
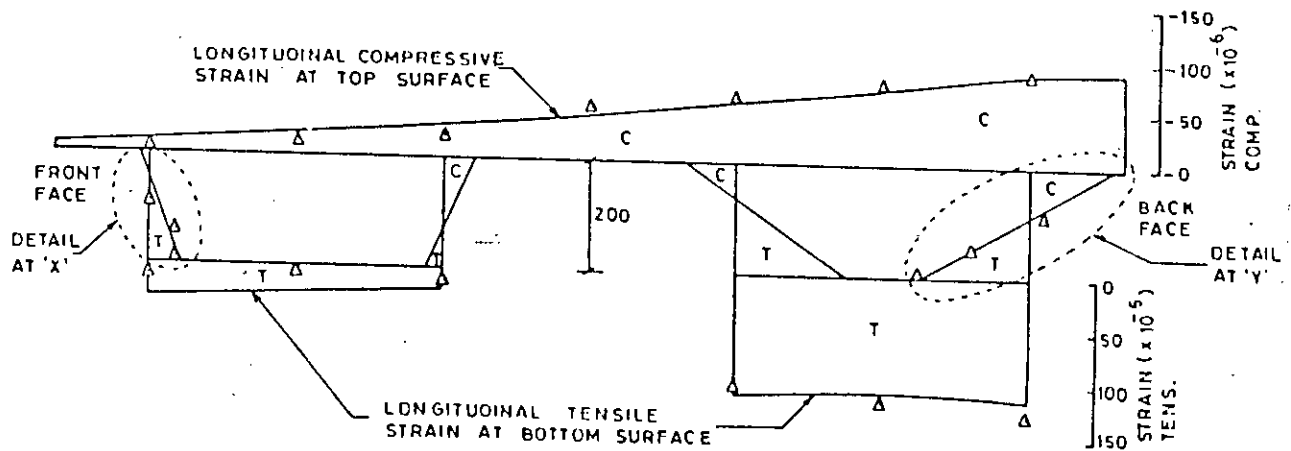


FIG. 5.30(b) - STRAIN VARIATION ACROSS THE CROSS-SECTION AT MID SPAN

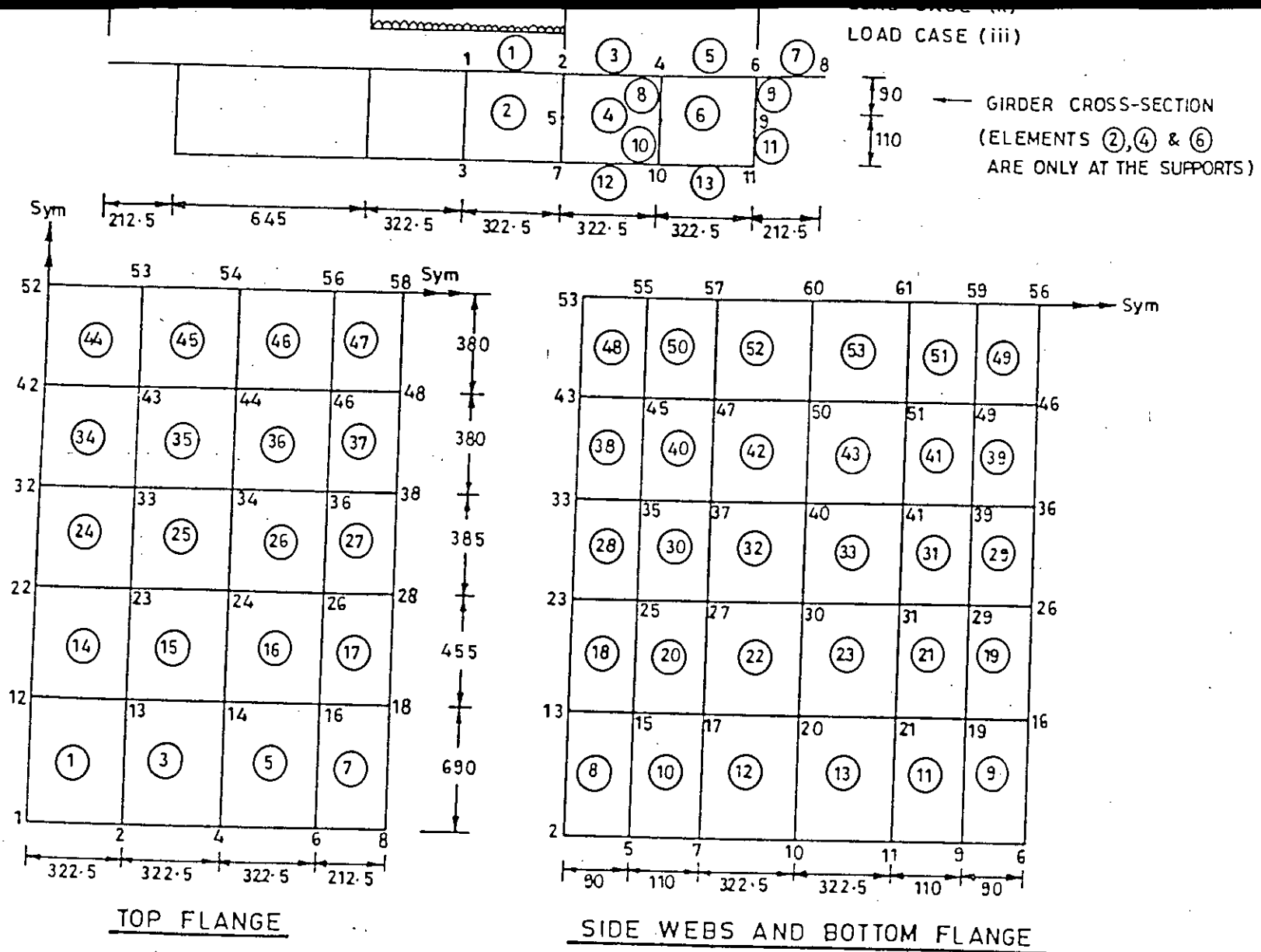


FIG. 5-31 — DISCRETIZATION OF DOUBLE CELL BOX GIRDER SUBJECTED TO SYMMETRIC LOADING CASES

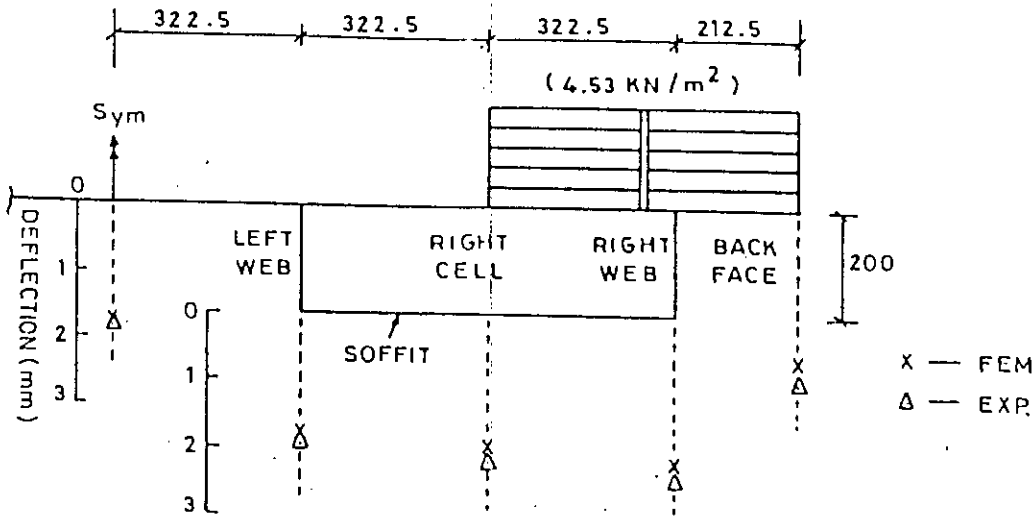


FIG. 5.32(d) DEFLECTIONS ACROSS THE CROSS-SECTION AT MID SPAN

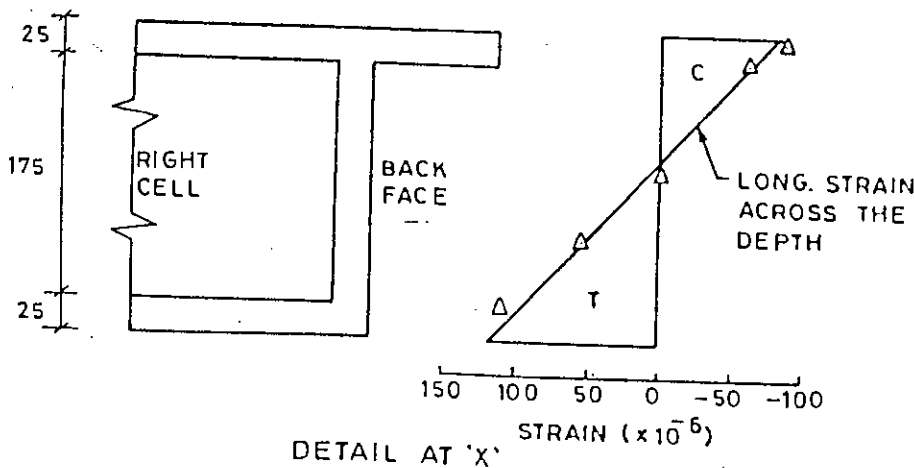
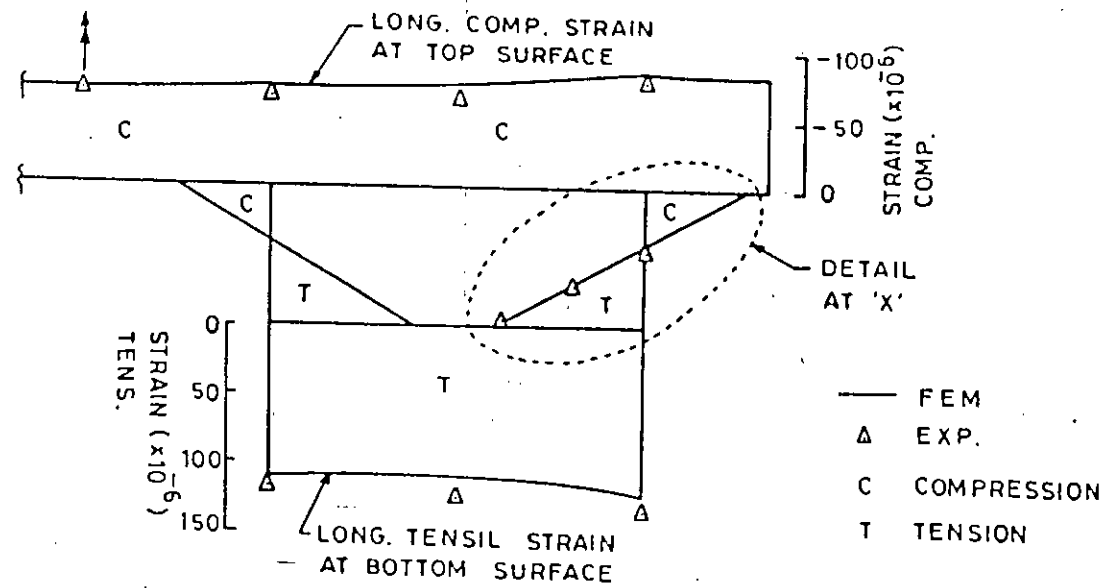


FIG. 5.32(b) STRAIN VARIATION ACROSS THE CROSS-SECTION AT MID SPAN

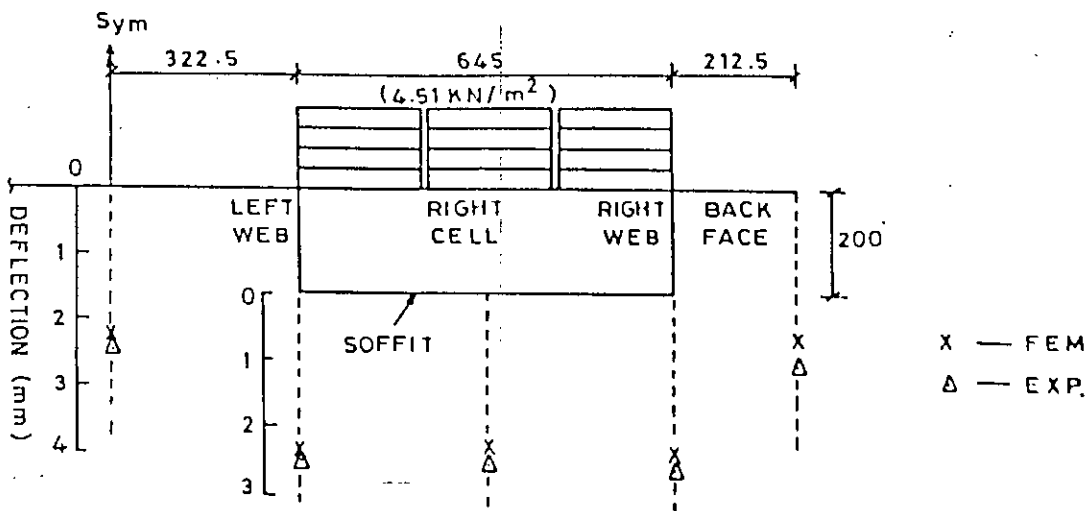


FIG.5-33(a) DEFLECTIONS ACROSS THE CROSS-SECTION AT MID SPAN

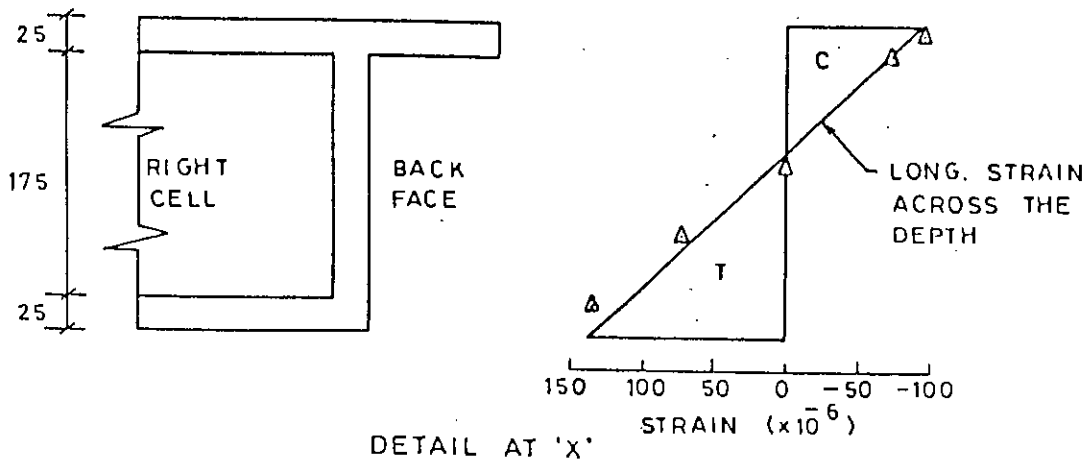
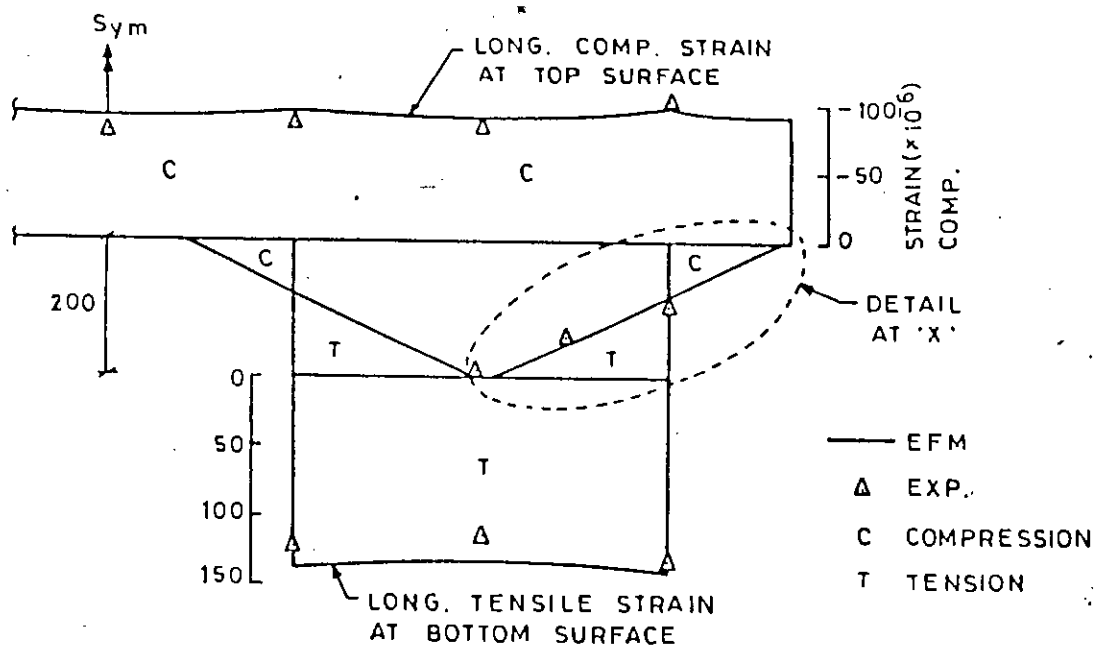


FIG.5-33(b) STRAIN VARIATION ACROSS THE CROSS-SECTION AT MID SPAN

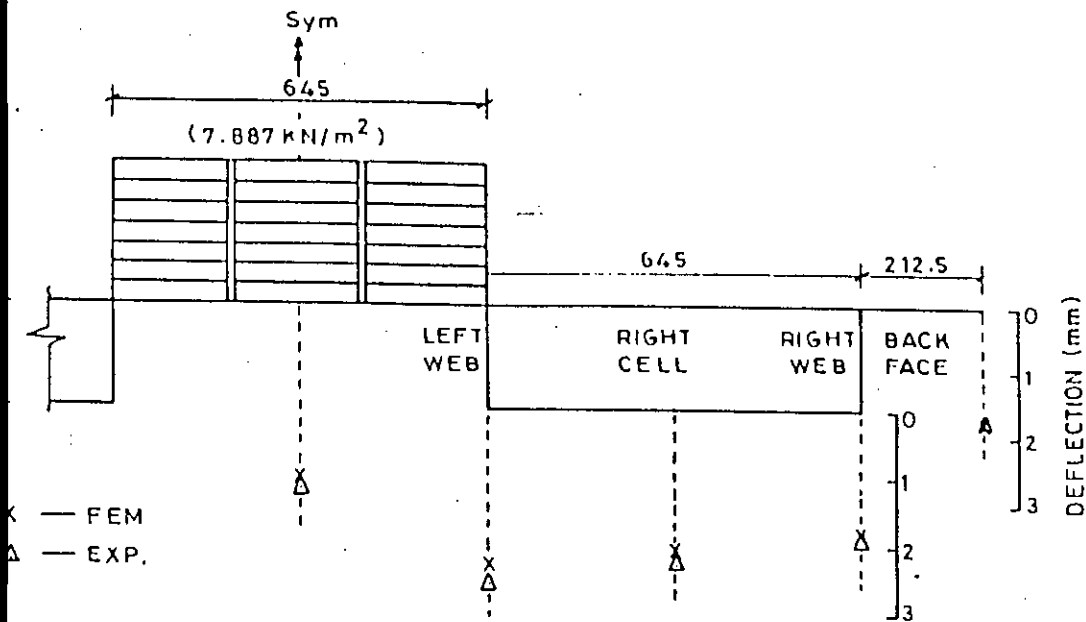


FIG.5.34(a) DEFLECTIONS ACROSS THE CROSS-SECTION AT MID SPAN

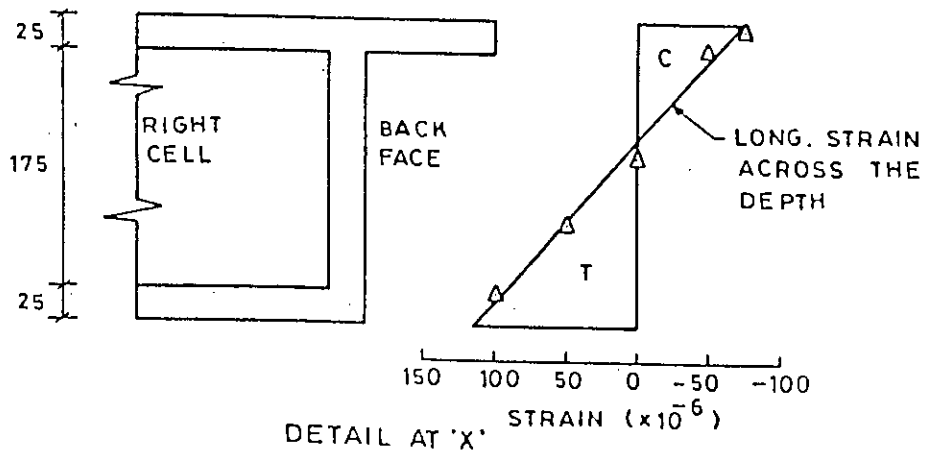
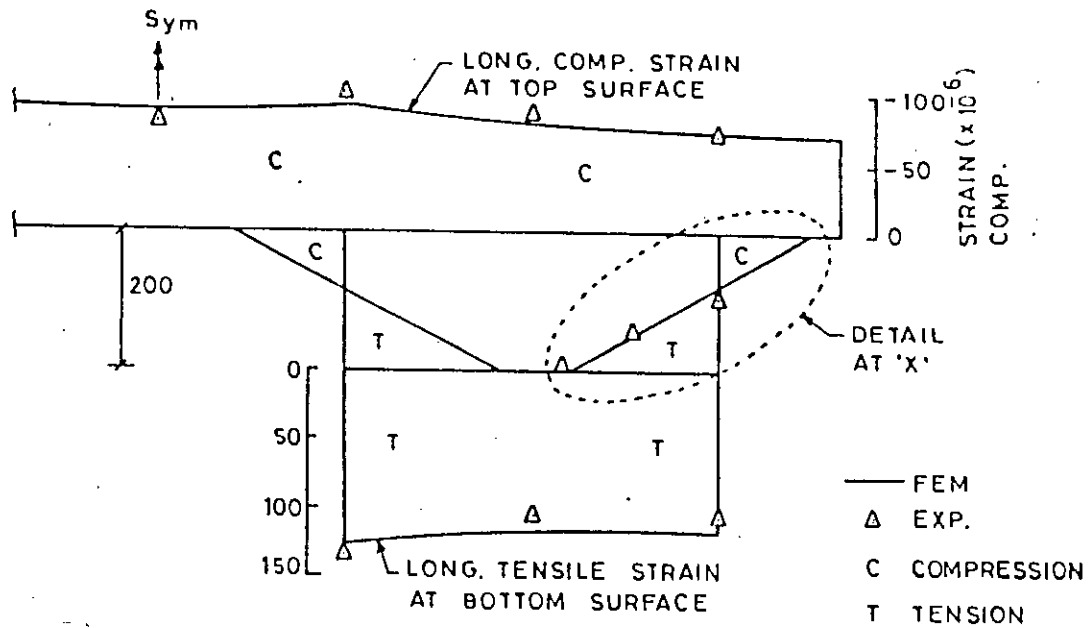


FIG.5.34(b) STRAIN VARIATION ACROSS THE CROSS-SECTION AT MID SPAN

CHAPTER VI

BEHAVIOUR UNDER SUSTAINED LOADS OF SHORT DURATION

6.1 GENERAL

Sometimes the structures are subjected to increasing loads in their service life which are sustained for short durations. Behaviour of ferrocement control specimens under sustained flexural loading has been investigated by Raisinghani and Sai⁽⁸⁶⁾, Ravindrarajah and Tom⁽⁹⁴⁾ and Swamy and Spanos⁽⁹⁵⁾. The magnitude of the sustained loadings was varied from 20 percent of the first crack load to 50 percent of the ultimate load and the duration from 80 to 365 days. Test results on prototype ferrocement specimens or structures subjected to sustained loads close to the failure load are not available. The purpose of this study is to investigate the changed behaviour of ferrocement box girders under monotonically increasing sustained loads of short durations compared to the behaviour under monotonically increasing loads.

The experimental investigation has been carried out on a double cell box girder under sustained loads of short duration. This girder was earlier subjected to various symmetric and unsymmetric loading cases in the pre-cracking zone as described in section 5.5. Due to time constraints a specimen could not be tested under monotonically increasing loads for comparison purposes. Since the validity of the proposed analytical method has been checked and established with the help of the test/analytical results of other researchers in Chapter III and the test results of the present investigation in Chapter V, it has been considered fit to generate the experimental load-deflection/strain results for the double cell girder under monotonically increasing loads by using the computer program developed. The predicted behaviour can be assumed to represent within ± 20 percent variation the experimental load-deflection/strain

response under monotonically increasing loads. The predicted experimental results under monotonically increasing loads have been compared with the experimental results under sustained loading in section 6.3.

6.2 EXPERIMENTAL INVESTIGATIONS

After a rest of about one month, the uncracked double cell box girder was subjected to monotonically increasing sustained loads of short durations (Plate 6.1). The sustained loading was in the form of brick layers applied over the entire top flange. Each brick layer was allowed to remain on the girder for a few days till the deflections stabilized i.e. the increase in deflections in the previous past 24 hours being less than 0.05 mm. The girder was loaded upto six brick layers (66.57 kN or 6.16 kN/m^2) in this manner in 75 days time. The mid span deflections stabilized at one, two, three, four, five and six brick layers in 3, 11, 23, 10, 13 and 15 days respectively.

After the application of two brick layers (2.05 kN/m^2) a few cracks appeared in the bottom flanges and side webs. The maximum crack width increased from 0.05 mm after the application of second brick layer to 0.06 mm at the stabilization of deflections. After the application of three brick layers (3.08 kN/m^2) a large number of cracks appeared. The maximum crack width increased from 0.10 mm to 0.12 mm at the stabilization of deflections. With the application of subsequent brick layers, more cracks appeared. The length and the width of the earlier cracks increased. At six brick layers, the maximum crack width after the stabilization of deflections was 0.40 mm. The average spacing of cracks in the central part of the bottom flange was about 50 mm. The crack-pattern of the bottom flanges and side webs after the sustained loading of six brick layers is shown in Plate 6.2.

6.3 FINITE ELEMENT IDEALIZATION AND COMPARISON OF RESULTS

Nonlinear analysis of the double cell box girder was carried out by discretizing one quarter of the girder by 87 elements with 97 nodes (Fig. 6.1). A total load of 66.57 kN. was applied in five load increments of 22.19 kN, 11.1 kN, 11.1 kN, 11.1 kN and 11.1 kN each. The theoretical first crack load was obtained at 18.75 kN (or 1.73 kN/m^2). The ultimate failure of the girder at 66.57 kN load was indicated by a large increase in the residual vector norm and energy norm ratio. The total computer time taken for complete displacement and stress output was 10 minutes and 22 seconds.

A comparison of the experimental mid span deflections under sustained loads with the predicted deflections under monotonically increasing loads is shown in Fig. 6.2. The experimental deflections under sustained loads are on the flexible side of the deflections under monotonically increasing loads upto the predicted yielding of skeletal steel occurring at about four and half brick layers (4.64 kN/m^2). The predicted deflections at six brick layers are large as compared to the deflections under sustained loads due to the predicted yielding of the skeletal steel and wire mesh layers of the bottom flanges.

Due to sustained loading, the deflections stabilised rapidly in the uncracked range. At three brick layers a large number of cracks appeared and it took maximum number of days (twenty three) for deflections to stabilize. At four, five and six brick layers, it took lesser number of days for deflections to stabilize. At these brick layers the average percentage increase in deflection after two to three hours of the load application was observed to be about 30 percent of the total percentage increase in deflection in about two weeks, while it was about 50 and 60 percent after 24 and 48 hours of the load application. Defining the creep deflection coefficient in this case as the ratio

of time dependent deflections to the deflection after the application of load (including the sustained deflections at lower load levels), the maximum creep deflection coefficient was 0.39 in the initial portion of the cracked range (i.e. at three brick layers) while it was 0.11, 0.09 and 0.08 at four, five and six brick layers respectively.

If sustained deflections at all the load levels are neglected, then the experimental deflections in the cracked range are highly on the stiffer side of the predicted deflections under monotonically increasing loads. Thus the instantaneous deflection due to the application of the load increment (having sustained loading at lower load levels) appears to be less than the instantaneous deflection which would have occurred if the load had been applied in a monotonically increasing manner. The increased stiffness of the girder may be due to compaction of the mortar matrix under sustained loading. Similar behaviour under sustained loading at lower load levels was observed by Ravindrarajah and Tom⁽⁹⁴⁾ and Raisinghani and Sai⁽⁸⁶⁾.

An examination of the load-deflection curves clearly shows that the effect of sustained loading of short duration is maximum in the initial portion of the cracked range (i.e. at three brick layers). At higher load levels, the effect is small.

A comparison of the longitudinal tensile strains at 25 mm above the soffit at mid span due to sustained loads and due to values predicted under monotonically increasing loads is shown in Fig. 6.3. The strains due to sustained loads are on the flexible side of the strains due to monotonically increasing loads upto the predicted yielding of skeletal steel occurring at about four and half brick layers of load. Defining creep strain coefficient as the ratio of time dependent strain to the strain after the application of load (including the strain due to sustained loading at lower load levels), the tensile creep strain

coefficient is maximum (0.62) at three brick layers. The creep strain coefficient reduces at higher load levels i.e. 0.18, 0.14 and 0.12 at four, five and six brick layers.

The comparison of longitudinal strains across the girder depth at mid span due to sustained loads and due to monotonically increasing loads (predicted) is shown in Fig. 6.4. The comparison is shown for three, four and five brick layers. At three and four brick layers, the strains due to sustained loading are on the flexible side of the strains due to monotonically increasing loads across the entire girder depth. At five brick layers, the longitudinal compressive strain (at 5 mm below the top surface) due to sustained load is on the flexible side of the strain due to monotonically increasing loads, while longitudinal tensile strains (at various depth levels in the web) due to sustained load are on the stiffer side of the strains due to monotonically increasing loads after the application of the fifth brick layer and reach the flexible side at the end of the sustained loading period.

A comparison of the longitudinal compressive strains at the top surface of the girder due to sustained loads and due to monotonically increasing loads is shown in Fig. 6.5. The compressive strains due to sustained loads are on the flexible side of the compressive strains due to monotonically increasing loads, upto five brick layers. At six brick layers, the predicted compressive strains due to monotonically increasing loads are on the flexible side of the compressive strains due to sustained loading due to predicted yielding of skeletal steel and wire mesh layers of the bottom flanges. In this case also, the compressive creep strain coefficient is maximum at three brick layers (0.41) and less at four, five and six brick layers (i.e. 0.27, 0.15 and 0.27).

6.4 CRACK WIDTH AND CRACK SPACING

In the cracked stage, the effect of sustained loading leads to an increase in the width of cracks, formation of new cracks and extension of cracks formed earlier. The load versus maximum crack width curve of the double cell box girder is shown in Fig. 6.6. Defining the creep crack width coefficient as the ratio of the increase in crack width due to sustained loading to the crack width after the application of load (including the increase in crack width due to sustained loading at lower load levels), the creep crack width coefficients at three, four, five and six brick layers are 0.20, 0.10, 0.20 and 0.14 respectively.

Including the time dependent effect on the crack width, the load taken by the double cell box girder at the recommended crack width of 0.1 mm (Fig. 6.6) is about 29 kN (or 2.68 kN/m^2). At this load level, the span/deflection ratio is about 600. At the recommended span/deflection ratio of 250, the load taken by the double cell box girder is about 48 kN (or 4.44 kN/m^2) which is close to the load at which yielding of skeletal steel is predicted. At this load level, the maximum crack width in the girder is about 0.25 mm (Fig. 6.6).

The average crack spacing after the sustained loading of six brick layers was about 50 mm in the central part of the bottom flanges. The average crack spacing predicted by the expressions given by Naaman and Shah⁽³²⁾, Huq and Pama⁽³⁸⁾ and Desayi and Ganesan⁽⁶⁸⁻⁷⁰⁾ are 20.5 mm, 25.5 mm and 31.3 mm respectively. The large variation in the experimental and predicted values of the average crack spacing may be attributed to the nonuniform compaction of the mortar and the near prototype size of the double cell box girder specimen. Also, the experimental result is from only one specimen.

Comparison of experimentally obtained maximum crack widths with the values predicted by various researchers is shown in Table 6.1. The yielding of the extreme layer of wire mesh is predicted at a load of about 5.25 kN/m^2 , slightly more than five brick layers. The predicted values at the yielding of extreme layer of wire mesh by Huq and Pama⁽³⁸⁾ and Desayi and Ganesan⁽⁶⁸⁻⁷⁰⁾ are far less than the experimental values while the values predicted by Naaman⁽⁴⁴⁾ and Logan and Shah⁽⁵⁹⁾ have shown relatively better comparison. The values of maximum crack width predicted by the above researchers in the initial portion of the cracked range (i.e. at three and four brick layers) are far less than the experimental values. The probable reasons for this discrepancy are mentioned in Chapter V.

At six brick layers, a few diagonal shear cracks appeared in the web at support. Diagonal shear cracks in the web are also predicted by the finite element analysis at six brick layers with the principal tensile strains in the web reaching a maximum value of 184 micron.

The predicted crack pattern at two, three, four, five and six brick layers under monotonically increasing loads are shown in Fig. 6.7. The predicted crack-pattern of the bottom flanges and side webs at six brick layers compares well with the corresponding experimental crack-pattern shown in Plate 6.2. At six brick layers the predicted crack-pattern shows transverse cracks on the bottom surface of the top flange in the mid span region. However, no cracking was observed on the bottom surface of the top flange (between the two cells). The reason for the cracking predicted on the bottom surface of the top flange is due to the large values of strains predicted on account of predicted yielding of the skeletal steel and wire mesh layers of the bottom flanges. At this load, longitudinal cracks are also predicted in the mid span region on the top surface along the junction of side webs. The appearance of

Values Predicted by Various Researchers for Double Cell Box Girder

Load	Exp. Value (mm)		Predicted Value (mm) by			
	After the application of load	At stabilization of deflections	Naaman Eq. 2.6	Huq & Pama Eq. 2.8	Logan & Shah Eq. 2.15	Desayi & Ganesan Eq. 2.27
(i) Three Brick Layers (3.08 kN/m ²)	0.10	0.12	0.024	-	0.012	0.011
(ii) Four Brick Layers (4.11 kN/m ²)	0.20	0.22	0.050	0.022	0.081	0.047
(iii) Five Brick Layers (5.13 kN/m ²)	0.25	0.30	0.151	0.080	0.196	0.091
(iv) Six Brick Layers (6.16 kN/m ²)	0.35	0.40	0.166*	0.089*	0.216*	0.247

* predicted values at the yielding of extreme layer of wire mesh occurring at a load less than six brick layers.

such cracks, if any, could not be seen due to the brick loading. On unloading the girder, no cracks were seen on the top surface of the top flange.

6.5 RELOADING THE COMPOSITE BOX GIRDER AND SUBJECTING IT TO SUSTAINED LOADING AT VARIOUS LOAD LEVELS

After loading the single cell composite box girder upto six brick layers, it was unloaded. The instantaneous recovery at the mid span was about 50 percent. There was a further small recovery in the mid span deflection during the first 2-3 days. There was no recovery afterwards and in fact there was a small downward vertical deflection due to self weight. After a rest of about three months, the girder was again loaded with uniformly distributed load over the entire top flange (Plate 6.3) in a manner similar to the double cell box girder. In this case, the deflections stabilized at various load levels in lesser number of days. The load versus mid span deflection curve is shown in Fig. 6.8. Defining the creep deflection coefficient in this case as the ratio of time dependent deflection to the total deflection after the application of load (including residual deflection and sustained deflections at lower load levels), the creep deflection coefficients for sustained loading of short duration at one, two, three, four and five brick layers are 0.002, 0.02, 0.04, 0.05 and 0.05 respectively. The girder remained loaded with six brick layers for 318 days. The creep deflection coefficient for sustained loading of 318 days is 0.32. It was also observed that the increase in deflection in the first three weeks under six brick layers was about 40 percent of the total increase in deflection in ten and half months. On unloading the girder, the recovery in the mid span deflection was about 32 percent.

Before subjecting the composite girder to sustained loading, cracks had already appeared in the central 3.25 m (i.e. 0.71 times the span) length

in the bottom flange and side webs and the maximum crack width was 0.20 mm. After subjecting the girder to 318 days of sustained loading under six brick layers, the cracks spread over a length of 4.10 m (i.e. 0.90 times the span). A few diagonal shear cracks also appeared in the web at the supports. The maximum width of cracks reached 0.30 mm. The photograph of the crack-pattern of the bottom flange and side webs is shown in Plate 6.4.

6.6 CONCLUDING REMARKS

- (i) The effect of a sustained loading of short duration on deflections and strains is maximum in the initial portion of the cracked range.
- (ii) The instantaneous deflection of the girder is reduced due to the sustained loading at lower load levels as compared to the instantaneous deflection that would have occurred under monotonically increasing loads.
- (iii) The ultimate load of the girder is not affected by monotonically applied sustained loads of short durations.
- (iv) The sustained loading increases the width of the cracks and the region of crack formation.

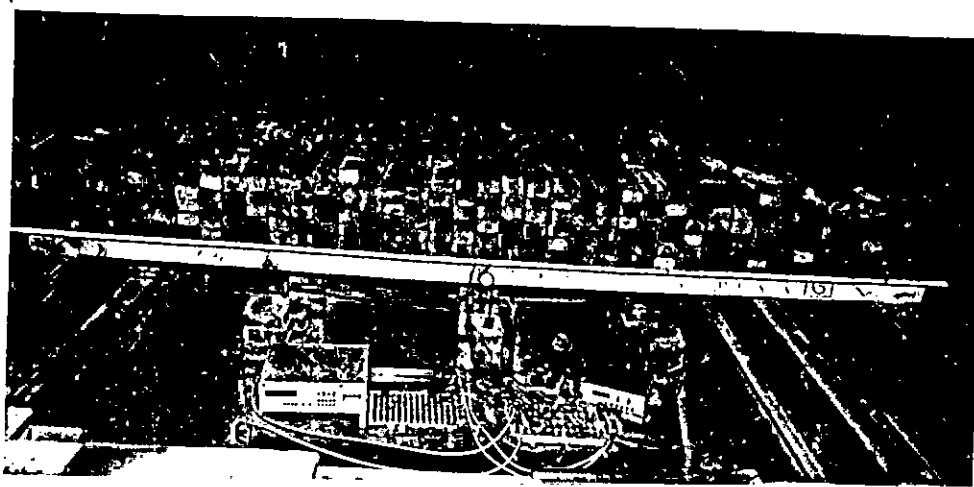
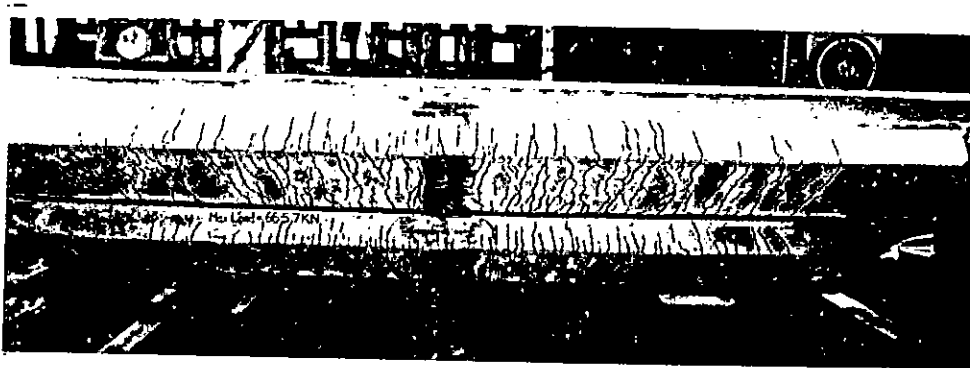
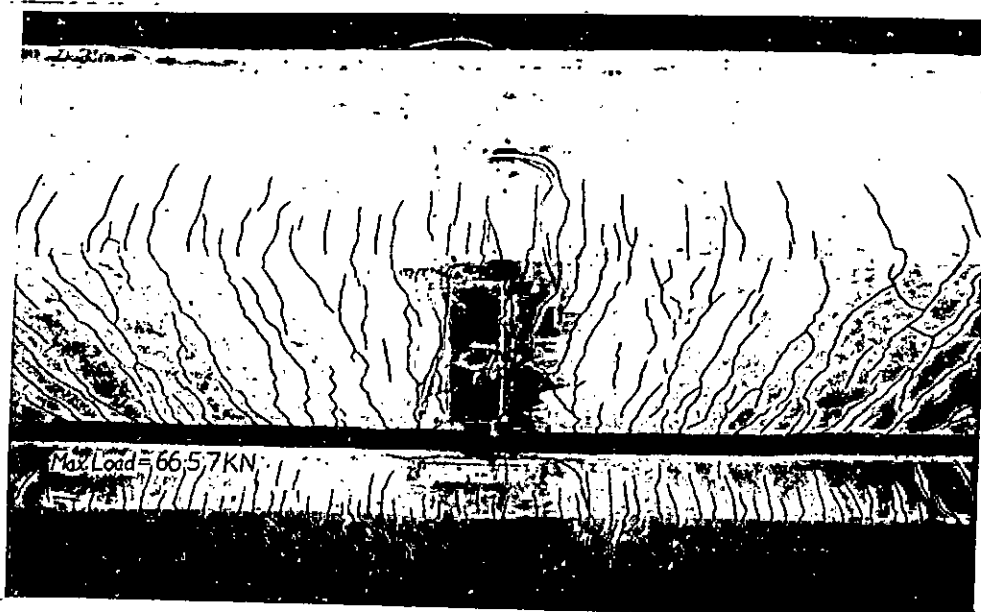


PLATE 6.1 DOUBLE CELL BOX GIRDER SUBJECTED TO
SUSTAINED LOADING OF SHORT DURATION



(A)



(B)

PLATE 6.2 CRACK PATTERN OF THE DOUBLE CELL
BOX GIRDER :(A) FULL VIEW,(B) CLOSE-UP



PLATE 6.3 RELOADING THE COMPOSITE BOX GIRDER
AND SUBJECTING IT TO SUSTAINED LOADING
AT VARIOUS LOAD LEVELS

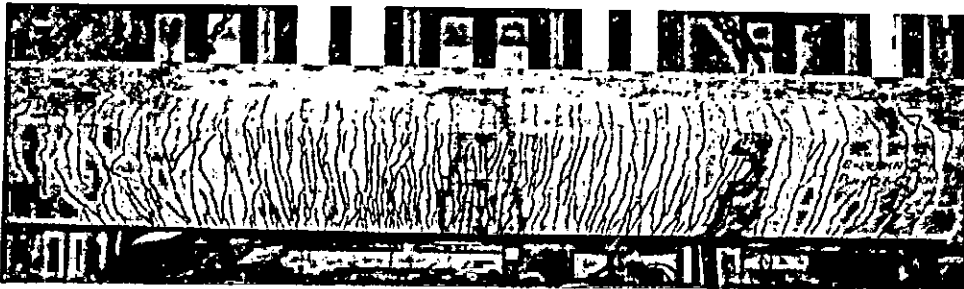


PLATE 6.4 CRACK-PATTERN OF THE COMPOSITE BOX
GIRDER AT THE END OF SUSTAINED LOADING

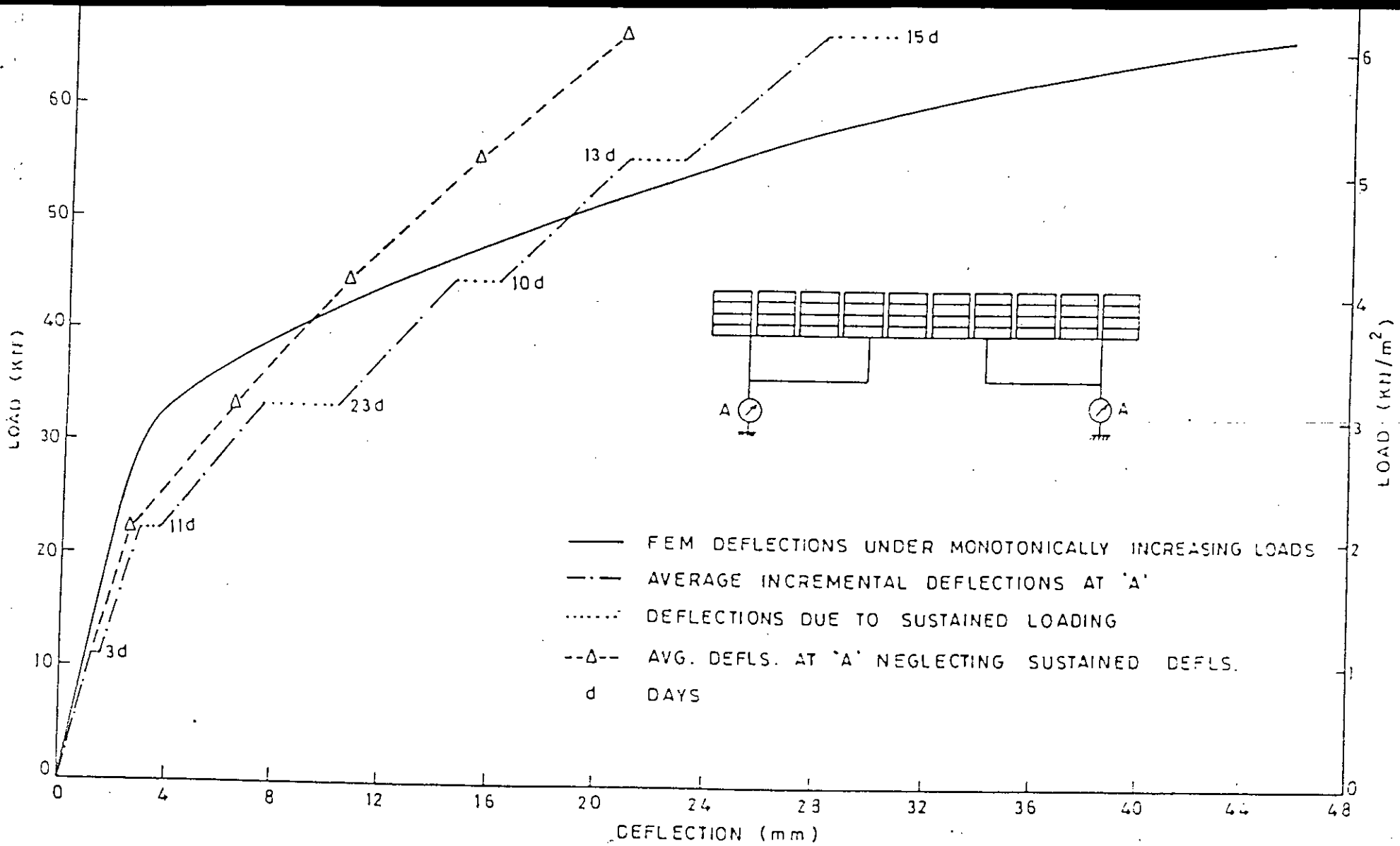


FIG. 6.2 - LOAD VS. MID SPAN DEFLECTION UNDER OUTER WEBS 'A'

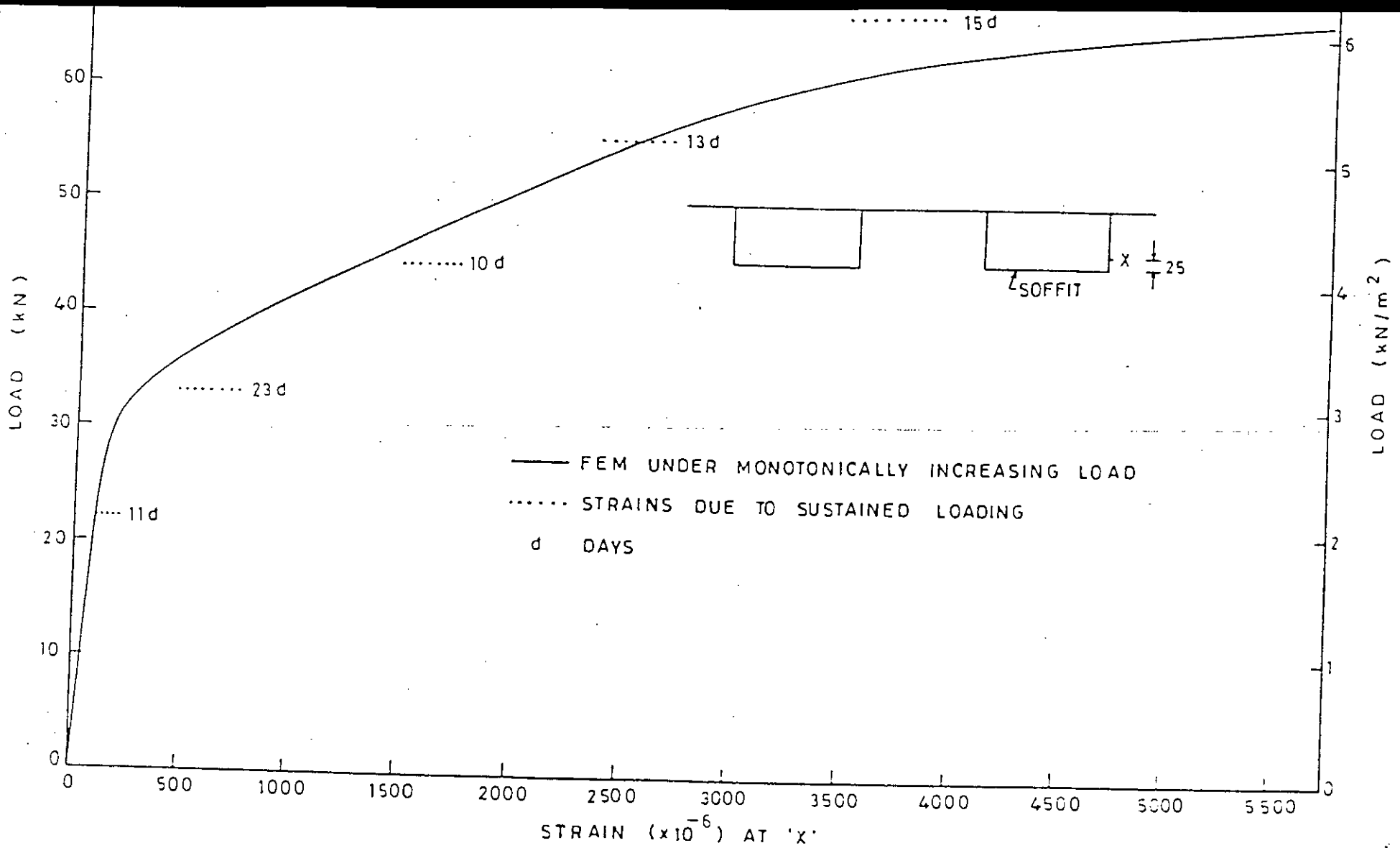


FIG. 6.3— LOAD VS. LONGITUDINAL TENSILE STRAIN 25 mm ABOVE THE SOFFIT

3L: THREE BRICK LAYERS (33.29 kN OR 3.08 kN/m²)
 4L: FOUR " " (44.38 " OR 4.11 ")
 5L: FIVE " " (55.48 " OR 5.13 ")

— FEM STRAINS UNDER MONOTONICALLY INCREASING LOADS

..... STRAIN DUE TO SUSTAINED LOADING

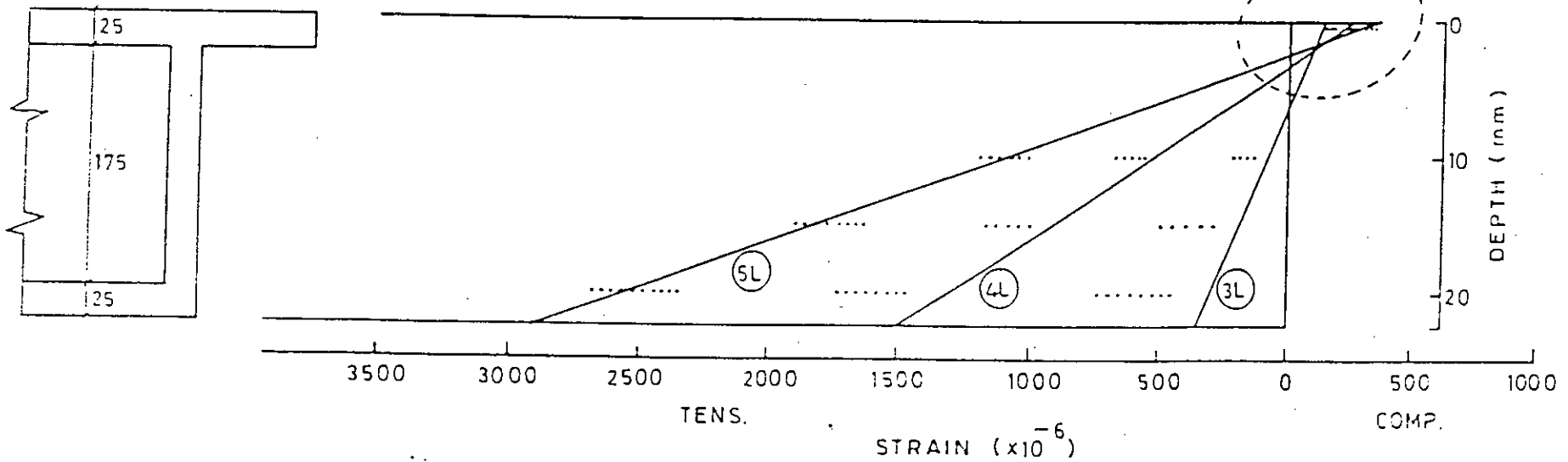


FIG. 6.4 - LOAD VS. LONGITUDINAL STRAIN DISTRIBUTION ACROSS THE DEPTH AT MID SPAN

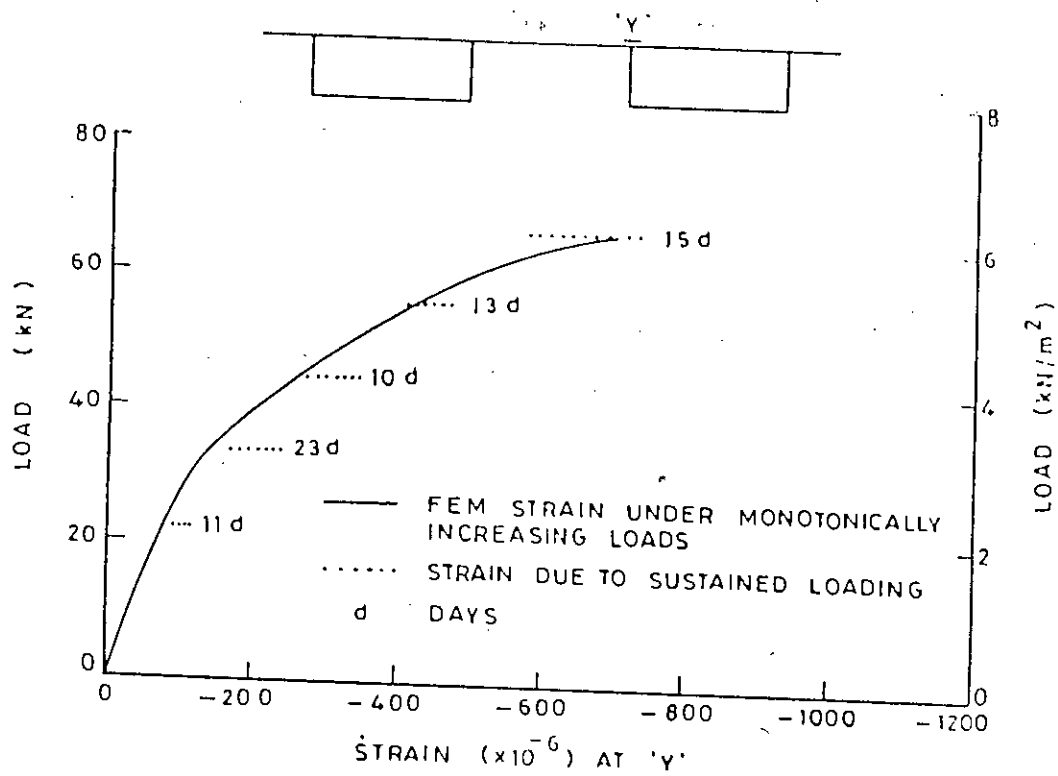


FIG. 6.5 - LOAD VS. LONGITUDINAL COMPRESSIVE STRAIN AT TOP SURFACE

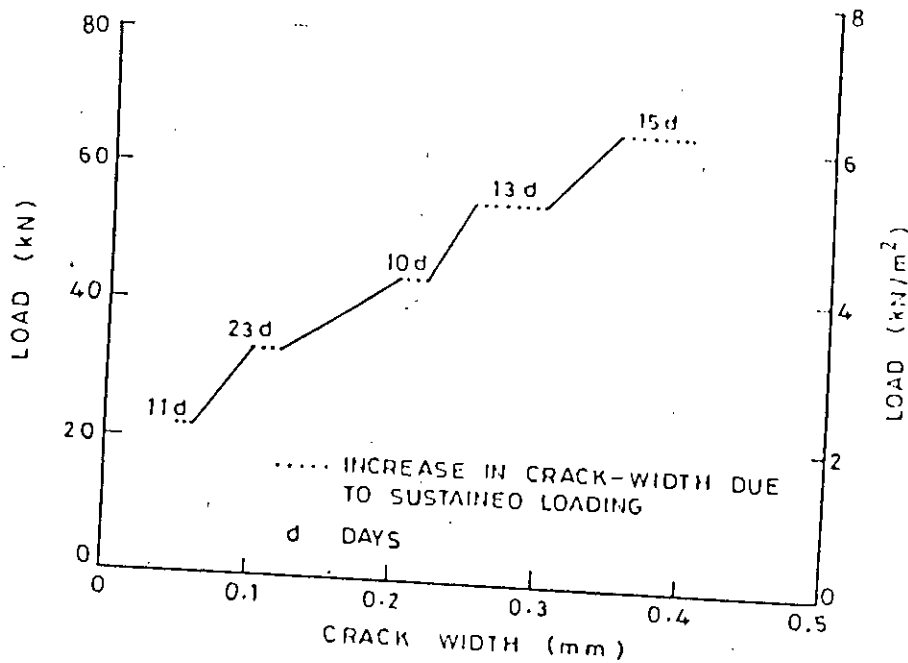
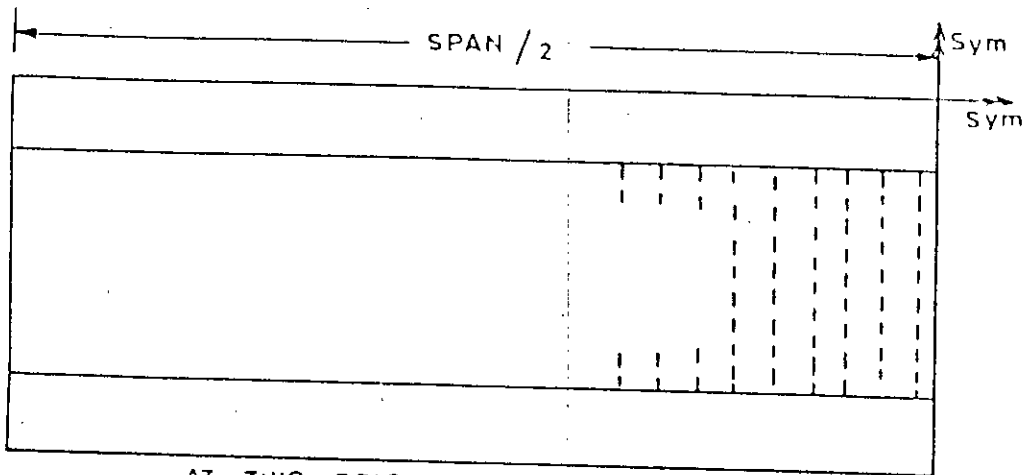
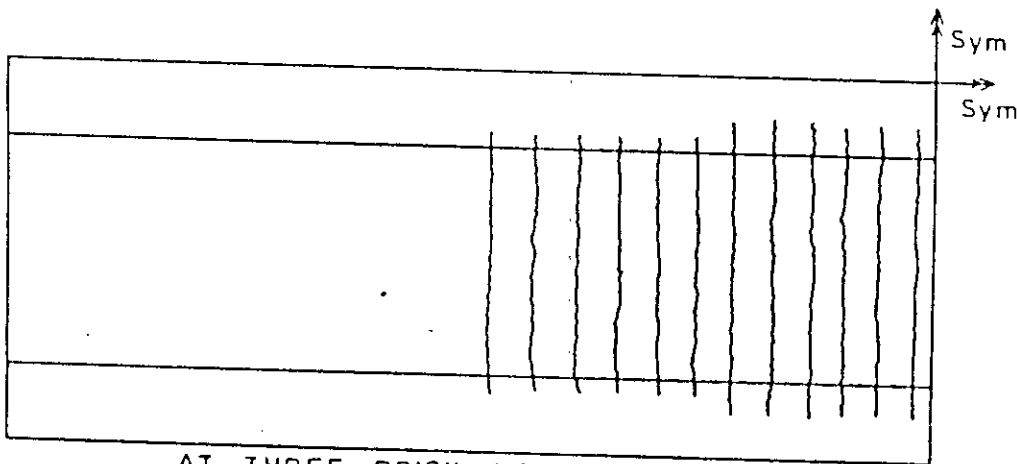


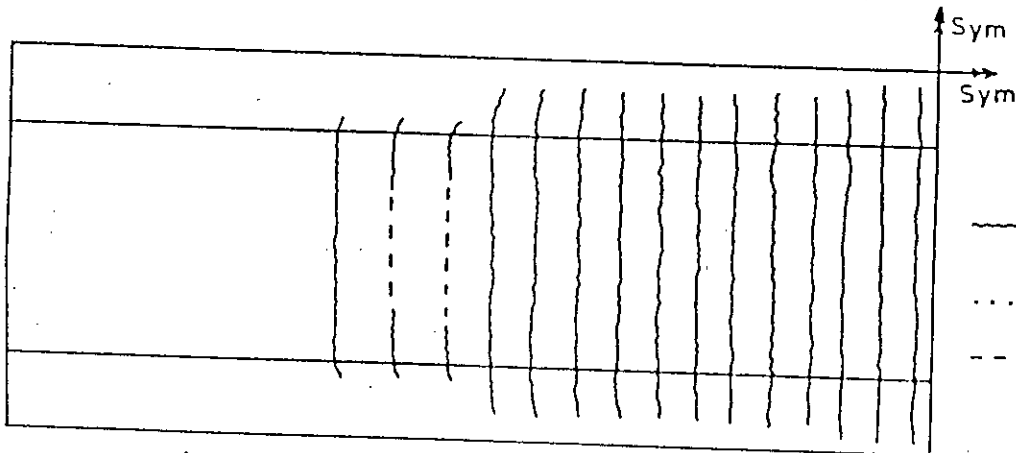
FIG. 6.6 - LOAD VS. MAXIMUM CRACK WIDTH CURVE



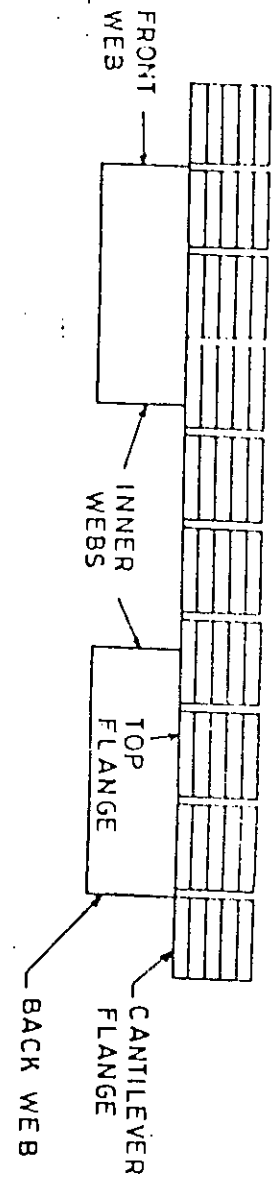
AT TWO BRICK LAYERS (22.19 kN)



AT THREE BRICK LAYERS (33.29 kN)

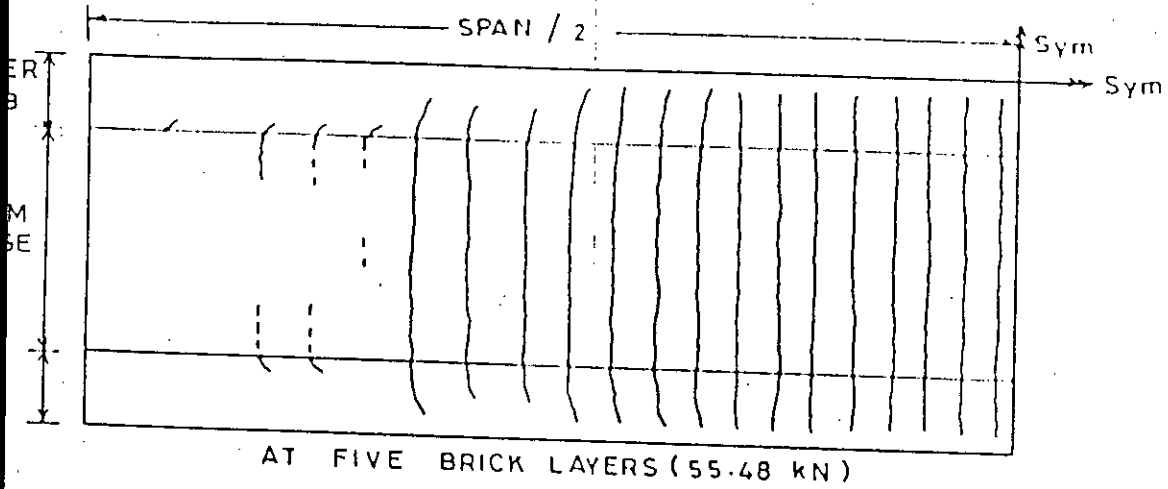


AT FOUR BRICK LAYERS (44.38 kN)

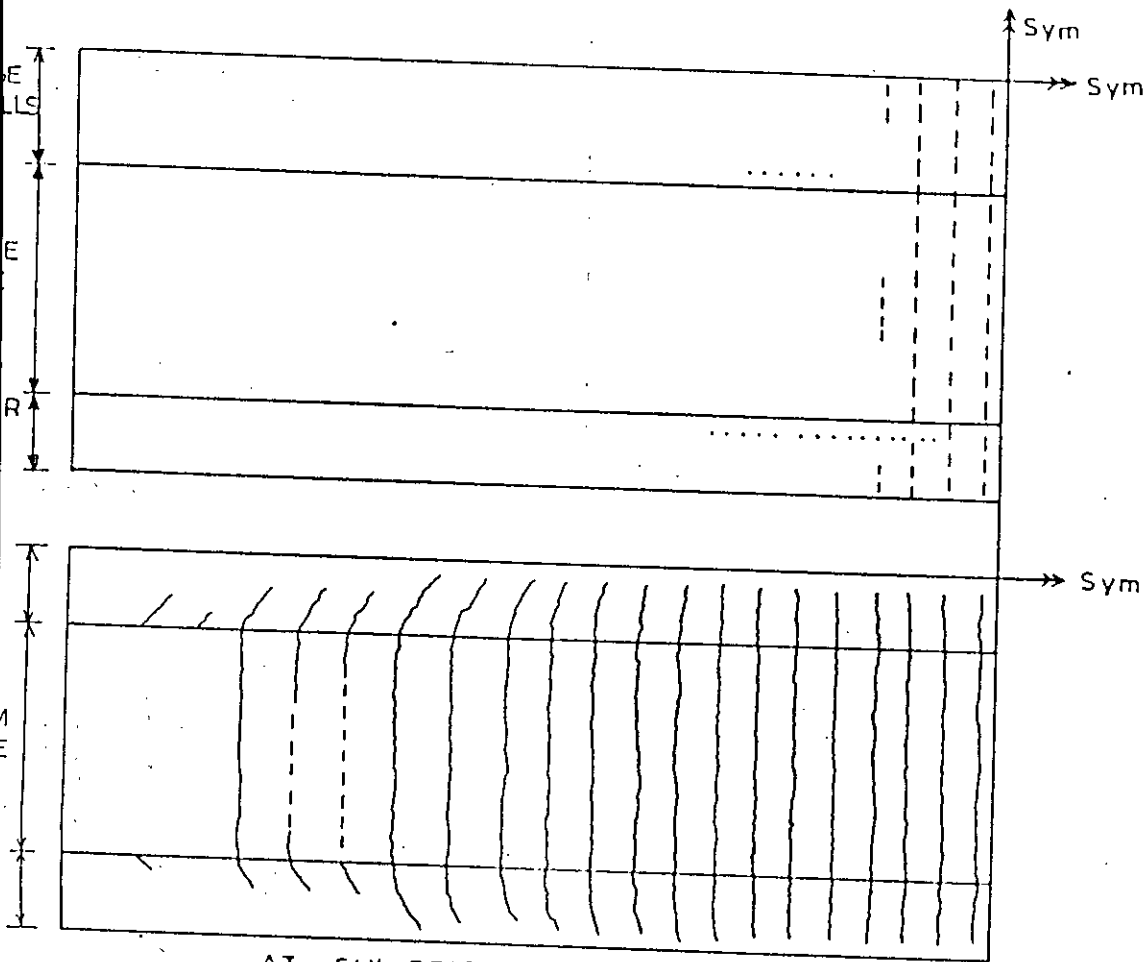


- FULL DEPTH CRACKED
- TOP CRACKED
- BOTTOM CRACKED

CONTD.



AT FIVE BRICK LAYERS (55.48 kN)



AT SIX BRICK LAYERS (66.57 kN)

6.7- PREDICTED CRACK-PATTERNS OF DOUBLE CELL BOX GIRDER SUBJECTED TO UDL OVER THE ENTIRE TOP FLANGE

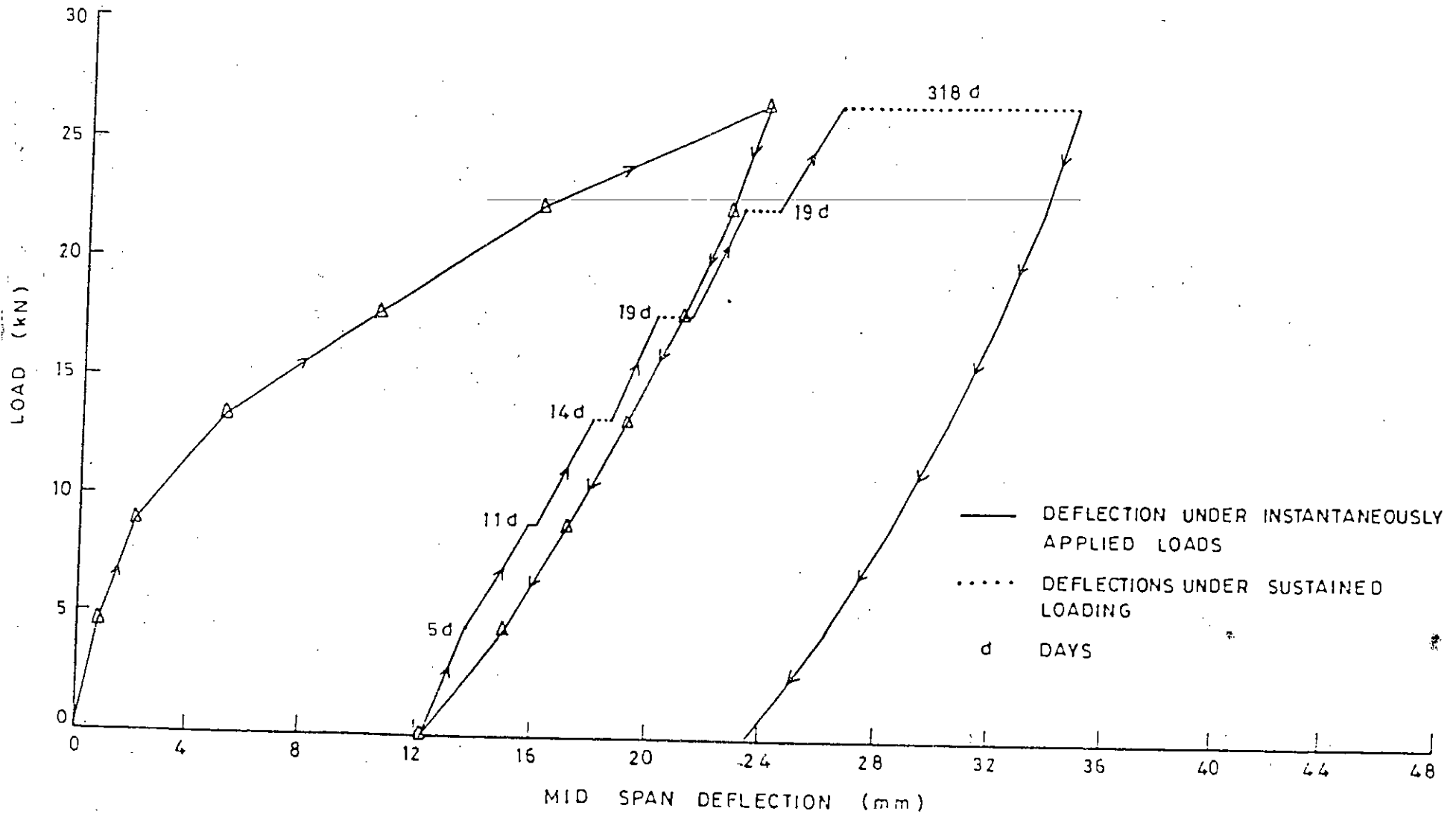


FIG. 6.8 — LOAD VS. MID SPAN DEFLECTION DUE TO SUSTAINED LOADING FOR COMPOSIT BOX GIRDER

CHAPTER VII

CONCLUSIONS AND SCOPE FOR FURTHER WORK

7.1 SUMMARY

The behaviour of ferrocement roofing/flooring elements in the form of channel sections, ribbed slabs, folded plates and shells of various shapes has been investigated by many researchers. Of the above, only channel sections and ribbed slabs provide a flat top surface. These elements possess small flexural rigidities and, therefore, undergo large deflections and cracking at service loads. In the present study, the behaviour of a new type of roofing/flooring element in the form of box section has been investigated both experimentally and analytically in the pre and the post cracking range.

The experimental investigation has been carried out by testing near prototype size ferrocement box girders. Two box girders were tested under udl over the entire top flange and two other under udl over half flange width and full span. Two box girders were joined at the level of top flange. The combined box girder was loaded and unloaded under various load combinations in the uncracked stage. The girder was later subjected to monotonically increasing sustained loads of short durations. One box girder with bottom flange and side webs of ferrocement and top flange of reinforced concrete was cast and tested under udl over the entire top flange. After unloading, it was again subjected to sustained loads of short durations upto the penultimate load and for ten and half months at maximum applied load. The experimental results in the form of deflections, strains and crack widths were recorded at various load levels.

The finite element method has been used to predict the behaviour of ferrocement box girders through the elastic, cracked and ultimate stages as

the conventional methods do not take into account the changing rigidity of the material at different sections, material anisotropy and yielding of the reinforcement leading to local redistribution of stresses. Further to economize the finite element solution, the conventional layered approach has been suitably modified for thin ferrocement plated structures. Instead of considering the element to be consisting of suitable number of layers of mortar and reinforcement, the element is assumed to be consisting of single mortar layer in the uncracked stage, uncracked and cracked mortar layers in the cracked stage and smeared layers of wire mesh and skeletal steel. In the cracked stage, the depth of cracked/yielded/crushed mortar is determined. The stiffness of the element in the cracked stage is obtained by adding the contributions due to uncracked mortar layer, cracked/yielded mortar layer and unyielded layers of wire mesh and skeletal steel.

The finite element analysis has been carried out under dead loads and monotonically increasing live loads. A rectangular flat shell element capable of representing membrane action, bending action and the interaction between membrane and bending action is adopted. Only material nonlinearity due to cracking of mortar, tension stiffening effect of mortar between the cracks and the nonlinear stress-strain relationships for the mortar, wire mesh and skeletal steel is considered. Since the box section provides large flexural and torsional rigidity, the deflections in the cracked range are assumed to be small. Hence, geometrical nonlinearity is not considered. Also not considered in the analysis are bond slip between the reinforcement and mortar, time dependent and thermal effects.

The validity of the proposed analytical method has been checked by comparing the predicted results with the reported experimental/analytical results of typical test problems taken from the literature as well as with the experimental results of the present investigation.

The proposed analytical method does not determine the spacing of cracks and the crack widths. The experimentally obtained average spacing of cracks and maximum crack widths are compared with the values predicted by analytical/empirical expressions reported by various researchers.

7.2 CONCLUSIONS

Based upon the results of the experimental and the analytical study undertaken and the comparison of the test results with the predicted ones, the following conclusions are drawn :

1. The proposed finite element formulation and the failure criteria adopted for the constituent materials are adequate for undertaking a nonlinear analysis of three dimensional ferrocement structures such as box girders. The predicted values from the proposed analytical method are generally in good agreement with the experimental values except near the ultimate failure load where predicted values are on the flexible side.
2. The proposed formulation is quite economical as compared to the conventional layered approach and yet capable of tracing the complete response of the structure through elastic, cracked and ultimate stages.
3. The maximum experimental compressive strains at the ultimate load (or maximum applied load) in single cell and double cell ferrocement box girders are within the linear elastic portion of the stress-strain curves of the mortar and the concrete respectively. Hence, the assumed linearly elastic-perfectly plastic stress-strain curves of the mortar and concrete in compression are adequate.
4. The maximum experimental deflection in the girders at the ultimate load is about span/150 (i.e. small). This justifies the neglecting of the geo-

metrical nonlinearity in the proposed finite element analysis of the box girders.

5. The predicted first crack loads show a good agreement with the experimental first crack loads of the various girders whereas the predicted ultimate loads are lower than the experimental ultimate loads due to the assumed linearly elastic-perfectly plastic stress-strain curves of skeletal steel and wire mesh.
6. The limit state of serviceability is governed by the maximum crack width. At the recommended crack width of 0.1 mm, the span/deflection ratio is much above the value of 250 as permitted by I.S. Code⁽¹⁶²⁾. At a span/deflection ratio of 250, the load taken by the girders is close to the yielding of the reinforcement.
7. The double cell box girder under various combinations of symmetrical and unsymmetrical loads in the uncracked stage has behaved as one single unit by undergoing downward deflections along the entire length and width. This demonstrates the large load distribution capability of the box section.
8. Replacing the top ferrocement flange by a reinforced concrete one results into the lowering of the first crack load. Thus the advantage of economy is offset by the reduction in the first crack load by about 30 percent. However, the load taken by the composite box girder at the recommended crack width of 0.1 mm is about the same as taken by single cell ferrocement box girders. The ultimate load taken by the girder is also reduced by about 14 percent.
9. The failure of the girders is characterized by well distributed flexural cracks over the bottom flange and the side webs. Shear cracks which

developed at near ultimate loads were not significant. The girders have shown high ductility by taking an ultimate load of 2.0 to 3.0 times the load at the appearance of first cracks or by undergoing deflection at ultimate load equal to 5.0 to 6.0 times the deflection at the appearance of first cracks.

10. The predicted crack-patterns of the bottom flange and the side webs (at ultimate or maximum applied loads) of various girders show good agreement with the experimental crack-patterns. The added advantage of the analytical method is the prediction of cracks on the soffit of the top flange at ultimate or near ultimate loads which can not be seen or noticed otherwise due to the closed form of the cell.
11. The average spacing of cracks predicted by the expressions given by Desayi and Ganesan⁽⁶⁸⁻⁷⁰⁾ has shown better agreement with the experimental values of the present investigation as compared to the values predicted by the expressions given by Naaman and Shah⁽³²⁾ and Huq and Pama⁽³⁸⁾.
12. None of the expressions considered are able to predict the values of the maximum crack width in the initial portion of the cracked range satisfactorily. The predicted values are far less than the experimental values of the girders. The probable reasons for this discrepancy may be (i) low volume fraction of mesh reinforcement, (ii) relatively large mortar cover (≈ 6.33 mm), (iii) the large size of the specimens, and (iv) compaction difficulty in casting ferrocement box girders. The predicted values of maximum crack width in the later portion of the cracked range and upto the yielding of the extreme layer of wire mesh using the expressions due to Logan and Shah and Naaman have shown relatively better agreement with the experimental values.

13. The effect of monotonically increasing sustained loads of short duration on the deflections and strains is maximum in the initial portion of the cracked range.
14. The instantaneous deflection of the girder is reduced due to the sustained loading at lower load levels as compared to the instantaneous deflection that would have occurred under monotonically increasing loads.
15. The ultimate load of the girder is not affected by the mode of loading i.e. monotonically applied instantaneous or sustained loads of short durations.
16. The effect of sustained loading is to increase the width of cracks and the region of crack formation.

7.3 SCOPE FOR FURTHER WORK

1. Behaviour of ferrocement box girders joined in the longitudinal direction by prestressing should be investigated to encourage prefabrication of standard sized elements.
2. The cracking behaviour of the box girders should be investigated using higher volume of reinforcement, different types of wire mesh and smaller cover in the bottom flange and side webs.
3. The method may be extended to include creep, shrinkage and temperature effects.
4. Factors like bond slip and strain hardening of the reinforcement may be incorporated in the formulation by using suitable strain compatibility factors.

5. There is a need to correlate the properties of the mortar matrix as determined by the control specimens to its actual state in the ferrocement element because of the difficulty of compaction. Until it is achieved, some discrepancy in the analytical and the actual behaviour is bound to occur.

REFERENCES

1. ACI Committee 549, "State-of-the-Art Report on Ferrocement", Concrete International : Design and Construction, August 1982, Vol.4, No.8, pp.13-28.
2. Nervi, P.L., "Structures", Translation by Giusappina and Salvadori, F.W. Lodge Corporation, New York, 1956, pp. 50-62.
3. Shah, S.P., "New Reinforcing Materials in Concrete", ACI Journal, Proceedings Vol.71, May 1974, p. 257.
4. Paramasivam, P., Nathan, G.K. and Lee, S.L., "Influence of Discrete Fibers on Behaviour of Ferrocement", Journal of Ferrocement, Vol.10, No.2, April 1980, pp. 105-110.
5. Atcheson, M. and Alexander, D., "Development of Fibrous Ferrocement", ACI Publication SP-61, Ferrocement-Materials and Applications, 1979, pp. 81-101.
6. Ohama, Y. and Shirai, A., "Prediction of Flexural Strength of Polymer-Ferrocement with Steel Fibers", Proceedings of the Second International Symposium on Ferrocement, Bangkok, Jan. 1985, pp. 145-156.
7. IS:269-1976, "Indian Standard Specification for Ordinary or Low Heat Portland cement", Indian Standards Institution, New Delhi.
8. ASTM Standard C-150-Specifications for Portland Cement.
9. IS:383-1970, "Indian Standard Specification for Coarse and Fine Aggregates from Natural Sources for Concrete", Indian Standards Institution, New Delhi.
10. ASTM Standard C-33-Specifications for Concrete Aggregates.
11. ASTM C-40-Test for Organic Impurities in Sands for Concrete.
12. Paul, B.K. and Pama, R.P., "Ferrocement", International Ferrocement Information Centre, Asian Institute of Technology, Bangkok, Thailand, 1978.
13. Guide for the Design, Construction and Repair of Ferrocement, reported by ACI Committee 549, ACI Structural Journal, May-June 1988, pp. 325-351.
14. Christensen, K.A. and Williamson, R.B., "Solving the Galvanic Cell Problem in Ferrocement", Report No. UC SESM71-14, University of California, Berkeley, U.S.A., 1971.
15. Cornet, I., Williamson, R.B., Bresler, B., Nagarajan, S. and Christensen, K.A., "Chromate Admixture to Improve Performance of Galvanized Steel in Concrete Sea Structures", Proceedings of the FIP Symposium on Concrete Sea Structures, Tbilisi, September 1972, pp. 159-163.
16. Cairncross, C., "Ferrocement Boat Construction", International Marine Publishing Company, Maine, 1972.

17. Morgan, R.G., "History of and Experience with Concrete Ships", Proceedings of the Conference on Concrete Ships and Floating Structures, September 1975, University of California, Berkley, pp. 3-16.
18. Walkus, B.R. and Kowalski, T.G., "Ferrocement : A Survey", Concrete, Cement and Concrete Association of London, February 1971, pp. 48-52.
19. Oberti, G., "Structural Design and Testing, By Means of Models of Some Special Constructions", RILEM/ISMES International Symposium on Ferrocement, Bergamo, 1981, pp. 2/17-2/32.
20. Mironkov, B.A., "Ferrocement Applications in the U.S.S.R.", Journal of Ferrocement, Vol.8, No.3, 1978.
21. National Academy of Sciences, "Ferrocement : Applications in Developing Countries", a report of an Ad Hoc Panel of the Advisory Committee on Technological Innovation, BOSTID, Washington, D.C., 1973.
22. Chang, W.F. and Nani, A., "Ferrocement factory Built Home", Proceedings of the Second International Symposium on Ferrocement, Bangkok, January 1985, pp. 445.
23. Barberio, V., "On Several Recent Ferrocement Constructions in Italy : Design and Construction Criteria", RILEM/ISMES International Symposium on Ferrocement, Bergamo, Italy, 1981, pp. 2/79-2/91.
24. Anon, "Hong Kong : Roslyn I - Ferrocement Trawler", Fishing News International, July 1971, p. 33.
25. Hurd, M.K., "Ferrocement-Boat Building and Beyond", Concrete Construction, April 1977, 4 pp.
26. Tang, T., Li, S. and Zhao, G., "Cost Analysis and Operational Performance of Ferrocement U-Aqueducts", Proceedings of the Second International Symposium on Ferrocement", Bangkok, 1985, pp. 559-564.
27. Verizhnikov, S., "Egg-Head Idea for Siberian Housing", New Scientist, 27 January 1972.
28. Reinhorn, A.M. and Prawel, S.P., "Ferrocement in a Large Shaking Table", Journal of the Structural Division, ASCE, Vol.112, No.2, Feb. 1986, pp. 401-416.
29. Ferrocement Applications : State-of-the-Art Reviews, Vol.1, IFIC Publication No.30/82, Bangkok.
30. RILEM/ISMES International Symposium on Ferrocement, Bergamo, Italy, 1981.
31. Second International Symposium on Ferrocement, Bangkok, 1985.
32. Naaman, A.E. and Shah, S.P., "Tensile Tests of Ferrocement", ACI Journal, Proceedings, V.68, No.9, Sept. 1971, pp. 693-698.
33. Desayi, P. and Jacob, K.A., "Strength and Behaviour of Ferrocement in Tension and Flexure", Proceedings of the Symposium on Modern Trends in Civil Engineering, University of Roorkee, Roorkee, Nov, 1972, pp.274-279.

34. Pama, R.P., Sutharatnachaiyarorn, C. and Lee, S.L., "Rigidities and Strength of Ferrocement", Proceedings, First Australian Conference on Engineering Materials, University of New South Wales, Sydney, 1974, pp. 287-308.
35. Johnston, C.D. and Mattar, S.G., "Ferrocement in Tension and Compression", Journal of the Structural Division, Proceedings ASCE, Vol.102, ST5, May 1976, pp. 875-899.
36. Walkus, B.R. and Mackiewicz, A., "Composites as Applied to the Thin Walled Structures in Poland", Bulletin, International Association for Shell and Spatial Structures (Madrid), Vol.18, No.69, August 1977, pp. 3-13.
37. Lee, S.L., Raisinghani, M. and Pama, R.P., "Mechanical Properties of Ferrocement", FAO Seminar on the Design and Construction of Ferrocement Vessels, October 1972.
38. Huq, S. and Pama, R.P., "Ferrocement in Tension : Analysis and Design", Journal of Ferrocement, Vol.8, No.3, July 1978, pp. 143-167.
39. Naaman, A.E. and McCarthy, M.R., "Efficiency of Ferrocement Reinforced with Hexagonal Mesh", Proceedings of the Second International Symposium on Ferrocement, Bangkok, Jan. 1985, pp. 121-134.
40. Bezukladov, V.F., Ameil'yanovich, K.K., Verbitskiy, V.D. and Bogoyavlenskiy, L.P., "Ship Hulls Made of Reinforced Concrete", NAVSHIPS Translation No. 1148, 1968.
41. Naaman, A.E., "Reinforcing Mechanisms in Ferrocement", M.S. Thesis, Massachusetts Institute of Technology, Sept. 1970.
42. Robinson, J.R., "Cours de Beton Arme de l'Ecole Nationale des Ponts et Chaussees", Paris, 1962-1963.
43. Robinson, J.R. and Morisset, A., "Parameters Fondamentaux de la fissuration des Tirants en Beton Arme", Annales de l'Institut Technique du batiment et des Travaux Publics, Paris, Feb. 1969.
44. Naaman, A.E., "Design Predictions of Crack Width in Ferrocement", Ferrocement-Materials and Applications, SP-61, American Concrete Institute, Detroit, 1979, pp. 25-42.
45. Bianchini, A.C., Kesler, C.E. and Lott, J.L., "Cracking of Reinforced Concrete Under External Load", Causes, Mechanism and Control of Cracking in Concrete, SP-20, American Concrete Institute, Detroit, 1968, pp. 73-85.
46. Pama, R.P., Intaragumhaeng, V. and Paul, B.K., "Study of Tensile Cracks and Bond-Slip in Ferrocement", Ferrocement-Materials and Applications, SP-61, American Concrete Institute, Detroit, 1979, pp. 43-79.
47. Somayaji, S. and Naaman, A.E., "Stress-Strain Response and Cracking of Ferrocement in Tension", Journal of Ferrocement, Vol.11, No.2, April 1981, pp. 127-142.
48. Somayaji, S. and Shah, S.P., "Prediction of Tensile Response of Ferrocement", RILEM/ISMES International Symposium on Ferrocement, Bergamo, Italy, 1981, pp. 1/73-1/84.

49. Akhtaruzzaman, A.K.M. and Pama, R.P., "Cracking Behaviour of Ferrocement in Tension", Proceedings of the Third International Symposium on Ferrocement, New Delhi, 1988, pp. 3-11.
50. Rao, A.K. and Gowder, C.S.K., "A Study of Behaviour of Ferrocement in Direct Compression", Cement and Concrete (New Delhi), Vol.10, No.3, Oct. 1969, pp. 231-237.
51. Desayi, P. and Jacob, A.K., "Ferrocement-Its Strength and Behaviour in Compression", Paper presented at the National Seminar on Materials Science and Technology, Madras, Feb. 1973.
52. Rajsekharan, S., Raju, G. and Palanichamy, K., "Behaviour of Ferrocement Specimens in Bending and Compression", Journal of Structural Engineering, Vol.2, No.4, Jan. 1975, pp. 145-154.
53. Kameswara Rao, C.B. and Kamasundra Rao, A., "Stress-Strain Curve in Axial Compression and Poisson's Ratio of Ferrocement", Journal of Ferrocement, Vol.16, No.2, April 1986, pp. 117-128.
54. Desayi, P. and Joshi, A.D., "Ferrocement Load Bearing Wall Elements", Journal of the Structural Division, Proceedings, ASCE, Vol.102, No. ST9, Sept. 1976, pp. 1903-1916.
55. Sandowicz, M. and Grabowski, J., "The Properties of Composite Columns made of Ferrocement Pipes Filled up with Concrete, Tested in Axial and Eccentric Compression", RILEM/ISMES International Symposium on Ferrocement, Bergamo, Italy, 1981, pp. 1/93-1/99.
56. Winokur, A. and Rosenthal, J., "Ferrocement in Centrally Loaded Compression Elements", Journal of Ferrocement, Vol.12, No.4, October 1982, pp. 357-364.
57. Collen, L.D.G. and Kirwan, R.W., "Some Notes on the Characteristics of Ferrocement", Civil Engineering and Public Works Review, Feb. 1959, Vol.54, pp. 195-196.
58. Rao, A.K. and Gowder, C.S.K., "A Study of the Behaviour of Ferrocement in Flexure", The Indian Concrete Journal, Vol.45, No.4, April 1971, pp. 178-183.
59. Logan, D. and Shah, S.P., "Moment Capacity and Cracking Behaviour of Ferrocement in Flexure", ACI Journal, Proceedings, Vol.70, No.12, December 1973, pp. 799-804.
60. Johnston, C.D. and Mowat, D.N., "Ferrocement-Material Behaviour in Flexure", Journal of the Structural Division, Proceedings ASCE, Vol.100, No. ST10, Oct. 1974, pp. 2071-2090.
61. Surya Kumar, G.V. and Sharma, P.C., "An Investigation of the Ultimate and First Crack Strength of Ferrocement in Flexure", Indian Concrete Journal, Nov. 1976, pp. 335-340 & 344.
62. Balaguru, P.N., Naaman, A.E. and Shah, S.P., "Analysis and Behaviour of Ferrocement in Flexure", Journal of Structural Engineering Division, Proceedings ASCE, Vol.103, No. ST10, October 1977, pp. 1937-1951.

63. Huq, S. and Pama, R.P., "Ferrocement in Flexure : Analysis and Design", *Journal of Ferrocement*, Vol.8, No.3, July 1978, pp. 143-167.
64. Balaguru, P., "Predictions of Crack Widths in Ferrocement Beams" *Journal of Ferrocement*, Vol.11, No.3, July 1981, pp. 203-214.
65. Balaguru, P., Naaman, A.E. and Shah, S.P., "Ferrocement in Bending, Part I : Static Non-linear Analysis", Report No. 76-2, Department of Materials Engineering, University of Illinois at Chicago Circle, Chicago, Ill., August 1976.
66. Swamy, R.N. and Al-wash, A.A., "Cracking Behaviour of Ferrocement in Flexure", RILEM/ISMES International Symposium on Ferrocement, Bergamo, Italy, pp. A/1-A/11.
67. Swamy, R.N. and Spanos, A., "Deflection and Cracking Behaviour of Ferrocement with Grouped Reinforcement and Fiber Reinforced Matrix", *ACI Journal, Proceedings*, Vol.82, No.8, Jan.-Feb. 1985, pp. 79-91.
68. Desayi, P. and Ganesan, N., "Determination of Maximum Crack Width in Ferrocement Flexural Elements of Channel Cross-section", *The International Journal of Cement Composite and Light-weight Concrete*, Vol.6, No.3, 1984, pp. 169-177.
69. Desayi, P. and Ganesan, N., "A Method for the Prediction of Maximum Crack Width in Undulated Ferrocement Roofing Elements", In *Proceedings, Asia Pacific Symposium on Ferrocement Applications for Rural Development*, Roorkee, 1984, pp. 221-231.
70. Desayi, P. and Ganesan, N., "Prediction of Spacing and Maximum Width of Cracks in Ferrocement Built-up I-Joists", *Journal of Ferrocement*, Vol.17, No.2, April 1987, pp. 117-130.
71. Desayi, P., "Determination of the Maximum Crack Width in Reinforced Concrete Members", *ACI Journal, Proceedings*, Vol.73, No.8, 1976, pp.473-477.
72. Yen, T. and Su, C.F., "Influence of Skeletal Steel on the Flexural Behaviour of Ferrocement", *Journal of Ferrocement*, Vol.10, No.3, July 1980, pp. 177-188.
73. Mansur, M.A. and Paramasivam, P., "Cracking Behaviour and Ultimate Strength of Ferrocement in Flexure", *Proceedings of the Second International Symposium on Ferrocement*, Bangkok, 1985, pp. 47-59.
74. Kaushik, S.K., Trikha, D.N. and Kotdawala, R.R., "Ultimate Strength Behaviour of Ferrocement Beams", RILEM/ISMES International Symposium on Ferrocement, Bergamo, Italy, 1981, pp. 2/115-2/126.
75. Prawel Jr., S.P. and Reinhorn, A., "Properties in Flexure of Ferrocement Panels in Two Way Bending", RILEM/ISMES International Symposium on Ferrocement, Bergamo, Italy, 1981, pp. 1/101-1/112.
76. Trikha, D.N., Kaushik, S.K. and Kotdawala, R.R., "Limit Analysis of Ferrocement Thin Slabs", *Journal of Ferrocement*, Vol.11, No.2, April 1981, pp. 111-126.

77. Meek, J.L., "Ultimate Strength of Simply Supported Ferrocement Slabs", *Journal of Ferrocement*, Vol.11, No.3, July 1981, pp. 215-228.
78. Mansur, M.A. and Ong, K.C.G., "Shear Strength of Ferrocement Beams", *ACI Structural Journal*, Vol.84, No.1, Jan.-Feb. 1987, pp. 10-17.
79. Venkata Krishna, H.V. and basa Gouda, P., "Some Studies on the Behaviour of Ferrocement in Shear", *Proceedings of the Third International Symposium on Ferrocement*, New Delhi, 1988, pp. 99-105.
80. Picard, A. and Lachance, L., "Preliminary Fatigue Tests on Ferrocement Plates", *Cement and Concrete Research*, Vol.4, 1974, pp. 967-978.
81. McKinnon, E.A. and Simpson, M.G., "Fatigue of Ferrocement", *Journal of Testing and Evaluation*, JTEVA, Vol.3, No.5, 1975, pp. 359-363.
82. Karasudhi, P., Mathew, A.G. and Nimityongskul, P., "Fatigue of Ferrocement in Flexure", *Journal of Ferrocement*, Vol.7, No.2, October 1977, pp. 80-95.
83. Balaguru, P.N., Naaman, A.E. and Shah, S.P., "Fatigue Behaviour and Design of Ferrocement Beams", *Journal of Structural Division*, *Proceedings ASCE*, ST7, July 1979, pp. 1333-1345.
84. Paramasivam, P., Das Gupta, N.C. and Lee, S.L., "Fatigue Behaviour of Ferrocement Slabs", *Journal of Ferrocement*, Vol.11, No.1, January 1981, pp. 1-10.
85. Bennet, E.W., Fakhri, N.A. and Singh, G., "Fatigue Characteristics of Ferrocement in Flexure", *ACI Journal*, *Proceedings*, March-April 1985, pp. 129-135.
86. Raisinghani, M. and Sai, A.S.R., "Creep and Fatigue Characteristics of Ferrocement Slabs", *Journal of Ferrocement*, Vol.14, No.4, October 1984, pp. 309-322.
87. Shah, S.P. and Key, W.H., "Impact Resistance of Ferrocement", *Journal of Structural Division*, *ASCE*, Vol.98, No.ST1, January 1972, pp. 111-123.
88. Greenius, A.W. and Smith, D., "Ferrocement for Canadian Fishing Vessels", Vol.2, Project Report No.48, Industrial Development Branch, Fisheries Service, Department of Environment, Ottawa, January 1972.
89. Burgess, W.M. and Allen, D.C., "Impact Resistance of Reinforced Concrete as a Problem of Containment", *Research Report No. R251*, University of Sydney, August 1974.
90. Nimityongskul, P., Bor-Shiun, C. and Karasudhi, P., "Impact Resistance of Ferrocement Boat Hulls", *Journal of Ferrocement*, Vol.10, No.1, January 1980, pp. 1-10.
91. Srinivasa Rao, P., Achyutha, H., Mathews, M.S. and Srinivasan, P.P., "Impact Studies on Ferrocement Slabs", *RILEM/ISMES International Symposium on Ferrocement*, Bergamo, Italy, 1981, pp. 1/7-1/19.
92. Grabowski, J., "Ferrocement Under Impact Loads", *Journal of Ferrocement*, Vol.15, No.4, October 1985, pp. 331-341.

93. Brauer, F.E., "The Mechanical Properties of Ferrocement", Naval Ship Research and Development Centre, Materials Department, Annapolis, Report 3588, August 1972.
94. Ravindrarajah, R. and Tom, T.C., "Dimensional Stability of Ferrocement", Journal of Ferrocement, Vol.13, No.1, January 1983, pp. 1-12.
95. Swamy, R.N. and Spanos, A., "Creep Behaviour of Ferrocement Sections", Proceedings of the Second International Symposium on Ferrocement, Bangkok, January 1985, pp. 103-118.
96. Illston, J.M. and Stevens, R.F., "Long-term Cracking in Reinforced Concrete Beams", Proceedings, Institution of Civil Engineers (London), Vol.53, Part 2, 1972, pp. 445-459.
97. Greenuis, A.W., "Ferrocement for Canadian Fishing Vessel", No.88, Technical Report Series of the Industrial Development Branch, Fisheries and Marine Service, Environment, Canada, 1975.
98. Naaman, A.E. and Sabins, G.M., "Tentative Guidelines for the Use of Ferrocement in Some Structural Applications", Proceedings of the International Conference on Materials of Construction for Developing Countries, Bangkok, Thailand, pp. 677-688.
99. Bigg, G.W., "An Introduction to Design for Ferrocement Vessels", Industrial Development Branch, Fisheries Service, Canada, 1972.
100. Mathews, M.S., Achyutha, H. and Rao, P.S., "Environmental Effects on Cracked Ferrocement", In Proceedings of the Asia-Pacific Symposium on Ferrocement Applications for Rural Development, Roorkee, India, 1984, pp. 217-220.
101. Trikha, D.N., Sharma, S.P., Kaushik, S.K., Sharma, P.C. and Tiwari, V.K., "Corrosion Studies of Ferrocement Structures", Journal of Ferrocement, Vol.14, No.3, July 1984, pp. 221-233.
102. Selvi Rajkumari, S., Neelamegam, M., Rajmane, N.P. and Peter, J.A., "Effect of Sea Water on Ferrocement With and Without Polymer Impregnation", Proceedings of the Second International Symposium on Ferrocement, Bangkok, January 1985, pp. 681-688.
103. Chowdhury, S.M.M.I. and Nimityongskul, "Some Aspects on Corrosion of Galvanized Wire Mesh in Ferrocement Under Simulated Adverse Environments", Proceedings of the Second International Symposium on Ferrocement, Bangkok, January 1985, pp. 689-700.
104. Ravindrarajah, S.R. and Paramasivam, P., "Influence of Weathering on Ferrocement Properties", Proceedings of the Second International Symposium on Ferrocement, Bangkok, January 1985, pp. 75-88.
105. Yozuqullu, O., "Durability of Sulfur Impregnated Precast Ferrocement Elements", Journal of Ferrocement, Vol.16, No.4, October 1986, pp. 429-435.
106. Irons, M.E., "Corrosion and Corrosion Prevention in Ferrocement Hulls", Journal of Ferrocement, Vol.14, No.2, April 1984, pp. 159-162.

107. Sharma, P.C., "Coating of Ferrocement Surface", Proceedings of the Second International Symposium on Ferrocement, Bangkok, January 1985, pp. 641-654.
108. Paramasivam, P. and Mansur, M.A., "Tensile and Flexural Behaviour of Joints in Ferrocement", ACI Journal, Proceedings, September-October 1985, pp. 710-715.
109. Kaushik, S.K., Gupta, V.K. and Rahman, M.K., "Efficiency of Mesh Overlaps of Ferrocement Elements", Journal of Ferrocement, Vol.17, No.4, October 1987, pp. 329-336.
110. Desayi, P. and Ramesh, N.L., "Tests on Ferrocement Channel Units", RILEM/ISMES International Symposium on Ferrocement, Bergamo, Italy, 1981, pp. 2/69-2/77.
111. Venkatakrishna, H.V. and Honne Gowda, H., "Precast Ferrocement Channel Types Slab and Beam Units", In Proceedings Asia-Pacific Symposium on Ferrocement Applications for Rural Development, Roorkee, India, 1984, pp. 87-94.
112. Sandowicz, M., "Application of Ferrocement Channel Elements to Housing", Proceedings of the Second International Symposium on Ferrocement, Bangkok, January 1985, pp. 493-505.
113. Sarid, M., Tatsa, E.Z. and Bljoger, F., "Ribbed Slabs Made of Ferrocement", Journal of Ferrocement, Vol.9, No.4, October 1979, pp. 185-189.
114. Bljoger, F., "Agricultural Buildings of Ribbed Ferrocement Elements", Journal of Ferrocement, Vol.12, No.1, January 1982, pp. 35-39.
115. Lukashenko, I.A., Galitch, V.D., Dubinski, A.M. and Borisova, T.V., "Experimental Investigations of Ribbed Ferrocement Vault of 18 m Span", RILEM/ISMES International Symposium on Ferrocement, Bergamo, Italy, pp. 2/53-2/57.
116. Kaushik, S.K., Trikha, D.N., Kotdawala, R.R. and Sharma, P.C., "Prefabricated Ferrocement Ribbed Elements for Low-Cost Housing", Journal of Ferrocement, Vol.4, No.4, October 1984, pp. 347-364.
117. Vishwanath, T., Mhatre, R.P. and Seetharamulu, K., "Test of a Ferrocement Precast Folded Plate", Journal of the Structural Division, Proceedings ASCE, Vol.91, No. ST6, Dec. 1965, pp. 239-249.
118. Fernandes, R., Gopalratnam, V.S. and Nimityongskul, P., "Evaluation of Ferrocement Folded-Plate Roofing Panels", Journal of Ferrocement, Vol.10, No.2, April 1980, pp. 69-88.
119. Lee, P.S., "Evaluation of a Corrugated Asbestos Cement Roof Panel", M. Engg. Thesis No. 817, Asian Institute of Technology, Bangkok.
120. Desayi, P., Viswanatha, C.S. and Kanappan, S., "Some Studies on Ferrocement Roofing Elements", Journal of Ferrocement, Vol.12, No.3, July 1982, pp. 273-288.

121. Paramasivam, P., Shanmugam, N.E., Ravindrarajah, R.S. and Lee, S.L., "A Prefabricated Ferrocement Folded Plate Bus Shelter", Proceedings of the Second International Symposium on Ferrocement, Bangkok, January 1985, pp. 547-558.
122. Bathe, K.J., Wilson, E.L. and Peterson, F.E., "SAP IV : A Structural Analysis Program for Static and Dynamic Response of Linear System", Report No. EERC 73-11, University of California, Berkley, California, U.S.A., 1974.
123. Paramasivam, P. and Lee, S.L., "Ferrocement Structural Elements", RILEM/ISMES International Symposium on Ferrocement, Bergamo, Italy, p. 3/37-3/46.
124. Das Gupta, N.C., Paramasivam, P. and Lee, S.L., "A Ferrocement Hyperbolic Paraboloid Shell", Journal of Ferrocement, Vol.10, No.4, Oct. 1980.
125. Elangovan, S. and Santha Kumar, A.R., "Behaviour of Room Size Ferrocement Funicular Shell", Journal of Ferrocement, Vol.14, No.4, October 1984, pp. 323-328.
126. IS : 875-1964, "Indian Standard Code of Practice for Structural Safety of Buildings : Loading Standards", Indian Standards Institution, New Delhi.
127. Subrahmanyam, B.V., Karim, E.A., Babu, K.G. and RAMAIIH, M., "Ferrocement Ribbon Roofs for Long Spans", Journal of Structural Engineering, 1981, pp. 39-47.
128. Rajagopalan, R. and Parameswaran, V.S., "Analysis of Ferrocement Beams", Journal of Structural Engineering, Vol.2, No.4, January 1975, pp. 155-164
129. Tatsa, E.Z., Prawel, S.P. and Reinhorn, A., "Long Span Composite Roof Systems of Ferrocement and Frame Components", Journal of Ferrocement, Vol.11, No.1, January 1981, pp. 55-66.
130. Maisel, B.I. and Roll, F., Methods of Analysis and Design of Concrete Box Beams with Side Cantilevers, Technical report TRA 42494, The Cement and Concrete Association, November 1974.
131. Richmond, B., "Twisting of Thin Walled Box Girders", Proceedings of the Institution of Civil Engineers, April 1966, pp. 659-675.
132. Kupfer, H., "Box Beam with Elastically Stiffened Cross-Section Under Line- and Point Loads", Edited by Knitted, G. and Kupfer, H., W. Ernst U. Sohn, Berlin, 1969, pp. 251-263.
133. Steinle, A., "Torsion and Cross-Sectional Distortion of the Single Cell Box Beam", Beton-und Stahlbetonbaus, September 1970, pp. 215-22, October 1970, pp. 249-254 and June 1972, pp. 143-144.
134. Goldberg, J.E. and Leve, H.L., "Theory of Prismatic Folded Plate Structures", IABSE Publications, Zurich, Switzerland, Vol.17, 1957, pp. 59-86.
135. Scordelis, A.C., Analysis of Simply Supported Box Girder Bridges, Structural Engineering and Structural Mechanics Report No. SESM 66-17, University of California, Berkeley, 1966.

136. Chu, K.H. and Dudnik, E., "Concrete Box Girder Bridges Analysed as Folded Plates", Concrete Bridge Design, ACI Publications SP-23, 1969, pp. 221-246.
137. Cheung, Y.K., "Folded Plate Structures by Finite Strip Method", Journal of Structural Division, Proceedings ASCE, Vol.95, No. ST12, December 1969, pp. 2963-79.
138. Cheung, Y.K., "Analysis of Box Girder Bridges by Finite Strip Method", Concrete Bridge Design, ACI Publications SP-26, 1971, pp. 357-378.
139. Cheung, Y.K., Finite Strip Method in Structural Analysis, Pergamon Press, 1976.
140. Kaushik, S.K., Gupta, V.K. and Sehgal, V.K., "Performance Evaluation of Ferrocement Box Girder Elements for Roofs and Floors", Journal of Ferrocement, Vol.18, No.4, October 1988, pp. 413-420.
141. Jofriet, J.C. and McNeice, G.M., "Finite Element Analysis of Reinforced Concrete Slabs", Journal of the Structural Division, ASCE, Vol.97, No. ST3, Proceedings Paper 7963, March 1971, pp. 785-806.
142. Bell, J.C., "A Complete Analysis for Reinforced Concrete Slabs and Shells", Thesis presented to the University of Canterbury, at Christchurch, New Zealand, in 1970, in partial fulfillment for the degree of Doctor of Philosophy.
143. Prakhya, K.V.G. and Adidam, S.R., "Finite Element Analysis of Ferrocement Plates", Journal of Ferrocement, Vol.17, No.4, October 1987, pp. 313-320.
144. Zienkiewicz, O.C. and Cheung, Y.K., "Finite Element Procedures in the Solution of Plate and Shell Problems", Chapter 8 of Stress Analysis (Eds. O.C. Zienkiewicz and G.S. Holister), Wiley, 1965.
145. Zienkiewicz, O.C. and Cheung, Y.K., "Finite Element Method of Analysis for Arch Dam Shells and Comparison with Finite Difference Procedures", Proceedings of the Symposium on Theory of Arch Dams", Southampton University, 1964 (Pergamon Press, 1965).
146. Ergatoudis, J.G., Irons, B.M. and Zienkiewicz, O.C., "Curved Isoparametric, Quadrilateral Elements for Finite Element Analysis", International Journal of Solids and Structures, Vol.4, 1968, pp. 31-42.
147. Hinton, E., Razaque, A. and Zienkiewicz, O.C., "A Simple Finite Element Solution for Plates of Homogeneous, Sandwich and Cellular Construction", Proceedings of the Institution of Civil Engineers, London, Part 2, 59, March 1975, pp. 43-65.
148. Gibson, J.E. and Mitwally, M.H., "An Experimental and Theoretical Investigation of Model Box Beams in Perspex and Micro-Concrete", The Structural Engineer, Vol.54, No.4, April 1976, pp. 147-151.
149. Zienkiewicz, O.C., The Finite Element Method, Third Edition, McGraw-Hill Publication, London, 1977.

150. McLeod, I.A., "New Rectangular Finite Element for Shear Wall Analysis", Journal of Structural Division, Proc. ASCE, Vol.95, 1969, pp. 399-409.
151. Lim, T.K., "Elastic Analysis of Bridge Structures by Finite Element Method", Ph.D. Thesis, Imperial College London, June 1971.
152. Zienkiewicz, O.C., Taylor, R.L. and Too, J.M., "Reduced Integration technique in General Analysis of Plates and Shells", International Journal of Numerical Methods in Engg., Vol.3, 1971, pp. 275-290.
153. Kupfer, H., Hilsdorf, H.K. and Rush, H., "Behaviour of Concrete Under Biaxial Stresses", Proc. ACI Journal, Vol.66, August 1969, pp. 656-666.
154. Liu, T.C.Y., Nilson, A.H. and Slate, F.O., "Biaxial Stress-Strain Relations for Concrete", ASCE Journal, May 1972.
155. Hand, F.R., Pecknold, D.A. and Schnobrich, W.C., "Nonlinear Layered Analysis of R.C. Plates and Shells", Journal of Structural Division, Proc. ASCE, Vol.99, No. ST7, July 1973, pp. 1491-1505.
156. Scanlon, A., "Time Dependent Deflection of Reinforced Concrete Slabs", Ph.D. Dissertation, Deptt. of Civil Engg., University of Alberta, Edmonton, Dec. 1971.
157. Scordelis, A.C., Cray, E.L. and Stubbs, I.R., "Experimental and Analytical Study of a Folded Plate", Journal of Structural Division, Proc. ASCE, Dec. 1961, pp. 139-160.
158. Scordelis, A.C. and Gerasimenko, P.V., "Strength of Reinforced Concrete Folded Plate Models", Journal of Structural Division, Proc. ASCE, Vol.92, No. ST-1, Feb. 1966, pp. 351-363.
159. McNeice, G.M., "Elastic-Plastic Analysis of Flat Plates by the Finite Element Method", Thesis presented to the University of London, at London, England, in 1967, in partial fulfillment of the requirements for the degree of Doctor of Philosophy.
160. Lin, C.S. and Scordelis, A.C., "Nonlinear Analysis of R.C. Shells of General Form", Journal of the Structural Division, Proc. ASCE, Vol.101, No. ST3, March 1975, pp. 523-538.
161. Al-Sulaimani, G.J. and Ahmad, S.F., "Deflections and Flexural Rigidity of Ferrocement I - and Box - Beams", Journal of Ferrocement, Vol.18, No.1, January 1988.
162. IS : 456-1978, "Indian Standard Code of Practice for Plain and Reinforced Concrete", Indian Standards Institution, New Delhi.
163. Gamski, K., "Ferrocement", RILEM/ISMES International Symposium on Ferrocement, Bergamo, Italy, 1981, pp. 1/1-1/6.

